Simultaneous EEG and fMRI at High Fields

By Karen Julia Mullinger, BSc.

Thesis submitted to the University of Nottingham for the degree of Doctor of Philosophy.

March 2008

Acknowledgements

I would firstly like to thank my supervisors Richard Bowtell and Paul Morgan for their help and patience over the last three years. Without them this would not have been possible and how they have put up with my endless questions I will never know, so *thank you*! I would also like to thank Kay Head and Andrew Peters for all they have taught me about using the scanners and the Suns and all the computer programs which have gone with this work. Thank you also to Ron Coxon for help in combining EEG and fMRI data. A large thanks also goes to Matthew Brookes for all his help in my project. Thank you for helping with programming, experiments and all the conversations with abstract ideas flying around! I would also like to thank all the people at Philips Medical Systems, especially Matthew Clemence, who have helped me through this PhD both with experiments and financially. I have enjoyed all the opportunities working with the company have presented. I must also thank all those people who have volunteered for me both internals and externals.

Next I would like to thank all of my friends at the MR Centre and elsewhere. A special thanks goes to Eleanor, Claire, Mary, Lesley, Nicki, Matt, Nic and Alex-thank you for all the laughs and fun you have provided me over the last three years-it would not have been as enjoyable without you! Thanks also to my housemates and friends for keeping me sane and helping me maintain perspective. I must especially thank Anna for calming me down when things got tough and for making me realise the more important things in life. Thank you also Clare, Helen and Jess who have been amazingly understanding and patient-living with me can't have been easy for the last year! Thanks also to Fi, Linz, Nath, Bryan, Grace, Julia, Lucy, Jenny, Jen and Vicki for pretending to be interested even if they weren't!

Finally I must thank my family. Mum and Dad thank you for always believing in me even when I didn't. I couldn't have asked for more support and a better grounding through school and university. Thanks for all your interest in what I do, although Dad, it's still all magic! Thank you Debbie for always bringing me back down to earth and reminding me that I am not that clever-you will always ensure that my head doesn't get too big!

Contents

Abstract vi

Chapter 1 1

Introduction 1

1.1 Why Investigate the Brain? 1

1.1.1 Direct Measures of Brain Activity 3

1.1.2 Indirect Measures of Brain Activity 5

1.1.3 Compete or complement? 7

1.2 Thesis overview 8

1.3 References 10

Chapter 2 13

Nuclear Magnetic Resonance 13

2.1 Introduction 13

2.2 Properties of Nuclei 13

2.2.1 Spin Angular Momentum 13

2.2.2 Magnetic Moments 15

2.3 Magnetic Resonance: A Classical description 17

2.3.1 Static Magnetic field: Larmor Precession 17

2.3.2 Time Dependent Magnetic Field: Interactions with RF radiation. 19

2.4 More than one spin? 22

2.4.1 Bulk Magnetisation 22

2.4.2 Spin interactions 25

2.5 References 34

Chapter 3 35

Magnetic Resonance Imaging 35

3.1 Introduction 35

3.2 Image formation 35

3.2.1 *k*-space 35

3.2.2 Slice selection 38

3.3 Spin warp imaging 42

- 3.4 Image Contrast 44
- 3.5 Echo Planar Imaging 46
  - 3.5.1 Limitations of EPI 47
  - 3.5.2 Multi-Shot 51
  - 3.5.3 Sensitivity Encoding 51
- 3.6 Instrumentation 52
  - 3.6.1 Magnet 53
  - 3.6.2 Gradient System 54
  - 3.6.3 RF coils and transmission 55
  - 3.6.4 Control 57
- 3.7 Safety 57
  - 3.7.1 Static fields 57
  - 3.7.2 Gradients 58
  - 3.7.3 RF field 59
  - 3.7.4 Electric Field 59
- 3.8 References 60

Chapter 4 63

Brain Anatomy and Physiology 63

- 4.1 The Brain and how it functions 63
  - 4.1.1 Cellular Brain Structure 63
  - 4.1.2 Neurotransmission 66
  - 4.1.3 Macroscopic Brain Structure and function 70
- 4.2 Detecting Brain Activity 71
  - 4.2.1 Electroencephalography 72
  - 4.2.2 Functional Magnetic Resonance Imaging 89
- 4.3 References 102

Chapter 5 106

Multimodality Imaging-EEG and fMRI 106

- 5.1 Introduction 106
- 5.2 Combination Issues 106
  - 5.2.1 EEG data quality 106
  - 5.2.2 MR data quality 113
  - 5.2.3 Safety 115

5.3 Uses 116
5.3.1 Fusing the data 118
5.4 Conclusion 124
5.5 References 125

Chapter 6 129

Simultaneous EEG and fMRI: EEG Artefact Correction. 129

6.1 Introduction 129
6.2 Background 129
6.3 Methods 131
6.3.1 Experiment 1: The effectiveness of synchronisation and the VCG on artefacts removal. 134
6.3.2 Experiment 2: Increasing the range of frequencies of detected neurological signals. 134
6.4 Analysis 135
6.4.1 Experiment 1: The effectiveness of synchronisation and the VCG on artefacts removal. 135
6.4.2 Experiment 2: Increasing the range of frequencies of detected neurological signals. 138
6.5 Results 139
6.5.1 Experiment 1: The effectiveness of synchronisation and the VCG on artefacts removal. 139
6.5.2 Experiment 2: Increasing the range of frequencies of detected neurological signals. 145
6.6 Discussion 147
6.7 Conclusion 151
6.8 References 153

Chapter 7 155

Effect of Simultaneous EEG recording on MRI Data Quality 155

7.1 Introduction 155
7.2 Background and Theory 155
7.2.1 Magnetic susceptibility effects (B_0-inhomogeneity) and detection 156
7.2.2 B_1-Inhomogeneity 161
7.3 Methods and Analysis 163

7.4 Results 170

7.4.1 B_0-Inhomogeneity: 170

7.4.2 B_1-Inhomogeneity: 172

7.4.3 MPRAGE data 174

7.5.3 Effects of Caps on EPI data: 175

7.5 Discussion 179

7.6 Conclusion 183

7.7 References 185

Chapter 8 187

Combining EEG with fMRI at 7T: What is Possible? 187

8.1 Introduction and Background 187

8.3 Noise Sources in EEG from Magnet Hall 194

8.3.1 Methods 194

8.3.2 Results and Discussion of Noise Sources 195

8.4 Preliminary Experiments 198

8.4.1 Methods 198

8.4.2 Analysis of Human data 200

8.4.3 Results and Discussion of the Preliminary Experiments 201

8.4.4 Conclusion to the Preliminary Experiments 204

8.5 Optimised Experiment 205

8.5.1 Methods 206

8.5.2 Analysis of Human data 208

8.5.3 Results and Discussion 209

8.6 Conclusion 216

8.7 References 217

Chapter 9 220

Combined EEG/fMRI study of the response to periodic visual stimulation. 220

9.1 Introduction 220

9.2 Background 221

9.3 Methods 228

9.3.1 Subject Screening 228

9.3.2 Experimental method 230

9.4 Analysis 234

9.4.1 General 234
9.4.2 Experiment 1: Oscillatory rhythms and the BOLD response 235
9.4.3 Experiment 2: Stimulus Frequency Variation 237
9.5 Results and Discussion 238
9.5.1 Experiment 1: Oscillatory rhythms and the BOLD response 238
9.5.2 Experiment 2: Stimulus Frequency Variation 250
9.6 Conclusions 254
9.7 References 256
Chapter 10 **260**
Conclusion **260**
10.1 Summary 260
10.2 The Future 262
10.3 Concluding Remarks 263
10.4 References 265
Publications of Author **266**

Abstract

The work described in this thesis involves an investigation of the implementation and application of simultaneous EEG and fMRI. The two techniques are complementary, with EEG providing excellent temporal resolution and fMRI having good spatial resolution. Combined EEG/fMRI thus forms a powerful tool for neuroscience studies.

In initial work, methods for improving the removal of the gradient and pulse artefacts, which are induced in EEG traces recorded during concurrent MRI, have been developed.

Subsequently, the effects of the EEG hardware on MR images were investigated. This involved acquiring a series of scans to identify the sources of B_0- and B_1-inhomogeneities and the extent to which these affect EPI data.

The adverse effects on data quality of combining EEG and fMRI increase with field strength. Consequently, EEG-fMRI at 7T is particularly challenging, although a number of advantages make its implementation desirable. Safety tests were performed which showed the presence of the EEG system caused a negligible increase in RF heating effects during scanning at 7T. After elimination of a number of noise sources, the first simultaneous EEG-fMRI experiments at 7T using commercially available equipment were performed.

Concurrent EEG/fMRI at 3T was then used to investigate the correlation between the BOLD (blood oxygenation level dependent) response measured during visual stimulation and both the preceding alpha power and the strength of the driven, electrical response. In considering the correlation of the range of variation of the alpha power and BOLD response, a trend emerged which allowed tentative conclusions to be drawn. Variation of the BOLD and driven response with the frequency of visual stimulation relative to a subject's individual alpha frequency (IAF) was also investigated. A significant increase in the driven response, accompanied by a decrease in the BOLD response was observed in visual cortex when it was driven at the IAF.

Chapter 1

Introduction

1.1 Why Investigate the Brain?

The brain with 10^{10} cells in its outermost layer alone [1] and a multitude of functions is an organ which has fascinated people for thousands of years. However, early hieroglyphic writings from ancient Egypt suggest that they believed the heart rather than the brain was the important part of the body that contained the 'mind'. This was a belief also held by Aristotle around 350BC, who thought the brain was a radiator used to cool the heart! However, during the same period Plato suggested that the brain was the site of mental processes which, of course, reflects today's beliefs.

During the 1700's it was discovered that the nervous system was electrical in nature and this dispelled other theories which now seem amusing. Gall in the late 1700's was the first to suggest that different regions of the brain were responsible for different functions, with these functions varying from language to hope. His reasoning was somewhat mis-guided, but, to some extent, the thought process turned out to be correct. By the late 1800's Jackson had helped to add substance to Gall's theory with a demonstration that seizures in epileptic patients spread from one area of the body to another and originated in the brain. The first tangible area to be localised was the speech area, which was discovered by Broca in 1862 who had a patient with a lesion due to a stroke which meant that they could not speak. This speech area is now known as Broca's area. A similar demonstration was also given by Wernicke soon after, giving further credence to Broca's findings. Brodmann used histology techniques involving staining of tissues after this time to categorise the brain into 52 areas based on cellular organisation. In 1906 Golgi and Cajal were jointly awarded the Nobel Prize for their work in discovering that neurons were discrete unitary entities and that conduction only occurred in one direction along them. Cajal establish the Neuron Doctrine '*which is the fundamental organization and functional principle of the nervous system, stating that the neuron is the anatomical, physiological, genetic and metabolic unit of the nervous system.*'[2]. In the early 20th Century Penfield added greatly to the field of neuroscience by mapping different regions of the brain during neurosurgery of epilepsy patients. He showed that electrical stimulation of certain areas would give varying responses, such as motion of an area of the body.

This potted history along with the fact that in the last century at least 24 Nobel prizes have been awarded for contributions in the area of neuroscience shows the importance humans place on understanding the brain. We have come a long way from thinking the heart contains the mind to being able to identify regions of the brain which are responsible for performing certain tasks *in vivo* using a variety of techniques such as Electroencephalography (EEG), Magnetoencephalography (MEG), functional Magentic Resonance Imaging (fMRI), Positron Emission Tomography (PET) and Near Infrared Spectroscopy (NIRS).

Today, the study of the brain unites people from many different disciplines to develop new imaging methods to study both the anatomy and function of the brain *in vivo*. To do this it is necessary for physicists, engineers, biologists, psychologists, neuroscientists and medics to draw expertise together with the aim of discovering and better understanding the operation of the brain and what goes wrong when the brain is attacked by neurological diseases. The aim of this work tends to be to help fellow humans who are suffering from disease or damage to the brain.

Currently there are many methods for studying or imaging brain function which can be divided into two categories: those which provide direct measurements of electrophysiological activity, and those which indirectly measure this activity by monitoring either metabolic or haemodynamic changes within the brain. Here, a brief description of five of the main imaging modalities is given. This contains an outline of how brain activity is monitored using the specific techniques.

1.1.1 Direct Measures of Brain Activity

1.1.1.1 EEG

Electroencephologygraphy (EEG) measures the electrical signals produced when neurons fire [3] and therefore is a direct measure of brain activity. This technique was developed by Hans Berger [4] in 1929 and was the first method used to monitor neuronal activity *in vivo*.

The technique is based on the fact that when neurons are activated, electrical signals are produced. These signals are measured by taking the potential difference between electrodes placed on the scalp. The recorded signals generally have an amplitude of the order of micro-volts. Due to the nature of these measurements the temporal resolution of EEG is of the order of milliseconds [5, 6]. Using this technique Berger first documented the natural brain rhythm of alpha activity in the 8-13 Hz frequency band, [4, 7] which he noted was strongest when the subject was awake with their eyes closed. Since then many other rhythms have been found, details of which will be explored in greater depth in later chapters. Abnormalities in these rhythms have also been documented and used in the diagnosing certain diseases such as epilepsy.

It is relatively easy using Maxwell's equations to calculate the potential pattern that would be produced within a homogeneous, conductive medium by neuronal current flow. However, the brain is not such an ideal medium, as there are local inhomogeneities within the brain as well as many significant barriers to conduction, such as the skull and air spaces. Since current always flows along the path of least resistance, the barriers within the head result in significant distortions in the current pathways limiting the spatial resolution that can be obtained using EEG. In order to use EEG for imaging, one has to produce a map of the current sources within the brain from the map of potentials obtained on the surface of the scalp. This is known as the inverse problem and, by its nature, has no unique solution [8] making source localisation difficult. The majority of solutions to the inverse problem are therefore based on inclusion of *a-priori* information such as the number of sources expected for a given paradigm. The limited accuracy of source localisation is the main restriction of EEG as a neuronal imaging technique, since to understand the role of specific activity fully it is useful to know the location of the sources. Another limitation is the fact that deep sources of neuronal activity often cannot be measured due to the small voltages which are produced at the scalp. The limitations of this technique will be explored in greater depth in Chapter 4.

1.1.1.2 MEG

Magnetoencephalography (MEG) is the counterpart to EEG and measures the magnetic fields produced by the electrical currents which flow when a neuron fires. These magnetic fields are very small, of the order of 50-500 fT [9]; therefore detecting them requires the use of specialist equipment, namely superconducting quantum inference devices, SQUIDs. SQUIDS were developed for general use in the late 1960's by Zimmermann *et al* [10] and soon after applied to measuring brain activity. Due to the requirement for such equipment, MEG has only been around for a few decades with the first measurement of spontaneous alpha activity documented by Cohen *et al* [11] in 1972 and the first measurement of evoked activity using this technique being reported by Brenner *et al* [12] and Teyler *et al* [13] three years later.

The main advantage of MEG over EEG is that it is not affected by the heterogeneous electrical conductivity profile of the head. The magnetic permeability of the different tissues of the head does not differ greatly from that of free space thus there are no distortions of the magnetic field pattern on the scalp due to the tissues within the head. However, MEG is still plagued by the problems associated with the inverse problem, namely the lack of a unique solution, and therefore has difficulties providing accurate source localisation. Despite this problem the spatial localisation provided by MEG is far superior to that of EEG and recent reports show some promising correlations of localisation of neuronal activity measured using MEG and other imaging techniques [14, 15]. Another limitation of MEG, which is not a problem for EEG, is the fact that any neurons which are radial to the surface of the head are 'invisible' to detection by the MEG system. This however, is not a great limitation of the technique, as the surface of the brain is so folded that most neurons will have a tangential component and so will produce detectable magnetic fields [16].

1.1.2 Indirect Measures of Brain Activity

1.1.2.1 PET

Positron Emission Tomography (PET) was invented in the mid 1970's [17]. When used to investigate brain activity it does not measure neuronal activity directly, but instead takes advantage of the fact that the firing of neurons is an energy demanding process and therefore blood flow to regions where there is elevated neuronal activity increases. The first study on humans using this imaging technique to look at brain function was carried out in 1976 by Jones *et al [18].*

The premise of PET is that a radioactively labelled carrier is injected into the blood stream. This carrier ideally has properties chosen to collect in a specific area of the body. The radioactive nuclei in the carrier emit single positrons which annihilate local electrons within millimetres of the emission site. Two gamma photons are produced in the annihilation process and they travel in opposite directions and pass out of the body where they are detected by a scintillator material which produces a light burst that is detected by photomultiplier tubes. From the detection of a simultaneous pair of photons the position of the activity can be calculated using appropriate algorithms. The most commonly used radiolabelled metabolic substrates are ^{15}O or [^{18}F], part of fluorodeoxyglucose [19]. A direct relationship between the cerebral metabolic rate of oxygen and the regional cerebral blood flow has been found [19]. Therefore using these radiolabelled substrates the regional cerebral metabolic rate can be monitored using PET, and assuming a relationship between the metabolic rate of the tissue and the neuronal activity then PET can be used to measure brain activity with good spatial resolution. However, due to the chain of events required between the neuronal activation and the measured change in metabolism, the temporal resolution of this technique is poor.

1.1.2.2 NIRS

Near Infrared Spectroscopy (NIRS) is a technique which has been around since 1977 [20], but which was not used for functional brain imaging on humans until the early 1990's [21]. This technique, when applied to functional brain imaging, again relies upon the change in oxygen demand and uptake when an area of the brain is activated.

The procedure uses light at several different wavelengths in the spectral region spanning wavelengths of 700-1000nm and monitors the absorption of this light by the tissues or blood constituents (for further details refer to [22]). Haemoglobin exhibits different absorption properties depending on whether it is oxygenated or deoxygenated and therefore the oxygen concentration within the blood can be measured. Thus changes in blood oxygenation due to neuronal activation can be monitored. Amazingly, light in this region of the electromagnetic spectrum can penetrate the bone of the skull, making this another non-invasive technique for measuring neuronal activity. Tissue however attenuates the near infra-red radiation significantly, meaning that activity that occurs deep within the head cannot be monitored. However, as the majority of grey matter is on the surface of the brain this is not a major limitation, although often in experiments on animals, parts of the skull are removed to allow the near infra-red radiation to penetrate the soft tissues to a greater extent [23].

NIRS has the advantage of a better spatial resolution than PET [24] and can be used in conjunction with other imaging techniques such as single neuron recordings. However, like PET, this technique suffers from a poor temporal resolution, as the neuronal activity is not measured directly.

1.1.2.3 fMRI

Functional Magnetic Resonance Imaging (fMRI) makes use of an endogenous contrast agent, deoxygenated blood. This technique is relatively new having only been in use since the early 1990's [25].

The increase in neuronal activity in a region demands an increase in cerebral blood flow (CBF) to the region to provide more oxygenated blood. However, the increase in CBF overcompensates for the oxygen demand within the region, resulting in an increase of oxygenated blood and consequently a decrease in deoxygenated blood within the region. Since oxy-haemoglobin is diamagnetic whilst deoxy-haemoglobin is paramagnetic this change in blood constituents in the region surrounding the neuronal activity causes a change in the measured signal of the surrounding tissue when imaged using appropriate MRI sequences. This blood oxygen level dependent

(BOLD) contrast is the basis of the majority of fMRI experiments and gives excellent spatial resolution. However, as with PET and NIRS, fMRI is dependent on the reaction of the blood flow to changes in neuronal activity and therefore suffers from a temporal lag in the haemodynamic response compared with the time-course of neuronal activation, thus making the temporal resolution of fMRI poor. The other confound to all these indirect measures of neuronal activity is the fact that the exact coupling mechanisms between the neuronal activity and the measured physiological responses are poorly understood. Consequently, exact interpretation of results can be difficult, although large advances have been made in understanding these mechanisms [24], as will be discussed in Chapter 4.

1.1.3 Compete or complement?

It is apparent from the descriptions given above that each of the techniques has advantages and disadvantages for imaging brain function depending on the importance of the temporal or spatial information to an investigation. To this end it is clear that these techniques are, in fact, complementary rather than competitive.

With each of these techniques existing for over a decade it is unsurprising that information from the different modalities is now being combined [14, 15] with the aim of gaining further insight into what is happening within the brain. However, many of these techniques are not conducive to combination in a manner which allows multi-modal, simultaneous recordings of neuronal activity. This is an appealing goal as it may provide the key to understanding exactly what we are measuring in any single technique thus providing us with a greater knowledge of how the brain functions. Two of the most obvious, and practical, of the above techniques to combine are EEG and fMRI. This combination was first successfully demonstrated in a truly simultaneous manner at the beginning of this century by Allen *et al [26]*, with other groups rapidly showing the benefits of this multi-modal imaging technique [27].

1.2 Thesis overview

This thesis aims to explore the quality of the data acquired from both modalities during simultaneous EEG-fMRI recordings and to develop methods, where possible, to improve data quality. By implementing these improvements the multi-modal approach is then used to explore possible correlations between electro-physiological measurements provided by EEG and the haemodynamic changes measured using fMRI.

In Chapters 2 and 3 the physics behind magnetic resonance imaging (MRI) is explored. These chapters firstly explain the physics underlying the signals that can be obtained from the nuclei of atoms. With this basic knowledge, the theory of how MR images are formed and the different phenomena affecting the measured signal can be explained. This gives an overview of why fMRI is possible, as well as exploring the concepts that underlie the EEG system's effect upon fMRI data: a topic which is investigated in depth in a later experimental chapter. Chapter 4 aims to give the reader a basic understanding of neuronal activity and the anatomy of the brain. This chapter explores, in detail, how EEG and fMRI can be used to record brain activity. A discussion of the main physical limitations that are faced when combining these imaging techniques is given in Chapter 5, along with current methods for overcoming these problems. An overview of how combined EEG-fMRI has already been implemented by various groups is also provided in this chapter.

Chapter 6 is the first describing the experimental work of this thesis and details methods for improving the EEG data quality when performing simultaneous EEG-fMRI experiments via the use of synchronisation and the vectorcardiogram. The ways in which these techniques complement methods devised by other groups are highlighted. Chapter 7 explores the effect the EEG hardware has on the MR data quality. This is done by mapping both B_0 and B_1 inhomogeneities on a phantom and a head across a number of field strengths. The effect of the EEG system on the signal to noise ratio of the images is also considered. Chapter 8 shows the first data recorded during a visual task on human subjects using commercially available hardware for both EEG and fMRI recordings in a 7 T MR scanner. Before this was possible a number of safety and technical obstacles needed to be overcome; experiments and results related to this process are also described in this chapter. The final experimental chapter brings together knowledge that has been accumulated over the course of the previous experiments to study how the preceding alpha power and driven response measured with the EEG system corresponds to the BOLD response during a simple visual paradigm. This chapter also investigates, with a second experiment, if the frequency of an individual's alpha power has an effect on the frequency at which the maximum EEG and BOLD responses are found. This was done by presenting visual stimuli at a variety of frequencies based on the individual's alpha frequency whilst recording EEG and fMRI responses.

Chapter 10 concludes this thesis by drawing conclusions from all the experimental work presented in preceding chapters. Some discussion of future work that should be conducted in light of these findings is then given, with an emphasis placed on future applications of simultaneous EEG-fMRI on understanding the function of the brain.

1.3 References

1. Bear, M.F., Connors, B.W., Paridiso, M.A., *Neuroscience: Exploring the brain - Second Edition.* 2001, Philadelphia: Lippincott, Williams and Wilkins.
2. Cajal, S.R., *History of Neuroscience.* 2007, http://www.columbia.edu/cu/psychology/courses/1010/mangels/neuro/history/history.html.
3. Orrison, W.W., Jr, J.D. Lewine, J.A. Sanders, and M.F. Hartshorne, *Functional Brain Imaging; Chapter 8: Clinical Electroencephalography and Event-Related Potentials*, ed. S.M. Gay. 1995, St Louis: Mosby. 479.
4. Berger, H., *Uber das Elektrenkephalogramm des Menschen.* Arch. Psychiatrie Nerv, 1929. **87**: p. 527-570.
5. Amor, F., D. Rudrauf, V. Navarro, K. N'diage, L. Garnero, J. Martinerie, and M. Le Van Quyen, *Imaging brain synchrony at high spatio-temporal resolution: application to MEG during absence seizures.* Signal Processing, 2005. **85**(11): p. 2101-2111.
6. Kashikura, K., J. Kershaw, S. Yamamoto, X. Zhang, T. Matsuura, and I. Kanno, *Temporal Characteristics of Event-related BOLD Response and Visual-Evoked Potentials from Checkerboard Stimulation of Human V1: A Comparison Between Different Control Features.* Magnetic Resonance In Medicine, 2001. **45**: p. 212-216.
7. Berger, H., *On the Electroencephalogram of Man.* Electroencephalography and Clinical Neurophysiology, 1969. **Supplement 28**: p. 37-73.
8. Michel, C.M., G. Thut, S. Morand, A. Khateb, A.J. Pegna, R. Grave de Peralta, S. Gonzalez, M. Seeck, and T. Landis, *Review: Electric source imaging of human brain functions.* Brain Research Reviews, 2001. **36**(2-3): p. 108-118.
9. Brookes, M.J., *PhD Thesis: A multi-modal approach to functional neuroimaging*, in *Sir Peter Mansfield Magnetic Resonance Centre, School of Physics and Astronomy.* 2005, University of Nottingham: Nottingham.
10. Zimmerman, J.E., P. Thiene, and J.T. Harding, *Design and operation of stable re-biased superconducting point-contact quantum devices and a note on the properties of perfectly clean metal contacts.* Journal of Applied Physics, 1970. **41**: p. 1572-1580.
11. Cohen, D., *Magnetoencephalography: Detection of the brain's electrical activity with a superconducting magnetometer.* Science, 1972. **175**: p. 664-666.
12. Brenner, D., S.J. Williamson, and L. Kaufmann, *Visually evoked magnetic evoked magnetic fields of the human brain.* Science, 1975. **190**: p. 480-482.
13. Teyler, T.J., B.N. Cuffin, and D. Cohen, *Visual evoked magnetoencephalogram.* Life Sciences, 1975. **17**(5): p. 683-692.

14. Brookes, M.J., A.M. Gibson, S.D. Hall, P.L. Furlong, G.R. Barnes, A. Hillebrand, K.D. Singh, I.E. Holliday, S.T. Francis, and P.G. Morris, *GLM-beamformer method demonstrates stationary field, alpha ERD and gamma ERS co-localisation with fMRI BOLD response in visual cortex.* Neuroimage, 2005. **26**(1): p. 302-308.

15. Stevenson, C.M., M.J. Brookes, G.R. Barnes, A. Hillebrand, S.T. Francis, and P.G. Morris, *Neuromagnetic correlates of the fMRI BOLD response.* International Congress Series, 2007. **1300**: p. 325-328.

16. Hamalainen, M., R. Hari, R.J. Ilmoniemi, and K. J., *Magnetoencephalography-theory, instrumentation and applications to noninvasive studies of the working human brain.* Reviews of Modern Physics, 1993. **65**(2): p. 413-497.

17. Terpogossian, M.M., M.E. Phelps, E.J. Hoffman, and N.A. Mullani, *Positron-emission transaxial tomograph for nuclear imaging (PETT).* Radiology, 1975. **114**(1): p. 89-98.

18. Jones, T., D.A. Chesler, and M.M. Terpogossian, *Continuous inhalation of oxygen-15 for assessing regional oxygen extraction in brain of man.* British Journal of Radiology, 1976. **49**(580): p. 339-343.

19. Fox, P.T. and M.E. Raichle, *Stimulus rate dependence of regional cerebral blood-flow in human striate cortex, demonstrated by positron emission tomography.* Journal of Neurophysiology, 1984. **51**(5): p. 1109-1120.

20. Jobsis, F.F., *Noninvasive infrared monitoring of cerebral and myocardial oxygen sufficiency and circulatory parameters.* Science, 1977. **198**: p. 1264-1267.

21. Villringer, A., J. Planck, C. Hock, L. Schleinkofer, and U. Dirnagl, *Near infrared spectroscopy (NIRS): a tool to study hemodynamic changes during activation of brain function in human adults.* Neuroscience Letters, 1993. **154**: p. 101-104.

22. Cope, M. and D.T. Delpy, *System for long-term measurement of cerebral blood and tissue oxygenation on newborn infants by near infra-red transillumination.* Medical and Biological Engineering and Computing, 1988. **26**(3): p. 289-294.

23. Bonhoeffer, T. and A. Grinvald, *Brain Mapping: the Methods. Chapter 3: Optical Imaging Based on Intrinsic Signals:The Methodology.* 1 ed, ed. A.W. Toga and J.C. Mazzoitta. 1996, London: Academic Press Limited. 471.

24. Logothetis, N.K., *The neural basis of the blood-oxygen-level-dependent functional magnetic resonance imaging signal.* Philosophical Transactions of the Royal Society of London series B Biological Sciences, 2002. **357**: p. 1003-1037.

25. Ogawa, S., Menon, R.S., Tank, D.W., Kim, S-G., Merkle, H., Ellermann, J.M., Ugurbil, K., *Functional brain mapping by blood oxygenation level dependent contrast magnetic resonance imaging.* Biophysical Journal, 1993. **64**: p. 803-812.

26. Allen, P.J., O. Josephs, and R. Turner, *A Method for removing Imaging Artifact from Continuous EEG Recorded during Functional MRI.* Neuroimage, 2000. **12**(2): p. 230-239.

27. Lemieux, L., A. Salek-Haddadi, O. Josephs, P.J. Allen, N. Toms, C. Scott, K. Krakow, R. Turner, and D.R. Fish, *Event-Related fMRI with Simultaneous and Continuous EEG: Description of the Method and Initial Case Report.* Neuroimage, 2001. **14**: p. 780-787.

Chapter 2

Nuclear Magnetic Resonance

2.1 Introduction

This chapter aims to provide the background theory of Nuclear Magnetic Resonance (NMR) which is the phenomenon upon which Magnetic Resonance Imaging (MRI) is based and therefore this theory underpins large sections of this thesis. The information for this chapter was based on the following texts [1-5] The field of NMR and thus MRI is based on the principle of spin angular momentum which was first formulated by Pauli in 1924. However, it was not until 1928 when Dirac derived a relativistic quantum mechanical wave equation [6] that a logical link could be formed between quantum mechanics and the classical equivalent description of angular momentum. In this work, the majority of the explanations that will be given will be classical as the quantum mechanics does not provide further insight. However, in some instances the quantum mechanical description will be given to aid the understanding of the reader.

2.2 Properties of Nuclei

2.2.1 Spin Angular Momentum

It is easy to understand in a classical sense that an object which is rotating possesses angular momentum. In a classical sense this momentum can take any finite value. However, in the case of the quantum mechanics the total spin angular momentum is described by $I\hbar$, where I is the spin quantum number which can only take integral or half integral values. Thus the spin angular momentum can only take discrete values. As I is a characteristic property of the nucleus, atoms of different elements will have a different value of I. In the case of the hydrogen atom $I=\frac{1}{2}$. Since the hydrogen atom is the only atom used in the imaging experiments described in the later chapters of this thesis, it is the only atom which will be considered here. The magnitude of the spin angular momentum, $|\mathbf{P}|$, is given by

$$|\mathbf{P}| = \hbar\sqrt{I(I+1)}\,.$$

[2. 1]

As the angular momentum is a vector, one can divide **P** into three components following Cartesian coordinates, P_x, P_y and P_z, each of these having an associated quantum mechanical operator:

$$P_x \rightarrow \hbar\hat{I}_x \qquad P_y \rightarrow \hbar\hat{I}_y \qquad P_z \rightarrow \hbar\hat{I}_z$$

thus

$$\mathbf{P} \rightarrow \hbar\hat{\mathbf{I}}\,.$$

[2. 2]

$\hbar$ appears because the operators are dimensionless quantities. As **P** is a vector quantity it is necessary to also define the orientation of the spin. The orientation of the spin is also quantised with the quantum number, m_I, defining the 'spin state' and characterising the z-component of the angular momentum. This quantum number can take one of $2I+1$ possible values representing states which are degenerate in the absence of an external magnetic field. For the case of the hydrogen atom m_I has 2 possible values which are depicted in Figure 2.1. The alternative Dirac notation is also given in Figure 2.1 for the spin states. This notation may be used interchangeably if other texts are referred to.

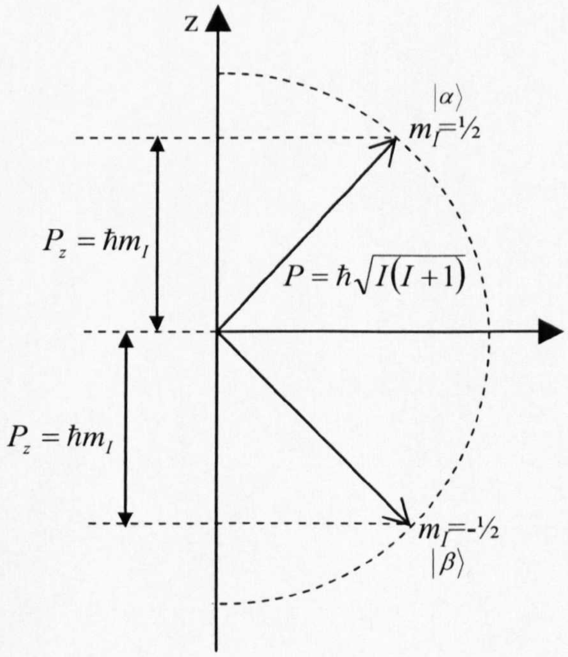

Figure 2.1: The spin angular momentum states for a hydrogen atom.

2.2.2 Magnetic Moments

Several sources of magnetism are associated with the atom; these originate from the circulation of electric currents, the magnetic moments of the electrons and the magnetic moment of the nucleus. Here, the magnetic moment of a nucleus, $\boldsymbol{\mu}$, will be considered. The direction of the vector, $\boldsymbol{\mu}$, is parallel to the spin angular momentum associated with it, **P**. This is easy to visualise in a classical sense as a charge rotating in a loop would have an associated magnetic moment and therefore a proton spinning will have a magnetic moment.

$$\boldsymbol{\mu} = \gamma \mathbf{P}$$

[2. 3]

Here γ is the magnetogyric ratio which is a property of the nucleus that is different for each type of nucleus. For a hydrogen nucleus, γ takes the value of 2.67×10^{8} radians $T^{-1}s^{-1}$.

According to classical description within electromagnetism the energy of a magnetic moment placed in an external magnetic field can be written as:

$$E = -\boldsymbol{\mu}.\mathbf{B}.$$

[2. 4]

Here the negative sign indicates that the lowest energy is when the magnetic moment is parallel to **B**. This is analogous to a compass needle which will rotate to align with the earth's magnetic field so as to minimise its energy. The classical expression for E can be replaced with the Hamiltonian operator equivalent, $\hat{H}$, using Equations 2.2, 2.3 and 2.4 one can derive:

$$\hat{H} = -\hbar\gamma\mathbf{B}.\hat{\mathbf{I}}.$$

[2. 5]

Convention dictates that the external, static magnetic field for NMR is applied along the z-axis and therefore $\mathbf{B}=B_z\mathbf{k}$ thus Equation 2.5 can be simplified to:

$$\hat{H} = -\hbar\gamma B_z \hat{I}_z.$$

[2. 6]

This Hamiltonian is known as the Zeeman Hamiltonian. To calculate the energy of the spin in a magnetic field, the eigenvalue equation

$$\hat{H}\left|m_I\right\rangle = E\left|m_I\right\rangle$$

[2. 7]

must be solved. Writing the Hamiltonian operator explicitly then:

$$\hat{H}\left|m_I\right\rangle = -\hbar\gamma B_z \hat{I}_z\left|m_I\right\rangle .$$

[2. 8]

Since the eigenvalue of the operator $\hat{I}_z\left|m_I\right\rangle$ is $m_I\left|m_I\right\rangle$ [3] Equations 2.7 and 2.8 yield

$$E = -\hbar\gamma B_z m_I .$$

[2. 9]

From Equation 2.9 it is clear that the energy depends on the magnetogyric ratio, the strength of the magnetic field and the spin state of the nucleus. For the hydrogen nucleus there are two possible energy states which are shown in Figure 2.2. This separation of the energy states is known as the Zeeman splitting and is given by $\Delta E = \hbar\gamma B_z$.

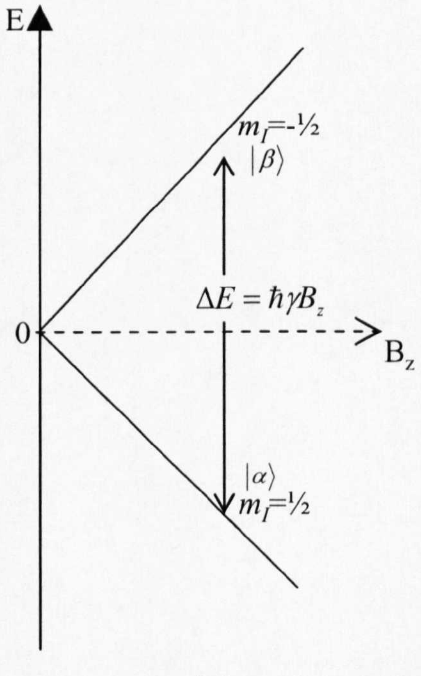

Figure 2.2: Zeeman splitting of the hydrogen atom.

To change the quantum state of the spin, electromagnetic radiation can be applied with an energy that matches the Zeeman splitting, ΔE. Classically it is known that $\Delta E = h\nu$, where v is the photon frequency. Therefore the frequency of electromagnetic radiation which must be applied to cause a change in spin state is given by:

$$\nu = \frac{\gamma B_z}{2\pi}.$$

[2. 10]

For a hydrogen atom in a 1 Tesla applied magnetic field we therefore know that v=42.58 MHz which is in the radiofrequency region of the electromagnetic spectrum. Application tuned of electromagnetic radiation to a sample containing nuclear spins is the basis for all NMR and MRI experiments.

2.3 Magnetic Resonance: A Classical description

2.3.1 Static Magnetic field: Larmor Precession

To understand the basis of MR fully, it is now necessary to consider in depth the interaction of the magnetic moment with the external, static magnetic field. This can be done both classically and quantum mechanically. The classical description will be covered here, as understanding of the quantum mechanics is not necessary for comprehending this body of work.

When a magnetic moment, **μ**, with associated angular momentum, **P**, is placed in an external, static magnetic field, **B**, it will experience a torque, $\boldsymbol{\mu}\times\mathbf{B}$. The rate of change of the angular momentum is equated with the torque experienced by the magnetic moment in the external magnetic field, such that:

$$\frac{d\mathbf{P}}{dt} = \boldsymbol{\mu} \times \mathbf{B}.$$

[2. 11]

Substituting in Equation 2.3 and rearranging gives:

$$\frac{d\boldsymbol{\mu}}{dt} = \gamma\boldsymbol{\mu} \times \mathbf{B}.$$

[2. 12]

As a static magnetic field along the z-axis is being considered here, this equation becomes:

$$\frac{d\mu_x}{dt} = \gamma\mu_y B_z \qquad \frac{d\mu_y}{dt} = \gamma\mu_x B_z \qquad \frac{d\mu_z}{dt} = 0.$$

[2. 13]

The solutions to these equations are then given by:

$$\begin{aligned}
\mu_x(t) &= \mu_x(0)\cos\gamma B_z t + \mu_y(0)\sin\gamma B_z t \\
\mu_y(t) &= -\mu_x(0)\sin\gamma B_z t + \mu_y(0)\cos\gamma B_z t \\
\mu_z(t) &= \mu_z(0)
\end{aligned}$$

[2. 14]

These equations describe a precessional motion, which is depicted in Figure 2.3. The angle between $\boldsymbol{\mu}$ and $\mathbf{B}$ does not change, thus the tip of the magnetic moment will precess tracing out a conical shape as a function of time. The angular frequency of this precession is given by

$$\omega_L = -\gamma B_z$$

[2. 15]

this can also be defined as

$$v_L = \frac{\omega_L}{2\pi} = -\frac{\gamma B_z}{2\pi}.$$

[2. 16]

Notice the minus sign in Equation 2.15 which indicates the sense of precession. Most nuclei (including the hydrogen nucleus) have a positive γ and therefore the Larmor frequency is negative. The result of this is that the precession is in the clockwise direction (Figure 2.3)[2]. Also one should note the similarity of Equations 2.16 and 2.10: v_L derived from this classical description is identical to the photon frequency which is required to drive a transition between quantum states of the spin system. Unlike a classical system, however, the magnetic moment can only take on discrete values, which in the case of the hydrogen nucleus, can be labelled, $\boldsymbol{\mu}^{\alpha}$ and $\boldsymbol{\mu}^{\beta}$ whose rotations are shown in Figure 2.3.

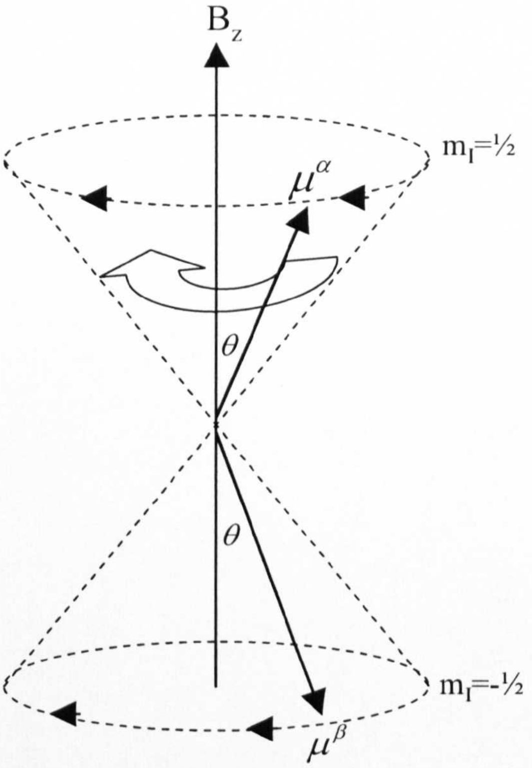

Figure 2.3: Larmor precession of nuclei with m_I=±½.

2.3.2 Time Dependent Magnetic Field: Interactions with RF radiation.

As alluded to in Section 2.2.2, to induce a change in spin state the nuclear spin must interact with electromagnetic photons. This interaction is driven by an oscillating magnetic field which is associated with the electromagnetic radiation. If one applies radio-frequency (RF) radiation to a single nuclear spin in the presence of a static magnetic field, **B**, then it is important to consider the oscillating *B*-field (as it is this which interacts with the nuclear magnetisation). This oscillating field, which is commonly applied perpendicular to **B**, can be described by Equation 2.17. It can be resolved into two components one rotating clockwise, $\mathbf{B_c}$, with angular frequency $-\omega$ and the other anticlockwise, $\mathbf{B_a}$, with angular frequency ω (Equation 2.18).

$$\mathbf{B}_1(t) = \mathbf{i}2B_1 \cos\omega t \tag{2. 17}$$

$$\mathbf{B}_c(t) = B_1(\mathbf{i}\cos\omega t - \mathbf{j}\sin\omega t)$$

$$\mathbf{B}_a(t) = B_1(\mathbf{i}\cos\omega t + \mathbf{j}\sin\omega t)$$

[2. 18]

The torque experienced by the magnetic moment will now change from the situation described in Equation 2.11 as the newly introduced, temporally varying magnetic field also has an effect. The equation of motion of the magnetic moment therefore becomes:

$$\frac{d\boldsymbol{\mu}}{dt} = \gamma\boldsymbol{\mu} \times (\mathbf{B} + \mathbf{B}_1(t)).$$

[2. 19]

Since the $\mathbf{B_a}$ field precesses in the opposite sense to the magnetic moment it will have little effect on the torque which the magnetic moment experiences. It is said to be "off-resonance" and thus, for purposes of simplicity, it can be ignored. The other component of $\mathbf{B_1}$, $\mathbf{B_c}$, precesses in the same direction as the magnetic moment and is termed "on-resonance". This component of the oscillating magnetic field will have an effect on the torque experienced by the magnetic moment. The strongest effect will occur when $\omega=\omega_L$, as at this frequency the rotating RF field 'keeps up' with the precessing spin and therefore the contribution to the torque will be constantly in the same direction. The effect of this oscillating field is to cause a change in the precession angle, θ (Figure 2.3). This is where this classical description breaks down as clearly in this quantum system a continuum of angles of θ are not possible, but instead a switch between the orientation $\boldsymbol{\mu}_\alpha$ and $\boldsymbol{\mu}_\beta$ can occur, thus inducing a change in the energy state of the spin. Using the fact that only $\mathbf{B_c}$ contributes to the torque experienced by $\boldsymbol{\mu}$ then by substitution of Equation 2.18 into 2.19 the equation of motion becomes:

$$\frac{d\boldsymbol{\mu}}{dt} = \gamma\boldsymbol{\mu} \times (\mathbf{k}B_z + B_1(\mathbf{i}\cos\omega t - \mathbf{j}\sin\omega t).$$

[2. 20]

At this point it becomes instructive to switch into a rotating frame of reference (x', y', z) where B_1 is stationary, $\mathbf{B_1(t)}=B_1\mathbf{i}'$. From classical mechanics if the time derivative of a vector, $\mathbf{r}$, in the non-rotating frame is given by $\left(\frac{d\mathbf{r}}{dt}\right)_{x,y,z}$ then the time derivative of the vector viewed from the rotating frame is given by:

$$\left(\frac{d\mathbf{r}}{dt}\right)_{x,y,z} = \boldsymbol{\omega}\times\mathbf{r} + \left(\frac{d\mathbf{r}}{dt}\right)_{x',y',z}.$$

Where $\boldsymbol{\omega}=-\omega\mathbf{k}$ is the angular velocity, which when applied to Equation 2.19 gives:

$$\begin{aligned}\boldsymbol{\omega}\times\boldsymbol{\mu} + \left(\frac{d\boldsymbol{\mu}}{dt}\right)_{x',y',z} &= \gamma\boldsymbol{\mu}\times\left(\mathbf{B}+\mathbf{B}_1(t)\right)\\ &= \gamma\boldsymbol{\mu}\times\left(B_z\mathbf{k}+B_1\mathbf{i}'\right).\end{aligned}$$

Rearranging this gives:

$$\left(\frac{d\boldsymbol{\mu}}{dt}\right)_{x',y',z} = \gamma\boldsymbol{\mu}\times\left(\left(B_z-\frac{\omega}{\gamma}\right)\mathbf{k}+B_1\mathbf{i}'\right) = \gamma\boldsymbol{\mu}\times\mathbf{B}_{eff}$$

[2. 21]

where

$$\mathbf{B}_{eff} = B_1\mathbf{i}' + \left(B_z - \frac{\omega}{\gamma}\right)\mathbf{k}.$$

[2. 22]

By comparing Equation 2.21 with 2.12 it is clear that in this new rotating frame of reference the magnetic moment will precess about the axis of $\mathbf{B}_{\mathrm{eff}}$ (Figure 2. 4A). In the case of $B_z = \frac{\omega}{\gamma}$ (or $\omega=\omega_L$), the latter terms in Equation 2.22 reduce to zero and the magnetic moment rotates about the x'-axis (Figure 2. 4B).

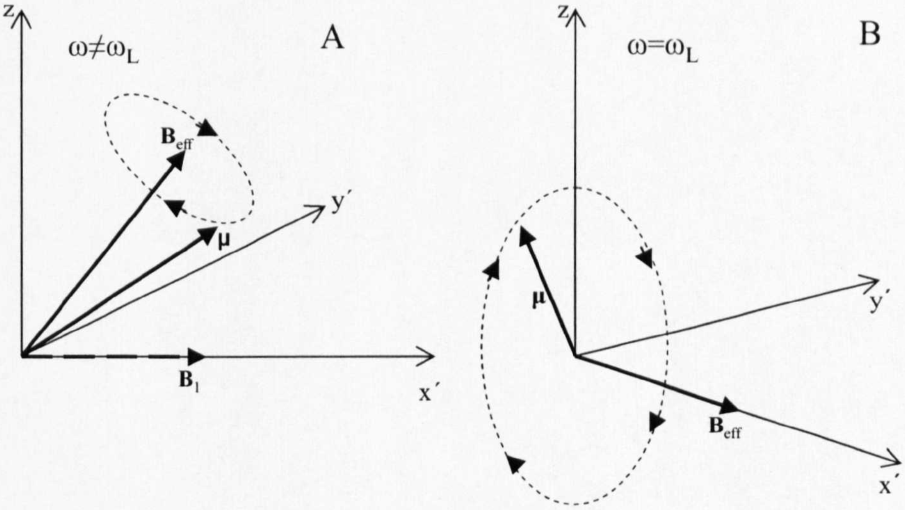

Figure 2. 4 Precession of the magnetic moment, μ, of a proton in the rotating frame during the application of a rotating magnetic field in the general case where $\omega\neq\omega_L$ (A) and in the case of $\omega=\omega_L$ (B).

The angular frequency of this new precession is given by $\omega_1 = \gamma B_1$. Thus if the RF is applied for a time t_w then **μ** will rotate through an angle:

$$\theta = \gamma B_1 t_w .$$

[2. 23]

This equation indicates how a magnetic resonance experiment can be performed: by applying a RF pulse of duration, t_w, and frequency, ω_L, polarised in a direction perpendicular to the static field then the magnetic moment will be tipped through an angle, θ, corresponding to an induced transition between spin states. When this occurs the absorption and stimulated emission of photons will be observed.

2.4 More than one spin?

Up until this point we have only considered the effect of a magnetic field on an individual nucleus. However, in a typical sample there will be many millions of spins (for example, from Avogadro's constant one mole of a substance contains 6×10^{23} particles) so, what happens then?

2.4.1 Bulk Magnetisation

If we consider the spins to be non-interacting and precessing independently of one another then it is unsurprising to realise that in the absence of an external magnetic field the spins 'wander' randomly and their orientations are therefore uniformly distributed such that the net magnetisation is zero. In the presence of an external magnetic field all spins will execute Larmor precession and the 'wandering' motion is biased towards aligning with the external magnetic field with slightly more spins coming to thermal equilibrium in the lower energy state, $|\alpha\rangle$ (Section 2.2.2), resulting in a net magnetisation of the sample. At room temperature the difference in population of the two states can be explained using Boltzmann statistics:

$$\frac{N_\alpha}{N_\beta} = \exp\left(-\frac{\Delta E}{k_B T}\right)$$

[2. 24]

where N_α and N_β are the number of spins in each state, k_B is Boltzmann's constant and T is the temperature of the system. If one assumes that $k_BT >> \Delta E$ (which is a good approximation above a few Kelvin), then substituting in $\Delta E = \hbar\gamma B_z$ Equation 2.24 becomes:

$$\frac{N_\beta}{N_\alpha} = 1 - \frac{\hbar\gamma B_z}{k_B T}.$$

Since the total number of spins, $N = N_\alpha + N_\beta \approx 2N_\alpha$ then rearranging the above and including this approximation gives:

$$N_\alpha - N_\beta = \frac{N\hbar\gamma B_z}{2k_B T}.$$

[2. 25]

Knowing this relationship between the population of the spin states it is possible to calculate the bulk magnetisation, **M**, of the sample, as this is simply the vector sum of the magnetic moments. The magnitude of the magnetisation parallel to the static magnetic field can be calculated from:

$$M_z = N_\alpha \mu_z^\alpha + N_\beta \mu_z^\beta.$$

Since from Equations 2.2 and 2.3 we know that $\mu_z^\alpha = -\mu_z^\beta = \frac{1}{2}\gamma\hbar$ (for a proton) by substitution of this and Equation 2.25 into the above expression, the bulk magnetisation can be derived:

$$M_z = \frac{N(\hbar\gamma)^2 B_z}{4k_B T}.$$

[2. 26]

It is clear from this equation that the bulk magnetisation in the longitudinal direction (*i.e.* parallel to the static magnetic field) of a system depends on the static magnetic field and the temperature of the sample. As it is not possible to reduce the temperature of the subject in the clinical setting, the increase in static magnetic field has proved important within MRI, for reasons which will become clear in later chapters.

The magnetisation of the spins in the transverse direction (*i.e.* perpendicular to the static magnetic field) is dependent upon the phase coherence of the spins. Generally, in a state of equilibrium, the phase of the spins will be random and therefore the vector sum in the transverse direction will be zero resulting in no observed transverse bulk magnetisation. However, the bulk magnetisation obeys the same simple equations of motion that are used to describe a single spin (Section 2.3.1) so that

$$\frac{d\mathbf{M}}{dt} = \gamma\mathbf{M} \times \mathbf{B}\,.$$

[2. 27]

Here, **B** accounts for both static and oscillating magnetic field terms and therefore the equations derived in Section 2.3.2 will also apply. Applying an oscillating magnetic field to the bulk magnetisation will have two effects. The first is that the proportion of spins in the two spin states will be changed thus changing the longitudinal magnetisation. The second effect is that a phase coherence between the spins will be introduced thus producing a transverse component of the magnetisation. This means that if an oscillating RF field is applied at the Larmor frequency then the bulk magnetisation will be tipped through an angle θ (Equation 2.23) thus producing a transverse component of the bulk magnetisation and changing the magnitude of the longitudinal component. It is worth noting that unlike the single spin situation the bulk magnetisation does not obey quantum mechanics. This is because the bulk magnetisation represents a population of spins and therefore the angle through which it can be tipped is not quantised. By varying the time for which the RF-pulse is applied, the angle through which the magnetisation is tipped can be changed as shown in Figure 2.5. If the RF-pulse causes the bulk magnetisation to be tipped through 90° then the relative populations of $|\alpha\rangle$ and $|\beta\rangle$ would be equal and the longitudinal magnetisation would be zero whilst the transverse magnetisation would be maximal.

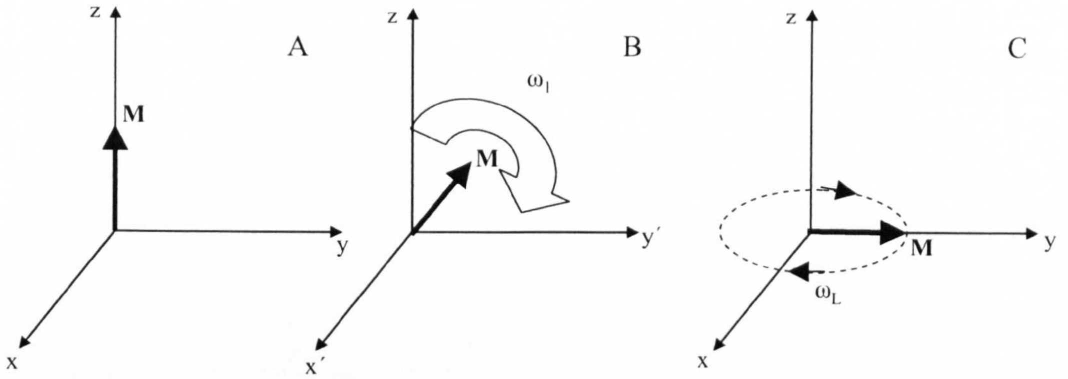

Figure 2. 5: The path of the bulk magnetisation during a 90° RF pulse. A: Initially the bulk magnetisation is in the z-plane (laboratory frame of reference). B: during the application of the RF pulse the magnetisation rotates about the x′-axis (rotating frame). C: Immediately after the application of the RF pulse bulk magnetisation precesses in the x-y plane at frequency ω_L (laboratory frame).

2.4.2 Spin interactions

Up to this point we have considered the spins within the system to be non-interacting. However, this is a simplification and there are interactions between the spins which cause relaxation of the spins to their thermal equilibrium state after the application of a RF-pulse. In this section we will briefly explore what these interactions are and how they affect the magnetic state of the spins. The mathematical description of these interactions will not be discussed as it is not necessary for the understanding of the work of this thesis (the interested reader can refer to [4, 5] for further details).

2.4.2.1 Spin-Lattice Relaxation

We have ascertained that when a RF pulse is applied to a system in the presence of a static magnetic field the bulk magnetisation properties of the system are changed. If for instance a 90° RF-pulse is applied then the longitudinal magnetisation will be set to zero and the spin populations are equalised. However, over time the spin populations recover back to their equilibrium values. This process is known as *spin-lattice relaxation.* The name of this process originates from the fact that it involves an exchange of energy between the spin system and the molecular surroundings (the lattice). Qualitatively this can be understood in much the same way that the RF pulse induces a change in energy of the spins. A single spin 'sees' the fluctuating electromagnetic fields from the motion of the surrounding spins. If this motion is at the same frequency as the Larmor frequency an interaction between the spins may occur causing the relaxation of the spin of interest [7]. This process is characterised by the time constant T_1. Different materials have different T_1 properties which depend upon a number of parameters including temperature and viscosity (if the sample is liquid). This time constant can be measured using simple NMR techniques, described in latter sections of this chapter. However, direct measurement of the longitudinal magnetisation is almost impossible in NMR due to the diamagnetic properties associated with the electrons in the sample normally being four orders of magnitude larger than the properties of nuclei. NMR measures the magnitude of **M** perpendicular to the main static magnetic field.

2.4.2.2 Spin-Spin Relaxation

We now know that the application of an RF pulse causes the phase of the spins to become coherent and the precession of these spins then occurs at the Larmor frequency, so that the bulk magnetic moment precesses at this frequency too. It has been discovered that the frequency of precession of the individual spins is dependent upon the local magnetic field experienced by that spin. Whereas on average all spins (in an ideal situation with a completely homogeneous external magnetic field) experience the same magnetic field; at a particular instant in time the magnetic fields experienced by different spins vary due to the magnetic fields of surrounding spins. These fields change over time due to the random Brownian motion of the molecules within the sample and changes in spin state. These variations in magnetic field cause all the spins to precess at slightly different frequencies resulting in a loss of coherence, or dephasing, of the spins thus causing the transverse magnetisation to diminish. This decay of the transverse magnetisation is exponential with time and known as *spin-spin relaxation*. This process is characterised by the time constant T_2 which is generally shorter than T_1.

The resultant motion of the bulk magnetic moment from excitation to relaxation can be seen to follow a precession as shown in Figure 2.6. One can see from this figure how the path of precession depends upon both the T_1 and T_2 properties of the sample.

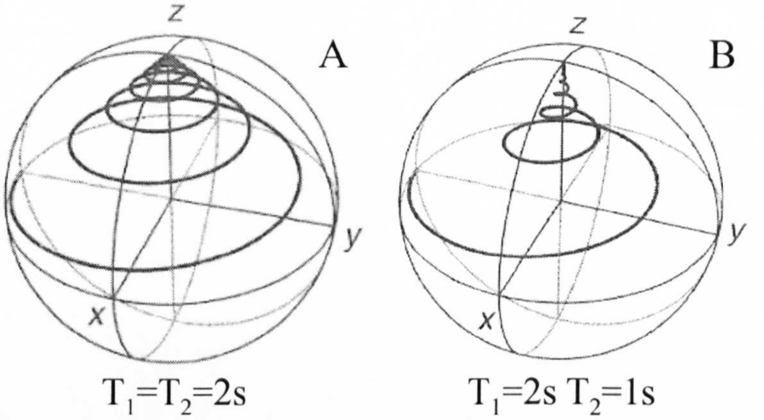

Figure 2. 6: The trajectory taken by the tip of the bulk magnetisation vector after a 90° RF pulse for three different combinations of T_1 and T_2 values. Adapted from [4].

2.4.2.3Field inhomogeneities

In a real experiment, as well as the spin-spin relaxation there is a secondary effect which causes dephasing of the spins in the *x-y* plane. This effect is due to field inhomogeneities, which may be the result of imperfections in the static magnetic field or, more commonly, differences in susceptibility of materials causing changes in the magnetic field experienced by the nuclei (in clinical cases this is often due to interfaces between different tissues, tissue-bone or tissue–air boundaries). The consequence of these deviations in field are accounted for by the time constant, T_2'. The result of these effects, along with the spin-spin relaxation, is the observed decay of the transverse magnetisation described by the decay constant T_2^*. This effect will be discussed in greater detail in Chapter 7 where the problems of field inhomogeneities in experimental situations will become apparent.

$$\frac{1}{T_2^*}=\frac{1}{T_2}+\frac{1}{T_2'}\,. \qquad [2.\ 28]$$

2.4.2.4 Bloch Equations

Since there are interactions between molecules within the sample which affect the evolution of the bulk magnetisation this should be accounted for in Equation 2.27. Accounting for these additional interactions can be done as follows:

$$\frac{d\mathbf{M}}{dt} = \gamma\mathbf{M} \times \mathbf{B} - \frac{1}{T_1}(M_z - M_0)\mathbf{k} - \frac{1}{T_2}(M_x\mathbf{i} + M_y\mathbf{j})$$

[2. 29]

where $\mathbf{B} = B_z\mathbf{k} + B_1(t)\mathbf{i}$. This is the general form of the Bloch equation [8] which can be separated out as follows:

$$\frac{dM_z}{dt} = -\frac{(M_z - M_0)}{T_1}$$

$$\frac{dM_x}{dt} = \gamma M_y B_z - \frac{M_x}{T_2}$$

$$\frac{dM_y}{dt} = -\gamma M_x B_z - \frac{M_y}{T_2}.$$

[2. 30]

If one considers the application of an RF-pulse of flip angle θ, then immediately after the pulse, $M_x=0$, $M_y=M_0\sin\theta$ and $M_z=M_0\cos\theta$ and the solutions to Equation 2.30 will be:

$$M_x = M_0 \sin\theta \sin(\omega_L t)\exp\left(-\frac{t}{T_2}\right)$$

$$M_y = M_0 \sin\theta \cos(\omega_L t)\exp\left(-\frac{t}{T_2}\right)$$

$$M_z = M_0\left\{1 - (1 - \cos\theta)\exp\left(-\frac{t}{T_1}\right)\right\}.$$

[2. 31]

These equations describe how the bulk magnetisation of the sample changes after a RF pulse has been applied and demonstrate clearly the independence of T_1 and T_2 in effecting the magnetisation of the sample as shown graphically in Figure 2. 7.

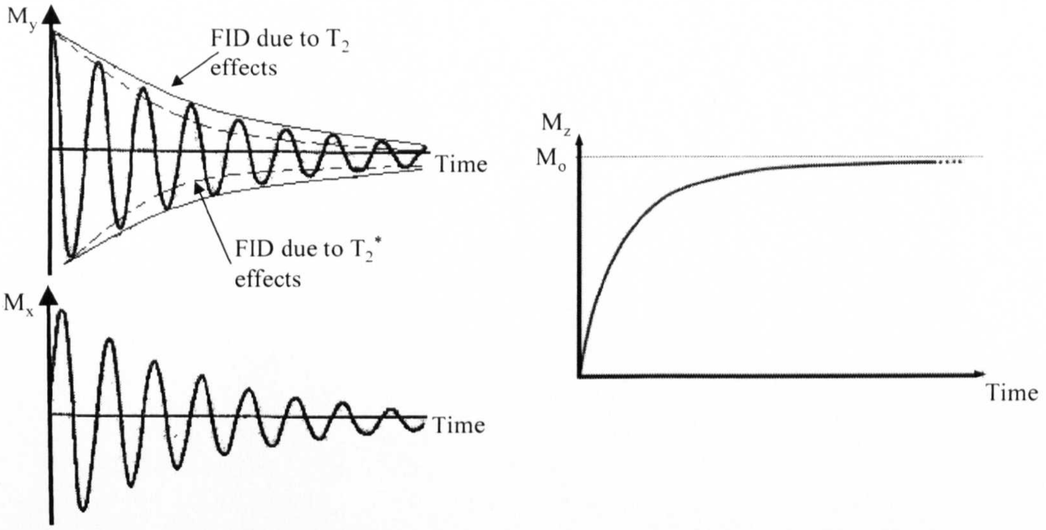

Figure 2. 7: The relaxation of the transverse (left) and longitudinal (right) magnetisation after application of a 90° RF pulse.

The decay of magnetisation that is observed in the transverse plane (Figure 2. 7A) produces a measurable signal whose amplitude reduces over time and which is known as a free induction decay (FID). Notice how the decay of the FID is faster when T_2' effects are accounted for as well as those of spin-spin relaxation. By fitting the measured FID due to T_2^* effects to the correct Bloch equation, the T_2^* of the sample can be calculated. The precise method of detection of these signals is through phase sensitive detection, which is described in detail in Chapter 7 (Section 7.2.1) where the importance of this technique for my experimental work is also explained.

2.4.2.5 Spin Echo

To measure the T_2 of a sample, a more complicated pulse sequence is required as the T_2 and T_2' effects must be separated. This separation is possible when the spin echo sequence [9] shown in Figure 2. 8 is used.

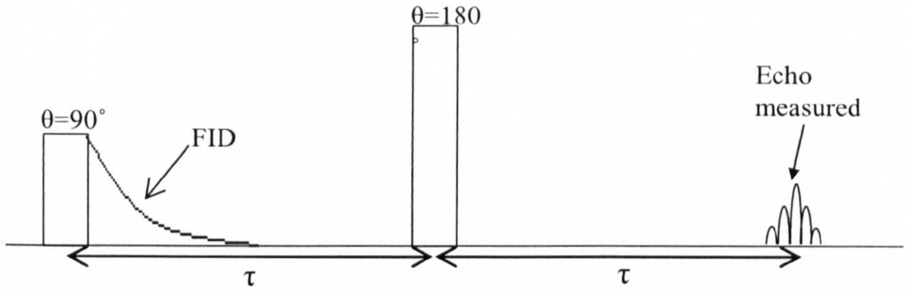

Figure 2. 8 Spin Echo pulse sequence

As one can see, this sequence works by firstly applying a 90° RF pulse which rotates all the magnetisation into the *x-y* plane. The spins then precess at approximately the Larmor frequency, but dephase at the same time (Figure 2. 9 B) with some of the spins getting 'behind' the Larmor frequency (rotating anticlockwise in the rotating frame) whilst others get 'ahead' (rotating clockwise in the rotating frame) the net result is the spins 'fan out' (or dephase). After time, τ, a 180° RF pulse is applied, serving to rotate the magnetisation about the y'-axis. Although this process does not change the frequency at which any of the spins are precessing it does mean that those which were 'behind' the spins precessing at the Larmor frequency are now 'ahead' and vice versa (Figure 2. 9C). This means that at a time 2τ, a rephasing of the spins will occur causing an observable spin echo (Figure 2. 8 and Figure 2. 9D). For this process to produce a perfect spin echo the magnetic fields that each spin experiences must not change for the duration of the experiment. This requirement is the key to measuring T_2 effects. The field inhomogeneities due to susceptibility differences and apparatus imperfections fulfil this criterion; however those differences in magnetic field due to other nuclei and the Brownian motion of the surrounding molecules do not and therefore this part of the accrued phase is not cancelled. The consequence is that the spin echo technique allows the measurement of T_2 as the T_2' effects can be eliminated. By varying τ a number of times and measuring the amplitude of the spin echo for each experiment, a plot of the decay of the magnetisation due to T_2 effects can be formed, from which (using the appropriate Bloch equation) the T_2 of the sample can be calculated.

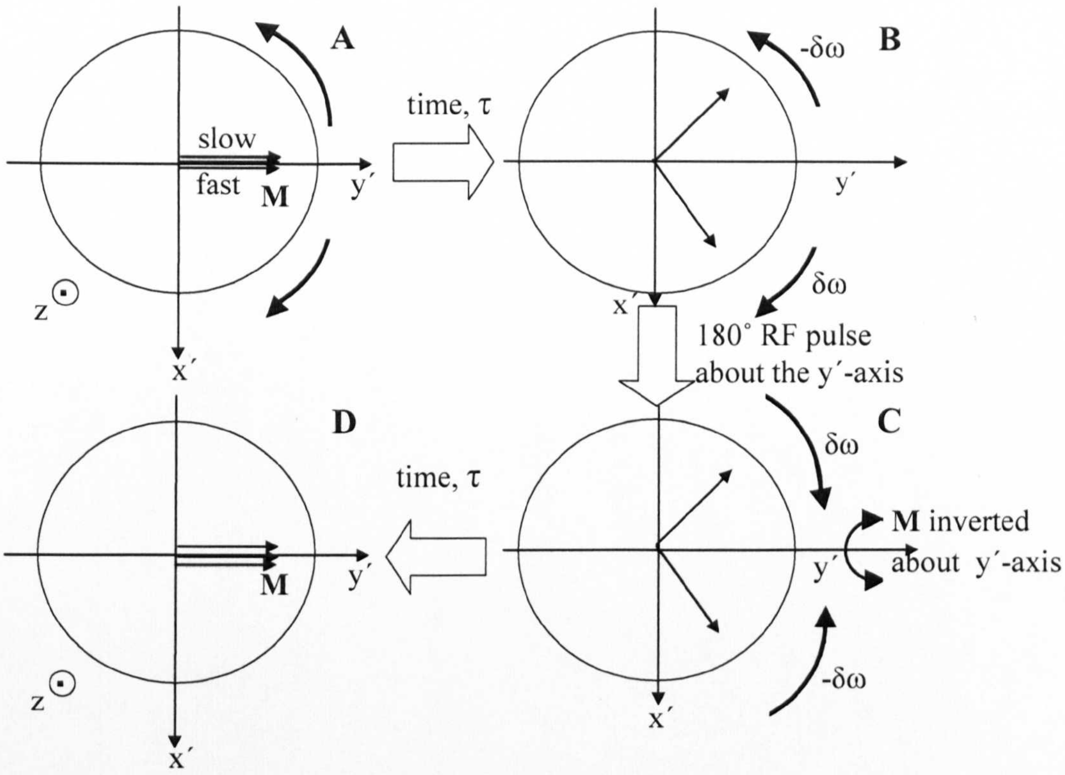
A
slow
fast
M
y′
z
x′
time, τ
-δω
B
y′
δω
x′
180° RF pulse
about the y′-axis
D
C
δω
time, τ
M inverted
about y′-axis
y′
M
y′
z
x′
-δω
x′

Figure 2. 9: An illustration of the precession of the spins in the rotating frame during a spin echo sequence. A 90° pulse is first applied, causing the spins to become phase coherent (A.) Over a time τ, some coherence is lost due to T_2 and T_2' effects (B). Applying a 180° pulse inverts the magnetisation in the y′-axis (C). The dephasing due to the T_2' effects is then refocused producing an echo (D).

2.4.2.6 Inversion recovery

Measurement of T_1 can provide information about the motion and dynamics of the molecules within the sample. There are a number of sequences that can be used to measure this parameter, the most common being the inversion recovery pulse sequence.

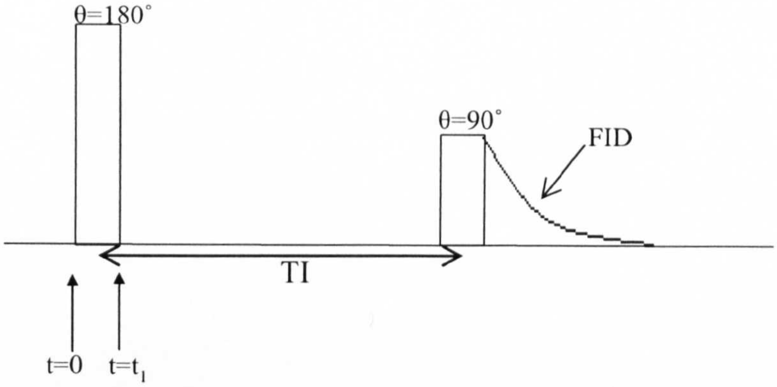

Figure 2. 10: Inversion Recovery Pulse sequence

This sequence consists of a 180° RF pulse followed by a 90° RF pulse, which is applied after a time *TI*, often known as the inversion time (see Figure 2. ***10***10). Assuming the system is in equilibrium when the pulse sequence is applied, then since the 180° RF pulse acts to invert the magnetisation of the system ***M(t₁)=-M(0)***. The spins are then left for a time *TI*, during which longitudinal relaxation back to the equilibrium state occurs. By applying the 90° pulse any longitudinal magnetisation will be rotated into the transverse plane, where it can be measured. This process can then be repeated a number of times for various values of *TI*, thus building up a plot of how the spins relax as shown in Figure 2. ***11***11. The form of this curve is described by the Bloch equation for M_z shown in Equation 2.31 where θ=180° and therefore the T_1 of the sample can be found from this plot.

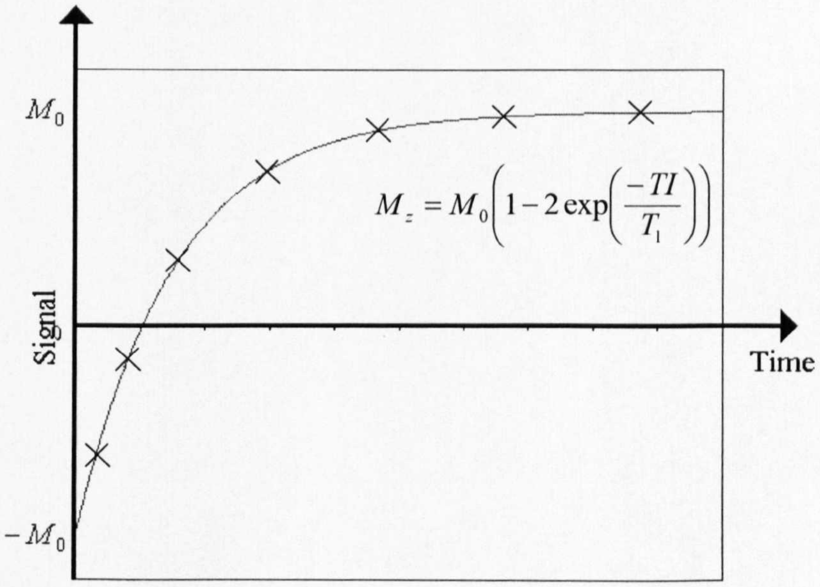

Figure 2. 11: Inversion recovery curve and associated Bloch equation

It is important to remember that when this sequence is executed for various *TI* values, it is imperative to leave a long time between measurements. This is to allow the spins to relax fully to a state of equilibrium, otherwise the premise on which the whole sequence is based is void. To ensure the system is fully relaxed before application of an 180° pulse then a time, $t>>5T_1$ is usually left after the previous 90° pulse.

Here, the principles behind NMR and how a signal can be obtained from a sample of nuclei have been explained. The relevance to MRI of each of the ideas and phenomena discussed here will become clear in the next chapter. In Chapter 3 the method by which spatial encoding of data can be achieved will be explained, thus making apparent the process by which a proton density image can be produced.

2.5 References

1. Francis, S.T., *Third Year Magnetic Resonance course notes.* 2004.
2. Levitt, M.H., *Spin Dynamics: Basics of Nuclear Magnetic Resonance. Chapter 2.* 5 ed. 2005, Chichester. 686.
3. Levitt, M.H., *Spin Dynamics: Basics of Nuclear Magnetic Resonance. Chapter 6.* 5 ed. 2005, Chichester. 686.
4. Levitt, M.H., *Spin Dynamics: Basics of Nuclear Magnetic Resonance. Chapter 10.* 5 ed. 2005, Chichester. 686.
5. Levitt, M.H., *Spin Dynamics: Basics of Nuclear Magnetic Resonance. Chapter 16.* 5 ed. 2005, Chichester. 686.
6. Dirac, P.A.M., *The quantum theory of the electron.* Proceedings of the Royal Society of London Series A, 1928. **117**: p. 610-624.
7. Morris, P.G., *Nuclear Magnetic Resonance Imaging in Medicine and Biology.* 2nd ed. 1990, Oxford: Oxford University Press.
8. Bloch, F., *Nuclear Induction.* Physical Review, 1946. **70**: p. 460-474.
9. Hahn, E.L., *Spin echoes.* Physical Review, 1950. **80**(4): p. 580-594.

Chapter 3

Magnetic Resonance Imaging

3.1 Introduction

Chapter two has provided the reader with a basic understanding of the principles behind the interactions of nuclei with magnetic fields and how a signal may be obtained by exciting nuclei into precession. This chapter builds on that understanding; with an explanation of how one can obtain an image from a sample using a variety of pulse sequences and how the images can be weighted according to proton density, T_1 or T_2 properties of the tissues. The basic principles which must be understood for all imaging sequences will first be explained. These principles were initially devised by Lauterbur and Mansfield [1, 2] in the 1970's. The details of key pulse sequences used within the body of this work will then be described. How to perform MRI in a clinical setting in terms of equipment and safety issues will also be explored.

3.2 Image formation

3.2.1 *k*-space

To understand how an image is formed using magnetic resonance it is important to understand how the signal is spatially encoded. This involves the concept of k-space, or reciprocal space, the general theory of which was described by Mansfield and Grannell [2]. We know from Chapter 2 that the precessional frequency of the nuclei in a sample is given by $\omega_L = -\gamma B_0$ where B_0 denotes the static magnetic field parallel to the z-axis. It is easy to comprehend that if the strength of B_0 varies linearly across space then the frequency of precession of the spins will also vary in a linear fashion. Therefore by Fourier transforming the detected signal, information about the range of frequencies induced by the varying magnetic field is obtained. Hence, variation of the magnetic field is a clear way to encode information spatially and is the concept which underpins magnetic resonance imaging.

When a sample is excited with an RF pulse whilst also subjected to time dependent magnetic field gradients then the Larmor frequency will be dependant upon both the static magnetic field and the gradients such that:

$$\omega(\mathbf{r}) = \gamma(B_0 + \mathbf{G}.\mathbf{r})$$

[3. 1]

where **G** is the gradient vector such that:

$$\mathbf{G} = G_x x\mathbf{i} + G_y y\mathbf{j} + G_z z\mathbf{k}$$

and **r** is the position vector. If one neglects T_2 effects then the resultant signal measured (using quadrature phase sensitive detection at frequency, $\omega = \gamma B_0$) will be oscillating at a frequency, $\gamma\mathbf{G}.\mathbf{r}$, and can be described by:

$$S(t) = \iiint_V \rho(\mathbf{r})\exp(i\gamma\mathbf{G}.\mathbf{r}t)d\mathbf{r}$$

[3. 2]

where $\rho(\mathbf{r})$ describes the spin density as a function of position within the sample and V represents the volume of the sample. The phase evolution induced by the gradients can be defined by the vector, **k**, so that:

$$\mathbf{k} = \gamma\mathbf{G}t.$$

[3. 3]

By substituting Equation 3.3 into Equation 3.2 one gets:

$$S(\mathbf{k}) = \iiint_V \rho(\mathbf{r})\exp(i\mathbf{k}.\mathbf{r})d\mathbf{r}.$$

[3. 4]

The application of the Fourier transform yields the spin density across the sample:

$$\rho(\mathbf{r}) = \frac{1}{(2\pi)^3}\iiint_V S(\mathbf{k})\exp(-i\mathbf{k}.\mathbf{r})d\mathbf{k}.$$

[3. 5]

Therefore one can produce a spatial map of spin density using Equation 3.5. A simple schematic of how a one dimensional spin density map may be formed is shown in Figure 3. 1. By varying the gradients, **G**, over time then the whole of k-space can be sampled. By then performing the inverse Fourier transform on the signal, a spin density map in real space can be obtained. Hence, Equation 3.2 coupled with Equation 3.5 forms the basis of the theory behind producing a magnetic resonance image. This encoding according to frequency is conceptually fairly easy to grasp and is known as *frequency encoding*.

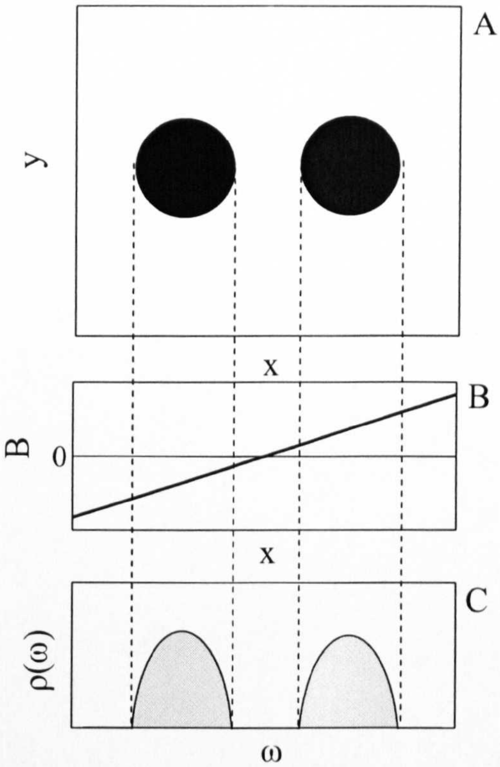

Figure 3. 1: Application of a magnetic field gradient in the x-direction to 2 test tubes of water: the spatial variation of spin density (A) the magnetic field applied to the samples (B) and the frequency density plot (C) Adapted from [3].

There is a second type of encoding which it is necessary to understand, that of *phase encoding,* which is possible due to the quadrature signal detection. Here the phase of the spins varies linearly with spatial position. This is also achieved by the application of a gradient; this time in a different direction to the frequency encoding gradient, for example in the y direction with an amplitude, G_y. If this gradient is applied for a time t_y then the angle through which the phase will be shifted is given by:

$$\phi(y) = \gamma G_y t_y y \, . \qquad [3.\ 6]$$

Notice the similarity to Equation 2.23 since the same principles apply. This means the phase will now be shifted by $\phi(y)$ relative to the original phase, providing another method of spatial encoding which is important for the imaging techniques described here.

The method by which k-space is sampled depends on a variety of factors such as the speed, resolution and contrast required for a particular image. There are now numerous methods that have been developed to sample k-space which vary in complexity; a few of these will be described in the following sections. The explanation of imaging thus far has ignored the effects of relaxation on the sample, but this can also be exploited with the right sequence parameters to provide different image contrasts. A brief explanation of how T_1 and T_2 can be used to enhance image contrast is given in Section 3.4.

3.2.2 Slice selection

By applying a gradient in the direction perpendicular to the plane of interest during the RF excitation the problem of spatial encoding described above can be reduced from three dimensions to two dimensions. This technique for initially selecting a slice (often termed *slice selection*) before spatially encoding the image is used in many pulse sequences. It can be assumed that the RF pulse applied for slice selection occurs for a short time and therefore relaxation effects can be ignored and the evolution of the magnetisation can be described by Equation 2.27:

$$\begin{aligned}\frac{d\mathbf{M}}{dt} &= \gamma\mathbf{M}\times\mathbf{B}\\ &= -\gamma\mathbf{B}\times\mathbf{M}\,.\end{aligned}$$

[3. 7]

If one considers the application of an oscillating RF magnetic field, B_1, at the same time as a magnetic field gradient, $B_z=G_z z$ then the rate of change of the magnetic field in the rotating frame of reference can be expressed as follows:

$$\begin{aligned}\frac{d\mathbf{M}}{dt} &= \begin{pmatrix}-\gamma B_1\\ 0\\ -\gamma B_z\end{pmatrix}\times\begin{pmatrix}M_{x'}\\ M_{y'}\\ M_z\end{pmatrix}\\ &= \begin{pmatrix}\gamma M_{y'}B_z\\ \gamma M_z B_1-\gamma M_{x'}B_z\\ -\gamma M_{y'}B_1\end{pmatrix}\end{aligned}$$

[3. 8]

At this point, it is necessary to make another assumption to enable an analytical solution to be obtained. This assumption, known as the *small tip angle approximation [4]*, is that $M_z=M_0$ (*i.e.* the *z*-component of the magnetisation does not change with the application of the RF pulse). This can be considered true if the magnetisation is only perturbed from the *z*-axis by a small angle. With this assumption in mind, the change of magnetisation in the longitudinal direction when time is zero and the transverse magnetisation can be expressed with the complex form $M_{x'y'} = M_{x'} + iM_{y'}$, such that:

$$\frac{dM_{x'y'}}{dt} = \frac{dM_{x'}}{dt} + i\frac{dM_{y'}}{dt}.$$

By substitution of the correct parts of Equation 3.8 into this and expressing the magnetic field variables as $\omega_1=-\gamma B_1$ and $\omega_2=-\gamma B_z$ one gets:

$$\begin{aligned}\frac{dM_{x'y'}}{dt} &= -\omega_2 M_{y'} + i\omega_2 M_{x'} - i\omega_1 M_0 \\ &= i\omega_2(M_{x'} + iM_{y'}) - i\omega_1 M_0 \\ &= i\omega_2 M_{x'y'} - i\omega_1 M_0.\end{aligned}$$

Rearranging this and multiplying through each side by $e^{-i\omega_2 T}$ gives:

$$e^{-i\omega_2 T}\left(\frac{dM_{x'y'}}{dt} - i\omega_2 M_{x'y'}\right) = -i\omega_1 M_0 e^{-i\omega_2 T}$$

$$\frac{d}{dt}\left[e^{-i\omega_2 T} M_{x'y'}\right] = -i\omega_1 M_0 e^{-i\omega_2 T}.$$

[3. 9]

Assuming the duration of the RF pulse is $2T$ then by integrating between $-T$ and $+T$ the transverse magnetisation immediately after the RF pulse can be calculated:

$$M_{x'y'}(t) = -iM_0 e^{i\omega_2 T}\int_{-T}^{T}\omega_1(t) e^{-i\omega_2(t)t}\,dt.$$

Knowing that $\omega_1=-\gamma B_1$ and $\omega_2=-\gamma B_z=-\gamma G_z z$ then by substitution one can obtain the relationship:

$$M_{x'y'} = i\gamma M_0 e^{-i\gamma G_z zT}\int_{-T}^{T} B_1(t) e^{i\gamma G_z(t)zt}\,dt.$$

[3. 10]

Equation 3.10 provides us with two pieces of information. The first thing to note from the latter part of this equation is that the spatial profile of the transverse magnetisation follows the Fourier transform of the amplitude profile $B_1(t)$ of the RF pulse so, for example, excitation of a rectangular slab profile (a slice through the sample) can be achieved by modulating the RF field with a sinc function. The draw-back of the sinc function is that to obtain an exact top hat function in space the sinc function must extend to infinity in either direction. Of course, in reality this is not possible as the RF pulse must be of finite duration. It has been found that truncating the sinc function to only two side lobes is a reasonable compromise between pulse duration and excitation profile (see Figure 3. 2). The excitation profile for the sinc pulse containing 2 side lobes appears to significantly deviate from a top hat function produced by the Fourier transform of a pure sinc pulse. To ensure the slice profile is closer to a top hat function the sinc pulse with the reduced number of side lobes is convolved with a Gaussian function to smooth out the excitation profile.

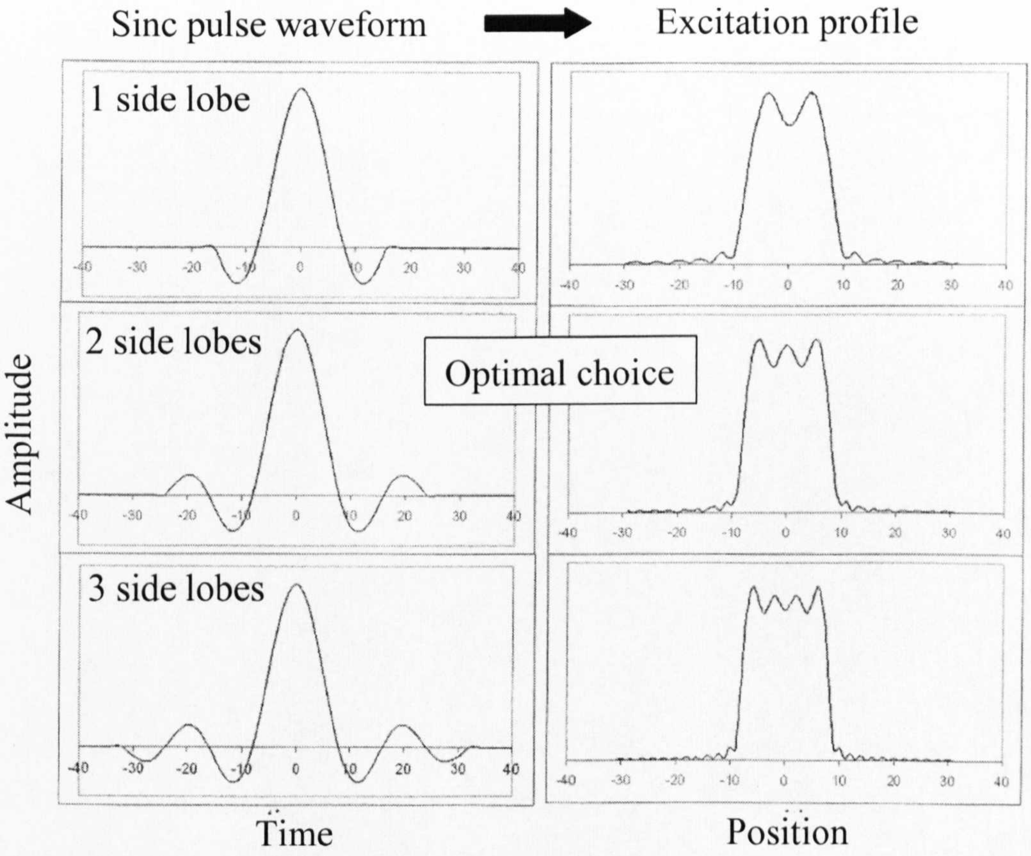

Figure 3. 2: Correspondence of sinc profiles and respective excitation profiles for a variety of durations of sinc pulse. Adapted from [5].

The bandwidth (BW) of a sinc pulse is defined as $\Delta\nu = \frac{1}{t_0}$ where t_0 is the time from the maximum amplitude of the sinc pulse to the first zero crossing (Figure 3. 3). The thickness of the excited slice is then given by:

$$d = \frac{2\pi\Delta\nu}{\gamma G_z}.$$

[3. 11]

Therefore it can be seen that both the pulse bandwidth and the gradient strength affect the thickness of the slice selected. In reality it is usually preferable to have both a high BW and high gradient strength. In this way, the frequency difference between adjacent slices is maximised therefore errors in slice selection due to field inhomogeneity are minimised.

The second piece of information which can be gained from Equation 3.10 is that there is a phase term, $e^{-i\gamma G_z zT}$, meaning that whilst the RF pulse is applied the spins dephase through an angle $\gamma G_z zT$ with respect to spins at $z=0$. This dephasing can be overcome by applying another gradient of equal amplitude and opposite direction for a time, *T,* immediately after the RF pulse thus refocusing the spins (Figure 3. 3).

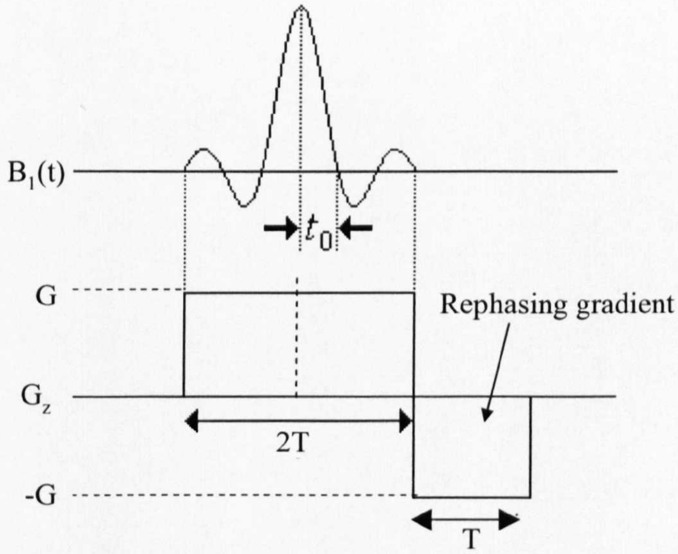

Figure 3. 3: The RF pulse and associated gradients in the z-axis required for slice selection.

One should note that all of the information derived here has been for the small tip angle approximation and therefore for larger flip angles the conclusions drawn here do not necessarily hold. For bigger flip angles, a different shaped RF pulse must be used in order to excite a rectangular slab. Surprisingly however, the small tip angle approximation does hold reasonably well up to 90°. Therefore within this work a modified sinc RF pulse will be used extensively within the pulse sequences employed.

3.3 Spin warp imaging

As I have already briefly mentioned there are many ways to sample k-space and different methods have been developed to optimise parameters such as acquisition speed, image resolution or contrast. It is beyond the scope of this work to consider many of the different pulse sequences and therefore only a couple of the key ones necessary for the understanding of this work will be covered. Spin warp imaging is one of these sequences. It was invented in 1980 [6] and is used regularly in clinical settings today.

After initial application of slice selective pulse to the sample Equation 3.5 can be reduced to:

$$\rho(x,y)=\frac{1}{(2\pi)^2}\iint_A S(k_x,k_y)\exp(-i\{k_x x+k_y y\})dk_x dk_y .$$

[3. 12]

Therefore only two dimensions of k-space must now be sampled which can be done using the frequency and phase encoding described earlier. From Equation 3.3 we know that:

$$k_x=\gamma G_x t_x \text{ and } k_y=\gamma G_y t_y$$

[3. 13]

where t_x and t_y are the durations of the x and y gradient pulses respectively. Therefore by varying either the time or strength of the gradient pulses it is possible to sample the whole of k-space. The pulse sequence for a gradient echo Spin Warp sequence is shown in Figure 3. 4.

After the application of a 90° RF pulse in conjunction with a slice selective gradient, which excites a thin slab of material within the sample, a gradient in the phase encoding, G_y, direction is applied. This causes a phase shift of the magnetisation. From Equation 3.6 it is clear that the degree of this phase shift will depend upon both the duration and strength of the gradient applied along this axis. It is therefore possible to step through the phase encoding by either fixing the gradient and varying the time it is applied for or fixing the time and varying the gradient strength. It has proved advantageous to fix the time and change the gradient strength. This is because if a B_0 field inhomogeneity is present then, by keeping the duration of the gradient pulse the same, the extra phase is accumulated due to the inhomogenteity will be kept the same for each line of k-space.

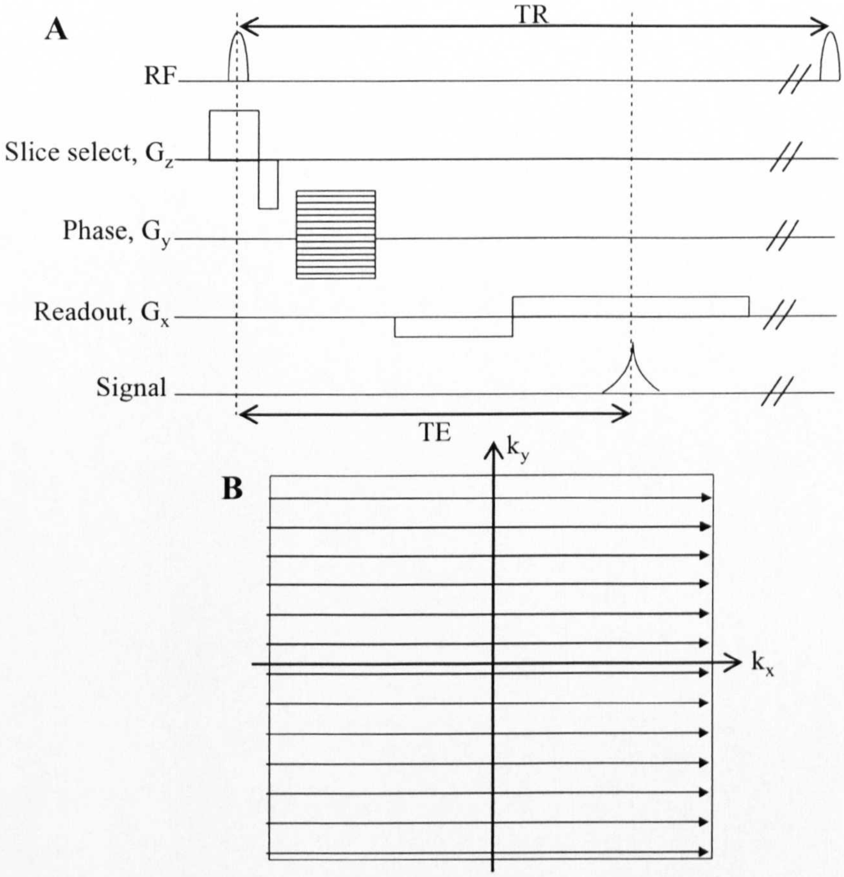

Figure 3. 4: Spin Warp pulse sequence (A) with associated k-space trajectory (B).

Once the phase shift has been generated, a gradient in the readout direction is applied with a magnitude $-G_x$ which serves to dephase the spins. The second positive lobe of this gradient with magnitude G_x, serves to rephase the spins and thus to produce a gradient echo. For the application of each phase encoding gradient, one line of k-space in the k_x direction is sampled and therefore the generation of N_y gradient echoes is necessary to produce an image of dimensions $N_x \times N_y$. The phase encoding gradient is increased in increments of ΔG_y between $-G_y$ and G_y. For each of these steps N_x samples of the signal are measured. Both the field of view (FOV) and the resolution (δx, δy) of an image depend upon the choice of gradient strengths and timings, as can be seen in Equations 3.14 and 3.15.

$$FOV_x = \frac{2\pi}{\Delta k_x} = \frac{2\pi}{\gamma G_x t_x} \qquad FOV_y = \frac{2\pi}{\Delta k_y} = \frac{2\pi}{\gamma G_y t_y} \qquad [3.\ 14]$$

$$\delta x = \frac{2\pi}{N_x \Delta k_x} = \frac{2\pi}{\gamma G_x t_x N_x} \qquad \delta y = \frac{2\pi}{N_y \Delta k_y} = \frac{2\pi}{\gamma G_y t_y N_y} \qquad [3.\ 15]$$

where $t_x N_x$ is the duration of the sampling window.

This description of the Spin Warp sequence has used a gradient echo (for full description of a gradient echo refer to Chapter 7) in which T_2' effects are not refocused thus the image is weighted by T_2^* effects. It is possible by the insertion of a 180° RF pulse after the phase encoding step to produce a Spin Warp sequence using a spin echo and therefore to generate image contrast which depends purely on T_2 decay.

3.4 Image Contrast

As briefly mentioned at the end of the last section, image contrast strongly depends on the imaging sequence used and this can be a deciding factor when choosing a pulse sequence. For the description of the Spin Warp sequence above, two assumptions were made: firstly that the acquisition time for a line of k-space was short compared to T_2^* and secondly that the time between the RF pulses was long so that thermal equilibrium of the magnetisation is reached before each RF pulse is applied. In this case the image intensity would be proportional to the proton density of the tissues alone. However, it is clear from Figure 3. 4 that a time, *TE*, elapses between the excitation of a slab and the acquisition of an echo during which the signal of the protons decays with T_2 (or T_2^* for a gradient echo). Therefore different tissues with different T_2 relaxation properties produce different signals. Equally if a series of RF excitation pulses are applied in quick succession then there will not be enough time for the full recovery of the longitudinal magnetisation in the inter-pulse period and a steady state of longitudinal magnetisation is reached. The amplitude of transverse magnetisation in the steady-state can be described for most imaging sequences by the Ernst formula [3]:

$$S_{echo} = E_2 M_0 \frac{1 - E_1}{1 - E_1 \cos\theta} \sin\theta$$

[3. 16]

where $E_1 = e^{-TR/T_1}$ and $E_2 = e^{-TE/T_2}$ (T_2 should be replaced with T_2^* for gradient echo sequences). θ is the flip angle, TR is the time between consecutive RF pulses and TE is the time between excitation and echo. It is clear that because different tissues have different T_1 and T_2 relaxation times by selecting the TE and TR parameters appropriately, maximum differences in the strength of signals from different tissues can be obtained with either T_1 or T_2 weighting. A simplified illustration of how to achieve such contrast differences is given in Figure 3. 5. To weight an image with T_1 contrast it is normally necessary to have a relatively short TR to maximise the difference in the signal recovery between different tissues. To weight an image towards T_2 relaxation times it is necessary to have a long TR to minimise the T_1 effects and a long TE to maximise the sensitivity of the sequence to the differences in T_2 relaxation times.

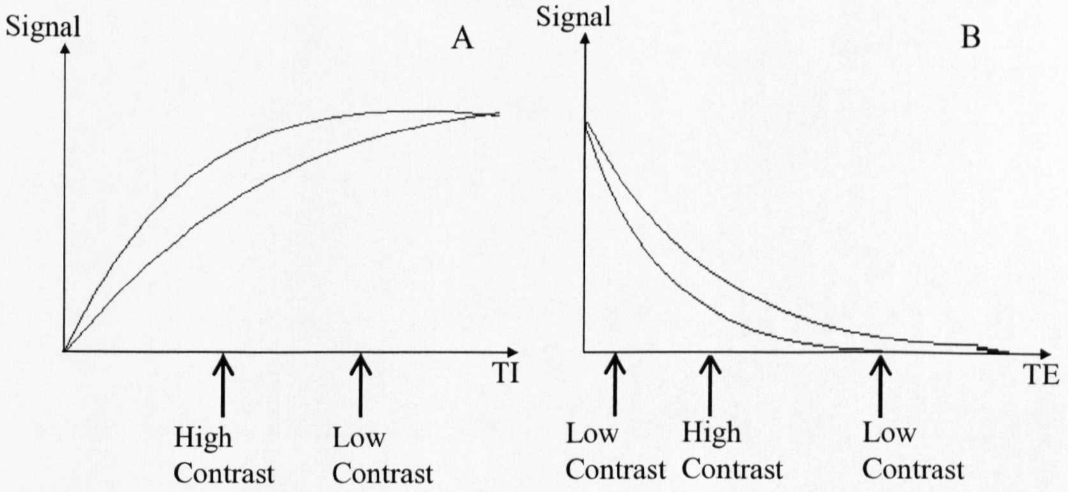

Figure 3. 5: Possible contrasts possible to produce T_1 weighting (A) or T_2 weighting (B) to an image.

It should also be realised that T_1, T_2 and T_2^* are dependent on field strength. T_1 increases with field whilst T_2 and T_2^* decrease. The result of this is that if the same sequence is run at two different field strengths the image contrasts obtained at each field strength are likely to differ.

3.5 Echo Planar Imaging

Echo Planar Imaging (EPI) was the brain-child of Sir Peter Mansfield who first proposed the concept in 1977 [7]. It is a pulse sequence which allows the whole of two dimensional k-space to be acquired with one RF pulse excitation and therefore it has a much higher temporal resolution than the Spin Warp imaging sequence described above. Therefore using this technique it is possible to perform real time imaging of the heart as well as functional imaging of blood flow and oxygenation changes in the brain. Despite these advantages over previous pulse sequences, at the time of its invention technological difficulties relating to fast gradient switching and computer reconstruction power hampered the advancement of this technique in the MR community for a number of years. However, the group at the University of Nottingham continued to develop this method and technological advances have allowed this sequence to come into common usage on modern clinical MR scanners, such as the Philips Acheiva systems used in this work.

EPI allows two-dimensional k-space to be sampled entirely from the signal generated by one excitation pulse. An EPI sequence is made up of three parts: a preparation phase; slice selective pulse and finally, a readout section as shown in Figure 3. 66A. This figure does not show the preparation phase as it is optional; it usually consists of fat suppression and/or inversion pulses. Therefore within the illustrated sequence, a slice selective excitation pulse (I) is first applied. This is usually a 90° pulse, which excites a thin slab of spins across the object of interest (as described previously). Slice selection is then followed by the readout period (II) during which the k-space information is encoded; all lines of k-space are acquired under a switched readout gradient, G_x. After the slice selection pulse, G_z, one begins in the centre of k-space. Therefore pre-excursion pulses are needed in both the k_x and k_y direction to move to the edge of k-space where sampling will begin (Figure 3. 6 B). A sequence of gradient echoes is then formed using the switched read-out gradient. The readout gradient dephases and rephases the magnetisation allowing the first line in k-space (k_x direction) to be acquired. A blipped phase encode gradient, G_y, is then applied which steps up in the k_y direction to the next line in k-space. The readout gradient is then applied with opposite polarity and another line of k-space running in the k_x

direction is acquired. These two gradients are alternated until the whole of k-space has been sampled. This method of crossing k-space is often known as the Modulus Blipped Echo-planar Single-pulse Technique (MBEST)[8].

Alternate echoes are acquired under opposite polarity of the readout gradient (Figure 3. *6*6A) resulting in differences between those lines (Figure 3. *6*.6B). Therefore alternate echoes have to be time-reversed (switched around the *t=0* line) before a Fourier transform can be applied to generate the image.

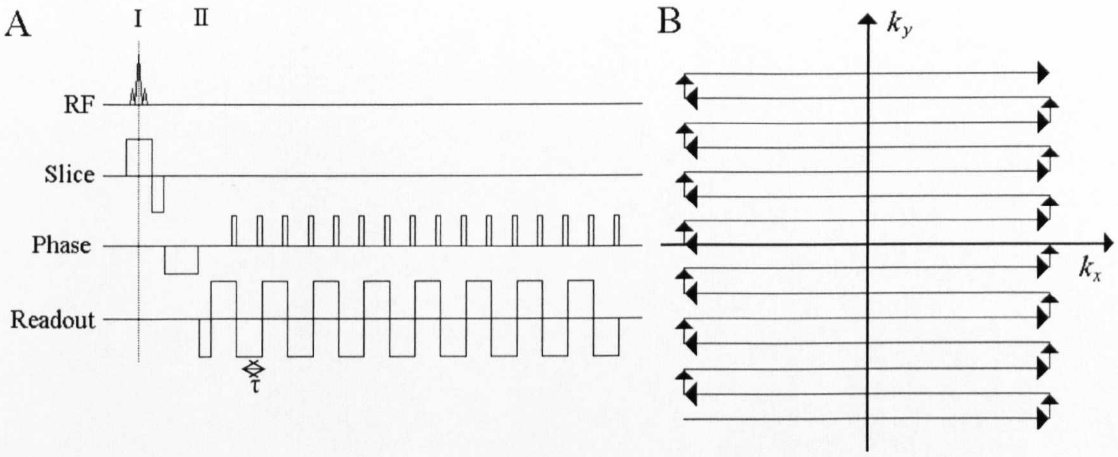

Figure 3. 6: Diagram of the basic EPI sequence (A) and associated k-space trajectory (B).

3.5.1 Limitations of EPI

As with all pulse sequences there are limitations in the performance of EPI along with the advantages of fast acquisition time described earlier. Here, some details are given of the main limitations of the sequence in terms of artefacts which may be encountered. Greater detail on some of these problems is given in Chapter 7, where the implications of these artefacts in terms of multi-modal imaging will become apparent.

3.5.1.1 Voxel bandwidth

The first limitation is the bandwidth of each voxel which is defined by the way in which k-space is sampled. The relationship between the voxel bandwidth, Δυ, and sampling in k-space for each axis is given by:

$$\Delta\nu_x = \frac{1}{\tau} \text{ (A) and } \Delta\nu_y = \frac{1}{N_y\tau} \text{ (B)}$$

[3. 17]

where τ is the time between echoes (Figure 3.6) and N_y is the number of echoes (or the number of phase encoding blips). The voxel bandwidth indicates the maximum frequency separation between voxels that can be adequately sampled. So, for example, if one takes a typical set of parameters corresponding to a 128×128 matrix size at a gradient switching frequency of 1000Hz; the pixel bandwidth in the x-direction is 2000Hz, but the pixel bandwidth in the y-direction is only $2000/128 = 15.6Hz$. This means if the difference in precessional frequencies within a voxel is of the order of 15.6 Hz there will be mis-registration of information in the phase encoding direction. Such differences in precessional frequency result from magnetic field inhomogeneity. The linewidth in the absorption spectrum is given by $\Delta\omega_L = \frac{2}{T_2^*}$ by substitution of Equation 3.17B into this expression and assuming that $\Delta\upsilon_y$=15.6 Hz, for the situation described above we can deduce that the adjacent pixels within the image will be distinguishable if $T_2^* > \frac{2}{2\pi\Delta\nu_y} \approx 20ms$. If this requirement is not met then blurring of the image will occur. This becomes a particular problem at higher field strengths where T_2^* decreases.

Normally the problem of line broadening is mainly overcome by the use of effective shims, ensuring good homogeneity of the static magnetic field. However, looking at Equation 3.17 it is clear another feasible method would be to reduce the echo spacing thus increasing the bandwidth per voxel. The disadvantage of this is that $SNR \propto 1/\sqrt{BW}$. Therefore an important trade-off exists between the voxel bandwidth and signal to noise.

3.5.1.2 Chemical shift

This phenomenon relates to the NMR frequency variations resulting from intrinsic magnetic shielding of anatomic structures. Both the molecular structure and the electron orbitals contribute to a proton's chemical shift. In MRI of the body the most apparent chemical shift differences are between protons in fat molecules and those in water (*i.e.* in tissue). The resonance frequencies differ by 147 Hz T^{-1} [9] between these two types of protons. Therefore for the imaging sequence described in the previous sub-section the mis-registration between images of the two species would be $^{147}\!/_{15.4} \approx 9.5$ pixels per Tesla. The result of this is an artefact (often known as a fat ring) within the image which is a ring of fat that is spatially shifted relative to the rest of the image. This can be overcome by deciding before imaging if the fat or free water is to be imaged and then nulling the signal from the other species.

3.5.1.3 Magnetic Susceptibility

Differences in the magnetic susceptibility of tissues will cause spatial variation of the magnetic field, leading to signal attenuation and misregistration. This effect tends to occur at tissue boundaries or where a foreign object with a distinctly different magnetic susceptibility is near (or in) the body. This process is described in more detail in Chapter 7 where the effects of magnetic susceptibility differences between EEG cap materials and the human head are relevant.

3.5.1.4 Eddy currents

Rapidly switched magnetic field gradients induce eddy currents within electrical conductors positioned close to gradient coils. These eddy currents generate a decaying magnetic field which varies spatially and temporally depending on the form of the conductor. These eddy currents can therefore introduce another source of field inhomogeneity into the sample which manifest in image artefacts, such as ghosting and distortion. Such artefacts can be overcome by shielding of the gradient coils or by adjusting experimental methods [10].

3.5.1.5 Nyquist Ghost

This form of ghosting (also known as the N/2 Ghost) is due to the method in which k-space is sampled during EPI. As already discussed each alternate line of k-space is sampled in the opposite direction during EPI (not the case in Spin Warp Imaging). This means that alternate lines of k-space must be reversed before the image is reconstructed. There are a number of factors which may cause differences in the acquisition of the odd and even lines of k-space and result in ghosting. One of these occurs if there are offsets from the centre of k-space in the read direction for each line since in this situation after reversal of every other line, this offset will alternate from line to line. Offsets from the centre of k-space are not uncommon and can result from a myriad of factors including timing errors between the start of the read gradient and the start of sampling or imperfections in the profile of the gradients.

The result of this alternating offset is that, following the Fourier transform, an extra periodicity is introduced into the image with a frequency $2\Delta k_y$. This leads to a ghost being observed in the image which is shifted in the phase encode direction by half the FOV. It is possible to eliminate ghosting by using algorithms which correct the phase of alternate lines of k-space [11] and therefore Nyquist ghosting was not a significant problem in the work described in this thesis.

3.5.1.6 Foldover Artefacts

Foldover artefacts occur as a result of undersampling of the frequencies contained within the measured signal. To avoid this problem it is necessary to satisfy the Nyquist limit: the inverse of the sample point spacing in k-space must be at least twice the maximum spatial offset from the origin that occurs in the object. If this criterion is not satisfied then the Fourier transform cannot distinguish locations that are present outside of this range and therefore assigns these positions to smaller offsets. The result of this is to wrap this part of the image (which was outside the FOV) around to the opposite side of the image.

A low-pass filter can be applied in the frequency encoding direction to avoid this problem. In the phase encode direction it is necessary to reduce the distance between lines in k-space to avoid aliasing or to use inner volume excitation or outer volume suppression. Another method to avoid the problem, if there is a particular piece of anatomy to be viewed, is to change the direction of the phase and frequency encoding so that any foldover does not obscure the object of interest.

3.5.2 Multi-Shot

The description of EPI thus far has been for single shot EPI (*i.e.* the whole of k-space is sampled with one RF excitation). However, it is also possible to conduct multi-shot EPI in which not all lines of k-space are acquired under one FID. This is performed by increasing the distance of sampling positions in k-space (*i.e.* making Δk_y larger) while keeping the maximum and minimum values of k_y fixed; then in a subsequent FID acquisition the other lines of k-space can be "filled in". This process means that ghosting can be reduced as the frequency separation between points in the phase encode direction is increased by this acquisition method. This leads to a reduction in artefacts. The other advantage of the multi-shot method is that less strain is placed on the gradient coils. However, the clear disadvantage is the increase in acquisition time relative to that of single shot EPI which raises problems for functional work as well as increasing the potential for motion artefacts to be introduced to the images.

3.5.3 Sensitivity Encoding

Sensitivity encoding, or SENSE, is a method often employed to reduce acquisition time which was first proposed in 1999 by Pruessmann [12]. Although this method can be applied to a wide variety of pulse sequences it is mainly used in conjunction with EPI in the body of this work. SENSE is a method by which the number of lines of k-space to be sampled can be reduced without reducing the resolution or FOV of the image. The reduction in k-space sampling means the *TE* of the EPI sequence can be reduced without having to put further demand on the gradients. This method relies on the premise that the contribution of a source at the receiver coil varies appreciably with its position relative to the coil. Therefore "knowledge of spatial receiver sensitivity implies information about the origin of the detected MR signal, which may be utilized for image generation"[12]. This means that by using distinct receivers in parallel one can obtain spatial information about the sample.

With the use of SENSE, scan time is reduced while spatial resolution is maintained by increasing the separation of sampling positions in k-space (*i.e.* making Δk_y larger) while keeping the maximum and minimum values of k_y fixed. The reduction in the number of samples acquired in k-space due to the implementation of SENSE is referred to in this work as the SENSE factor. From Equation 3.14 it is clear that normally if Δk_y is increased then the FOV will decrease. In SENSE imaging an image which is aliased (due to the foldover effects mentioned above) with a reduced FOV, is obtained for each receiver coil. To create a full FOV image the superposition of the signals is undone resulting in an image with the desired FOV being collected in a reduced time. To unwrap the signals it is necessary to know the sensitivity of each of the coils and therefore a reference scan is first acquired to help with the decoding of the superposition of the signals. To carry out this imaging technique it is necessary to have more receiver coils than the SENSE factor otherwise the unwrapping is not possible. The use of SENSE, for example, allows an increase in the coverage of the brain that can be achieved without compromising the temporal resolution of the acquisition. Implementing SENSE also potentially reduces acoustic noise as fewer demands are made on the gradients as less lines of k-space must be acquired. This is advantageous as it makes the MR scanner a less hostile environment for subjects. Another advantage particularly relevant to this work is the reduction in EPI distortion via the implementation of SENSE. This is because the decrease in acquisition time that is made possible by implementation of SENSE leads to a reduction in problems associated with time evolution such as phase distortion. The disadvantage of this technique is that the SNR reduces as the SENSE factor is increased.

3.6 Instrumentation

During the course of the work described in this thesis MR Scanners operating at three different magnetic field strengths (1.5, 3 and 7 Tesla) have been used; each of these came from the Philips Acheiva family. Since these systems are commercially available only a general overview of their instrumentation will be described here. An MR system is made up of four main components: magnet, gradient, RF and control subsystems. A schematic of an MR system is shown in Figure 3. 77 indicating how all the parts relate to one another.

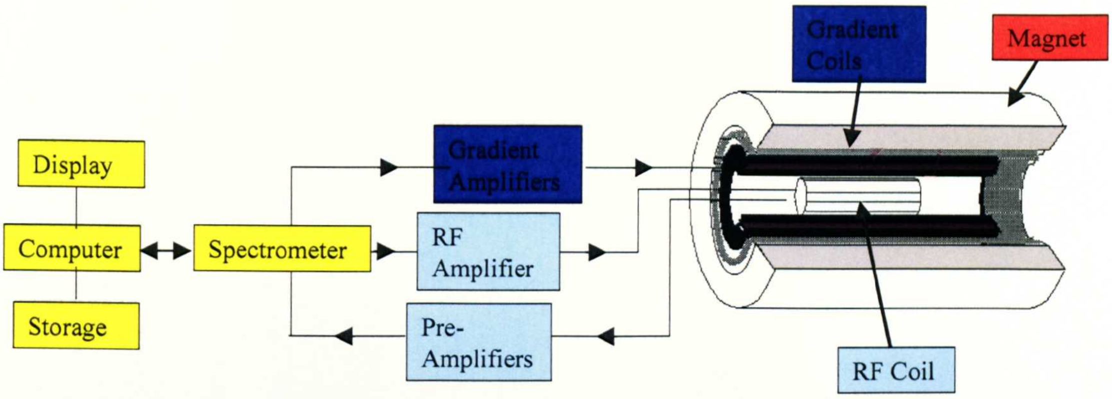

Figure 3. 7: A schematic diagram of a typical MRI scanner showing the four main subsystems.

3.6.1 Magnet

To create a large, homogeneous magnetic field, a superconducting magnet (*i.e.* a solenoid made from superconducting wire) is used. Superconductivity is a characteristic of certain materials (such as niobium-titanium alloys) which means that below a critical temperature (usually a few Kelvin) the material loses all resistance and therefore becomes superconducting. This property is lost however, if the magnetic field is too large, therefore limiting, to some extent, the capabilities of this technology in MRI. However, up to 7 T the superconducting properties of niobium-titanium alloys remain and this type of superconductor is used in all the systems employed in this work. To keep the superconducting material below the critical temperature, liquid helium is generally used as a cryogenic coolant. The use of cryocooler pumps reduces the boil-off of the liquid helium by converting the helium gas back to a liquid by changes in pressure, similar to the heat-engine concepts used in a refrigerator.

It is unsurprising that the area over which the high magnetic field produced by the magnet of an MR scanner extends is large. The fields outside the bore of the magnet are termed the *fringe fields*. These fringe fields are a potential hazard to the public and staff and therefore it is necessary to limit their extent as much as possible. The acceptable magnetic field for people with pace-makers to experience is 5 Gauss (0.5 mT). Therefore it is advantageous for the fringe fields to decay to this value as rapidly as possible. This is achieved by active shielding [13] within the 1.5 and 3 T systems, where counter wound current loops are placed at the ends of the superconducting solenoid resulting in a significant reduction of the extent of the fringe fields. This approach is not yet possible however, at 7 T and therefore a large amount of ferromagnetic material is placed around the magnet to reduce the fringe fields. In the case of our 7 T system, 213 tonnes of iron form a box around the system.

As has already been discussed in the previous and current chapters, execution of MRI requires an extremely homogeneous magnetic field. Although the superconducting magnet inherently generates a field with good homogeneity it is generally necessary to use shimming to improve this further. Shimming can take two forms: active and passive. Passive shimming is used to correct for magnet defects such as coil winding errors. In passive shimming, small quantities are of iron are placed within the magnet bore. These serve to contribute to the magnetic field and balance inhomogeneities out [14]. Due to the effects of paramagnetism and diamagnetism when a sample is placed within the coil the field can again be distorted and therefore active shims are used to restore the homogeneity. These shims are coils of wire which are designed to produce small magnetic fields which vary with position and when carrying appropriate currents act to balance out any inhomogeneities. First order shims produce fields which vary linearly whereas, second order shims generate quadratically varying fields. Both first order shims (using the gradients) and second order shims are available for use on the Philips scanners. These shimming systems implemented on the Philips scanners follow the designs of Gruetter [15]. This shimming process is automatic on the Philips system with the operator able to either use the automatic shimming or dictate the volume over which to shim.

3.6.2 Gradient System

Magnetic field gradients are needed to provide the spatial encoding that has been described in this chapter. The gradient coils must produce a variation in the z-component of the magnetic field in three orthogonal directions, x, y and z. The linear variation of the magnetic field along the z-axis is conventionally produced using a Maxwell coil pair arrangement, in which a pair of co-axial coils of radius, r, are separated axially by a distance $\sqrt{3}r$ and wound in opposite directions. This arrangement serves to produce a linear gradient where the field is zero half-way between the two coils. A magnetic field variation in the x-y plane can typically be produced using a Golay coil arrangement, where two pairs of saddle coils are used to produce variations in the magnetic field along the x or y axes. These coil designs are however, simplistic and more complex ones have now been developed. Designing such coils is still an area of active research [16].

From inspection of the EPI pulse sequence it is clear that rapid switching of the gradients is necessary. To achieve this switching, the inductance of the gradient coils must be low, resulting in a requirement for large currents in order to reach appropriate magnetic field gradient amplitudes. The currents to drive the gradient coils are digitally generated by the computer and then converted into analogue voltages which are fed through power amplifiers to get the currents required. It is the rapid switching of these gradients which is responsible for the noise heard within the MR scanner as the gradient coils flex as they experience time varying forces resulting from the Lorentz force which the coil windings experience.

3.6.3 RF coils and transmission

The number of designs for RF coils is ever increasing; which is demonstrated by the number of coils available to use with the Philips Achieva 3 T system [17]. One reason for this is that it is advantageous to use an RF receiver coil which is tailored to the specific anatomy under investigation. Also the development of new pulse sequences and acquisition methods can change the RF coil requirements.

RF coils are required to both transmit the time varying B_1 field as well as to receive the signal from the precessing nuclei. The properties that make an RF coil efficient for the transmission of signals also make it good at receiving the signal from the sample and therefore one coil is often used for both transmission and reception. However, to increase the signal to noise of the received signal it is often better to use separate transmit and receiver coils, so the receive coil can be placed near to the region of interest. Separate receiver coils are also needed when parallel imaging, such as the SENSE technique, described in Section 3.5.3, is used.

In its simplest form, a RF coil consists of a loop of low resistance wire and a couple of capacitors (Figure 3. 8). In order that there is no reflection of the transmitted or received signal at the connection between the coil and the amplifiers it is necessary to place one of the capacitors (C_m) in series so as to match the impedance of the amplifier to that of the RF coil. The second capacitor (C_t) is used to tune the coil to the Larmor frequency (approximately 128 MHz at 3 T).

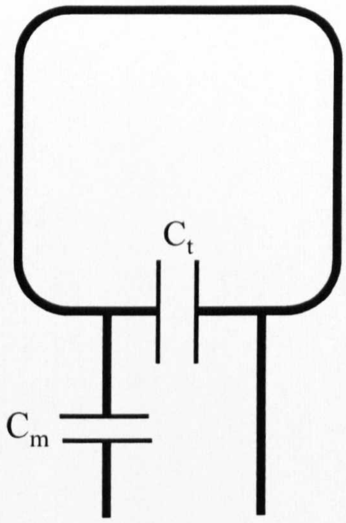

Figure 3. 8: Simple RF coil design.

The RF coil design shown in Figure 3.8 is far simpler than those used in the experimental work here, but an explanation of the design of the coils which were used is not necessary for understanding the work described in this thesis. All the coils used in this work have been specifically designed for head imaging and are commercially available. However, a variety of RF coils have been used for transmission and reception and therefore a brief description of the coil type used is given where the methods of each experiment are described. Transmission of the RF pulses has often been carried out using the body coil which provides a homogeneous B_1 field over a large region. However, using a body coil increases the SAR level the subject experiences and therefore at 7 T a head coil is used to reduce the SAR levels experienced by the subject.

3.6.4 Control

The MR scanner is controlled by a series of computers and other pieces of equipment which ensure the execution of an imaging sequence as specified by the operator. How these inter-relate with the magnet, gradients and RF subsystems can be seen schematically in Figure 3. 7. The operator enters the desired parameters for the sequence they wish to run. The computer then calculates the RF pulses and the gradient waveforms necessary along with all the timing information as well as things such as automatic shimming. This information is sent to the spectrometer which converts the signals from digital to analogue. Gradient and RF signals are then amplified appropriately before being sent to the relevant coils. On reception of a signal the RF coils send the signal to the pre-amplifiers to ensure the final signal to noise ratio is dominated by the coils and sample rather than later electronics. It is then sent to the spectrometer again where it is converted from an analogue to digital signal. The converted signals are then Fourier transformed, displayed and stored appropriately.

3.7 Safety

The most important consideration, to be made when conducting an MRI scan on a human is the subject's safety. MRI as a clinical tool has a great advantage over other techniques, such as CT, in that it is free from known harmful effects as the electromagnetic radiation used for excitation is low frequency and therefore has relatively low energy. Therefore, theoretically there is no limit to the number of times you can go in an MRI scanner. Having said this, there are still potential dangers to a subject which must be considered.

3.7.1 Static fields

The static magnetic fields used are extremely large and although, in itself, this is not harmful to a subject the introduction of foreign objects can make this a lethal environment. If any magnetic object is brought into the magnetic field then it will be attracted to it. As the object gets closer to the field's isocentre the force on it (due to the magnetic attraction) will increase causing it to accelerate towards that magnet. If a person is between the magnetic object and the magnet then this could cause a painful, and in extreme circumstances lethal, collision. This danger can however, easily be avoided by the careful screening of subjects before letting them enter the MRI suite.

Another cause of danger from the static field for subjects is if they have had operations where foreign objects such as pace-makers or ferromagnetic aneurysm clips have been inserted. The magnetic field can cause the malfunctioning of pacemakers and the movement of aneurysm clips (potentially starting an internal bleed). Again screening of subjects and keeping any person who may be in danger outside the 5 Gauss line avoids any harm being caused to people.

Although there are no known long term effects of exposure to large static magnetic fields some people have reported short term effects such as nausea, metallic taste, visual phosphenes and vertigo [18]. These are normally experienced due to movement within the magnetic field resulting in the body experiencing large changes in flux (a change of 2-5 Ts^{-1} will induce phosphenes [19]). Some of these effects have been reported in our 7 T system [20] by a number of subjects. Usually limiting the speed of movement within the field will eliminate these adverse effects.

3.7.2 Gradients

The main danger caused by the switching of the gradients is induced eddy currents in the nervous system. These currents can cause stimulation of the nerves if the rate of change of field is greater than about 60 Ts^{-1} [21, 22]. This is known as peripheral nerve stimulation and can be prevented by keeping the gradient switching below the threshold. These eddy currents can also potentially cause heating within the body as discussed in detail in Chapter 8. A second safety issue caused by gradient switching is excessive acoustic noise. To protect the subject from this noise (so it is not painful for the subject) ear plugs and defenders are provided.

3.7.3 RF field

The transmission of energy into the body via the RF field is the final major potential cause of hazard for subjects [23]. The absorption of the RF energy into the body can cause tissue heating. Although most tissue within the body is well perfused with blood which acts as a coolant, a few areas, such as the lens of the eye are not, and heating can be more of a potential problem here. The measure of RF heating within MRI is the specific absorption rate (SAR) with units of Wkg^{-1}. SAR can be calculated for a given tissue if the weight of the subject, tissue conductivity (σ), RF pulse sequence duty cycle (D), tissue density and induced electric field are known. For a sphere of tissue of radius, r, $SAR \propto \sigma r^2 B_0^2 \theta^2 D$, where θ is the flip angle. The precise calculation of SAR varies to some extent between manufacturers, but safety limits are always placed on the system to prevent the operator running a sequence with too high a SAR level. The SAR limit on the Philips 3 T system for head tissue is set to 3.2 Wkg^{-1} whereas it is set at 2 Wkg^{-1} at 7 T. The introduction of metallic objects into the system which may come into contact with the subject can lead to the production of RF eddy currents and increased power deposition in local areas causing burning. It is therefore important to carry out safety testing and heating measurements before introducing any untested foreign objects into the scanner. This is discussed in detail in Chapter 8.

3.7.4 Electric Field

Although the electric field associated if the RF field has not be considered in terms of interaction with the spins it is important to consider this field when investigating the safety MRI [24]. It is known that a current will flow in a conducting material if a time varying magnetic field is applied. Equally current will flow if there is a potential difference between two points. In accordance with Ohms law the total current flow is proportional to the electric field, **E**. This field can be represented by:

$$\mathbf{E} = -\nabla\phi - \frac{\partial \mathbf{A}}{\partial t} \qquad [3.\ 18]$$

where ϕ is the electric potential field and **A** is the vector potential. Equation 3.18 can be interpreted as the first term representing the conservative electric fields related to the accumulation of charge and the second term the non-conservative fields related to the time-varying magnetic field. When conducting materials are present in the RF field then a concentration of electrical currents can occur which are sufficient to cause the heating or burning of tissue. The nature of the high frequencies used for the RF field mean that the energy can be transmitted through space and insulators so extreme caution must be taken when positioning the subject so that no skin is in contact with the RF transmit coils [25]. Equally when considering EEG-fMRI extreme caution must be taken as described by Lemieux *et al [24]*. To measure the potential differences across the scalp necessary for EEG (as discussed in Chapter 4) conducting loops will be present. These loops normally have high impedance (due to resistors and amplifiers used) and therefore current is unlikely to flow through them. However, low impedance loops may also form if: i) two leads are in direct electrical contact ii) a wire bends back on itself and current flows through the insulation (as described by Shellock [25]) or iii) the failure of the EEG pre-amplifier. These potential causes of conducting loops must therefore be removed by the careful set up of the equipment surrounding the subject and heating testing carried out in each different RF field before conducting experiments on subjects.

Despite the potential dangers of MRI, it is an inherently safe imaging technique. Consequently MRI is an imaging method which has enormous application in clinical and research settings today. One such use of this technique is in the investigation of neuronal activity. How MRI can be applied in this particular area is described in the next chapter.

3.8 References

1. Lauterbur, P.C., *Image formation by induced local interactions: examples employing nuclear magnetic resonance.* Nature, 1973. **242**: p. 190-191.
2. Mansfield, P. and P.K. Grannell, *NMR diffraction in solids?* Journal of Physical Chemistry, 1973. **6**: p. L422-466.
3. International School of Physics "Enrico Fermi" Course, t.V., *Magnetic Resonance and brain function: approaches from physics.* 1999, Amsterdam: IOS Press. 577.
4. Hoult, D.I., *Solution of the Bloch equations in the presence of a varying B1 field-approach to selective pulse analysis.* Journal of Magnetic Resonance, 1979. **35**(1): p. 69-86.
5. Bushberg, J.T., J.A. Seibert, E.M. Leidholdt, and J.M. Boone, *The Essential Physics of Medical Imaging: Chapter 15.* 2nd ed. 2002, Philadelphia: Lippincott Williams and Wilkins. 933.
6. Edelstein, W.A., J.M.S. Hutchinson, G. Johnson, and T. Redpath, *Spin Warp NMR imaging and applications to human whole-body imaging.* Physics in Medicine and Biology, 1980. **25**(4): p. 751-756.
7. Mansfield, P., *Multi Planar Image Formation using NMR Spin Echoes.* Journal of Physics C: Solid State Physics, 1977. **10**: p. p L55-L58.
8. Howseman, A.M., M.K. Stehling, and B. Chapman, *Improvements in snap-shot nuclear magnetic-resonance imaging.* British Journal of radiology, 1988. **61**: p. 822-828.
9. Mansfield, P., *Encyclopedia of Nuclear Magnetic Resonance: E, Echo Planar Imaging.* 1 ed, ed. D.M. Grant and R.K. Harris. Vol. 3. 1996, Chichester: John Wiley and Sons.
10. Chen, C.N. and D.I. Hoult, *Biomedical Magnetic Resonance Technology.* 1989, Bristol and New York: Adam Hilger.
11. Buinocire, M.H. and L.S. Gao, *Ghost artifact reduction for echo planar imaging using image phase correction.* Magnetic Resonance In Medicine, 1997. **38**(1): p. 89-100.
12. Pruessmann, K.P., M. Weiger, M.B. Scheidegger, and P. Boesiger, *SENSE: Sensitivity encoding for fast MRI.* Magnetic Resonance In Medicine, 1999. **42**(5): p. 952-962.
13. Mansfield, P. and B. Chapman, *Active Magnetic Screening of Gradient coils in NMR Imaging.* Journal of Magnetic Resonance, 1986. **66**(3): p. 573-576.
14. McGinley, J.V.M., V.C. Srivastava, and G.D. DeMeester, *Passive shimming technique for MRI magnets.* Magnetic Resonance Imaging, 1997. **15**(3): p. XIX.
15. Gruetter, R., *Automatic, Localized invivo adjustment of all 1st-order and 2nd-order shim coils.* Magnetic Resonance Imaging, 1993. **29**(6): p. 804-811.

16. Turner, R., *Gradient coil design-A review of methods.* Magnetic Resonance Imaging, 1993. **11**(7): p. 903-920.

17. Philips, *Achieva 3.0T Coils.* 2008, Philips Medical Systems: http://www.medical.philips.com/main/products/mri/products/achieva3t/coils/. p. Website.

18. Glover, P.M., I.D. Cavin, W. Qian, R.W. Bowtell, and P.A. Gowland, *Magnetic-field induced vertigo: A theoretical and experimental investigation.* Bioelectromagnetics, 2007. **28**(5): p. 349-361.

19. Rinck, P.A. and R.A. Jones, *Magnetic resonance in medicine: the basic textbook of the European Magnetic Resonance Forum.* 3rd ed. 1993. 241.

20. Cavin, I.D., P.M. Glover, R.W. Bowtell, and P.A. Gowland, *Thresholds for Perceiving Metallic Taste at High Magnetic Field.* Journal of Magnetic Resonance Imaging, 2007. **26**: p. 1357-1361.

21. *National Radiological Protection Board Statement on Clinical Magnetic Resonance Diagnostic Procedures.* Vol. 2. 1991.

22. Cohen, M.S., R.M. Weisskoff, R.R. Rzedzian, and H.L. Kantor, *Sensory Stimulation by time-varying magnetic-fields.* Magnetic Resonance In Medicine, 1990. **14**(2): p. 409-414.

23. Budinger, T.F., *Thresholds for Physiological-effects due to RF and Magnetic-fields used in NMR imaging.* IEEE Transactions on Nuclear Science, 1979. **26**(2): p. 2821-2825.

24. Lemieux, L., P.J. Allen, F. Franconi, M.R. Symms, and D.R. Fish, *Recording of EEG during fMRI Experiments: Patient Safety.* Magnetic Resonance In Medicine, 1997. **38**: p. 943-952.

25. Shellock, F.G., *Reference Manual for Magnetic Resonance Safety, Implants and Devices.* 2004 edition ed. 2004, Los Angeles: Biomedical research publishing group.

Chapter 4

Brain Anatomy and Physiology

4.1 The Brain and how it functions

The brain is by far the most complex organ within the human body. Containing 10^{10} cells in its outer layer alone and with at least 10^{14} connections between these cells [1], it is unsurprising that a number of techniques have been developed to study the function of the brain. As mentioned previously, understanding the brain in terms of its complex anatomy and physiology may help further understanding of how it works in both healthy and diseased states. Methods have been developed to study both the spatial and temporal characteristics of brain activity, either via direct measurement of neuronal responses or through monitoring physiological changes linked to the neuronal responses, with advantages and disadvantages to each, as described in Chapter 1. The way of detecting the activity of the brain varies between these techniques. Either the neural responses are measured directly, such as in EEG and MEG, or metabolic or haemodynamic responses associated with brain activity are measured, using modalities such as MRI, NIRS or PET. To comprehend the different attributes of these measurements it is important to understand the structure of the brain at both a cellular and regional level.

4.1.1 Cellular Brain Structure

The brain is made up of two main groups of cells: neurons and glial cells. There are approximately 10^{11} neurons in the brain and vastly more glial cells. Three types of glial cells exist: astrocytes, oligodendroglia and Schwann cells. The *astrocytes* metabolically support the neurons by providing nutrition to them, as well as removing toxic materials from the vicinity of the neurons. *Oligodendroglia*, on the other hand, offer structural support and electrical insulation to the neurons by providing a myelin sheath around the axon of the neuron, the role of which will be discussed later. The *Schwann cells* carry out the same role as oligodendroglia for nerve cells outside of the brain. However, glial cells have little relevance when considering brain function as they are not involved in processing or storing information.

4.1.1.1 Neurons

Neurons are characterised by their excitable membranes and are the primary building blocks of the brain and central nervous system. All neurons (Figure 4.1) consist of a *soma* (cell body) from which projects an *axon*, which is long and thin and is often covered by a *myelin sheath*, the axon ends in a *nerve ending*. The final parts of the neuron to consider are the *dendrites*, which are usually shorter and thinner than the axon and are highly branched. The dendrites have no myelinated sheath surrounding them. The myelinated axons form the main route of conduction within the nervous system and carry the electrical impulse, or *action potential*, from the neuron's soma to another part of the system. The nerve ending is separated from the next neuron by the *synapse*. The dendrites then carry the impulse from the synapse to the subsequent neuron's soma.

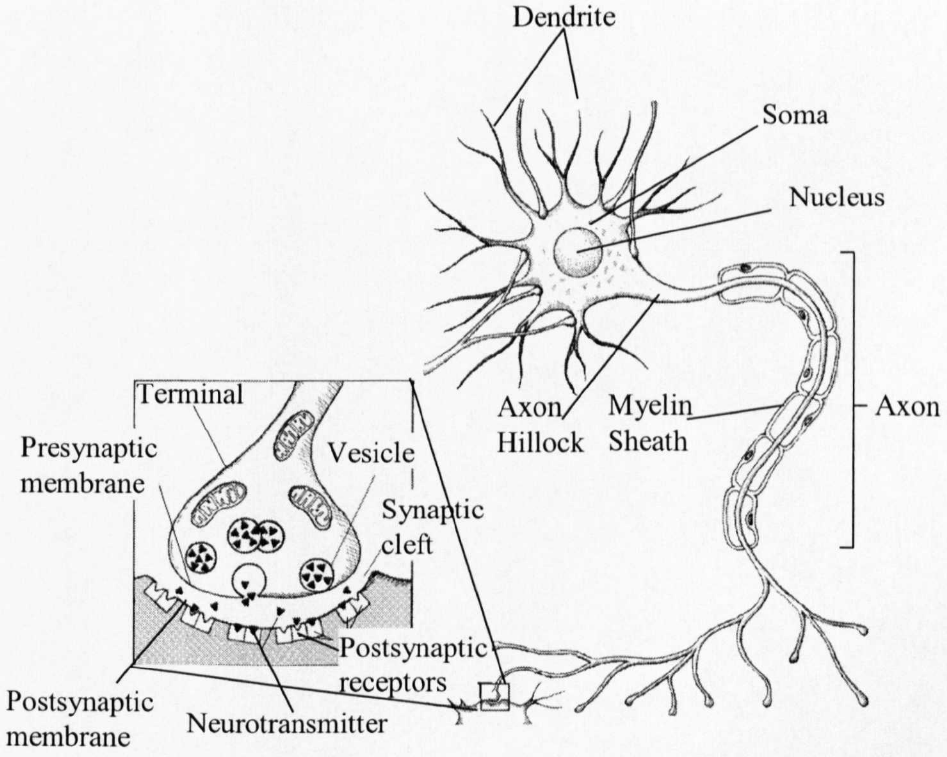
Dendrite
Soma
Nucleus
Axon
Axon Hillock
Myelin Sheath
Terminal
Presynaptic membrane
Vesicle
Synaptic cleft
Postsynaptic receptors
Postsynaptic membrane
Neurotransmitter

Figure 4.1: A neuron structure (including a zoomed version of the synapse area) adapted from [2]

The structures of neurons are diverse since they are adapted to different functions. The two main types of neuron are the *stellate cells* and *pyramidal cells*. Stellate cells have symmetrically distributed dendrites and thus the average current flow within them is isotropic, whereas pyramidal cells have dendrites orientated perpendicular to the cortical surface resulting in a current flow normal to the cortical surface. It is from these pyramidal cells that activity on the scalp can be detected using either EEG to measure the electrical potentials directly or MEG to measure the induced magnetic fields.

Brain tissue is divided into two main types: white and grey matter, so called due to the appearance of the tissue immediately after dissection. The grey matter is formed from the neuronal cell bodies and dendrites with the white matter formed from the axons. The white matter therefore provides the connections between different cortical areas within the two hemispheres of the brain, most prominently via the Corpus Callosum. White matter also connects the brain with the peripheral nervous system. Grey matter is mainly present on the surface of the brain forming the cerebral cortex, but is also present in deeper sub-cortical nuclei. Figure 4.2 illustrates the distribution of grey and white matter in the brain.

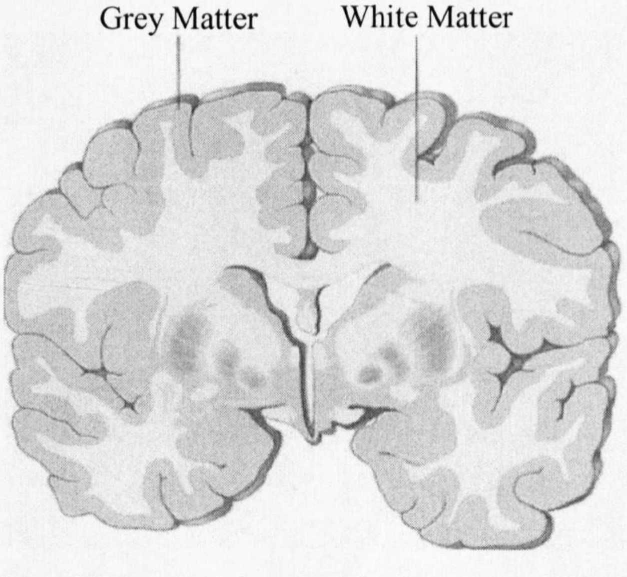

Figure 4.2: The organisation of grey and white matter adapted from [1]

4.1.2 Neurotransmission

4.1.2.1 Action Potential

The transmission of information to and along neurons relies upon the fact that neurons have a selectively permeable membrane, whose permeability only changes when stimulated by a neurotransmitter or a change in potential in the surrounding area. This selectively permeable membrane prevents the movement of ions and results in the resting potential of the neuron typically being -70 mV. The potential difference across the membrane, known as the 'Nernst' potential, is due to a higher extracellular concentration of Na^+ and Cl^-, along with a high intracellular concentration of K^+. This potential remains unperturbed until a neuro-chemical stimulation of the membrane occurs. The chemical binds to receptor molecules on the dendrites or soma of the postsynaptic cell causing the permeability of the membrane to change allowing the flow of ions (usually Na^+, Cl^- and K^+) across the membrane. The flow of ions is usually down the electrochemical gradient causing a change in potential across the membrane. If the change in potential is great enough (changes to approximately -40mV) then an action potential is stimulated along the axon. If the change in potential is greater than the threshold then the action potential that is generated is not bigger but the neuron 'fires' more frequently.

The action potential causes the permeability of the membrane at the axon hillock (Fig 4.1) to change leading to a flow of ions in this region and the cell becoming positively charged (to approximately +55mV) for a short period of time, after which the permeability returns to resting state. This change in potential stimulates the permeability of the membrane in the neighbouring regions to change and become depolarised (relative to the extracellular space) momentarily whilst the previous region is being repolarised by the use of ion pumps. The ion pumps, which are energy dependent, move both Na^+ and K^+ against the electrochemical gradients to bring the cell back to its resting state potential. This depolarisation and subsequent repolarisation propagates along the length of the axon therefore moving the action potential along its length as shown in Figure 4.3. Myelination around the axon increases the efficiency of the propagation along the axon by increasing the transmembrane resistance whilst decreasing the membrane capacitance.

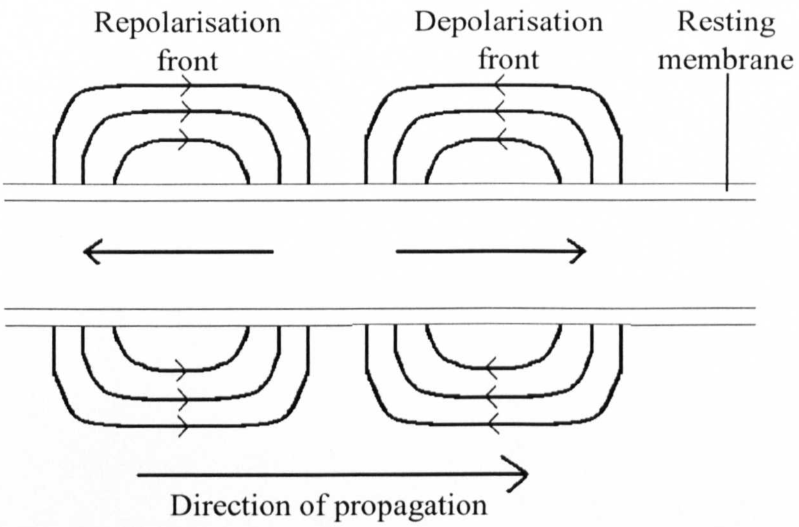

Figure 4.3 The action potential propagated along an axon; this illustrates the quadrupolar current configuration.

4.1.2.2 Postsynaptic Potential

On arrival at the nerve ending, the action potential generally stimulates the release of a neurotransmitter from the synaptic vesicles. The neurotransmitter then diffuses across the synaptic cleft, a gap of approximately 50 nm between the presynaptic and postsynaptic cells (Figure 4.1). On arrival at the postsynaptic cell, the neurotransmitter binds with proteins in the membrane causing one of two things to happen. In the case of an excitatory synapse where permeability to ions is increased the membrane becomes depolarised, while it becomes hyperpolarised in the case of an inhibitory synapse where the permeability to ions is decreased. In the case of an excitatory synapse, ions (mainly Na^+) flow into the cell and along the dendrite towards the soma setting up a primary current and a voltage change, known as the postsynaptic potential. This current is balanced by a volume current which is set up in the fluid surrounding the cell. After the influx of ions into the dendrite, the ions must then be expelled again for the neuron to reach its resting membrane potential. This is an energy demanding process as ions are pumped against the concentration gradient and potential difference causing an electrical field to be produced in the extracellular space, as shown in Figure 4.4. The volume currents which are produced are free to flow to the surface of the head causing potential differences across the head.

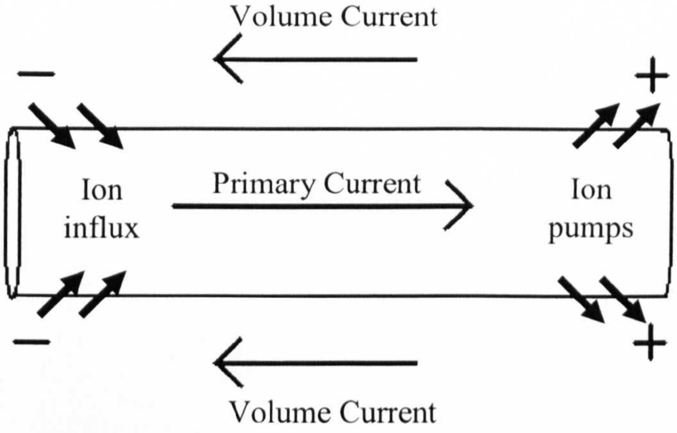

Figure 4.4 Postsynaptic current in the dendrite

4.1.2.3 Measuring neuronal currents

The action potential produces currents that are usually much stronger than those created in the synapse and along the dendrite. However, due to the nature of the propagating action potential which has proximal depolarisation and repolarisation fronts, the resulting potential and current flow at a distance are equivalent to those produced by two equal and opposite dipoles (Figure 4.3). The potential created by these dipoles at a distance mostly cancels out. The fact that the action potential is short in duration (of the order of one millisecond) also means that a strong accumulative effect of currents from multiple fibres is unlikely to happen.

The postsynaptic potential is smaller than the action potential, but is sustained for a longer period of time, between 10-20 ms [3]; therefore the effects of simultaneously active synapses are likely to sum up to produce larger potentials. The other reason the postsynaptic potential can be measured at a distance is the fact that it can be modelled as a single dipole of strength $|Q| = I\lambda$ directed along the dendrite. λ, the distance over which the intracellular current decays, is approximately 0.15 mm. The current dipole strength can be estimated from the change in voltage in a postsynaptic potential to be, ΔV=25 mV.

Given that

$$I = \frac{\Delta V}{R} = \frac{\Delta V}{\lambda r_s}$$

[4.1a]

and

$$r_s = neuron\ resistance\ per\ length = \frac{4}{\sigma \pi d^2}$$

[4.1b]

where σ = neuron conductivity = 1 $\Omega^{-1}m^{-1}$ and d = neuron diameter ≈ 1μm. Substituting Equation 4.1a and b into $|Q| = I\lambda$ and inserting the approximate values stated gives:

$$|Q| = \frac{\Delta V \sigma \pi d^2}{4} \approx 20 fAm .$$

[4.2]

Modelling current flow in the head is very complex and will be discussed later in this chapter but, if for simplicity, one assumes the head can be modelled as a sphere with a constant isotropic conductivity, σ_H, then one can roughly estimate the potential at the surface of the head due to a single postsynaptic potential as:

$$V(\mathbf{r}') = \frac{1}{4\pi\sigma_H} \mathbf{Q} . \frac{(\mathbf{r} - \mathbf{r}')}{|r - r'|^3}$$

[4.3] from [4]

where V is the potential produced at the position r' on the scalp by a current dipole at location **r**, **Q** is the current dipole moment whose magnitude is approximately 20 fAm (Equation 4.2), **d** is the distance between the observation point and source point and σ_H is the conductivity of the head. If one assumes the head is made of equal amounts of grey and white matter and that the neuron is firing at 10 Hz then $\sigma_H \approx 0.03$ $\Omega^{-1}m^{-1}$ [5]. Supposing that the current dipole is radial in direction and the potential is measured on the surface of the head directly above the source, let $|r - r'|$=5 cm, then the maximum voltage at the scalp is 20 pV. If the potential at a second electrode due to this current source is taken to be zero then the potential difference between electrodes is 20 pV.

Given that the potentials typically measured at the scalp are of the order of tens of microvolts for brain rhythms (discussed later is this chapter) then the measured activity must be due to many individual neurons (of the order of 10^6) firing in synchrony from a similar region of the brain.

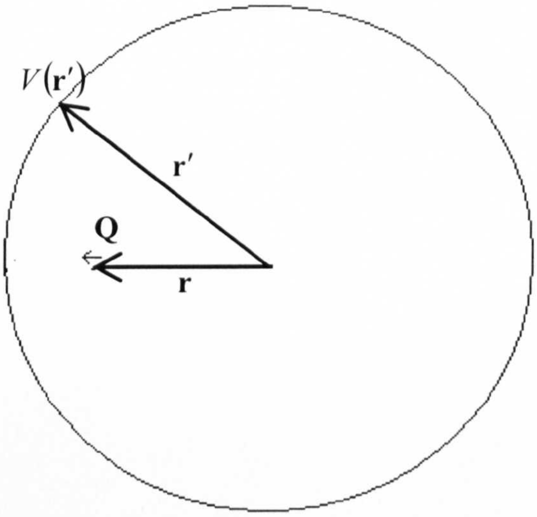

Figure 4.5: Basic head model of a single current dipole

4.1.3 Macroscopic Brain Structure and function

Although it is important to understand the constituents of the individual neurons when considering brain function it is actually neuronal activity from networks of neurons which will be measured. Therefore it is also vital to understand the main regions of the brain and their function. The brain consists of many parts some of the main components are the *cerebrum*, *cerebellum* and *brain stem* (Figure 4.6). The cerebrum is the largest part of the brain and is divided into right and left hemispheres which are connected via the *corpus callosum*. The outer layer of the cerebrum is know as the *cerebral cortex* and is the part which is of greatest interest for this work. The cerebral cortex is a 2-4 mm layer of grey matter which is folded to increase the surface area; the folds are known as *gyri* with the grooves between them known as *sulci*.

Figure 4.6 shows how the cortex is divided into 4 sections, or *lobes*, based on the positions of some of the sulci. The *frontal lobe* is divided from the *parietal lobe* by the *central sulcus,* whilst the *temporal lobe* is separated from these regions by the *lateral sulcus* (or *Sylvian fissure*). The *occipital lobe* is the posterior section of the brain. Different functions are carried out in each of these lobes and the lobes can be further divided into functional regions. For example primary motor tasks are carried out to the front of the central sulcus whilst somatosensory information is processed to the rear of this sulcus. Primary auditory processing takes place deep within the lateral sulcus in the primary auditory cortex. The visual cortex, which is of most interest for this work is located at the posterior of the brain in the occipital lobe (Figure 4.6). It is also worth noting that information from a stimulus crosses over from left to right and vice versa in the brain stem so that, for example, a somatosensory stimulus applied to the left hand will mainly activate somatosensory cortex in the right hemisphere of the brain.

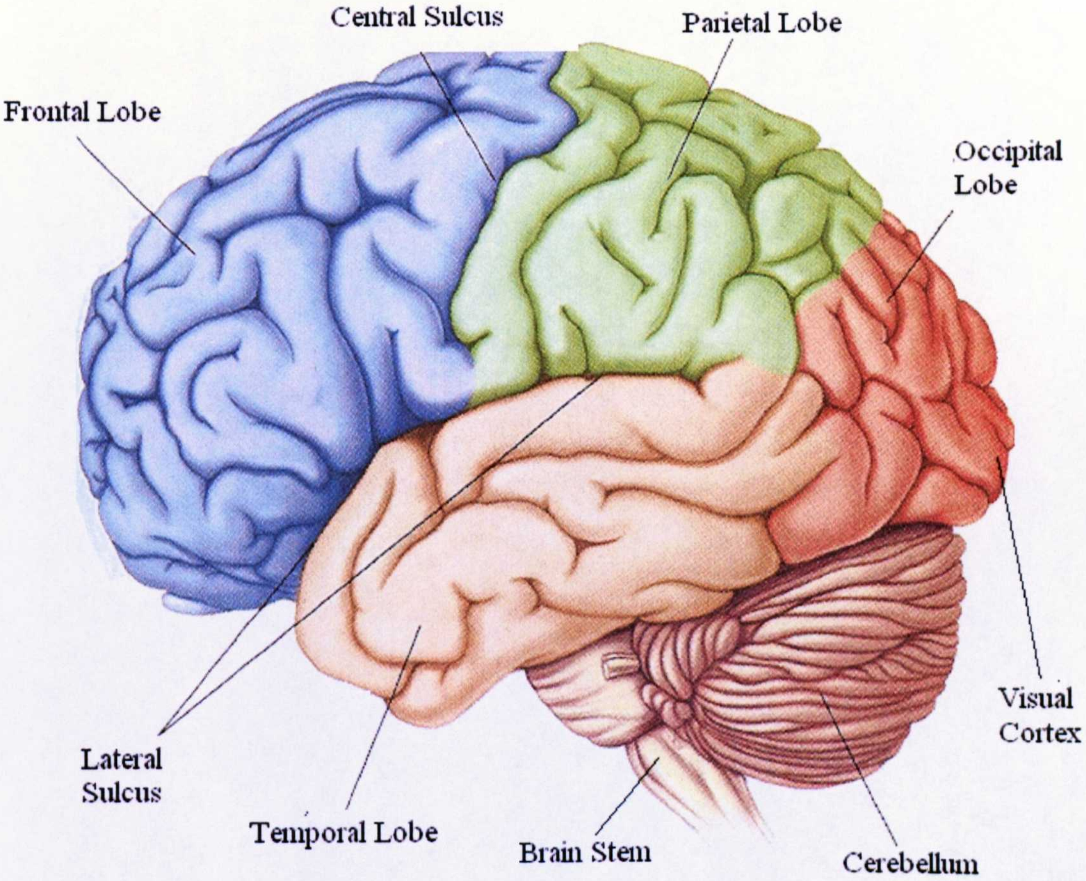
Central Sulcus
Parietal Lobe
Frontal Lobe
Occipital Lobe
Visual Cortex
Lateral Sulcus
Temporal Lobe
Brain Stem
Cerebellum

Figure 4.6: An illustration of the main areas of the brain. Adapted from [1].

4.2 Detecting Brain Activity

Following the brief description of brain anatomy and activity, techniques by which brain activity can be monitored will now be explored. Although many of these techniques have already been described in Chapter 1, two will now be explored in further detail. These are electroencephalography and functional magnetic resonance imaging.

4.2.1 Electroencephalography

Electromagnetic techniques are the only way to provide direct, real time measurements of neural activity in human subjects [1]. Electroencephalography (EEG) is one such technique, which has been used on humans for a relatively long time, and measures the synchronous firing of networks of neurons. In 1929, Hans Berger was the first to note patterns and rhythms within electroencephalogram recordings in both normal and abnormal brains of humans [6] (Figure 4.7). The first rhythm that he documented was the alpha rhythm, less commonly known as the Berger rhythm, which is prominent in restful wakefulness with the eyes closed and dramatically reduced by opening the eyes. He also documented the observation that the beta rhythm 'replaced' the alpha rhythm when the eyes were open. This work was then confirmed in the early 1930s by Edgar Adrian, who studied abnormalities in the alpha rhythm and also went on to study epilepsy using EEG. From this period to the present day people have been trying to understand the exact significance of these findings with extensive studies into these rhythms having been undertaken [7].

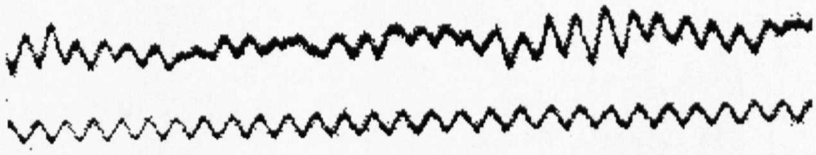

Figure 4.7: The first recording of the alpha rhythm on a human by Hans Berger. The lower trace shows a synthetic oscillation with a period of 0.1 s. Taken from [8]

4.2.1.1 Recording Equipment and Techniques

Berger originally recorded EEG signals using invasive electrodes implanted under the scalp of the subject. However, it was soon realised that with the use of the correct amplifier the signals could be recorded using surface electrodes on the scalp. Today electrodes are normally formed from small metal disks although occasionally needles are used and inserted into the cortex of the subject (such as when locating epileptic foci, normally preceding a surgical procedure). There are many types of electrodes that can be used when trying to identify the source of the epilepsy as described by Wieser in [9]. The key to using surface electrodes, which are used throughout this work, is to get a good electrical contact between the surface of the scalp and the electrode. To do this, the grease and dead skin cells are normally removed using alcohol and abrasive gels on the area where the electrode will be placed, before a conductive gel is used to make a good electrical connection between the scalp and the electrode. Typically the electrodes are held in place either using a conductive gel which also has adhesive properties or by the use of an elasticated cap. A cap has the electrodes built in and has the added advantage of holding the electrodes in the same positions relative to one another across subjects.

Care must be taken when selecting both the gels and electrodes so that they are compatible with one another. The metals of the electrodes can discharge positive ions into the conductive gels which can then adhere in close proximity to the electrode surface. In turn an oppositely charged layer of negative ions will form. However, if the rate of formation of these layers is different, current flow will be impeded, which may result in the potential differences measured being unrelated to the neural activity. This is not normally a problem in modern EEG systems as manufacturers will advise the customer on the gels to use on their system so as to avoid such confounding issues.

In clinical situations where EEG is recorded without other simultaneous measurements, such as fMRI, the clinician will aim to get the electrode-scalp impedance below 5 kΩ. However, it is possible with new high impedance amplifiers to get good quality recordings provided the scalp-electrode impedance is reduced below 60 kΩ [10]. The reason that low, scalp-electrode impedances are required is two-fold. First, the amplitude of the measured signal depends on the average impedance between the measurement and reference electrodes relative to the amplifier input impedance. This is because when a current flows through an impedance there is a potential drop. This problem is minimised by making the amplifier impedance much greater than the electrode-scalp impedances. This results in the current flow being low enough that the potential drop over the scalp-electrode barrier is minimal. Given this if the scalp-electrode impedances are less than 60 kΩ the amplitude loss will be minimal [10]. Second, the electrode impedances must be similar to one another to avoid the introduction of 50 Hz mains noise into the system. However, Ferree et al [10] also showed this matching of electrodes with modern amplifiers did not have to be too precise with a 40 kΩ mismatch still providing adequate data quality. An impedance below 20 kΩ was aimed for during the experimental work presented in this thesis. This relatively high value was chosen partially because a 5 kΩ resistor is already built into the electrodes for safety reasons (discussed in a later chapter) rendering it impossible to reduce impedances below 5 kΩ but also simply to reduce the length of time it takes to put the cap on subjects.

The EEG system works by measuring the potential difference between two electrodes connected to opposite ends of a differential amplifier. Therefore the recordings depend intimately on the positions of the individual electrodes and how they are paired. There are two main methods for pairing electrodes either using the referential or the bipolar strategy.

i) In the *bipolar strategy* the potential difference is measured between adjacent electrodes, which are normally paired in a chain. For a chain of 5 electrodes the pairings are likely to be as follows: 1-2, 2-3, 3-4 and 4-5. The electrodes which are common to two pairings are connected to opposite sides of the differential amplifier. This means that if, for example, electrode 2 in the chain was at a high voltage then there would be a change in polarity between the pairings 1-2 and 2-3. For this method of recording EEG this is a clear way to detect local voltage maxima. If the source of the current vector causing the cortical activity is normal to the skull surface then this is an excellent way to locate the source of brain activity. However, if the source is at an oblique angle to the skull then the voltage maxima and the source may be far from one another making source localisation with this information alone impossible.

ii) The *referential strategy* employs a different technique to obtain the potential differences. Here the potential differences are determined with respect to a single common electrode, the reference. The magnitude of the response measured using this technique is normally in tens of microvolts. This technique means that valid comparisons can be made between the signal amplitudes recorded at different electrodes, which is a significant advantage over the bipolar method. Inferences can also be made about the source of the electrical signal when using this method, as the electrode recording the

> largest signal is presumed to be nearest to the source. However, this is not always the case since the spatial pattern of the electrical signal produced at the scalp by an active area of neurons depends both on the spatial position of the area and the direction of relevant current vectors. The other reason that source locations cannot purely be related to the electrode with the maximum signal amplitude is that the reference cannot be placed in a truly inactive site on the head. Therefore if the source of interest lies beneath the reference electrode another electrode close to the reference may give a smaller reading to that provided by an electrode further from the site.

The placement of electrodes for either method of EEG recording usually follows the international 10-20 system (Figure 4.8). This is so named as the positions of the electrodes are spaced from one another either at 10% or 20% of the total distance between given landmarks on the head. These landmarks are the nasion, inion (for positions refer to Figure 4.8b) and left and right preauricular points (the depression in the bone in front of ear). By convention, electrodes are labelled with a prefix to denote the area of the head over which the electrode is situated (F is used for frontal regions, P for parietal, T for temporal and O for occipital, while C is used for the central region) this is normally followed with a number (odd numbered electrodes are to the left of the head and even numbers are to the right) the suffix z is used for those electrodes following the midline. The international 10-20 system has to be modified when an increased number of electrodes (such as 32 or 64) are added into the montage. For the caps used here, the first 21 electrodes follow the 10-20 system and then are adapted to include the extra electrodes, with all caps following equidistant montages (Figure 4.9).

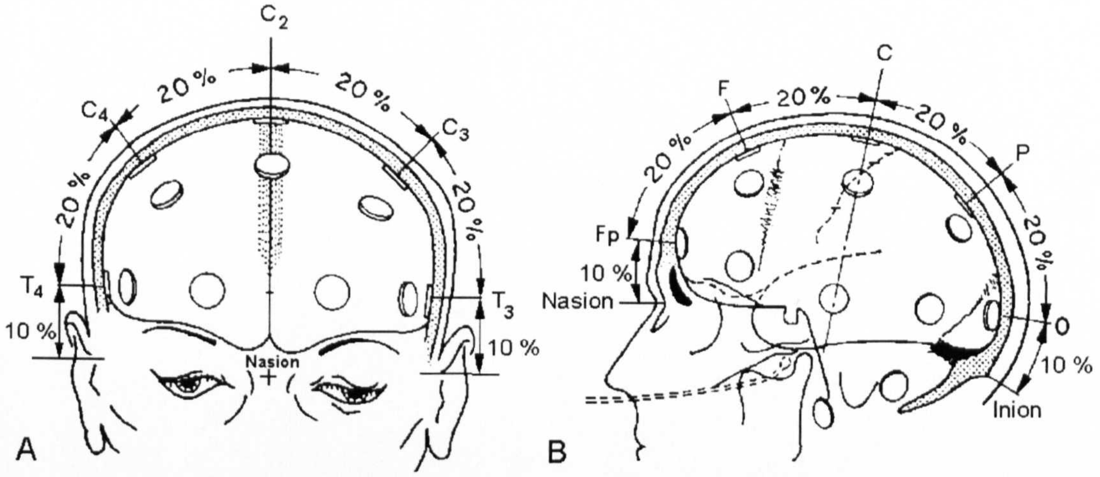

Figure 4.8: The original figure illustrating the international 10-20 system [11].

The method employed by the recording system used in the work described here is the referential strategy. The reference is placed on the top of the head, situated between electrodes Cz and Fz (Figure 4.9), in a position often known as FCz. A ground electrode is also used in EEG recordings to remove interference from common mode voltages. This ground electrode can also be termed an "*isolated common*" electrode. The potential of both the reference and the other leads are measured relative to the ground so only the differences in potential between the reference and another lead is amplified [10]. The ground electrode is placed somewhere convenient on the head, the exact location of this electrode is not crucial to the EEG recordings and therefore it can be found in different places on the 32 and 64 channel caps that were used (Figure 4.9).

The signals recorded on the scalp are fed down leads into a differential amplifier. The amplifier takes the active electrode-ground and the reference-ground signals. By a process of subtraction this method should remove the ambient noise of the system. Hardware filters then limit the frequency band in which recordings can be made. The Brain Products MR Amp employs a high pass filter at 0.016 Hz and a low pass filter at 250Hz (within the hardware). An analogue-to-digital converter is then employed to convert the signal to a digital signal which can be displayed and recorded by a computer.

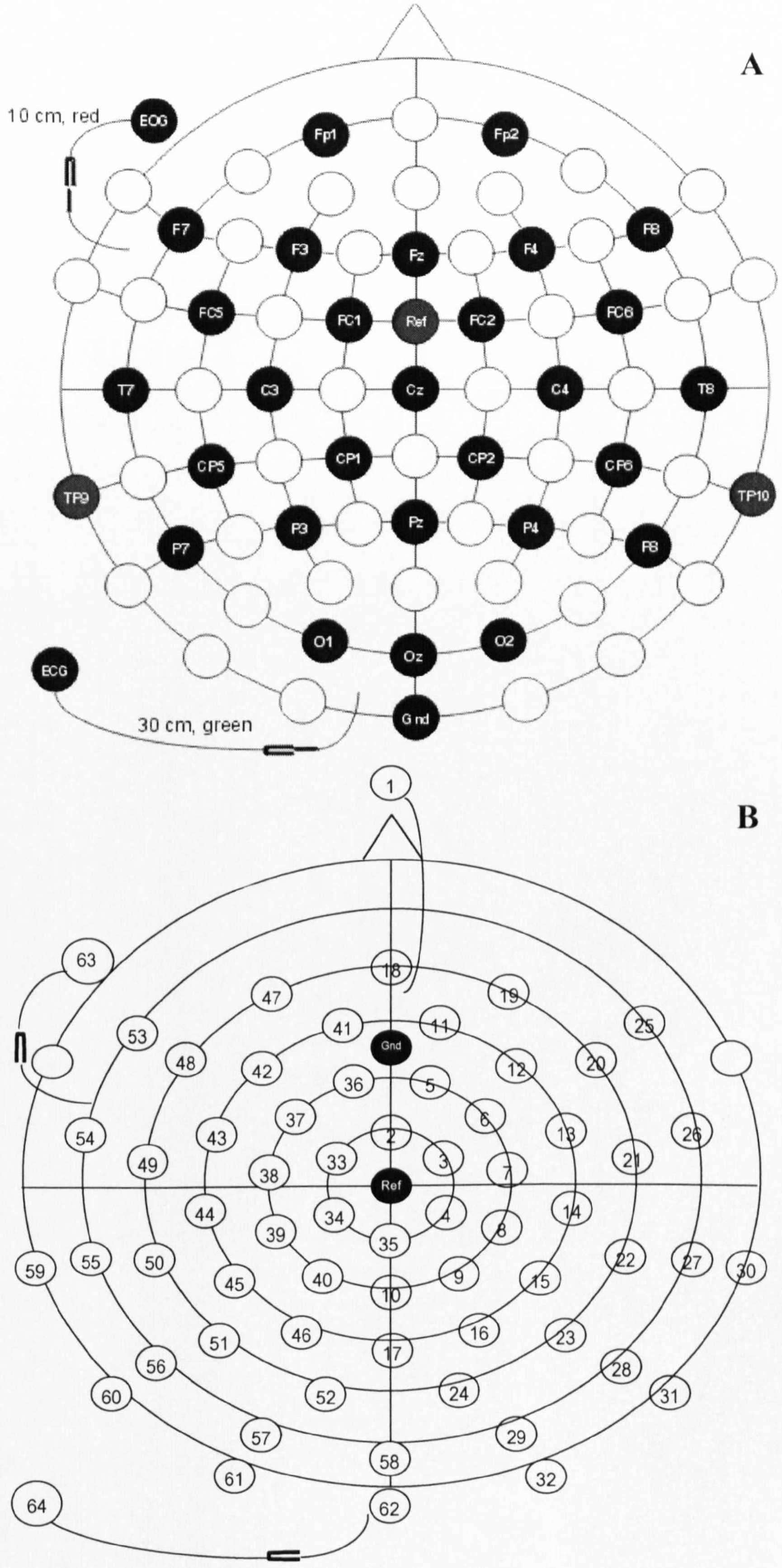
A
10 cm, red
EOG
Fp1
Fp2
F7
F3
Fz
F4
F8
FC5
FC1
Ref
FC2
FC6
T7
C3
Cz
C4
T8
CP5
CP1
CP2
CP6
TP9
TP10
P7
P3
Pz
P4
P8
O1
Oz
O2
ECG
Gnd
30 cm, green
B
1
63
18
47
19
41
11
53
25
48
Gnd
20
42
12
36
5
54
37
6
26
43
13
2
49
33
3
21
38
7
Ref
44
14
34
4
39
8
35
59
55
50
22
27
30
45
40
9
15
10
46
16
51
23
17
56
28
60
52
24
31
57
29
58
61
32
64
62

Figure 4.9: The electrode configurations used throughout this thesis for A) 32 channel cap B) 64 channel cap (courtesy of EasyCap GmbH).

4.2.1.2 What can be measured?

As already mentioned in this chapter, the EEG signals result from the volume currents produced by the primary currents due to postsynaptic potentials of the pyramidal cell structures when many neurons fire in synchrony. Hans Berger noted that the brain produced a strong signal called the alpha rhythm when the subject was awake, but resting with their eyes closed. This rhythm is one of a family of oscillatory rhythms which have been recorded from the brain. Along with these spontaneous oscillatory rhythms there are other forms of electrical activity which can be measured when a stimulus is presented. These come in the form of evoked potentials (EP) and are usually far smaller in magnitude than the signals obtained from the alpha rhythm.

Oscillatory Rhythms

Oscillatory rhythms were once thought of as being background noise, however, it is now recognised that these rhythms form an integral part of brain activity. Therefore understanding their source and function has become a rapidly growing area of research in the neuroscience community [7, 12]. The oscillatory rhythms can be divided into five main groups which are generally identified by the frequency band which they occupy, but also by their spatial location, amplitude and behavioural/functional correlates (Table 4.1). There are also some other rhythms which include lambda waves and the mu rhythms, but these are more related to specific activities rather than a particular frequency band. An increase in the strength of any of these rhythms with the onset of a stimulus is known as event related synchronisation (ERS), whilst a decrease is termed event related desynchronisation (ERD).

The Delta rhythm is actually most obvious in children, although it is also a dominant rhythm in adults in deep stages of sleep. The other rhythm that can be found in awake children is the theta rhythm. This rhythm can also occasionally be found in awake adults and when it is visible it is found over the anterior region of the head. Theta is however common in adults when drowsy or in the transition between being awake and asleep.

Name of Rhythm	**Frequency Band (Hz)**	**Typical Amplitude (μV)**	**Region of Prominence**	**State of subject**
Delta	< 4 Hz	20-200	Variable	Asleep
Theta	4-7.5 Hz	5-100	Frontal and Temporal	Awake, affective or stress
Alpha	8-13 Hz	5-100	Occipital and Parietal	Awake, relaxed, eyes closed
Beta	13-30 Hz	2-20	Precentral and Frontal	Awake no movement
Gamma	30-100 Hz	2-10	Precentral and Frontal	Awake

Table 4.1: The main oscillatory rhythms measured in EEG (adapted from [3])

The alpha rhythm is found to be at its strongest in adults who are awake, but with their eyes closed. This rhythm is prominent in most adults and has a relatively large amplitude. This rhythm appears to wax and wane over a period of 1-2 seconds. The peak frequency of the alpha rhythm varies between subjects. This rhythm can also be found in infants, but at lower frequency: it is found to be around 6 Hz at 12 months and 8 Hz at 3 years and is identified to be the same as the alpha rhythm in adults, as it is blocked by opening of the eyes [13].

Research into the alpha rhythm is currently undergoing a "renaissance" [12] as people realise this rhythm is not simply a noise source present in the resting state, but rather "it is a prototype of a dynamic process which governs a large ensemble of integrative brain functions"[14]. It is understood from a variety of studies summarised by Hughes, [15], that the alpha rhythm probably originates from the thalamus deep within the brain. However, a full understanding of the exact role of the alpha activity in cognitive functions is still a long way off. One thing that has been suggested is that the magnitude of ERD of the alpha rhythm may be linked to intelligence [16]! Desynchronisation may occur at alpha frequencies for a number of reasons. It is widely accepted, as already mentioned, that a visual stimulus blocks the alpha signal. However, there is evidence that non-visual stimuli (*e.g.*

somatosensory stimuli) also usually cause blocking of the alpha rhythm. The use of a mental task is a less reliable method of alpha blocking and its effect appears to depend partly on the mental state of the subject. The fact that higher cognitive tasks have more than one way of being solved may also be a contributing factor to this finding [13]. Niedermeyer has suggested "that alpha rhythms can become an important guiding device" in understanding higher cortical functions [13]. Whatever the precise role of alpha power in the human brain, this is an area of great interest which will be explored further in the later chapters of this work.

The mu rhythm lies in the same region of the frequency spectrum as the alpha rhythm, but is found over the central regions of the brain and is linked with sensori-motor function. It is much harder to find in adults than the alpha rhythm and is detectable in only about 10-20% of the healthy adult population [3].

The beta rhythm, also noted by Berger in the 1920's, is of a higher frequency and tends to be present when subjects are at rest with their eyes open. This rhythm is found more to the anterior of the head than the alpha rhythm (over the frontal and central regions) and is smaller in magnitude. ERD of this rhythm tends to occur during presentation of a tactile stimulation or motor activity.

The gamma rhythm is very small in amplitude and, consequently, is far harder to detect than other oscillatory rhythms. It is often associated with the visual cortex and thought to occur during active cortical processing (such as watching a drifting grating). It is thought that gamma oscillations may appear simultaneously to the blocking of alpha power (likely to be the mu rhythm) in the motor cortex [17]. This phenomenon has also been observed in the visual cortex by other groups [18-20]. The gamma frequency band is also of great interest as elevated gamma power appears to be more related to the onset of task execution. Despite recent advances, using a number of different techniques, gamma activity has origins which are still unclear [18].

Lambda spikes or waves are another part of the EEG spectrum, but are not defined by a specific frequency. They are biphasic or triphasic waves which last 200-300 ms and repeat themselves normally with a periodicity of 200-500 ms. These waves appear in the parietal and occipital lobes and are related to intent viewing of a visual stimulus.

Evoked Potentials

Along with these spontaneous brain rhythms one can also measure the reactions of the neurons to stimuli. The major defining difference between measured oscillatory and evoked activity is that evoked activity is phase-locked as well as time-locked to the stimulus. This means that one can average over trials to get the EEG response to a given stimulus thus increasing the magnitude of the phase-locked signal more rapidly than that of a non-phased locked signal. The more trials that are presented the clearer the response. Due to this phenomenon one often presents 40 trials or more of a stimulus to look at the evoked response; the results of averaging are shown in Figure 4.10. This figure also illustrates that an evoked response normally consists of multiple peaks (some are positive whilst others are negative) usually with one dominant peak. The neuronal activity due to an evoked response also tends to be more focal than oscillatory activity and therefore evoked responses may be recorded on fewer electrodes than the oscillatory ones.

The evoked response to a visual stimulus has been shown to occur at the same frequency as is used for stimulus presentation, thus demonstrating the high temporal resolution of EEG for detection of neuronal activity [21]. In particular a "flashing" visual stimulus can be used to drive electrical signals in visual cortex at the stimulus frequency and its harmonics. This phenomenon of being able to drive the visual cortex at the frequency of stimulus presentation has been used throughout the experiments described in Chapters 6, 8 and 9.

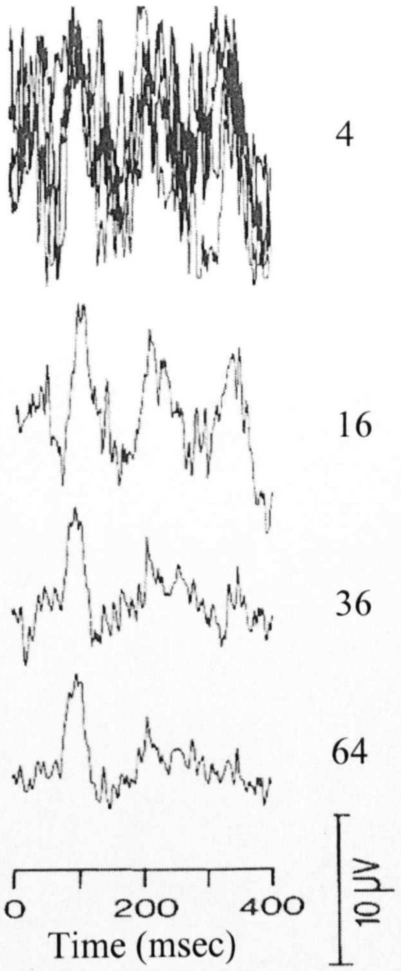

Figure 4.10: The effect of averaging the evoked response over multiple trials. Adapted from [3].

Epileptic Spikes

So far all the brain rhythms that have been discussed are for healthy subjects. However, for years EEG has also been used to detect abnormal brain rhythms associated with epilepsy. Epilepsy has many forms which fall into two main categories: partial and generalised seizures. The classification of the type of epilepsy is carried out according to the Commission on Classification and Terminology of the International League Against Epilepsy [22]. This involves taking into consideration relationships between the behaviour and EEG signals of the patient. The types of seizures which can be identified include: simple partial seizures, somatosensory seizures, complex partial seizures, generalised seizures. Each type of seizure has its own distinctive neuronal activity which can be recorded with EEG. For more details of this and other types of seizures refer to [3]. Given the high temporal resolution of

EEG the application of EEG on patients suffering from epilepsy can also inform doctors of the onset of seizures and also abnormal brain activity which is not necessarily accompanied by a visible external symptom of a seizure. Therefore it is clear that this technique to measure neuronal activity is very useful in the understanding and diagnosis of epilepsy.

4.2.1.3 Limitations of EEG

The excellent temporal resolution of EEG has been demonstrated by the high frequencies of spontaneous and driven oscillatory neural activity that can be measured. However, there are a couple of limitations of this imaging technique. The first of these is the limited sensitivity of the technique for detecting neuronal activity. Since it is necessary to measure the differences in potential between two locations on the scalp and to subsequently amplify this signal it is not possible to measure activity from neurons deep within the brain as the potential differences at the scalp surface will be negligible. Similarly it is not possible to measure activity from small networks of neurons, as shown in the calculations in Section 4.1.2.3. Another significant limitation of EEG is its poor spatial resolution. As alluded to earlier in this chapter, locating the source of the EEG signal within the brain is difficult due to a number of factors. The most important of these is the fact that the inverse problem has no unique solution, as mentioned in Chapter 1 and discussed in detail later in this section. Also difficulties arise due to the effects of variation in the direction of the current dipole which generates the measured potentials. If this dipole is not perpendicular to the skull then the electrode over the current source may not give the maximum amplitude. Another significant problem is the effect of the heterogeneous conductivities of the tissues of the head. Current always flows along the path of least resistance although this may not be the most direct path from source to scalp. Although both the brain and the scalp are highly conductive, the skull is not a good conductor and therefore its presence causes blurring of the signal. The fact that current flows along the path of least resistance means that it is important to get the electrode-scalp resistance as low as possible with all electrodes having similar impedances. If the impedances between electrodes differ significantly then electrodes where the impedance is low will record the neuronal activity at artificially high voltages relative to those electrodes where the electrode-scalp resistance is higher. The heterogeneous conductivity of the head also has a significant effect on the magnitude of the potential differences measured, further confounding the problem of source localisation.

To enable source localisation one needs to solve the EEG inverse problem which can be stated as: "given a measured set of electrical potentials at the scalp, can we reconstruct the distribution of current in the brain"[23]. The inverse problem is ill posed and so no unique solution exists, however, a number of optimisation techniques have been derived. For all inverse problem calculations one must first solve the forward problem which can be stated as: "given a known current density in the brain can we calculate the electrical potential at the scalp"[23]. To solve the forward problem, a realistic head model must be created to allow the current flow from source to scalp to be modelled. Many methods for modelling the head have been developed over the years ranging from the simple sphere of isotropic conductivity to far more complex models based on boundary element methods (BEM) [23]. The single sphere is a highly simplified model of the head and therefore the source localisation using this model is poor [24]. Modelling the head using BEM, however, is a complex process as well as being computationally very demanding, and therefore has limitations. Although investigating and developing models for use in the forward problem is beyond the remit of this work it is necessary to choose a forward solution which can be used in any chosen source localisation technique. Here, a forward solution which is relatively accurate and not too computationally demanding was chosen. This consisted of a triple sphere model as described by Zhang [24].

The inverse problem by its nature has no unique solution [25]. This is because a number of different combinations of current generators can produce the same pattern on the scalp. However, if *a priori* assumptions are made which are both physically and physiologically valid then an inverse solution can be found [25]. The ill posed nature of the inverse problem makes it necessary to provide some *a priori* assumptions when searching for a solution. Many methods have been developed to provide optimal solutions depending upon the assumptions made.

Dipole Source Localisation

A common method is dipole source localisation (DSL) which involves placing a dipole (or many dipoles depending on the number of sources assumed) where the source(s) of activation is(are) assumed to be located. An iterative numerical method is then used to move the dipoles around until the modelled surface potential map best fits the measured surface potentials. It is then assumed that the source(s) of the potentials measured on the scalp is(are) at the position of the dipole(s). This method is good for some data types particularly where there is likely to be a single source. However, a limitation of this method is that the number of sources needs to be known. This can be difficult with some experiments such as those testing higher cognitive functions.

Beamformers

The technique used in this work to locate the source of neuronal activity measured with EEG is a minimum variance adaptive beamformer (MVAB). A major difference between this technique and the DSL technique is that assumptions about the number of source(s) of the potential fields measured do not have to be made.

The beamformer technique has been used in conjunction with EEG recordings since 1997 when Van Veen *et al* [26] proposed the technique. Only the basics will be gone into here without derivation of the required equations since these have been described previously [26, 27]. Implementation of this technique in the context of recording EEG data in an MRI environment is the subject of interest for the experimental work which has been conducted here.

The potentials measured at the surface of the head, at a given moment in time, by N electrodes can be denoted by the $N\times 1$ vector $\mathbf{x}$. These potentials will be due to both the neuronal activity in the head as well as any interference caused by external noise sources. A location within the source space can be represented by a 3×1 vector (denoting x, y and z components), $\mathbf{r}$. Thus, $\mathbf{x}^T=\mathbf{L}^T(\mathbf{r})\mathbf{m}(\mathbf{r})$ where $\mathbf{m}(\mathbf{r})$ are the components of the dipole moment at location $\mathbf{r}$, and $\mathbf{L}(\mathbf{r})$ is an $N\times 3$ matrix which represents the solution to the EEG forward problem. As already discussed, choosing a forward solution and therefore obtaining the values for $\mathbf{L}(\mathbf{r})$ is one of the most significant problems encountered when applying a source localisation technique on EEG data. Here, the triple sphere model described by [24] was used as a model of the head. If many active neurons produced l active dipolar sources at locations $\mathbf{r}_i$ the potential measured at each sensor will be a linear sum of these potentials so that:

$$\mathbf{x}^{\mathrm{T}}=\sum_{i=1}^{l} \mathbf{L}(\mathbf{r}_i)^{\mathrm{T}}\mathbf{m}(\mathbf{r}_i)+\mathbf{n}$$

[4.4]

where $\mathbf{n}$ represents both external interference (correlated across sensors) and random noise (uncorrelated across sensors). If l is continuous then Equation 4.4 may be represented as an integral.

If the source space, formed by the subject's head, is split into M voxels then the beamforming technique allows one to estimate the source activity for a voxel at location , $\mathbf{r}_{\mathbf{target}}$, as a weighted sum of the field measurements $\mathbf{x}$. For any one voxel the beamformer can be thought of as a spatial filter. Mathematically the beamformer output for the target location is given by:

$$\hat{\mathbf{m}}(\mathbf{r}_{\mathrm{target}}) = \mathbf{W}^{\mathrm{T}}(\mathbf{r}_{\mathrm{target}})\mathbf{x}$$

[4.5]

and the properties of the spatial filter are given by the weighting parameters, $\mathbf{W}$. The requirements of the spatial filter would ideally be:

$$\mathbf{W}^{\mathrm{T}}(\mathbf{r})\mathbf{L}(\mathbf{r})=\begin{cases}\mathbf{I} & \mathbf{r}=\mathbf{r}_{target} \\ \mathbf{O} & \mathbf{r}\neq\mathbf{r}_{target}\end{cases}$$

[4.6]

where $\mathbf{r}$ represents any voxel within the brain aside from the voxel at location $\mathbf{r}_{\mathrm{target}}$ which represents the location of interest. $\mathbf{O}$ is a 3×3 matrix of zeros. In this ideal case the identity matrix, $\mathbf{I}$, ensures unit gain at the target voxel and $\mathbf{O}$ ensures zero contribution from elsewhere. However, as with temporal filters, it is not possible to produce a perfectly sharp cut-off in the stop band; this is because we have only N measurements to estimate responses in M voxels. Since generally M>>N, there are insufficient degrees of freedom to ensure a complete suppression of all other voxels.

The beamformer spatial filter therefore applies a power minimisation to reduce contribution from areas of no interest. The overall power of the estimated signal is minimised with the linear constraint that power originating at the location of interest must remain in the output signal. Mathematically this can be described as:

$$\min_{(\mathbf{W}_{\mathbf{r}_{\text{target}}})} \left[\mathrm{Tr}\left(\mathbf{W}(\mathbf{r}_{\text{target}})^{\mathrm{T}}\mathbf{C}\mathbf{W}(\mathbf{r}_{\text{target}})\right)\right]$$

subject to

$$\mathbf{W}(\mathbf{r}_{\text{target}})^{\mathrm{T}}\mathbf{L}(\mathbf{r}_{\text{target}}) = \mathbf{I}\,.$$

[4.7]

The solution to this is given by lagrange multipliers and can be shown to be:

$$\mathbf{W}(\mathbf{r}) = \left[\mathbf{L}(\mathbf{r})^{\mathrm{T}}[\mathbf{C} + \mu\Sigma]^{-1}\mathbf{L}(\mathbf{r})\ \right]^{-1}\mathbf{L}(\mathbf{r})^{\mathrm{T}}[\mathbf{C} + \mu\Sigma]^{-1}$$

[4.8]

where **C** is the data covariance matrix, μ is the regularisation parameter and Σ represents the sensor noise covariance. In the case where sensor noise is uncorrelated, Σ can be represented by a scalar multiplied by the identity matrix so that the diagonal values represent the variance of the Gaussian random noise from the sensors. The regularisation parameter μ adjusts the trade-off between spatial resolution and noise cancellation. For optimum spatial resolution this would be zero, but that is not always possible since an unregularised covariance matrix can be singular. Clearly the spatial resolution of an EEG beamformer is going to be substantially hindered by the inaccuracies of the forward model. The regularisation could therefore be biased towards random noise cancellation without a large loss in performance.

Given that $\mathbf{W}^{\mathrm{T}}_{\mathbf{r}}$ is known from Equation 4.8 and the sensor measurements, $\mathbf{x}(t)$, are also known, then using Equation 4.5 one can obtain a time course estimate of electrical activity for a particular location within the head. This is often known as a virtual electrode, VE, and has the advantage over data from real electrodes that the time-course has the majority of noise from spatially separate or external sources suppressed. Therefore if the VE is placed at the site of the source of activation a cleaned up time course presenting a clearer representation of neuronal activity is obtained [28].

The reason for applying a beamformer to the data acquired in the experimental work described in the later chapters, is that it can localise induced changes of cortical activity and for this work, more importantly, can be used as a noise cancellation technique. The latter is clearly provides a large advantage, when there is residual noise in the data after conventional MR artefact correction. The beamformer relies on the assumption that no two sources of neuronal activity are temporally correlated. This of course, is a limitation to the applications of this technique, but for the purpose of work conducted here does not pose a significant problem. This is because the visual cortex, which is studied, is based in the occipital lobe and although bilateral the two areas are close enough together that they appear as one source. For the purpose of this work the outer sphere for the forward solution was always fitted with a bias to the posterior of the head since the activity of interest occurs here. Since consideration of the recordings from the electrodes located on the anterior region of the head was also important for the optimal operation of the beamformer, the biasing was weak.

Using the beamformer, a pseudo-T statistic can be calculated for each voxel within the source space using the data in the frequency band of interest. A pseudo-T statistic, Ŧ, is a measure of the difference in activity in the active (act) and passive (pas) states of a paradigm divided by the sum of the noise inherent to the sensors in each of these states [27]:

$$Ŧ_r = \frac{(act)\hat{Q}_r^2 - (pas)\hat{Q}_r^2}{(act)\hat{\nu}_r^2 + (pas)\hat{\nu}_r^2}$$

[4.9]

where $\hat{Q}_r^2$ is the square of the dipole strength at a given voxel, **r**, in a specific state and $\hat{\nu}_r^2$ is the noise of the sensors related to the voxel and state and is given by:

$$\hat{\nu}_r^2 = \mathbf{W}^T{}_r \Sigma \, \mathbf{W}_r.$$

[4.10]

The location within the head which produced the maximum power in the frequency band of interest identified from the Ŧ-map was subsequently chosen as the site of a VE. A time course from the VE including all frequencies can then be acquired for the *x*, *y* and *z* components of the dipole strength. Due to the implementation of the beamformer these traces will have less noise from external sources contributing to them than raw data from individual electrodes [28]. The merits of implementing this technique on the data acquired will become apparent in Chapters 8 and 9.

4.2.2 Functional Magnetic Resonance Imaging

Compared to EEG, Functional Magnetic Resonance Imaging (fMRI) is still in its infancy, only having been around for approximately 15 years. This technique does not provide a direct measure of brain activity, but instead takes advantage of the fact that neuronal activation is energy-demanding and therefore more oxygenated blood flows to those regions of the brain where neurons are active [29, 30]. The exact mechanism is still debated, but many believe that there is an interplay between the following parameters: an increase in the neuronal activity causes a large increase in the regional cerebral blood flow (rCBF), whilst the cerebral metabolic rate of oxygen ($CMRO_2$) increases to a lesser extent resulting in a reduction of the oxygen extraction fraction (OEF). The result of this is that the capillaries, venules and veins surrounding a region of neuronal activity contain more oxygenated blood than prior to activation. Blood oxygen level dependent (BOLD) [29-31] signal changes are the most commonly measured using fMRI and explaining the effects underlying fMRI responses will be the focus of the remainder of this chapter.

4.2.2.1 The Contrast Mechanism

The key to using BOLD in fMRI is the difference in the magnetic properties of deoxygenated and oxygenated blood. Deoxygenated haemoglobin is paramagnetic, whilst oxygenated haemoglobin and brain tissues are diamagnetic. On activation, the concentration of oxygenated blood in the capillaries and venules is increased. The presence of an increased amount of oxygenated blood causes a decrease in the susceptibility difference between the blood and surrounding tissue. This results in a slower dephasing of the signal from tissue close to the vessels, leading to an increase in signal relative to when deoxygenated blood is present in the capillaries or venules. The consequence of activation is therefore a local increase in T_2 and T_2^*. BOLD therefore uses a natural MR contrast agent, oxygenated blood, to create contrast in the image and is consequently completely non-invasive. This is a great advantage of fMRI.

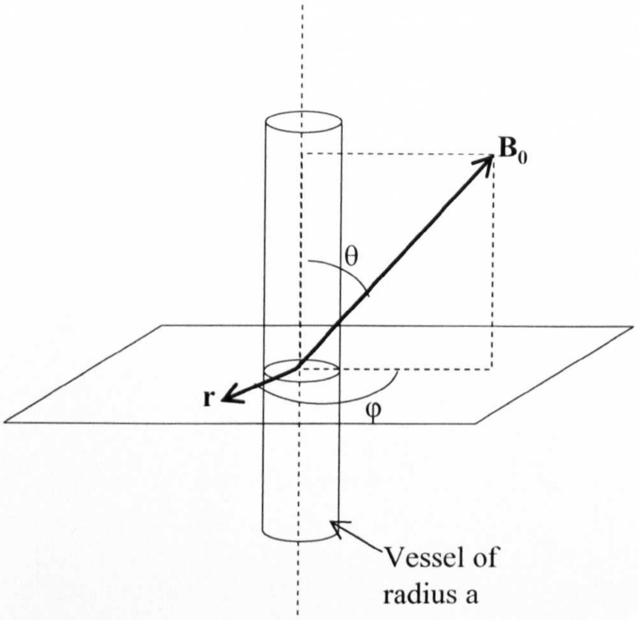

Figure 4.11: A model of a blood vessel in brain tissue orientated at an angle θ relative to the external magnetic field, B_0. Where φ is the angle between r and the projection of the B_0 field into the plane normal to the vessel. Adapted from [32] and [33].

To understand BOLD contrast in more detail one must model a portion of the brain as shown in Figure 4.11 and described in [30]. Here, the blood vessel is modelled as an infinitely long cylinder oriented at a random angle θ to the external magnetic field, B_0.

Using this model Ogawa *et al* [30] derived analytic expressions for $\Delta\omega_b$, the perturbation of the Larmor frequency from the value of ω_o due to the applied static field both within the vessel and in the surrounding area as follows:

$$(\Delta\omega_b)_{OUTSIDE} = 2\pi\Delta\chi(1-Y)\omega_0\left(\frac{a}{r}\right)^2 \sin^2(\theta)\cos(2\varphi)$$

[4.11]

$$(\Delta\omega_b)_{INSIDE} = 2\pi\Delta\chi(1-Y)\omega_0\left(\cos^2\theta - \frac{1}{3}\right).$$

[4.12]

Here Y is the fraction of oxygenated blood present within the vessel of radius a. $\Delta\chi$ is the maximum susceptibility difference between fully oxygenated and deoxygenated blood. It is clear therefore that the shift in precessional frequency,

$\Delta\omega_b$, increases with increasing susceptibility differences. Also it is apparent that for certain angles of θ and φ the field perturbation will effectively be 'invisible' or 'silent' in fMRI which could cause a problem. However, this is overcome by the fact that the vessels causing the signal changes are generally numerous within a single voxel and therefore it is assumed that within any one voxel there will be many vessel orientations, thus always creating an observed signal change.

As mentioned earlier, the changes in blood oxygenation result in changes in T_2 and T_2^*. Which of these parameters is affected can be understood by applying the principles of static dephasing and dynamic averaging. Static dephasing results from extravascular spatial field inhomogeneities as described by Equation 4.11. After the protons are excited by an RF pulse, spins at different locations precess at slightly different frequencies leading to spin dephasing over a time *TE*. This effect, which is due to the difference in local field strength across the voxel causes signal loss. This is a T_2^* effect which is observed when using gradient echo sequences. From Equation 4.11 one can see that the shift in precessional frequency depends on the square of the ratio of the radius of the vessel producing the field inhomogeneity to the radial distance from the vessel. Simulations and experimental data have shown that the static effect becomes independent of vessel size for vessels larger than a given radius (~10 μm at 4 T [30]) and becomes the dominant source of the measured BOLD contrast [34]. Since capillaries have a mean radius far smaller than 10 μm, static dephasing is not the dominant effect around these vessels and dynamic averaging plays an important role.

Dynamic averaging is the second extravascular process to be considered and is related to the diffusion of free water molecules through the inhomogeneous fields around vessels. As already discussed, if the vessel causing the magnetic field inhomogeneity is large then the distance spanned by the inhomogeneity will also be large. If this distance is very large relative to the distance the free water diffuses on the time scale of the signal life-time then there will be effectively no change in magnetic field experienced by the spins and thus no signal variation due to diffusion. Equally if the diffusion length is far greater than the inhomogeneity distance then the free water will experience regions where the field is increased and decreased and therefore, on average, the spins will not be affected by the inhomogeneity and again no signal change will occur. If however, the inhomogeneity distance and water diffusion length are approximately equivalent then the effect of diffusion will be maximal. This causes a T_2 effect as the change in field strength experienced by the water molecules is random as diffusion is a random process. Therefore the spins cannot be re-phased using either a spin echo or gradient echo sequence. One should also remember from Equation 4.11, that the extent of the field inhomogeneity is proportional to the external static magnetic field, ω_0 and therefore the diffusion length and thus the optimal TE will change with field strength. The key to BOLD-based fMRI is to maximise the signal difference between those images collected in the active and inactive states. It has been shown that this can be done by setting the TE to be approximately equal to the T_2^* of the grey matter [35, 36]. The result of this is that at higher field strengths, where T_2^* is reduced and therefore a shorter TE is used, the water molecules have less time to diffuse. Thus via the process of dynamic averaging the BOLD effect from smaller vessels will be relatively enhanced.

Within the vessels themselves dynamic averaging also has an effect. This is because the haemoglobin is contained within the red blood cells and therefore there is a difference in susceptibility between the red blood cells and the surrounding water molecules within the blood. The size of the red blood cell is small compared to the diffusion length of the free water and therefore the blood T_2 will decrease with the presence of deoxyhaemoglobin as a result of dynamic averaging. This T_2 effect is independent of the vessel size as suggested by Equation 4.12. The other intravascular effect comes from the difference in T_2 relaxation time between the blood and the surrounding tissue combined with the cerebral blood volume, CBV. If blood has a longer T_2 than the surrounding tissue then an increase in CBV will cause an increase in signal intensity. Whereas if the blood T_2 is less than that of the surrounding tissue the same increase in CBV would cause a signal decrease. At 3 T one finds the T_2 of oxygenated blood and grey matter are similar whereas the deoxygenated blood has a shorter T_2. Therefore if initially on activation there is an increase in CBV then there will be an increase in the blood oxygen fraction leading to an increase in signal. At 7 T the T_2 of blood is much shorter and therefore all intravascular signals are lost at the echo times commonly used.

In this section the differences that occur when using gradient echo and spin echo sequences have been highlighted. Within the body of work presented here gradient echo, echo planar imaging (GE EPI) sequence has been used to measure BOLD effects. A gradient echo has been used to allow the maximum SNR to be obtained. The advantage of using EPI for fMRI acquisition is the fact that one can rapidly acquire data from multiple slices and therefore cover large areas of the brain.

4.2.2.2 The haemodynamic response

Many factors contribute to the actual changes in the oxygenation of the blood which generates the BOLD contrast. Due to the complex interactions that take place there are a variety of changes in signal that occur after the presentation of a stimulus and these make up the haemodynamic response. The exact mechanisms behind the haemodynamic response are not fully understood and this lack of understanding is one of the major limitations of the use of the BOLD response when interpreting fMRI data. However, understanding the details of different theories is beyond the remit of this work and therefore only the most popular theory is presented here.

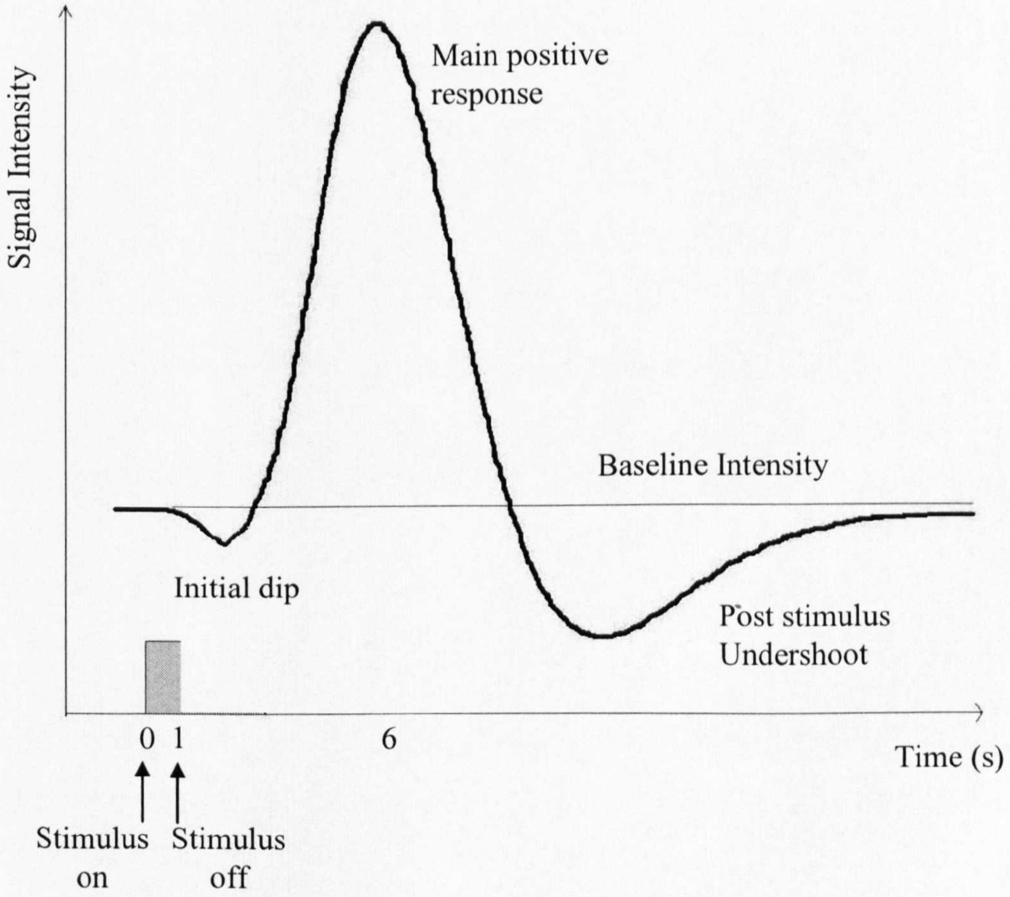
Signal Intensity
Main positive response
Baseline Intensity
Initial dip
Post stimulus Undershoot
0
1
6
Time (s)
Stimulus on
Stimulus off

Figure 4.12: A schematic drawing of the haemodynamic response.

A typical haemodynamic response curve elicited by the presentation of a stimulus is shown in Figure 4.12. This shows that the maximum in the BOLD signal occurs approximately 6 seconds after the onset of the stimulus. This is when the oxygenation of blood in the capillary and venous blood is at the highest. As previously mentioned, the increased oxygenation is thought to be caused by a large increase in cerebral blood flow, CBF, which over compensates for the increase in demand for oxygen from the activated neuronal tissue. The post stimulus undershoot is another feature that is consistently observed in the haemodyamic response, although its cause is not well understood. One popular theory is that there is an increase in the deoxygenated blood volume. This may be due to the vessels continuing to be dilated (CBV remains high) after the CBF has returned to baseline leading to a collection of deoxygenated blood and thus a decrease in signal within the voxel. The part of the haemodynamic response under the most contention is the initial dip, which occurs soon after the stimulus onset. This is questioned the most as it is not observed by all groups [37-39]. However, it is believed to be due to an increase in the demand for oxygen before CBF increases. This leads to an increase in the OEF and hence a reduction in signal intensity in the initial stages of the BOLD response.

After the stimulus has ended it can take between 5 to 9 seconds for the response to return to 10% of the baseline value. Due to this slow rebound it is important to consider the interstimulus interval (ISI) employed when presenting stimuli to subjects. Investigations have taken place to identify the effect of varying the ISI on the BOLD response, with a minimum ISI of 2 seconds found to be needed for the responses to individual stimuli to be resolved [40]. However, in this case the BOLD response is significantly attenuated and it has been shown that an ISI of at least 8 seconds is necessary for the BOLD response not to be significantly reduced [41].

4.2.2.3 Correlations between BOLD and neuronal activity.

The correlation of the BOLD response to neuronal activity is also an area which is still under some contention. As already discussed, in Section 4.2.1, neuronal activity is made up of many different rhythms and responses and which part of the neuronal response links to the BOLD response is a question which has not yet been fully answered. This question will be explored in detail in Chapter 9. However, in recent years some progress has been made in this area of research by using microelectrodes to record the spiking activity of individual neurons, as well as local field potentials (LFPs) and studying correlations of these to the BOLD response in animal models. While spiking activity is related to the firing of individual neurons and output activity of the neurons, LFPs, corresponding to activity in the frequency band 1-300 Hz, are thought arise from the combined activity of many neurons distributed over a large area of cortex. LFPs are thought to be related more to synaptic potentials and incoming inputs [42, 43]. Logothetis [42] demonstrated, in monkeys, that there was a strong correlation between LFPs and the BOLD response but this correlation was not observed when considering the higher frequency spiking activity and the BOLD response. However, other studies have found correlations between BOLD and spiking activity [44].

More recently, Nir *et al* [43] showed compelling evidence to explain the difference in results reported from various groups. They studied the activity in the auditory cortex both whilst watching a movie and at rest. They showed there was always a strong correlation between activity in the high-frequency gamma band (40-130Hz) and the BOLD response. However, correlations between the BOLD response and spiking activity varied throughout the course of the experiment. This was shown to be associated with the correlation of spiking activity between neighbouring neurons over time periods of several hundred milliseconds (rather than precise synchronisation). If the spiking activity of an individual neuron was correlated to the neighbouring neurons then the spiking activity of that neuron was well correlated with the BOLD response. However, in instances when the correlation of the activity between a neuron and the surrounding ones decreased, then the spiking activity was no longer correlated with the BOLD response. These results however, relate to only one area of the brain and it is necessary to investigate others as "the degree of coupling between spikes, LFP and BOLD may be dependent on the specific architecture of the brain circuitry"[45].

Although progress in understanding the correlations between the spiking activity in small ensembles of neurons and larger scale networks has been made, a great deal of further work needs to be done to build understanding of the complex interplay between these and the BOLD response [45].

4.2.2.4 The Spatial characteristics of the BOLD response

Spatially, the BOLD response appears to be well correlated with the expected source of neuronal activity [18, 46]. In fMRI it is of course necessary to acquire the images in a few seconds to detect the BOLD response and therefore this limits the accessible spatial resolution to an extent. However, given this limitation it is still common to acquire BOLD data with a spatial resolution of a few millimetres in standard fMRI studies. The quest for higher spatial resolution has led to the use of higher field strengths where the SNR is greater. It has been demonstrated by Menon *et al* that it is possible to acquire data with an in-plane resolution of 547 μm and slice thickness of 4 mm and temporal resolution of 3 seconds using a surface coil with an interleaved EPI sequence at 4 T [47]. Whilst at 7 T (as well as 4 T) an in plane resolution of 1 mm and slice thickness of 2 mm with a temporal resolution of 2 seconds has been achieved again using a surface coil, but with a selective refocusing technique [38]. An element of caution is also necessary when considering the spatial resolution of the BOLD response as the spatial resolution of the imaging is increased. With conventional GE BOLD there are limits to the resolution due to the area of the brain which is affected by the increase in blood oxygenation and in particular the effect of the draining veins. A recent study investigating the effect of large veins on spatial localisation concluded that "*the spatial errors introduced by large vein effects are significant, and they are unpredictable because they depend on the local geometry of the vasculature. Therefore the increase in resolution of the image may not lead to a proportional increase in the spatial localisation of the BOLD signal relative to the actual neuronal activity due to the draining veins. These effects are reduced at higher spatial resolutions and can be eliminated by identification and removal of voxels dominated by large veins.*"[48].

There are a number of other advantages and disadvantages to going to higher spatial resolution. The advantages are:

- improved spatial accuracy in identifying the origin of the BOLD response (to an extent).
- improved contrast to noise, CNR, as partial voluming effects are reduced.
- easier separation of draining veins from activation, especially at high field.

There are however some disadvantages in going to higher resolution which include:

- the signal to noise ratio, SNR, is reduced as there are less spins to contribute to the signal.
- the demands on the gradient system are heavy, which can be avoided by using longer gradient pulses rather than pulses of greater magnitude. However, this has the disadvantage of leading to long echo trains which, when the $TE>T_2^*$, will lead to reduced sensitivity of the BOLD response.
- interleaved EPI sequences can be used to alleviate the problem of long echo trains described above, but this leads to a reduced temporal resolution and therefore less rapid sampling of the BOLD response. Another disadvantage of interleaved EPI is it will result in a longer acquisition time which can result in greater motion artefacts and thus image distortion. However, by using SENSE (refer to Section 3.5.3) the TE can be reduced thus reducing the acquisition time therefore improving image quality problems associated with long acquisition times.

Therefore as with many imaging techniques there are trade-offs to be balanced. Depending on the experiment being conducted the importance of, for example, SNR may be greater than precise location of the BOLD response, therefore a larger voxel size may be chosen.

4.2.2.5 Temporal resolution of the BOLD response

The temporal resolution of the overall BOLD response is limited by two effects: the temporal resolution of the imaging technique and the temporal resolution of the haemodynamic response. As alluded to in the previous section there is a trade-off between the spatial resolution and the temporal resolution, with a third consideration being the volume of brain coverage necessary for a given experiment. The shorter the *TR* used the more accurately the haemodynamic response will be measured. This is of particular importance if, for example, the difference in the response to varying the frequency of the stimuli presented is to be investigated [49, 50]. A solution to the trade-off between *TR* and brain coverage is to use a *TR* which is not a multiple of the stimulus length and therefore jittering the presentation of the stimulus relative to the acquisition of the data over repeated trials. Using this method, different points on the haemodynamic curve will be sampled in different trials and when averaged together will provide more information on the haemodynamic response than in the case where no jittering is employed.

The other limitation relevant to the temporal resolution depends on the haemodynamic response itself. As mentioned in previous sections, the complex interaction between CBF, $CMRO_2$ and CBV means that the BOLD response is slow relative to the neuronal activity which is causing it. The response times of activation that have been reported depend both on the area of the brain that is activated and the stimulus that is used [31, 34, 41, 42], and these times are also affected by certain diseases of the brain as well as normal aging. Generally short stimuli allow the BOLD response to return to baseline quicker than if longer stimuli are used. However, even with this in mind there can be a variability in the onset of the measured haemodynamic response of 3 ± 2 seconds over an extended region of activity. The delay represents different areas of vasculature being activated, and the result is that the temporal resolution of the haemodynamic response is between 4-6 seconds. This is clearly a significant limitation of using the BOLD response to measure the timing of neuronal activity.

From the issues relating to the temporal and spatial characteristics of the BOLD fMRI discussed here it is clear that experimental design and physiological confounds are both important to consider before acquisition of data. This will be addressed in more detail in the next chapter.

4.2.2.6 Pre-processing and Statistical analysis

Once the data have been acquired there are many imaging processing steps which can be performed to derive results. There are numerous techniques for the processing of fMRI data which is a vast research area in itself, therefore only the techniques and processing steps used within this body of work will be discussed. All the techniques used can found in the SPM software with details at http://www.fil.ion.ucl.ac.uk/spm/.

The first problem to overcome once data have been collected is the effect of subject motion which can cause two types of artefact. The first is bulk motion, which is where the subject is assumed to have moved only between image acquisitions. Consider a time series of signal intensity from a specific voxel with x images collected. If the subject moves after the nth image acquisition subsequent images will be spatially displaced, and therefore the signal intensity acquired from the same voxel within the matrix after the nth image will in fact represent a different brain region. This problem can be overcome by the use of rigid body motion correction algorithms. These generally have 6 spatial parameters used to translate the images in three dimensions: 3 translations and 3 rotations. The second and slightly less intuitive artefact is the effect motion has on the steady state magnetisation (spin history effects). Steady state magnetisation builds up as the spins are unable to relax fully between excitations. This is hard to correct for without making $TR >> T_1$. Therefore to minimise the effect of this artefact on the images any data set where the bulk motion is greater than the voxel size is often discarded. The alignment of the EP images with a high resolution image is normally carried out using a similar algorithm to the motion correction algorithm, to allow various anatomical regions of the brain to be defined more precisely.

Once the data have been motion corrected spatial and temporal smoothing is applied. The spatial smoothing helps to improve the efficiency of detection of genuine BOLD activation. This is a necessary step as the signal due to the BOLD response and the noise often have similar amplitude; by spatially smoothing the data, the signal due to the BOLD effect is enhanced whilst the noise is reduced. This smoothing is also required for the implementation of Gaussian Random Field Theory, which is employed in the latter stages of statistical processing [51]. A disadvantage of the spatial smoothing is that it can cause the activation to be spread out. Therefore the size of the smoothing filter must be chosen carefully to improve efficiency, whilst not reducing the specificity of source localisation. Usually using a Gaussian smoothing kernel with FWHM of approximately 1.5 times the voxel dimension is a good compromise. Temporal filtering is carried out firstly to remove low frequency scanner drift, whilst temporal smoothing is also employed to attenuate high frequency thermal noise in the data.

After these steps have been carried out, statistical parametric maps can be created. This can be done using a multitude of methods but the one employed here, and the most common technique, is the General Linear Model (GLM). Only the basics of this will be described with full details given in [51, 52]. The GLM assumes that the fMRI data set can be modelled linearly as a weighted sum of a group of variables and an error term (the errors are assumed to be independent and normally distributed) at each voxel within the data set. If one assumes a simple boxcar function to denote the onset and duration of the stimulus then this can then be convolved with a haemodynamic response function to give a model of the expected neuronal response shown in Figure 4.13.

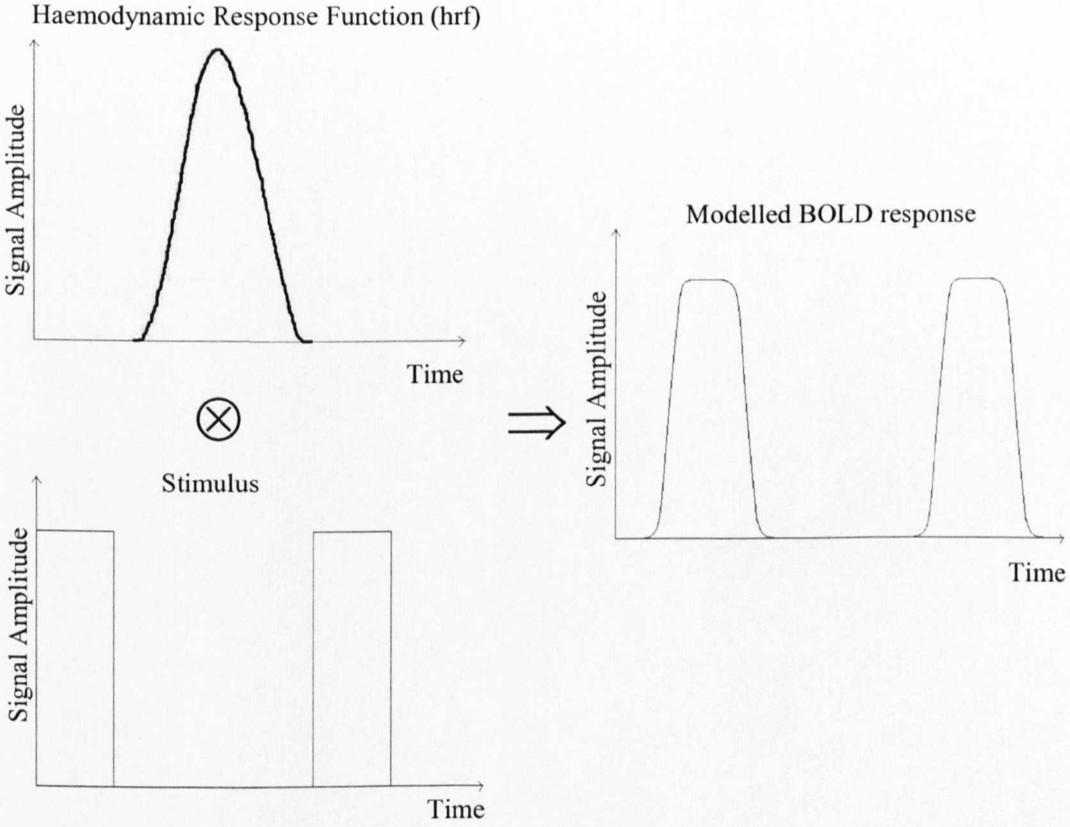
Haemodynamic Response Function (hrf)
Signal Amplitude
Time
⊗
Stimulus
Signal Amplitude
Time
⇒
Modelled BOLD response
Signal Amplitude
Time

Figure 4.13: A schematic illustration of the model used to represent the expected neuronal activity from a repeatedly presented stimulus.

Any voxel within the data whose time course matches that of the modelled response is identified as representative of neuronal activation. Bulk motion may however be a covariate of the stimulus and therefore it is important to include the motion parameters within the model so as to eliminate the effect of these parameters on the results. This is done by including the motion parameters within the model without finding the correlation of the data to these parameters as that is not of interest.

Z-score maps are then produced on a voxel by voxel basis so that the areas of cortical activity can be identified. The z-score is a statistical value given by the difference in means between two conditions scaled by variances [35]. One must create a null hypothesis to test the significance of the activity measured. In this case the null hypothesis is that the voxels in the fMRI data are not represented by the modelled time series. If the probability of this hypothesis holding is low (for example $p>0.1$) then one can assume that there is a significant correlation between the fMRI data and thus the activity represents neuronal activity. The threshold related to a given p value is calculated using the z-score and the number of degrees of freedom. A multiple comparison correction to allow for the fact that there are multiple voxels within the data set must be employed when using the GLM on fMRI data. The simplest way to do this is the Bonferroni correction, which is simply done by dividing the overall probability of a false positive by the number of voxels within the data set to give the probability of a false positive at each individual voxel. The problem with this method thus far is that no allowance has been made for the fact that the signal intensities in adjacent voxels are not independent in the case of fMRI data. Therefore Gaussian Random Field Theory can be employed [51, 53] this takes account of both the z-score maps and the size of the cluster of activated voxels to give a corrected probability of activation for the cluster. The threshold value that this is set to can be arbitrarily chosen, but normally for fMRI data sets it is set to $p<0.05$ corrected.

This chapter has identified the source of the responses measured using EEG and fMRI and outlined the theory and methods of these techniques. Explanations of why EEG has a high temporal resolution and low spatial resolution with the opposite true for BOLD fMRI have been given. The underlying principles discussed in this chapter are those that are required to understand the experimental work of this thesis and why it has been carried out. The advantages and limitations of the combined use of these imaging techniques will be covered in the remaining chapters of this work.

4.3 References

1. Bear, M.F., Connors, B.W., Paridiso, M.A., *Neuroscience: Exploring the brain - Second Edition*. 2001, Philadelphia: Lippincott, Williams and Wilkins.
2. Pfizer, *Brain: The world inside your head*. 2001, http://www.pfizer.com/brain/dlgame.html.
3. Orrison, W.W., Jr, J.D. Lewine, J.A. Sanders, and M.F. Hartshorne, *Functional Brain Imaging; Chapter 8: Clinical Electroencephalography and Event-Related Potentials*, ed. S.M. Gay. 1995, St Louis: Mosby. 479.
4. Mosher, J.C., R.M. Leahy, and P.S. Lewis, *EEG and MEG: Forward Solutions for Inverse Methods*. IEEE Transactions on Biomedical Engineering, 1999. **46**(3): p. 245-259.
5. Council, I.N.R., *Dielectric properties of Body Tissues*. 2007, http://niremf.ifac.cnr.it/tissprop/htmlclie/htmlclie.htm.
6. Berger, H., *Uber das Elektrenkephalogramm des Menschen*. Arch. Psychiatrie Nerv, 1929. **87**: p. 527-570.
7. Basar, E., *Brain Oscillations: Cutting edges*. International Journal of Psychophysiology, 2007. **64**(1): p. 1-2.
8. Berger, H., *On the Electroencephalogram of Man*. Electroencephalography and Clinical Neurophysiology, 1969. **Supplement 28**: p. 37-73.
9. Wieser, H.G., *Stereoelectroencephalography and Foramen Ovale Electrode Recording. In: Electroencephalography: Basic Principles, Clinical Applications, and Related fields*. 3rd ed, ed. E. Niedermeyer and F. Lopes Da Silva. Vol. 1. 1993, Baltimore: Williams and Williams. 1164.
10. Ferree, T.C., P. Luu, G.S. Russell, and D.M. Tucker, *Scalp electrode impedance, infection risk, and EEG data quality*. Clinical Neurophysiology, 2001. **112**(3): p. 536-544.
11. Jasper, H.H., *Report of the Committee on Methods of Clinical Examination in EEG: Appendix: The ten-twenty electrode system of the International Federation*. Electroencephalography and Clinical Neurophysiology, 1958. **10**: p. 371-375.
12. Basar, E., B.-E. C., S. Karakas, and M. Schurmann, *Are cognitive processes manifested in event-related gamma, alpha, theta and delta oscillations in the EEG?* Neuroscience Letters, 1999. **259**: p. 165-168.
13. Niedermeyer, E., *Alpha rhythms as physiological and abnormal phenomena*. International Journal of Psychophysiology, 1997. **26**: p. 31-49.
14. Schurmann, M. and E. Basar, *Functional aspects of alpha oscillations in the EEG*. International Journal of Psychophysiology, 2001. **39**(2-3): p. 151-158.
15. Hughes, S.W. and V. Crunelli, *Just a phase they're going through: The complex interaction of intrinsic high-threshold bursting and gap junctions in the generation of thalamic alpha and theta rhythms*. International Journal of Psychophysiology, 2007. **64**: p. 3-17.

16. Doppelmayr, M., W. Klimech, K. Holdlmoser, P. Sauseng, and W. Gruber, *Intelligence related upper alpha desynchronization in a semantic memory task.* Brain Research Bulletin, 2005. **66**: p. 171-177.

17. Pfurtscheller, G. and C. Neuper, *Simultaneous EEG 10-Hz desynchronisation and 40-Hz synchronisation during finger movements.* Neuroreport, 1992. **3**: p. 1057-1060.

18. Brookes, M.J., A.M. Gibson, S.D. Hall, P.L. Furlong, G.R. Barnes, A. Hillebrand, K.D. Singh, I.E. Holliday, S.T. Francis, and P.G. Morris, *GLM-beamformer method demonstrates stationary field, alpha ERD and gamma ERS co-localisation with fMRI BOLD response in visual cortex.* Neuroimage, 2005. **26**(1): p. 302-308.

19. Doesburg, S.M., A.B. Roggeveen, K. Kitajo, and L.M. Ward, *Large-scale gamma-band phase synchronization and selective attention.* Cerebral Cortex, 2008. **18**(2): p. 386-396.

20. Tikhonov, A., B. Handel, T. Haarmeier, W. Lutzenberger, and P. Thier, *Gamma oscillations underlying the visual motion aftereffect.* Neuroimage, 2007. **38**(4): p. 708-719.

21. Kashikura, K., J. Kershaw, S. Yamamoto, X. Zhang, T. Matsuura, and I. Kanno, *Temporal Characteristics of Event-related BOLD Response and Visual-Evoked Potentials from Checkerboard Stimulation of Human V1: A Comparison Between Different Control Features.* Magnetic Resonance In Medicine, 2001. **45**: p. 212-216.

22. *Commission on Classification and Terminology of the International League Against Epilespy: Proposal for classification of epilepsies and epileptic syndromes.* Epilepsia, 1985. **26**: p. 268-278.

23. Phillips, C., *Source estimation in EEG. Combining anatomical and functional constraints*, in *University de Liege.* 2000, University de Liege: Belgium. p. 122.

24. Zhang, Z., *A fast method to compute surface potentials generated by dipoles within multilayer anisotropic spheres.* Physics in Medicine and Biology, 1995. **40**: p. 335-349.

25. Michel, C.M., G. Thut, S. Morand, A. Khateb, A.J. Pegna, R. Grave de Peralta, S. Gonzalez, M. Seeck, and T. Landis, *Review: Electric source imaging of human brain functions.* Brain Research Reviews, 2001. **36**(2-3): p. 108-118.

26. Van Veen, B.D., W. van Drongelen, M. Yuchtman, and A. Suzuki, *Localization of Brain Electrical Activity via Linearly Constrained Minimum Variance Spatial Filtering.* IEEE Transactions on Biomedical Engineering, 1997. **44**(9): p. 867-880.

27. Vrba, J. and R. S.E., *Signal Processing In Magnetoencephalography.* Methods, 2001. **25**: p. 249-271.

28. Brookes, M.J., K.J. Mullinger, C.M. Stevenson, P.G. Morris, and R.W. Bowtell, *Simultaneous EEG source localisation and artifact rejection during concurrent fMRI by means of spatial filtering.* NeuroImage, 2008. **40**(3): p. 1090-1104.

29. Ogawa, S., T.M. Lee, A.R. Kay, and D.W. Tank, *Brain Magnetic-Resonance-Imaging with contrast dependent on blood oxygenation.* Proceedings Of The National Academy Of Sciences Of The United States Of America, 1990. **87**(24): p. 9868-9872.

30. Ogawa, S., Menon, R.S., Tank, D.W., Kim, S-G., Merkle, H., Ellermann, J.M., Ugurbil, K., *Functional brain mapping by blood oxygenation level dependent contrast magnetic resonance imaging.* Biophysical Journal, 1993. **64**: p. 803-812.

31. Kwong, K., J. Belliveau, D.A. Chesler, I.E. Goldberg, R.M. Weisskoff, B.P. Poncelet, D.N. Kennedy, B.E. Hoppel, M.S. Cohen, R. Turner, H.-M. Cheng, T.J. Brady, and B.R. Rosen, *Dynamic magnetic resonance imaging of human brain activity during primary sensory stimulation.* Proc. Nat. Acad. Sci. USA, 1992. **23**: p. 3963-3971.

32. Brookes, M.J., *PhD Thesis: A multi-modal approach to functional neuroimaging*, in *Sir Peter Mansfield Magnetic Resonance Centre, School of Physics and Astronomy.* 2005, University of Nottingham: Nottingham.

33. International School of Physics "Enrico Fermi" Course, t.V., *Magnetic Resonance and brain function: approaches from physics.* 1999, Amsterdam: IOS Press. 577.

34. Orrison, W.W., Jr, J.D. Lewine, J.A. Sanders, and M.F. Hartshorne, *Functional Brain Imaging; Chapter 7: Functional Magnetic Resonance Imaging*, ed. S.M. Gay. 1995, St Louis: Mosby. 479.

35. Van der Zwaag, W., *Techniques for High-performance fMRI*, in *Sir Peter Mansfield Magnetic Resonance Centre, School of Physics and Astronomy.* 2006, University of Nottingham: Nottingham. p. 190.

36. Ugurbil, K., M. Garwood, J. Ellermann, K. Hendrich, R. Hinke, X.P. Hu, S.G. Kim, R.S. Menon, H. Merkle, S. Ogawa, and R. Salmi, *Imaging at high magnetic fields-initial experiences at 4T.* Magnetic Resonance Quarterly, 1993. **9**(4): p. 259-277.

37. Duong, T.Q., E. Yacoub, G. Adriany, X. Hu, K. Ugurbil, J.T. Vaughan, H. Merkle, and S.G. Kim, *High-resolution, spin-echo BOLD and CBF fMRI at 4 and 7T.* Magnetic Resonance In Medicine, 2002. **48**: p. 589-593.

38. Yacoub, E., A. Shmuel, J. Pfeuffer, P. Van De Moortele, G. Adriany, K. Ugurbil, and X. Hu, *Investigation of the initial dip in fMRI at 7 Tesla.* NMR In Biomedicine, 2003. **49**: p. 655-664.

39. Zarahn, E., *Spatial localization and resolution of BOLD fMRI.* Current Opinions in Neurobiology, 2001. **11**: p. 209-212.

40. Bandettini, P.A. and R.W. Cox. *Contrast in Single-Trial fMRI: Interstimulus Interval Dependency and Comparision with Blocked Strategies.* in *Proceedings of the International Society of Magnetic Resonance in Medicine, 6th Annual Meeting.* 1998. Sydney.

41. Gibson, A.M., *PhD Thesis: High-speed functional magnetic resonance imaging*, in *Sir Peter Mansfield Magnetic Resonance Centre, School of Physics and Astronomy.* 2002, University of Nottingham: Nottingham. p. 184.

42. Logothetis, N.K., *The neural basis of the blood-oxygen-level-dependent functional magnetic resonance imaging signal.* Philosophical Transactions of the Royal Society of London series B Biological Sciences, 2002. **357**: p. 1003-1037.

43. Nir, Y., L. Fisch, R. Mukamel, H. Gelbard-Saglv, A. Ariell, I. Fried, and R. Malach, *Coupling between Neuronal Firing Rate, Gamma LFP, and BOLD MRI is related to Interneuronal Correlations.* Current Biology, 2007. **17**: p. 1275-1285.

44. Hyder, F., D.L. Rothman, and R.G. Shulman, *Total neuro-energetics support localization brain activity: implications for the interpretation of fMRI.* Proceedings Of The National Academy Of Sciences Of The United States Of America, 2002. **99**: p. 10771-10776.

45. Kreiman, G., *Brain science: From the very small to the very large.* Current Biology, 2007. **17**(17): p. R768-R770.

46. Mulert, C., L. Jager, R. Schmitt, P. Bussfeld, O. Pogarell, H.-J. Moller, G. Juckel, and U. Hegerl, *Integration of fMRI and simultaneous EEG: towards a comprehensive understanding of localization and time-course of brain activity in target detection.* Neuroimage, 2004. **22**(1): p. 83-94.

47. Menon, R.S. and B.G. Goodyear, *Submillimeter functional localization in human striate cortex using BOLD contrast at 4 Tesla: implications for the vascular point-spread function.* Magnetic Resonance In Medicine, 1999. **41**: p. 230-235.

48. Olman, C.A., S. Inati, and D.J. Heeger, *The effect of large veins on spatial localization with GE BOLD at 3T: Displacement, not blurring.* Neuroimage, 2007. **34**: p. 1125-1135.

49. Ozus, B., H.-L. Liu, L. Chen, M.B. Iyer, P.T. Fox, and J.-H. Gao, *Rate Dependence of human visual cortical response due to brief stimulation: An event-related fMRI study.* Magnetic Resonance Imaging, 2001. **19**: p. 21-25.

50. Thomas, C.G. and R.S. Menon, *Amplitude Response and Stimulus Presentation Frequency Response of Human Primary Visual Cortex Using BOLD EPI at 4T.* Magnetic Resonance In Medicine, 1998. **40**: p. 203-209.

51. Friston, K.J., A.P. Holmes, J.-B. Poline, P.J. Grasby, S.C.R. Williams, R.S.J. Frackowiak, and R. Turner, *Analysis of fMRI Time-Series Revisited.* Neuroimage, 1995. **2**: p. 45-53.

52. Friston, K.J., P. Jezzard, and R. Turner, *Analysis of functional MRI time-series.* Human Brain Mapping, 1994. **2**: p. 69-78.

53. Worsley, K.J. and K.J. Friston, *Analysis of fMRI Time-Series Revisited-Again.* Neuroimage, 1995. **2**: p. 173-181.

Chapter 5

Multimodality Imaging-EEG and fMRI

5.1 Introduction

Whilst EEG has been used for many decades and fMRI for a couple, these two techniques have only been combined in the last decade. The combination of the techniques is intuitively beneficial because of the complementary advantages and disadvantages of each imaging method. As mentioned in the previous chapter, EEG has excellent temporal resolution, but poor spatial resolution whilst fMRI exhibits the opposite characteristics of higher spatial resolution, but inferior temporal resolution. Therefore, via the simultaneous measurement of changes in neuronal activity using both methods, a greater depth of understanding of brain function may be acquired. However, there are a multitude of technical difficulties incurred when combining these techniques which has resulted in truly simultaneous acquisition only coming to fruition in recent years. This chapter provides a review of the work that has already been carried out to overcome technical difficulties and the problems which are still faced are also described. The uses of multi-modal scanning that have already been explored and some of the questions that the community hope to answer in the future using this technique are also discussed.

5.2 Combination Issues

5.2.1 EEG data quality

If data quality is compromised, phenomena, such as low amplitude oscillatory rhythms, normally observed in EEG recordings may be missed entirely in simultaneous EEG-fMRI recordings. Therefore it is important to understand and eliminate the sources of signal degradation as far as possible. Two physical effects form the main source of the problems surrounding combined EEG-fMRI and cause the degradation of EEG signals acquired in the magnet during MRI acquisition. The first effect is related to Faraday's Law of Induction: "An electromotive force (emf) is induced in a loop of wire when the magnetic flux for a surface bounded by the loop changes in time."[1]. The second is due to movement of blood (a conductor) normal to the magnetic field which induces an electrical field on the surface of the body; this is known as the blood flow effect [2]. These phenomena, described by Allen *et al [3]*, cause artefacts in the EEG signal for a number of reasons:

(i) Outside the centre of the magnet bore, the static B_0 field becomes non-uniform and movements of the electrode leads within the inhomogeneous field result in the wire experiencing a change of flux and thus an induced emf. This source of artefact can be reduced significantly, however, by simply twisting together electrode leads running from the patient's head to the amplifier inputs. This has the effect of reducing the area of the wire loops thus reducing the induced emf. Securely fixing the leads to a stationary surface further reduces the induced emf, as the wires are unable to cut lines of flux [3]. With these precautions in place there is little reason for this phenomenon to prevent the combination of fMRI and EEG.

(ii) Head rotation (caused by talking, swallowing, coughing or turning) has the potential to induce an emf on the scalp as the area of the scalp normal to B_0 may change. As subjects are required to keep still for fMRI then this is not a significant problem as any large movements will cause the fMRI data to be discarded anyway. Small movements are likely to only affect short segments of EEG data and therefore just these sections can be discarded.

(iii) The ballistocardiogram (BCG) or pulse artefact, which will be referred to as the PA, was previously believed to be due to small movements of the head resulting from the acceleration and abrupt directional change in blood flow in the aortic arch during each heart beat [4]. However, recent research has found that the cause of this artefact is not as simple as one movement of the head [5]. The exact aetiology of this pulse artefact is not well understood, but potential causes include the Hall voltage generated by blood flow in arteries in the brain and scalp, small head movements linked to the transfer of momentum to the head from in-rushing arterial blood and expansion of the scalp due to pulsatile blood flow. The magnitude of the pulse artefact scales with field strength [5] and is typically of order 100 μV in magnitude at 3 T. The pulse artefact waveform also shows a complicated pattern of spatial variation over the surface of the scalp, but its temporal and spatial characteristics are similar across repeated cardiac cycles. However, a full understanding of this artefact still has not been obtained and research into how blood flow and head movement interact to cause the pulse artefact continues today.

(iv) The final cause of artefact is the switching of the gradient fields which is necessary for spatial encoding in MR image acquisition as discussed in Chapter 3. The gradient switching causes large changes in magnetic flux over short periods of time in the head and at the leads and therefore, from Faraday's law, induces signals at the amplifier inputs which appear as artefacts in the signal. The gradient artefact therefore shows a topographical variation which depends on the position of the head and EEG cap with respect to the applied magnetic field gradients and has a temporal form that depends on the derivative with respect to time of the applied gradient waveforms. This artefact is the largest in magnitude (10-100 times that of the neurological signal [6]) and will be referred to as the gradient artefact.

The factors which have been most limiting to the successful execution of simultaneous EEG and fMRI are (iii) and (iv) as the other artefact sources can be minimised in the experimental set up. Techniques to correct for both the gradient and pulse artefact have been developed by a number of groups with each technique exhibiting different advantages. The main methods are outlined here, although other variations do exist.

5.2.1.1 Gradient Artefact elimination via the Stepping stone technique

The stepping stone technique can only be applied to the gradient artefact and does not remove the artefact subsequent to the acquisition of the data, but rather ensures that the gradient artefact is not present in the recorded signals. This is achieved by implementing a special MR imaging sequence so that the EEG and MRI data acquisition are interleaved on a millisecond level [7]. The advantage of this technique is that it allows collection of the EEG data without the continuous presence of time-varying MRI gradients. However, it has the disadvantage that MR sequences have to re-programmed and increased limitations are placed on the gradient waveforms that can be used in the MR sequence. Due to these limitations, this method has not been taken up by many investigators. Most other approaches that have been used for artefact elimination involve removing the gradient artefact through post processing.

5.2.1.2 Average Artefact Subtraction (AAS).

The average artefact subtraction technique for removal of gradient and pulse artefact via post processing of data was developed by Allen *et al [3, 6]*. This was the first method which allowed combined EEG-fMRI to be implemented in a truly simultaneous manner and currently is the most commonly used correction technique. There are two requirements that must be satisfied to implement this method successfully. First, the amplifiers must have a large enough dynamic range to prevent saturation of the signal on any channel. Second, the artefact waveforms must be precisely sampled.

Pulse Artefact

To remove the pulse artefact each QRS complex (Figure 5.1) must be correctly identified within the ECG trace. The cardiac peaks in the previous 10 s of data are identified and averaged together after further calculations (for more precise details refer to [3]) this averaged QRS complex is used as the basis for the subtraction of the pulse artefact.

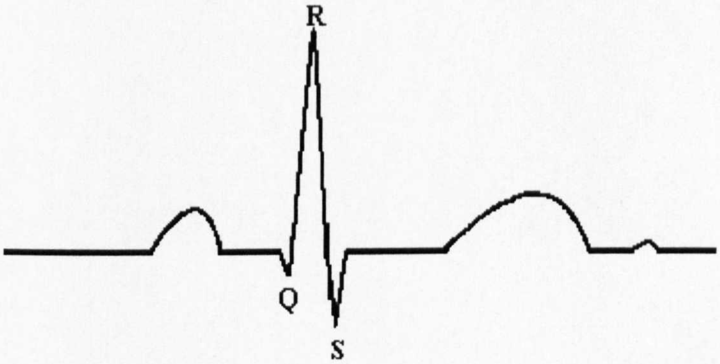

Figure 5.1: A sketch of the ECG trace obtained for one heart beat, including the QRS wave complex (adapted from [8])

The main limitation of this pulse artefact correction technique results from the temporal variation of the artefact due to its source. The correction technique does not allow for the possibility of temporal variation of the cardiac waveform within the

10 s over which the template is formed. However, a reduction in the length of this time window is not feasible, since using a smaller number of cycles to form the template would result in be the removal of some of the true neuronal signal from the recording, along with the pulse artefact.

Gradient Artefact

The technique introduced by Allen *et al* [6] for reduction of the gradient artefact can be used to remove the gradient artefacts from EEG data recorded during multi-slice EPI acquisition as is generally used for simultaneous EEG-fMRI work. It is a similar approach to that used for the removal of the pulse artefact. To obtain the template of the gradient artefact it is necessary to know the time at which each volume acquisition of the fMRI data occurs. Averaging over these volumes forms the basis of the gradient artefact removal. To obtain an accurate template of the artefact it has been specified that it is necessary to average over at least 20 volumes to average out any neuronal EEG signal from the template, which ideally should be unaffected by the artefact correction procedure [9]. An Adaptive Noise Cancellation (ANC) filter can then be applied to remove residual artefact from the EEG trace. This filter is ideal for gradient artefact correction as it can reduce signal components which are correlated to a reference signal. It relies upon the EEG software recording a marker produced by the MR scanner at the beginning of each slice acquired by the MR scanner thus producing a signal of the slice-timings relative to the EEG acquisition. To implement this filter for use in gradient artefact correction the reference signal is generated by low-pass filtering the slice-timing signals thus anything temporally correlated to the timing of the slice acquisition will be removed, for further details of this refer to [6]. However, even with the use of these techniques Allen suggested applying a 50 Hz low-pass filter to remove residual gradient artefact. Implementation of this filter was deemed not to be a problem as it was thought that above this frequency the EEG signal contained little information of value [10]. This has been found not to be the case and the filter is now set to 70 Hz by the majority of groups to allow more, useful data to be obtained from EEG traces. However, the disadvantage is that this still places a limit on the frequency range over which one can easily look for neuronal activity. In particular, this filter causes problems in the study of the gamma band frequency (range: 30-200 Hz) using combined EEG-fMRI. The gamma frequency band is of particular interest since despite recent advances using a number of different techniques, gamma activity has origins which remain unclear [11].

The advantage of implementing AAS for gradient artefact correction is that this artefact does not vary temporally between volumes in the same way as the pulse artefact, thus making it theoretically possible to remove the whole artefact. However, head motion during a long acquisition changes the signature of the gradient artefact at each electrode position and therefore makes full correction of the artefact using this technique difficult.

5.2.1.3 Independent Component Analysis (ICA)

ICA is another post-processing technique which may be employed for the removal of artefacts. ICA has been used in EEG data analysis for a few years [12-14] and more recently has been applied to PA correction. This technique is becoming ever more popular with numerous groups using it to remove the pulse artefact as ICA can accommodate temporal variations of the artefact. This method cannot correct for the gradient artefact however, and AAS must be implemented initially for gradient correction. Once gradient correction has been employed, ICA can be performed. The ICA method for PA correction relies on the fact that the PA is physiologically independent of the EEG data of interest [15]. It assumes that the recorded EEG data is a linear mixture of the PA and different components of the neuronal signals of interest. Once components have been separated out, those which correspond to the PA are identified via visual inspection, or by computing correlations with simultaneously acquired data from the ECG channel [15] and are removed from the data set. Remaining data can then be back-projected to obtain a PA-free EEG data set for further analysis.

This method seems to have produced varying success for different groups, with many reporting an excellent ability to remove the PA (for example [15, 16]). However, other groups report that using ICA alone to remove the PA may reduce the neuronal activity of interest as well as the PA, thus reducing the SNR of the data, so ICA may not be the best method for PA removal [17]. The ICA technique is certainly viable in some situations with the best results for this technique normally reported at lower field strengths where the PA is smaller in amplitude. There are still problems with this technique mainly due to the nature of the PA whose source rotates/moves around the head causing the largest artefact to be present on different sensors at different times [18, 19].

5.2.1.4 Optimal Basis Sets (OBS)

This method which has been proposed by Niazy *et al [19]* is designed to complement the AAS technique for the removal of the gradient artefact and can also be used to remove the pulse artefact.

Gradient Artefact

This method is designed to remove residual artefacts present after the implementation of AAS. Basis functions are derived by performing temporal Principle Component Analysis (PCA) on the data set, with the dominant components being used to form a basis set. A unique slice template is then formed for each slice acquisition in each EEG channel by taking a local moving average plus a linear combination of the basis functions which have been derived. This technique has been shown to be successful in removing residual artefacts [19].

Pulse Artefact

For implementation of OBS in correcting the pulse artefact, it is still necessary initially to identify the R-peaks. It is also necessary to make the following assumptions: that the occurrence of a BCG artefact in any given channel is independent of any previous occurrence and that the different occurrences are sampled from an unknown set of possible variations [19]. To apply OBS, a marker which is shifted 210 ms forward from the QRS peak is used for alignment (this shift is due to the delay between the heart beat and the PA [3]). The data from each channel is aligned to these markers forming a matrix. PCA is subsequently performed and this process is repeated for each channel. The first three principle components are then used to form the OBS and this is then fitted to, and the resulting fit removed from, each pulse artefact occurrence.

Implementation of this technique has been shown to produce a better removal of the PA than the standard AAS correction technique [19] and also to be better than ICA

[17]. A combination of OBS followed by ICA possibly offers the best correction technique [17] identified to date.

5.2.2 MR data quality

It is obvious that correction for the gradient and pulse artefacts in the EEG data is needed to enable the use of data acquired in combined EEG-fMRI experiments. Distortions and degradation also occur in MR images acquired in the presence of the EEG cap. However, since these degradations are relatively minor compared to those occurring in the EEG data, much less work has been carried out to ascertain the exact effects of the EEG cap on MR image quality or what causes these effects. Here, work that has previously been carried out to show the adverse effect of the EEG apparatus on the quality of MR image data is outlined.

Scarff *et al [20]* noted that the signal to noise ratio (SNR) of MR images decreased with the use of increasing numbers of EEG electrodes. Their analysis was carried out on T_2^*-weighted images acquired using echo planar imaging (EPI), the imaging technique that is most commonly used in fMRI studies (for further details refer to Chapters 3 and 4), and the SNR measurement was made by comparing the average signal in a brain region to the standard deviation across an area outside the head containing only noise. Some investigative work has also been carried out by Vasios *et al [21]* on the effects of their "InkCap" system on the SNR in echo planar images of the human brain. Here a 32 electrode cap was designed with conductive ink technology rather than wires running from the electrodes. The cap was tested both on a phantom and 11 humans at 7 T. They found the cap had a small effect on the SNR of EPI data collected (a 12 % reduction when comparing with and without the cap in white matter) and did not significantly affect the BOLD data collected in the presence of the cap. The same group has also measured the effect of EEG caps on the quality of retinotopic maps obtained using fMRI [22] showing the cap has little effect.

The work done by Krakow *et al* [23] was more extensive; involving a study of the effects of the different components of the EEG system on images of phantoms and human subjects acquired using EPI. The in-plane spatial extent of the image artefact was used as a measure of the severity of the effect produced by a variety of electrodes, resistors and leads. The largest artefacts were found to be produced by injudiciously chosen resistors. Using their results, the authors derived recommendations about the optimal components that should be used in an EEG system so as to cause minimal degradation of the MR images. They suggest that one should ideally use carbon or plastic covered silver or gold electrodes combined with resistors made from planar cermet. The materials the leads were made from (both copper and carbon wires were tested) seemed to make little difference to image quality. In addition, the artefact due to any combination of materials was found to be "comparable to that of the worst single component"[23]. These authors also investigated the artefacts caused by conductive gel and paste/gel mixtures used for conventional EEG recordings. These artefacts were found to be significant, leading to the recommendation that the minimum possible amount of gel should be used.

Recently, a more quantitative study of the effects that different EEG electrodes have on the B_0 and B_1 fields has been conducted by Stevens *et al [24]*. Here, three types of electrode were investigated with B_0 and B_1 mapping carried out for each. Heating tests to check the safety of using each type of electrode were also conducted. It was found that, as expected, the electrode containing a thin layer of ferromagnetic material produced much greater B_0 distortions than either of the electrodes made from diamagnetic materials and that the electrode made from Ag/AgCl produced the smallest perturbation. The B_1 field distortions were found to be much the same for each of the electrodes. The extent of these distortions were measured to be smaller than the average distance between scalp and brain in humans, so that in the B_1 distortions caused little degradation of image quality. Finally, they found that there was no significant heating of either the electrodes or the surrounding agar of the phantom when any of the electrodes were used, thus: "no significant temperature increases would be expected in human scalp tissue for typical scanning conditions at field strengths of 4 T or less due to the electrodes"[24]. However, this paper did not address the effects of the EEG leads, or the effects of the EEG system on overall SNR.

5.2.3 Safety

Data quality is of course important for the usefulness of conducting combined EEG-fMRI but, as with all foreign objects taken into the MR environment, safety is paramount and must be considered carefully. The currents induced in the leads and electrodes when the EEG system is taken into the MR environment can lead to potential localised heating and burning. Other health risks that are associated with the flow of the currents are ulcers due to electrolysis and electric shock or stimulation from currents below 100 Hz [25]. Standard modifications of EEG systems to make them MR compatible, include the introduction of 5 kΩ resistors between each lead and electrode. This reduces the possible flow of MR induced currents and therefore reduces the chance of RF heating [25]. Fibre optic cables are also employed to transmit the EEG signals out of the scanner room, thus optically isolating the subject from as many sources of danger as possible. After careful study of safety issues, Lemieux *et al* [25] concluded that with the correct precautions it was safe to conduct combined EEG-fMRI at 1.5 T and commercial EEG systems, such as the Brain Products one used in this work, have now been certified safe up to 3 T [26]. Given the potential interactions between the EEG and MR systems it is important to know the exact experimental setup, including wire paths, used for simultaneous EEG-fMRI acquisitions. The positions of the EEG cable trees relative to the head coils used for the studies in this thesis are shown in Figure 5.2. As one can see due to the nature of the head coils used at 3 T and 7 T (both of which have end caps but the 3 T head coil is open whilst the 7 T head coil is closed) the path of the EEG cable tree must be slightly different at these two field strengths although heating has not been observed in our experimental set up at either field strength. Also it is important to consider the coils that are used to transmit the RF field at the field strengths used. This is because if a system has been deemed to be safe using one coil it does not mean heating will not occur using a different transmit coil. For example a head transmit coil will transmit RF over a smaller area than a body transmit coil. Therefore long leads, such as the EOG and ECG leads, may behave differently due to the different methods of transmit. For the experiments in this work the body coil has been used for transmit at 3 T and the head coil at 7 T. Further in depth details of the safety issues that must be considered and how they change with field strength are detailed in Chapter 8.

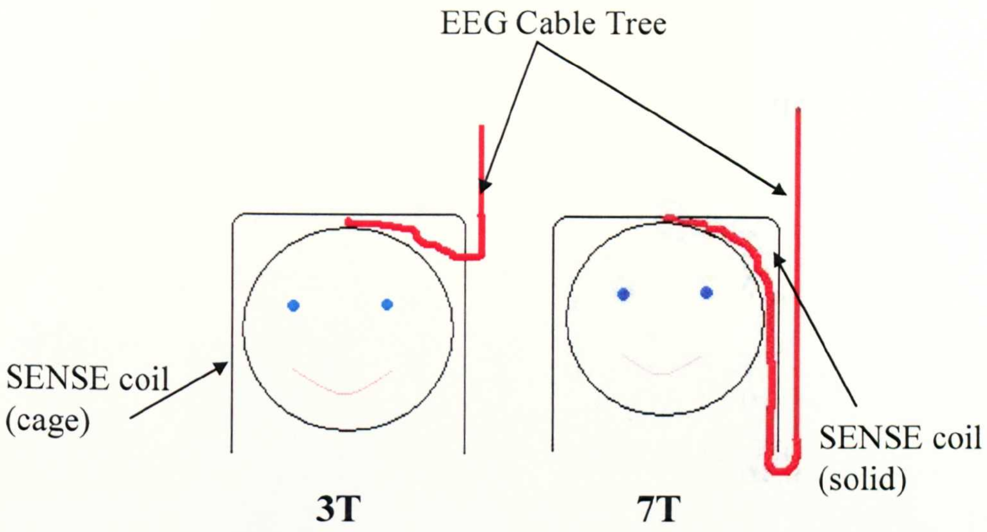

Figure 5.2: Schematic diagram of the position of the EEG cable trees relative to the head coils used at 3 T and 7 T.

5.3 Uses

It is clear that it is possible, and safe, to record EEG and fMRI data simultaneously although problems are encountered in data quality when this is done. There are three methods that can be used to record EEG-fMRI data. 1) To record EEG and fMRI data separately and subsequently to fuse the data. 2) To record the EEG and fMRI data simultaneously, but only to use EEG data acquired whilst the MR scanner is not running. (This method assumes that the fMRI response will be slow enough relative to the EEG response that the fMRI data can acquired immediately after the EEG data.) This method is known as interleaved acquisition and has the advantage that the EEG data does not suffer from gradient artefacts, but will still be degraded by the pulse artefact. 3) Truly simultaneous acquisition where the EEG and fMRI data are acquired at exactly the same time. This has the advantage that both techniques record exactly the same neuronal activity [27] but in this case, the EEG data is affected by the artefacts previously discussed.

	Separate	Simultaneous
Identical sensory stimulation	No	Yes
Habituation	No	Yes
Identical behaviour	No	Yes
Direct temporal correlation between EEG-fMRI signals	No	Yes
Optimal signal quality	Yes	No
Ability to optimise paradigm for imaging modality	Yes	No

Table 5.1: A summary of the advantages and disadvantages of collecting EEG and fMRI data simultaneously or separately. Adapted from [28].

There are of course relative advantages and disadvantages of these different methods for combining the data from the two modalities, which are listed in Table 5.1. Simultaneous EEG-fMRI data acquisition is the only way to guarantee the measurement of EEG and fMRI data under identical conditions, as recording in separate rooms provides different experimental environments for each recording. Also separate recording sessions may lead to unwanted differences due to habituation effects and tasks involving memory or learning where the performance in the task improves with practice cannot easily be conducted in this way. There is also evidence that ongoing brain fluctuations may interact with, and modify, the processing of sensory stimuli which can only be measured in simultaneous recordings [28].

A difficulty with the simultaneous acquisition of EEG and fMRI data can be the creation of a paradigm which is suitable for collecting both data types, since EEG data ideally need many repetitions, but the time between trials can be short. Whereas, when collecting fMRI data, the number of repetitions can be smaller, but the inter-stimulus interval needs to be longer to allow the haemodynamic response to recover before presentation of the next stimulus. Therefore it can sometimes be difficult to create a paradigm which enables the requirements of both imaging modalities to be met and which is not so long in duration that it leads to a compromise data quality due to subject movement. Due to the artefact correction that must take place a reduction in data quality of both data sets will occur to some extent regardless of the paradigms used for artefacts correction. Therefore it is important to only use simultaneous EEG-fMRI in situations where the neuronal activity cannot be predicted. Iannetti *et al* [29] discuss six circumstances where using simultaneous EEG-fMRI provides information that is unobtainable by conducting the two imaging techniques separately. The first is in epilepsy studies when the onset of the spiking activity is unpredictable and therefore must be measured by the EEG. Also simultaneous acquisition is useful in sleep studies to monitor the depth of sleep which can change in an unpredictable way. When the responses to a stimulus may change over time, when there are habituation effects or when scanner environment may sustainably affect neuronal responses (as discussed in the previous paragraph). Finally Iannetti *et al* suggest that the use of simultaneous EEG-fMRI is necessary when evaluating the effects of certain drugs where a variation within-subject between sessions is expected. In all these cases it is the unpredictability of the neuronal response which necessitates the use of simultaneous acquisition. Simultaneous acquisition is the only type of combination of EEG and fMRI data that will be considered in the work described in this thesis.

5.3.1 Fusing the data

Once the EEG and fMRI data have been collected, combining information from the two techniques is an art in itself and can be done in different ways depending on the experiment and what the aim of the study is.

5.3.1.1 Research Applications

Using EEG data to complement fMRI data

This method has been used to explore the temporal correlation of EEG responses in different frequency bands with the BOLD fMRI response. So far the most widely investigated frequency band using this technique is the alpha band. The natural oscillations in this frequency band have been chosen for a number of reasons: they have a relatively large amplitude and are easily detected in most people at rest (Chapter 4). They are also less affected by any residual gradient artefacts than higher frequency bands.

Goldman *et al* [30] were the first to implement this type of fusion of EEG and fMRI data. They convolved the power in the 8-12 Hz band of the EEG data with a haemodynamic response and then found the correlation of this with the BOLD fMRI data. They found that "increased alpha power was correlated with decreased BOLD signal in multiple regions of occipital, superior temporal, inferior frontal, and cingulate cortex, and with increased signal in the thalamus and insula"[30]. Subsequently Laufs *et al* [31] reported similar findings and Moosmann *et al* [32] extended this investigation with a similar set of results using combined EEG and fMRI, as well as combined EEG and near infra-red spectroscopy (NIRS). Interestingly, all of these studies have shown that there is a reduction of BOLD activity in the occipital lobes when alpha activity increases. This agrees with suggestions that activity in the alpha band represents a cortical inactivation and is an idling rhythm [28]. Gonçalves *et al* [33] conducted a similar experiment to those already mentioned, but looked at the variability in results between subjects. They found that although some of the subjects exhibited results similar to those previously presented from group analysis, other subjects showed different patterns of activity, with some subject's results even changing part way through the experiment demonstrating that the resting state varies over time. This work illustrates that a significant amount of further work is needed before we will fully understand the role of alpha power in brain function. The beta band (17-23 Hz) has also been explored by Laufs *et al* [31] in combined EEG-fMRI experiments with "positive correlation of the beta band power with activity (in the fMRI data) in retrosplenial, temporo-parietal, and clorsomedial prefrontal cortices" found. Another group explored a similar idea for the theta band whilst a mental-arithmetic task was carried out to enhance the production of theta power [34]. They found that there was positive correlation of neuronal activity and BOLD responses in "the insular cortex, hippocampus, superior temporal areas, cingulate cortex, superior parietal, and frontal areas" and concluded that these results provided evidence for "dynamic functional binding of widely distributed cortical assemblies, essential for cognitive processing"[34]. The work highlighted here, along with many other studies, shows the potential power of combining EEG and fMRI to understand the electrical brain rhythms which have been measured for years using EEG alone.

A second way in which the EEG data has been used to complement the fMRI data is in single trial work. This work is still in its infancy although a couple of interesting papers have now been published on this type of study. Single trial events are not reproducible and therefore cannot easily be averaged together to study the response of the brain. Averaging trials together is currently the standard technique in fMRI hence the assumption is made that the response to a stimulus or self-paced action is the same each time it is performed. By recording the EEG signals produced by the brain and using these to predict how the BOLD signal fluctuates, a whole new area of single-trial, event related experiments can be investigated. Eichele *et al* [35] used an auditory oddball paradigm to manipulate the event-related electrical responses and then used these results to identify brain regions where the fMRI responses were predicted by the changes. They found that there were single trial modulations of the latencies of the P2, N2 and P3 components of the evoked response which predicted spatially separate activation patterns in the fMRI data. Single-trial work has also been carried out by Debener *et al* [36] who used combined EEG and fMRI to study which areas of the brain are involved in the processing of response errors. Here, amplitude variations in the EEG data between trials when a performance monitoring task was conducted were analysed. These variations were used to predict the fMRI response. It was found that the single-trial EEG response, when used as a regressor, localised the fMRI response more specifically than conventional fMRI analysis methods. This work suggests that it is possible to use the EEG signal to "provide fine-grained information that can be used to pinpoint the role of different cortical regions in a given cognitive task."[28].

Using spatial information from fMRI to constrain EEG source localisation

In some respects this is the converse of the methodology discussed above, with the fMRI results imposing constraints on the EEG data in this case. This method exploits the high spatial resolution of the fMRI data and uses it to constrain EEG source localisation. The premise behind the method is that if the EEG and BOLD signals are due to activation of the same neuronal networks, then the inverse problem can be constrained by placing dipoles in regions where BOLD activation has been found, thus assisting in the solution of the inverse problem. This technique has been used by a number of groups who have shown that using this constraint on the source of the electrical/magnetic data recorded gave likely locations of the sources which agreed with other source localisation techniques [37, 38]. Further evidence that the source of EEG and fMRI evoked responses can be found in the same brain regions is given in studies by Scarff *et al* [20] and Mulert *et al [39]*, thus providing further justification for the use of fMRI data to constrain the EEG source localisation.

This type of data fusion must, however be performed cautiously, as it is possible that either there are fMRI signals which do not have an EEG correlate (perhaps because the source is too deep for the EEG system to detect) or there are EEG signals without an fMRI correlate (perhaps because the EEG signal represents a small neuronal network which requires minimal changes in metabolic activity)[27]. Finally an increase in the EEG signal could correspond to a decrease in the fMRI signal (such as for alpha band activity as discussed above) which could also pose problems for the constraints imposed. In these cases, constraining the EEG source localisation by using fMRI source locations could be detrimental in finding the correct source of the EEG activity. Weights are therefore normally created so that it is more likely that the EEG source is located where the fMRI sources have been found, without completely restricting EEG sources to such locations.

5.3.1.2 Clinical Applications

Using combined EEG-fMRI in research applications is indeed useful, but, as discussed in Chapter 1, the ultimate aim is to help those with neurological disorders. Therefore how can this multi-modal approach be employed in clinical practice?

Epilepsy

So far, the clearest clinical application of combined EEG-fMRI that has been presented in the literature is to investigate epilepsy. Epileptic events produce spikes in the EEG signal that are well recognised. However, accurate identification of the source of these spikes using EEG alone is difficult and normally involves the use of depth electrodes. With this method it is also difficult to identify boundaries of functional areas neighbouring epileptic foci. Therefore the combination of EEG and fMRI data could provide a viable method for non-invasive source localisation along with identification of neighbouring functional areas to be avoided in surgery, by a series of task tests.

Current research in epilepsy using combined EEG-fMRI tends to focus on interictal spikes, which are associated with epilepsy, but do not produce a seizure. This is because it would usually be unsafe to have a patient in an MR scanner during a seizure and movement would render data useless. Salek-Haddadi and Lemieux *et al* [40, 41] were the first to show a correlation between "ictal EEG activity localizing seizure generation and propagation sites" and BOLD fMRI changes in the grey matter. Research in this area has also been conducted by other groups who have mainly concluded that it is possible to correlate the spatial location of the spiking activity measured in the EEG and the haemodynamic BOLD response [42, 43]. However, no correlation between the amplitude of the EEG spikes and the BOLD response was found by Benar *et al [44]*. A detailed review of all research conducted in this area including work where spiking activity measured in the EEG has been used to trigger the acquisition of fMRI data can be found in [45]. Since the publication of this review, a number of other studies have been performed to further interrogate the properties of epilepsy. These have included studies such as [46] where correlations between generalised spike wave (GSW) activity and the BOLD response have been characterised for individual subjects, as well as across subjects. GSW usually arises from a normal background EEG in patients suffering from idiopathic generalised epilepsy (IGE). Before the advent of combined EEG-fMRI, localisation of the generators of GSW was difficult. The study by Hamandi *et al* [46] reported that BOLD and GSW were positively correlated in the thalamus, while negative correlation was found to occur in the cortex across the majority of subjects suffering from IGE. This correlation demonstrates how the frontiers of knowledge are being pushed by the implementation of the multi-modal combined EEG-fMRI technique.

In epilepsy studies particular care must again be taken when constraining EEG source localisation by using the fMRI data. However, it has been found that there is a good spatial agreement between haemodynamic responses and electric epileptic foci measured intraoperatively [27]. Laufs *et al* summarised the current position of research in this area with the statement: "Clinically EEG/fMRI studies may influence further investigations such as more detailed structural imaging or the planning of intracranial electrophysiological studies by generating hypotheses about the location of epileptic foci. Validation studies are underway to determine whether such clinical applications are appropriate. EEG/fMRI can also assess epileptogenic networks and changes in brain state, leading to a new dimension of understanding of dynamic cerebral processes in health and disease."[47]. This demonstrates the distance still to be covered before simultaneous EEG/fMRI can be used as a routine clinical procedure although already it is being used to help understanding of the disease.

Sleep Disorders

Although it is often clear if a subject is asleep or awake, identifying which stage of sleep they are in is difficult and currently can not be done with fMRI alone. EEG data can be used to identify which stage of sleep a subject is in (*i.e.* rapid eye movement (REM) sleep). HuangHellinger *et al* [48] showed it was feasible to identify the stage of sleep of a subject using EEG data when simultaneous fMRI data is acquired. Since then a few groups have used EEG to identify sleep stages and investigate BOLD responses in sleeping subjects. Lovblad *et al* [49] used a silent imaging sequence and investigated the difference in activation between REM and non-REM sleep states finding occipital activation and frontal deactivation during REM sleep states. Czisch *et al* [50] investigated how auditory processing changed in different stages of non-REM (NREM) sleep and compared the results to those obtained during wakefulness. They found that there was a decrease in auditory BOLD activity during NREM sleep and a "*pronounced negative BOLD signal in the visual cortex and precuneus*". They concluded from this study that "*provided that neurovascular coupling is not altered during sleep, the negative transmodal BOLD response which is most pronounced during NREM sleep stages 1 and 2 reflects a deactivation predominantly in the visual cortex suggesting that this decrease in neuronal activity protects the brain from the arousing effects of external stimulation during sleep, not only in the primary targeted sensory cortex, but also in other brain regions.*"[50]. None of these studies have investigated sleep disorders, however, it can be seen that a greater insight into what is happening in the brain due to these disorders may be possible with the use of simultaneous EEG-fMRI [27].

5.4 Conclusion

Despite the rapid growth of knowledge in both how to conduct and analyse data from simultaneous EEG-fMRI experiments as well as what information can be drawn from the data, questions recently posed by Debener *et al* [28] such as "what is the spectral signature of correlations between BOLD fMRI and EEG? Is there a homogenous relationship over distinct cortical areas?"; give a flavour of the possible research yet to come using simultaneous EEG-fMRI. Therefore it is unsurprising that there is still a drive to push forward the technological frontiers of this technique. With the aims of the research community to provide better EEG data quality and improve the understanding of the effects of the EEG hardware on MR data quality. Furthermore, identifying other questions about the brain and the interactions between the electrical and haemodynamic responses which can be answered via the implementation of simultaneous EEG-fMRI is key to the development of this area of functional imaging. In the next chapters, the experimental work of this thesis is presented with the aim of addressing some of these issues.

5.5 References

1. Keller, F.J., G. W.E., and S. M.J., *Physics: Classical and Modern*. 2nd ed. 1993, USA: McGraw-Hill.

2. Tenforde, T.S., C.T. Gaffey, B.R. Moyer, and e. al, *Cardiovascular alterations in Macaca monkeys exposed to stationary magnetic fields: Experimental observations and theoretical analysis.* Bioelectromagnetics, 1983. **4**: p. 1-9.

3. Allen, P.J., G. Poizzi, K. Krakow, D.R. Fish, and L. Lemieux, *Identification of EEG Events in the MR Scanner: The Problem of Pulse Artifact and a Method for Its Subtraction.* Neuroimage, 1998. **8**(3): p. 229-239.

4. Ives, J.R., S. Warach, F. Schmitt, R.R. Edelman, and D.L. Schomer, *Monitoring a patient's EEG during echo planar MRI.* Electroencephalography and Clinical Neurophysiology, 1993. **87**(6): p. 417-420.

5. Debener, S., K.J. Mullinger, R.K. Niazy, and R.W. Bowtell, *Properties of the ballistocardiogram artefact as revealed by EEG recordings at 1.5, 3 and 7 Tesla static magnetic field strength.* International Journal of Psychophysiology, 2008. **67**(3): p. 189-199.

6. Allen, P.J., O. Josephs, and R. Turner, *A Method for removing Imaging Artifact from Continuous EEG Recorded during Functional MRI.* Neuroimage, 2000. **12**(2): p. 230-239.

7. Anami, K., T. Mori, F. Tanaka, Y. Kawagoe, J. Okamoto, M. Yarita, T. Ohnishi, M. Yumoto, H. Matsuda, and O. Saitoh, *Stepping stone sampling for retrieving artifact-free electoencephalogram during functional magnetic resonance imaging.* Neuroimage, 2003. **19**(2): p. 281-295 (Part 1).

8. http://sprojects.mmi.mcgill.ca/cardiophysio/NormalEKG.htm, *The EKG waveform.* 2000, Molson Medical Informatics project.

9. Gutberlet, I., *BP_Press_Release_Issue_N3*, in *Brain Products*. 2001. p. 10.

10. Reilly, E.L., *EEG recording and operation. In Electroencephalography: Basic Principles, Clinical Applications and Related Fields.* 4th ed, ed. E. Niedermeyer and F. Lopes Da Silva. 1999: William and Wilkins. 122-142.

11. Brookes, M.J., A.M. Gibson, S.D. Hall, P.L. Furlong, G.R. Barnes, A. Hillebrand, K.D. Singh, I.E. Holliday, S.T. Francis, and P.G. Morris, *GLM-beamformer method demonstrates stationary field, alpha ERD and gamma ERS co-localisation with fMRI BOLD response in visual cortex.* Neuroimage, 2005. **26**(1): p. 302-308.

12. Iriarte, J., E. Urrestarazu, M. Valencia, M. Alegre, A. Malanda, C. Viteri, and J. Artieda, *Independent component analysis as a tool to eliminate artifacts in EEG: A quantitative study.* Journal of Clinical Neurophysiology, 2003. **20**(4): p. 249-257.

13. Jung, T.P., S. Makeig, C. Humphries, T.W. Lee, M.J. McKeown, V. Iragui, and T.J. Sejnowski, *Removing electroencephalographic artifacts by blind source separation.* Psychophysiology, 2000. **37**(2): p. 163-78.

14. Makeig, S., M. Westernfield, T.P. Jung, J. Covington, J. Townsend, T.J. Sejnowski, and E. Courchesne, *Functionally Independent components of the late positive event-related potential during visual spatial attention.* Journal of Neuroscience, 1999. **19**(7): p. 2665-2680.

15. Srivastava, G., S. Crottaz-Herbette, K.M. Lau, G.H. Glover, and V. Menon, *ICA-based procedures for removing ballistocariogram artifacts from EEG data acquired in MRI scanner.* Neuroimage, 2005. **24**(1): p. 50-60.

16. Mantini, D., M.G. Perrucci, S. Cugini, A. Ferretti, G.L. Romani, and C. Del Gratta, *Complete artifact removal for EEG recorded during continuous fMRI using independent component analysis.* Neuroimage, 2007. **34**(2): p. 598-607.

17. Debener, S., A. Strobel, B. Sorger, J. Peters, C. Kranczioch, A.K. Engel, and R. Goebel, *Improved quality of auditory event-related potentials recorded simultaneously with 3-T fMRI: removal of the ballistocardiogram artefact.* Neuroimage, 2007. **34**: p. 587-597.

18. Debener, S., http://www.debener.de/. 2007.

19. Naizy, R.K., C.F. Bechmann, G.D. Iannetti, J.M. Brady, and S.M. Smith, *Removal of fMRI environment artifacts from EEG data using optimal basis sets.* Neuroimage, 2005. **28**(3): p. 720-737.

20. Scarff, C.J., A. Reynolds, B.G. Goodyear, C.W. Ponton, J.C. Dort, and J.J. Eggermont, *Simultaneous 3-T fMRI and high-density recording of human auditory evoked potentials.* Neuroimage, 2004. **23**: p. 1129-1142.

21. Vasios, C.E., L.M. Angelone, P.L. Purdon, J. Ahveninen, J. Belliveau, and G. Bonmassar, *EEG/(f)MRI measurements at 7 Tesla using a new EEG cap ("InkCap").* Neuroimage, 2006. **33**(4): p. 1082-1092.

22. Bonmassar, G., N. Hadjikhani, J.R. Ives, D. Hinton, and J.W. Belliveau, *Influence of EEG Electrodes on the BOLD fMRI Signal.* Human Brain Mapping, 2001. **14**: p. 108-115.

23. Krakow, K., P.J. Allen, M.R. Symms, L. Lemieux, O. Josephs, and D.R. Fish, *EEG Recording During fMRI Experiments: Image Quality.* Human Brain Mapping, 2000. **10**: p. 10-15.

24. Stevens, T.K., J.R. Ives, L.M. Klassen, and R. Bartha, *MR Compatibility of EEG Scalp Electrodes at 4 Tesla.* Journal of Magnetic Resonance Imaging, 2007. **25**: p. 872-877.

25. Lemieux, L., P.J. Allen, F. Franconi, M.R. Symms, and D.R. Fish, *Recording of EEG during fMRI Experiments: Patient Safety.* Magnetic Resonance In Medicine, 1997. **38**: p. 943-952.

26. BrainProducts, *BrainAmp Operating Instructions.* 2004. 15.

27. Ritter, P. and A. Villringer, *Review: Simultaneous EEG-fMRI.* Neuroscience and Behavioural reviews, 2006. **30**: p. 823-838.

28. Debener, S., M. Ullsperger, M. Siegel, and A.K. Engel, *Single-trial EEG-fMRI reveals the dynamics of cognitive function.* Trends in Cognitive Sciences, 2006. **10**(12): p. 558-563.

29. Iannetti, G.D. and R.G. Wise, *BOLD functional MRI in disease and pharmacological studies: room for improvement?* Magnetic Resonance Imaging, 2007. **25**: p. 978-988.

30. Goldman, R.I., J.M. Stern, J. Engel, and M.S. Cohen, *Simultaneous EEG and fMRI of the alpha rhythm.* Neuroreport, 2002. **13**(18): p. 2487-2492.

31. Laufs, H., K. Krakow, P. Sterzer, E. Eger, A. Beyerle, A. Salek-Haddadi, and A. Kleinschmidt, *Electroencephalographic signatures of attentional and cognitive default modes in spontaneous brain activity fluctuations at rest.* Proceedings Of The National Academy Of Sciences Of The United States Of America, 2003. **100**(19): p. 11053-11058.

32. Moosmann, M., P. Ritter, I. Krastel, A. Brink, S. Thees, F. Blankenburg, B. Taskin, H. Obrig, and A. Villringer, *Correlates of alpha rhythm in functional magnetic resonance imaging and near infrared spectroscopy.* Neuroimage, 2003. **20**(1): p. 145-158.

33. Gonçalves, S.I., J.C. de Munck, P.J.W. Pouwels, R. Schoonhoven, J.P.A. Kuijer, N.M. Maurits, J.M. Hoogduin, E.J.W. Van Someren, R.M. Heethaar, and F.H. Lopes Da Silva, *Correlating the alpha rhythm to BOLD using simultaneous EEG/fMRI: Inter-subject variability.* Neuroimage, 2006. **30**(1): p. 203-213.

34. Sammer, G., C. Blecker, H. Gebhardt, M. Bischoff, M. Stark, K. Morgen, and D. Vaitl, *Relationship between regional hemodynamic activity and simultaneously recorded EEG-theta associated with mental arithmetic-induced workload.* Human Brain Mapping, 2007. **28**(8): p. 793-803.

35. Eichele, T., K. Specht, M. Moosmann, M.L.A. Jongsma, R.Q. Quiroga, H. Nordby, and K. Hugdahl, *Assessing the spatiotemporal evolution of neuronal activation with single-trial event-related potential and functional MRI.* Proceedings Of The National Academy Of Sciences Of The United States Of America, 2005. **102**(49): p. 17789-17803.

36. Debener, S., M. Ullsperger, M. Siegel, K. Fiehler, D. Yves von Cramon, and A.K. Engel, *Trial-by-Trial Coupling of Concurrent Electroencephalogram and Functional Magnetic Resonance Imaging Identifies the Dynamics of Performance Monitoring.* Journal of Neuroscience, 2005. **25**(50): p. 11730-11737.

37. Dale, A.M., A.K. Liu, B.R. Fischl, R.L. Buckner, J. Belliveau, J.D. Lewine, and E. Halgren, *Dynamic statistical parametric mapping: Combining fMRI and MEG for high-resolution imaging of cortical activity.* Neuron, 2000. **26**(1): p. 55-67.

38. Phillips, C., M.D. Rugg, and K.J. Friston, *Anatomically informed basis functions for EEG source localization: Combining functional and anatomical constraints.* Neuroimage, 2002. **16**(3): p. 678-695.

39. Mulert, C., L. Jager, R. Schmitt, P. Bussfeld, O. Pogarell, H.-J. Moller, G. Juckel, and U. Hegerl, *Integration of fMRI and simultaneous EEG: towards a*

comprehensive understanding of localization and time-course of brain activity in target detection. Neuroimage, 2004. **22**(1): p. 83-94.

40. Lemieux, L., A. Salek-Haddadi, O. Josephs, P.J. Allen, N. Toms, C. Scott, K. Krakow, R. Turner, and D.R. Fish, *Event-Related fMRI with Simultaneous and Continuous EEG: Description of the Method and Initial Case Report.* Neuroimage, 2001. **14**: p. 780-787.

41. Salek-Haddadi, A., K.J. Friston, L. Lemieux, and D.R. Fish, *Simultaneous EEG-Correlated Ictal fMRI.* Neuroimage, 2002. **16**: p. 32-40.

42. Baudewig, J., H.J. Bittermann, W. Paulus, and J. Frahm, *Simultaneous EEG and functional MRI of epileptic activity: a case report.* Clinical Neurophysiology, 2001. **112**(7): p. 1196-1200.

43. Iannetti, G.D., C. Di Bonaventura, P. Pantano, A.T. Giallonardo, P.L. Romanelli, L. Bozzao, M. Manfredi, and G.B. Ricci, *fMRI/EEG in paroxysmal activity elicited by elimination of central vision and fixation.* Neurology, 2002. **58**(6): p. 976-979.

44. Benar, C.G., D.W. Gross, Y.H. Wang, V. Petre, B. Pike, F. Dubeau, and J. Gotman, *The BOLD response to interictal epileptiform discharges.* Neuroimage, 2002. **17**(3): p. 1182-1192.

45. Salek-Haddadi, A., K.J. Friston, L. Lemieux, and D.R. Fish, *Review: Studying spontaneous EEG activity with fMRI.* Brain Research Reviews, 2003. **43**: p. 110-133.

46. Hamandi, K., A. Salek-Haddadi, H. Laufs, A. Liston, K.J. Friston, D.R. Fish, J.S. Duncan, and L. Lemieux, *EEG-fMRI of idiopathis and secondarily generalized epilepsies.* Neuroimage, 2006. **31**: p. 1700-1710.

47. Laufs, H. and J.S. Duncan, *Electroencephalography/function MRI in human epilespy: what it currently can and cannot do.* Current Opinion in Neurology, 2007. **20**(4): p. 417-423.

48. HuangHellinger, F.R., H.C. Breiter, G. McCormack, M.S. Cohen, K. Kwong, J.P. Sutton, R.L. Savoy, R.M. Weisskoff, T.L. Davis, J. Baker, J. Belliveau, and B.R. Rosen, *Simultaneous functional magnetic resonance imaging and electrophysiological recording.* Human Brain Mapping, 1995. **3**(1): p. 13-23.

49. Lovblad, K.O., R. Thomas, P.M. Jakob, T. Scammell, C. Bassetti, M. Griswold, J.R. Ives, J. Matheson, R.R. Edelman, and S. Warach, *Silent functional magnetic resonance imaging demonstrates focal activation in rapid eye movement sleep.* Neurology, 1999. **53**(9): p. 2193-2195.

50. Czisch, M., T.C. Wetter, C. Kaufmann, T. Pollmacher, F. Holsboer, and D.P. Auer, *Altered processing of acoustic stimuli during sleep: Reduced auditory activation and visual deactivation detected by a combined fMRI/EEG study.* Neuroimage, 2002. **16**(1): p. 251-258.

Chapter 6

Simultaneous EEG and fMRI: EEG Artefact Correction.

6.1 Introduction

The extent to which neuroimaging has already benefited from the availability of simultaneous EEG and fMRI recordings was shown in Chapter 5. The variety of applications ranging from investigating correlations between electrical and BOLD activity in the resting state [1, 2] to source localisation of epileptic activity [3, 4], which have already been explored using combined EEG-fMRI demonstrates the great potential of this technique. However, the presence of residual EEG artefacts still limits the avenues which can be investigated using this multi-modal approach. The most obvious areas affected are investigations of high frequency gamma activity, as well as single trial investigations where a high SNR within the EEG data is required. This chapter explores the reason for these limitations and demonstrates two methodological developments which can be used to improve the quality of EEG data recorded in combined EEG/fMRI experiments.

6.2 Background

The previous chapter outlined the causes of artefacts in EEG data recorded simultaneously with MRI and described the methods that have been developed to correct such artefacts. It is clear from the previous discussion that average artefact subtraction (AAS) [5, 6] is a widely used technique for correction of both gradient and pulse artefacts and it is often necessary to perform AAS before implementation of other correction techniques, such as OBS [7]. However, the implementation of AAS often leaves residual artefacts in the EEG data, limiting the frequency bands from which data can be used. As briefly discussed in Chapter 5, for successful implementation of the mean subtraction method there are key requirements which must be adhered to. First, the EEG amplifiers must have a high enough dynamic range to prevent saturation by the large artefact voltages, thus allowing an undistorted artefact template to be produced. Second, the artefact waveforms must be precisely and reproducibly sampled to provide an accurate template for each subtraction. The latter requires that the timing of each appearance of the artefact waveforms can be accurately measured.

Since the gradient waveforms used in fMRI show variations occurring on a timescale of 10^{-4} s, temporal localisation of the gradient artefact with an accuracy that is significantly better than a hundred microseconds is required for perfect correction of each occurrence of the artefact. The repetitive nature of the pulse sequences that are most commonly used for fMRI helps in this regard, since the gradient waveforms are generally played out identically in each *TR*-period, and the timing of the start of each of these periods is accurately known. However, with typical EEG sampling frequencies being less than 20 kHz, such that the dwell time between sample points is 50 μs or more, consistent sampling of the gradient artefacts requires that the EEG sampling is synchronised to the scanner waveform and that the repetition time is an integer multiple of the EEG sample time. Without synchronisation, the temporal position of the sampling can vary by up to one dwell time with respect to the gradient waveform across *TR*-periods leading to significant variation of the sampled form of the gradient artefact. In this situation, subtraction of a template formed by averaging over repeated *TR*-periods does not perfectly eliminate the gradient artefact. One result of this imperfect elimination of the gradient artefact is the need to use low-pass filtering, as suggested by Allen *et al [5]*. The ramifications of this filtering were discussed in Chapter 5.

Although the cardiac pulse artefact varies much more slowly in time and can be well characterised by digitisation at EEG sampling frequencies, AAS relies on the correct detection of the R peak within the QRS complex, as discussed previously. This detection can be difficult to perform especially at high fields where large flow-induced potentials occur in the ECG trace. The difficulty in identifying the QRS complex is not only limiting in the use of AAS correction but also in application of OBS.

In recent work, Mandelkow *et al [8]* provided the first demonstration that after synchronisation of the EEG sampling to the clock of the MR scanner, the gradient artefact can be sampled in a highly reproducible fashion across repeated *TR*-periods, allowing greatly improved gradient artefact correction via mean template subtraction and a consequently reduced need for low-pass filtering. In their experiments, Mandelkow *et al [8]* showed that the usable EEG bandwidth during concurrent MR image acquisition using multi-slice EPI could be extended to 150 Hz via the use of synchronisation. The majority of the experimental studies presented by these authors were however carried out on phantoms, which somewhat reduces the complexity of the process of artefact removal, as there is no motion or pulse artefact to deal with.

The aim of the work described here is to show further the importance of accurate template production when correcting for both gradient and pulse artefacts and to highlight the value of two methodological developments that help in this process. In particular, this chapter reports findings that complement and extend the previous work [8] by showing that synchronisation of the scanner clock to the EEG sampling improves gradient artefact correction in EEG data recorded from human subjects. We go on to show that higher frequency brain activity can be reliably measured when synchronisation is employed, thus highlighting the advantages of synchronisation. An alternative method based on the use of the vectorcardiogram recording provided by the MR scanner for accurately identifying the timing of the pulse artefact is introduced and shown to improve the correction of this artefact under some circumstances.

6.3 Methods

MRI data were collected using a Philips Achieva 3 T MR scanner (Philips Medical Systems, Best, Netherlands) employing a whole body RF coil for signal excitation and an eight-channel, SENSE head coil for signal reception. A standard multi-slice EPI sequence was implemented with $TE = 35$ ms, a 64×64 matrix, 3.25×3.25 mm^2 in-plane resolution and a slice thickness of 3 mm. Twenty transverse slices were acquired, using a parallel imaging SENSE factor of 2 [9]. Individual slice acquisitions were uniformly spaced within each repetition time (*TR*) period.

Dynamic stabilisation[*] was turned off to prevent the *TR*-period differing from the displayed *TR*. Since the process of dynamic stabilisation takes a finite time to perform, employing this procedure results in a slightly longer *TR* than the one the user inputs. Cardiac and respiratory cycles were simultaneously recorded using the scanner's physiological monitoring system (vector cardiogram (VCG) [10] and respiratory belt) whose outputs are sampled at 500 Hz. The VCG is based on recording signals from four leads, three placed along the mid-line of the chest and the fourth to the left of the heart forming a 'T'-shaped arrangement on the surface of the chest, as shown in Figure 6.1. This allows the generation of two orthogonal traces, effectively aligned parallel and perpendicular to the cardiac dipole vector orientation at the R-peak. The dipole vector representing the magnetic-field-related flow artefact recorded at the chest surface has been shown to be approximately perpendicular to that reflecting the R-peak [11], so that the trace aligned with the R-peak vector is not strongly confounded by flow effects and therefore allows optimal detection of the time of onset of the R-peak [10, 11].

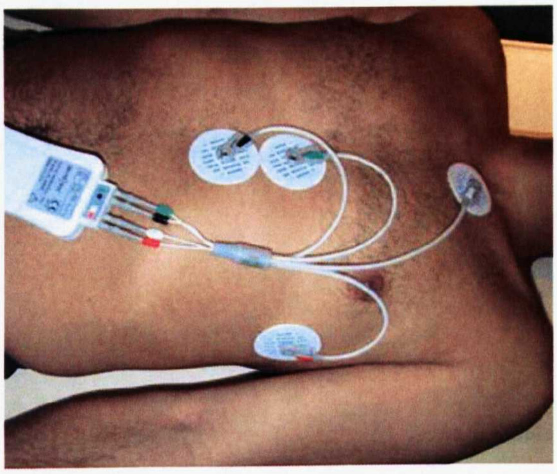

Figure 6.1: The placement of the VCG electrodes on a subject. Adapted from [12].

EEG data were recorded using a BrainAmp MR EEG amplifier, Brain Vision Recorder (Version 1.03) software (Brainproducts, Munich, Germany) and a BrainCap electrode cap (EasyCap, Herrsching, Germany) with 30 electrodes positioned on the scalp according to the international 10-20 system, and additional

---

[*] Dynamic Stabilisation: checks the resonance frequency before each volume acquisition to reduce the effects of possible fluctuations in this frequency due to the warming up of hardware such as gradients and shims.

ECG and EOG electrodes. In all studies, the 50 cm long ECG lead was positioned at the base of the back. The BrainAmp system uses a sampling rate of 5 kHz and incorporates hardware filters which limit the frequency range of the recorded signals to 0.016-250 Hz, with a roll-off 30 dB/octave at high frequency. The cap provides a reference electrode positioned between Fz and Cz positions (refer to Figure 4.9A).

As described by Mandelkow *et al [8]*, two main criteria have to be met in order to achieve optimal synchronisation of the EEG sampling and MR scanning: (1) the *TR* of the MR sequence must be a multiple of the EEG scanner clock period; (2) the clocks of the two systems must be phase locked. Here, the phase locking was achieved using a device made in-house which drives the BrainAmp clock using a 5 kHz signal which was derived by frequency division from the MR scanner's 10 MHz TTL, clock signal. The two systems are also opto-isolated to prevent damage to either system. Triggers sent from the MR scanner marking the beginning of each multi-slice, volume acquisition were recorded on the EEG system. To obtain the best quality fMRI data it is sensible to set the slice separation to equidistant within the *TR* so that all slices are obtained with a similar spin history throughout the experiment. This approach was used here, but did however, put a further constraint on possible *TRs* to be used, of *TR*/ (0.1ns×number of slices) =integer, as outlined by Mandelkow *et al [8]*. Analysis of the times at which the trigger pulses are recorded provides a useful indication of successful synchronisation: when the clocks are synchronised, the temporal spacing of the trigger pulses is always a fixed multiple of the EEG clock period; in the absence of synchronisation the measured inter-pulse spacing is found to vary over multiple *TR*-periods. Further evidence of synchronisation was provided by the perfect phase coherence of the 5 kHz signal derived from the scanner and the EEG clock signal which was seen when the two signals were viewed simultaneously on an oscilloscope [8].

Two different experiments were conducted in this study. The first was designed to measure the effect of synchronisation on the quality of resting state EEG data recorded from human subjects in the scanner during the execution of a multi-slice EPI sequence. Data from this experiment were also used to test the effectiveness of using the vectorcardiogram provided by the scanner rather than the ECG recorded using the EEG system in identifying R-peaks for the correction of the pulse artefact.

To ensure a direct comparison of the VCG and ECG traces for correcting the pulse artefact the ECG and VCG traces were recorded simultaneously. The second experiment was designed to be sensitive to the expected increase in the range of frequencies of neurological activity, which can be measured in EEG recordings made in the scanner when synchronisation is employed. Both experiments were performed in darkness and the subjects were asked to remain as still as possible. The experiments were approved by the local ethics committee and informed consent was obtained from each subject.

6.3.1 Experiment 1: The effectiveness of synchronisation and the VCG on artefacts removal.

Three healthy volunteers were scanned. Data were recorded continuously for 6 minutes (180 volumes) for three different situations:

(1.i) the EEG sampling and scanner waveforms were synchronised using the apparatus described above and a *TR* value of 2 s, which is a multiple of the EEG clock period, was chosen. This ensured that no jitter between the scanning time frames and the EEG sampling would occur.

(1.ii) the 5 kHz signal from the MR scanner was disconnected so that the EEG sampling was not synchronised to the MR scanner clock - all other parameters remained the same as in (1.i)

(1.iii) the EEG and MR clocks were synchronised, as in (1.i), but a *TR* of 2.0001s, which is not a multiple of the 200 μs EEG clock period, was employed.

Only arrangement (1.i) therefore satisfied the requirements for identical sampling of the gradient artefact in the EEG data recorded in all *TR*-periods.

6.3.2 Experiment 2: Increasing the range of frequencies of detected neurological signals.

EEG measurements were made on five healthy volunteers during presentation of a simple visual stimulus under each of the following conditions:

(2.i) outside the scanner lying down in a similar environment to that inside the scanner.

(2.ii) inside the scanner with the EEG sampling and scanner waveforms synchronised.

(2.iii) inside the scanner with the EEG sampling not synchronised to the MR scanner.

6.3.2.1 Paradigm

Using a mirror mounted on the RF coil, the subjects viewed a checkerboard flashing at 10 Hz, which was presented via a projector onto a screen located at the front of the scanner. A block paradigm, comprising 5 seconds of visual stimulation followed by 5 seconds of rest repeated 30 times, was employed. A *TR* value of 2.2 s was used and 160 volumes (corresponding to a 352 s acquisition time) and 20 slices per volume were acquired in experiments (2.ii) and (2.iii). The *TR* value was chosen to be a multiple of the EEG clock period and to yield a frequency of slice acquisition ($20/(2.2\text{ s}) \approx 9.09$ Hz) that was not an exact multiple of the frequency of visual stimulation. The latter consideration allowed better separation of signals due to neuronal activation and gradient artefacts in EEG spectra.

6.4 Analysis

Off-line EEG signal correction was based on averaging and then subtracting gradient and pulse artefacts, as implemented in Brain Vision Analyzer (Version 1.05, Brain Products, Munich, Germany)[5, 6].

6.4.1 Experiment 1: The effectiveness of synchronisation and the VCG on artefacts removal.

6.4.1.1 Gradient Artefact Correction

The gradient artefact correction process used an average artefact waveform of 2 s duration, formed from the average over the 180 *TR*-periods, which were segmented using the scanner-generated markers. No additional filtering or down-sampling were applied during the artefact removal process. Subsequently, down-sampling to 500 Hz was performed using the "change sampling rate" function within Brain Vision Analyser which uses a cardinal spline interpolation, in conjunction with an anti-aliasing filter with a cut-off frequency at 90 % of the new Nyquist frequency and a 24 dB/octave roll-off.

Once corrected, the data were exported to MATLAB where in-house written programs were used to compare the Fast Fourier transform (FFT) of the corrected and uncorrected data recorded in each of the situations (1.i-1.iii). Since the time between repetitions of the scanner waveforms used in acquiring each slice was $TR/20 \approx 100$ ms, gradient artefacts occurred at multiples of 10 Hz. The ratio of the amplitude of the EEG spectrum obtained by Fourier transformation of data recorded before and after correction was therefore evaluated at the fundamental slice frequency (10 Hz) and higher harmonics of this frequency for each of the three conditions. The average and standard deviation of this ratio over the 30 channels corresponding to scalp electrodes were calculated, providing a measure of the efficacy of gradient artefact correction.

The standard deviation of the signal average over all channels after artefact correction in each of the three subjects was also taken and averaged together. This gives a measure of the quality of gradient artefact correction in each of the three situations when considered over a range of subjects.

6.4.1.2 Pulse Artefact Correction

Pulse artefact correction, based on R-peak markers derived from either the ECG (measured by the EEG system) or VCG (measured by the MR scanner) traces, was carried out on the data that had been acquired with synchronisation of the EEG and scanner clocks (condition (1.i)) with gradient artefact correction performed as described above. Prior to pulse artefact correction, the data were also low-pass filtered via the Analyzer MRI artefact correction function which uses a finite impulse response (FIR) filter employing a Hanning window from 0 to a cut-off frequency of 70 Hz to further reduce residual gradient artefact, following common practice in analysis of EEG acquired simultaneously with fMRI [5, 13-15]. Following the common practice for gradient artefact rejection ensured that detection of the R peaks within the ECG trace was made as easy as possible, so that comparison with the VCG method was fair. Pulse artefact correction was carried out using the Brain Vision Analyser software (Version 1.05, Brain Products, Munich, Germany), which follows the method outlined by Allen *et al* [6] and creates a template of the pulse artefact using the previous 10 s of data recorded on each channel which is then subtracted from the data to eliminate each occurrence of the pulse artefact.

R-peak markers were generated from the ECG trace using the direct detection method [6] within the Brain Vision analyzer software. Any incorrectly positioned R-peak markers were manually repositioned. The R-peaks were detected from the VCG data using the "target-distance" algorithm [11] which is implemented within the physiological monitoring system on the scanner and usually used for the purpose of cardiac gating. This algorithm works by finding the difference in voltage between the actual VCG recording and the reference R-wave. This distance is used to scale the amplitude of the VCG. The more likely the lead is recording an R-wave, the smaller the distance. This information can be used to emphasize the magnitude of the R-wave into a sharp peak which can then be more readily detected. Further information on this algorithm and its advantages over other methods of detecting R peaks is given in [11]. The VCG and EEG recordings were aligned in time, based on the triggers generated by the scanner at the start of each volume acquisition, so that the R-peak times identified from the VCG could be directly applied to correction of the EEG data. Using these markers, the PA correction tool within Brain Vision Analyzer was again used to correct for the artefact.

The average and standard deviation of the pulse artefact waveform were found from the data before and after pulse artefact correction using R-peak markers based on both ECG and VCG recordings and compared in order to assess the efficacy of artefact removal.

6.4.2 Experiment 2: Increasing the range of frequencies of detected neurological signals.

Data from conditions (2.ii & 2.iii) were corrected for gradient and pulse artefacts. The gradient artefact correction employed an average artefact waveform of 2.2 s duration, which was produced by averaging over the 160 *TR*-periods. After gradient artefact correction the data were down-sampled to 500 Hz, using the anti-aliasing filter described above, but no further filtering was applied. The pulse artefact was corrected using the R-peak markers identified from the VCG recording. Data were then exported to MATLAB for further analysis.

After segmentation of the EEG data into epochs in which the visual stimulus was on or off, data from all the "stimulus on" periods were then concatenated and Fourier transformed to form a single EEG spectrum with a frequency resolution of approximately 0.007 Hz. As a result of the phase coherence of the stimulus across epochs, this spectrum was expected to show strong peaks corresponding to the frequencies of significant driven electrical activity. A similar procedure was applied to data from the "stimulus off" periods in which no visual stimulus was present. Data from the on and off states were then overlaid to highlight differences in the spectra. The data collected in condition (2.i) were analysed first to check that the paradigm and analysis procedure yielded clear spectral peaks in the data recorded with the visual stimulus on, in the absence of any scanner-induced artefacts.

The difference of spectra recorded in the stimulus on and stimulus off periods was evaluated by simple subtraction of data recorded both with and without synchronisation, so as to provide a clearer indication of the potential for detecting signals due to evoked brain activity in the presence of residual artefacts. A measure of the contrast to noise of induced activity was also made by evaluating the amplitude at the 6th harmonic of the stimulus frequency occurring at 60 Hz (which was the highest frequency driven response that that was found to be reliably detected) and comparing this value to the signal amplitude at frequencies corresponding to the adjacent harmonics of the gradient artefact, occurring at 54.54 and 63.63 Hz.

6.5 Results

6.5.1 Experiment 1: The effectiveness of synchronisation and the VCG on artefacts removal.

6.5.1.1 Gradient Artefact Correction

Figure 6.2A shows a schematic of the gradient pulses involved in the EPI sequence employed, with the full EPI pulse sequence shown in Figure 6.3. Figure 6.2B shows the average gradient artefact generated on electrode F7 during a single slice acquisition for Subject 1. This is a representative electrode and the exact morphology of the artefact will vary between electrodes and indeed may change between scan sessions if the electrodes are not placed in identical positions relative to the MR gradients each time. The form of the artefact is similar in all experimental situations that were investigated, however the standard deviation of this artefact calculated over repeated slice acquisitions varies significantly depending on whether data were acquired with or without synchronisation. With the scanner and EEG clocks synchronised and the *TR* set to a multiple of the scanner clock period the standard deviation is always less than a few microvolts in magnitude (Figure 6.2C). However, if either the clocks are not synchronised (Figure 6.2D) or the *TR* is not a multiple of the scanner clock period (Figure 6.2E) then the variation in the sampled gradient artefact causes a large increase in the standard deviation.

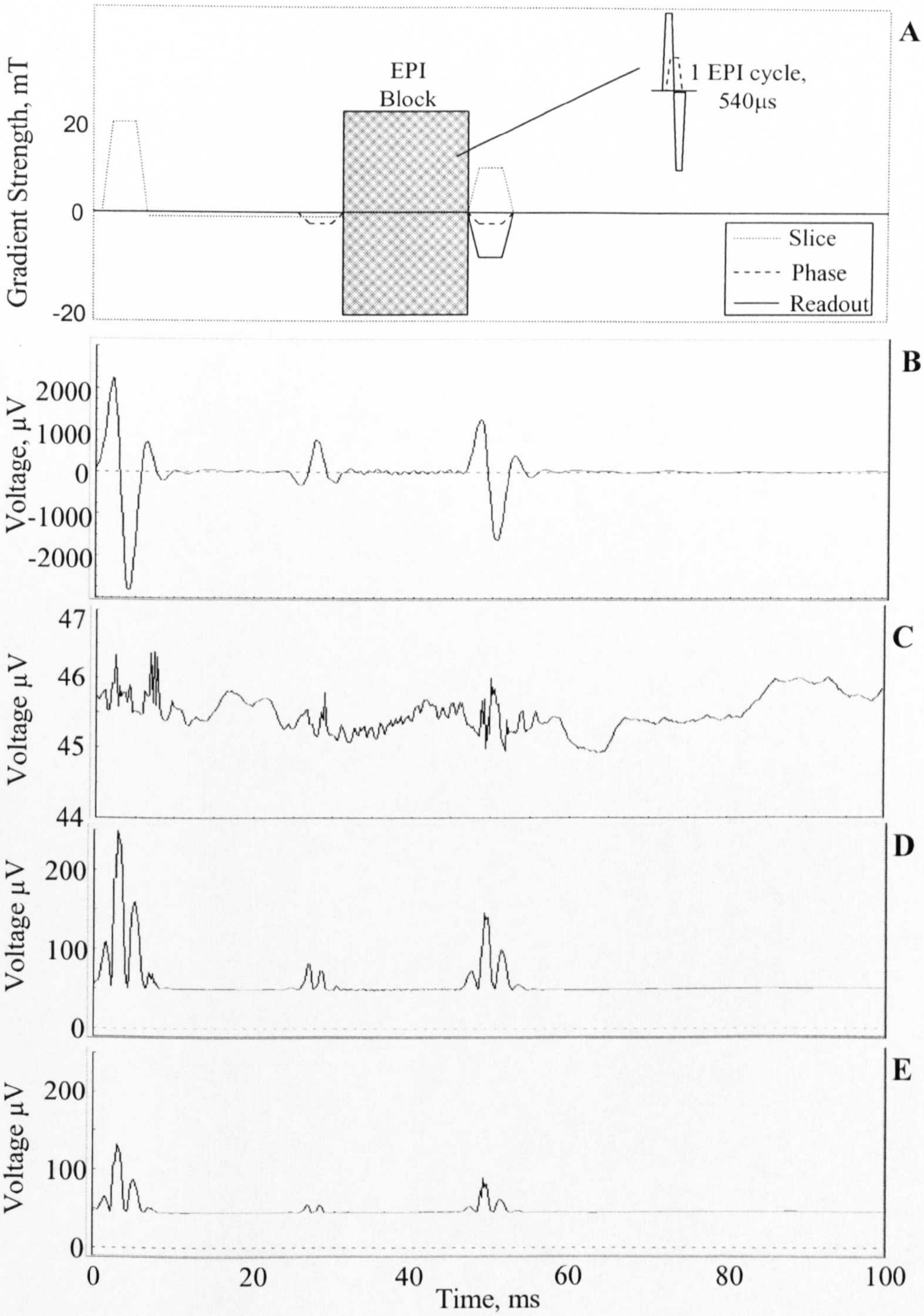

Figure 6.2: Graphs showing the gradient artefact, recorded on electrode F7, averaged over all slice acquisitions in condition (1.i): (B) with the associated standard deviation over all slice acquisitions for this electrode for C: TR=2s, with clock synchronisation; D: TR=2s with no clock synchronisation and E: TR=2.0001s, with clock synchronisation. Note the reduced scale used in C to allow depiction of the standard deviation of the trace. (A) shows the corresponding gradient waveforms, which generate the artefacts.

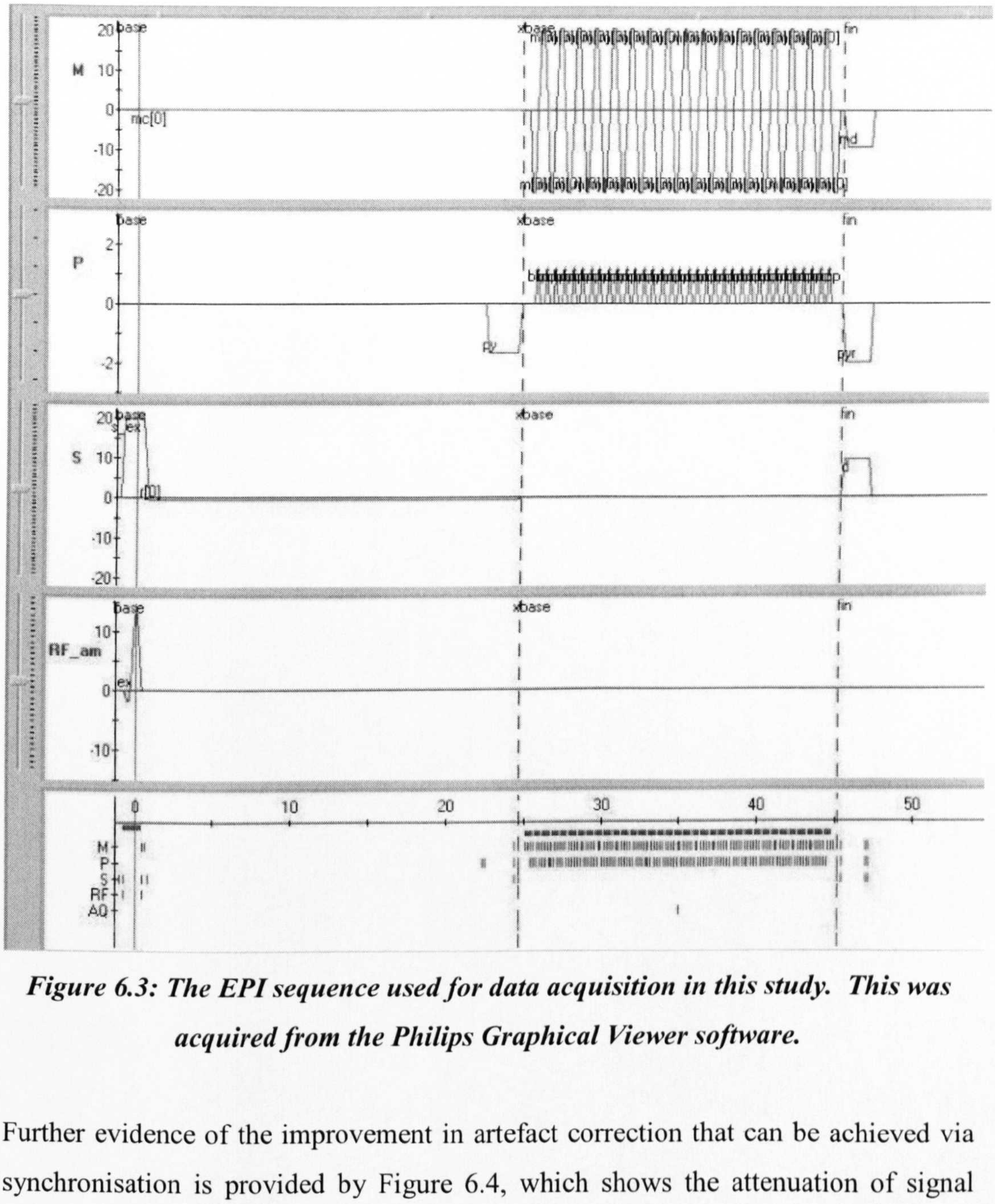
M
20
10
0
-10
-20
base
xbase
fin
mc[0]
md
P
2
0
-2
base
xbase
fin
S
20
10
0
-10
-20
base
xbase
fin
RF_am
10
0
-10
base
xbase
fin
ex
0
10
20
30
40
50
M
P
S
RF
AQ

Figure 6.3: The EPI sequence used for data acquisition in this study. This was acquired from the Philips Graphical Viewer software.

Further evidence of the improvement in artefact correction that can be achieved via synchronisation is provided by Figure 6.4, which shows the attenuation of signal amplitude at multiples of 10 Hz produced by gradient artefact correction for the three subjects studied. The greatest attenuation occurs in condition (1.i) where the scanner and EEG clocks are synchronised and the *TR* is a multiple of the EEG clock period. These results are also reflected in Table 6.1 which shows the standard deviation of the signal in each of the three situations averaged over all the channels and all the subjects.

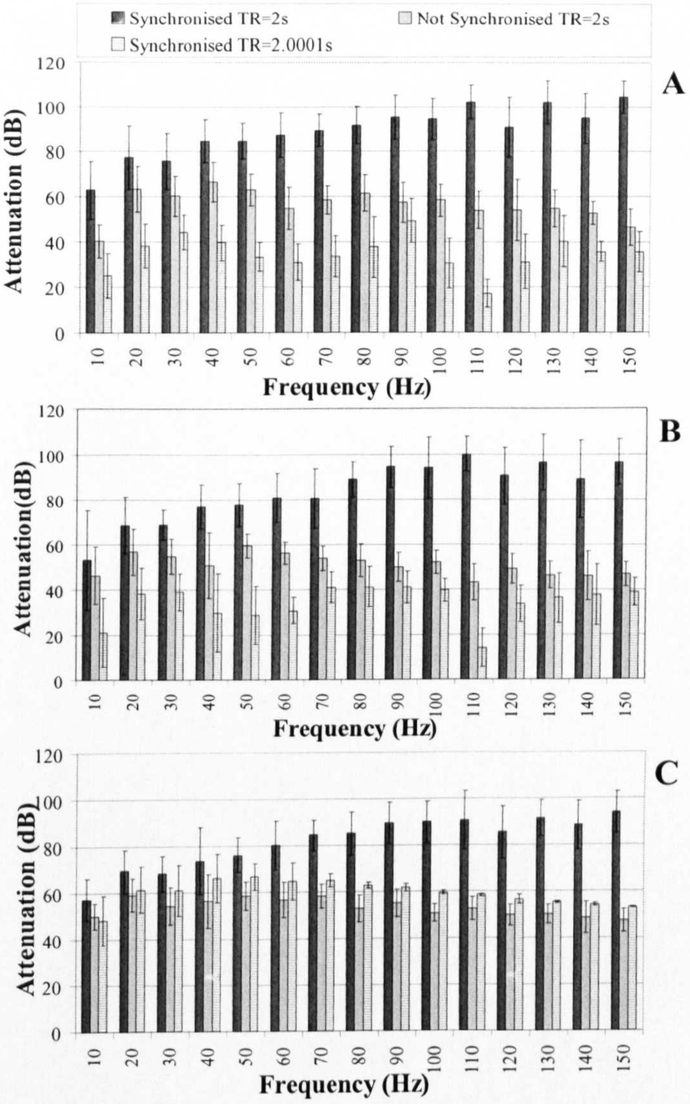

Figure 6.4: Attenuation of signal amplitude (-20log$_{10}$(corrected/uncorrected)) due to gradient artefact correction averaged over all channels. Measurements are made at harmonics of the 10 Hz slice acquisition frequency, at which the gradient artefacts are strongest for three different conditions. Error bars show the variation in attenuation across all channels. Data are shown for the three different subjects studied in Experiment 1.

Synchronised, TR=2s	0.14±0.03
Not Synchronised, TR=2s	0.17±0.02
Synchronised, TR=2.0001s	0.18±0.05

Table 6.1: The ratio of standard deviation in the signal corrected:uncorrected, averaged over all subjects and channels. Errors are the standard deviation of the ratio across subjects.

6.5.1.2 Pulse Artefact Correction

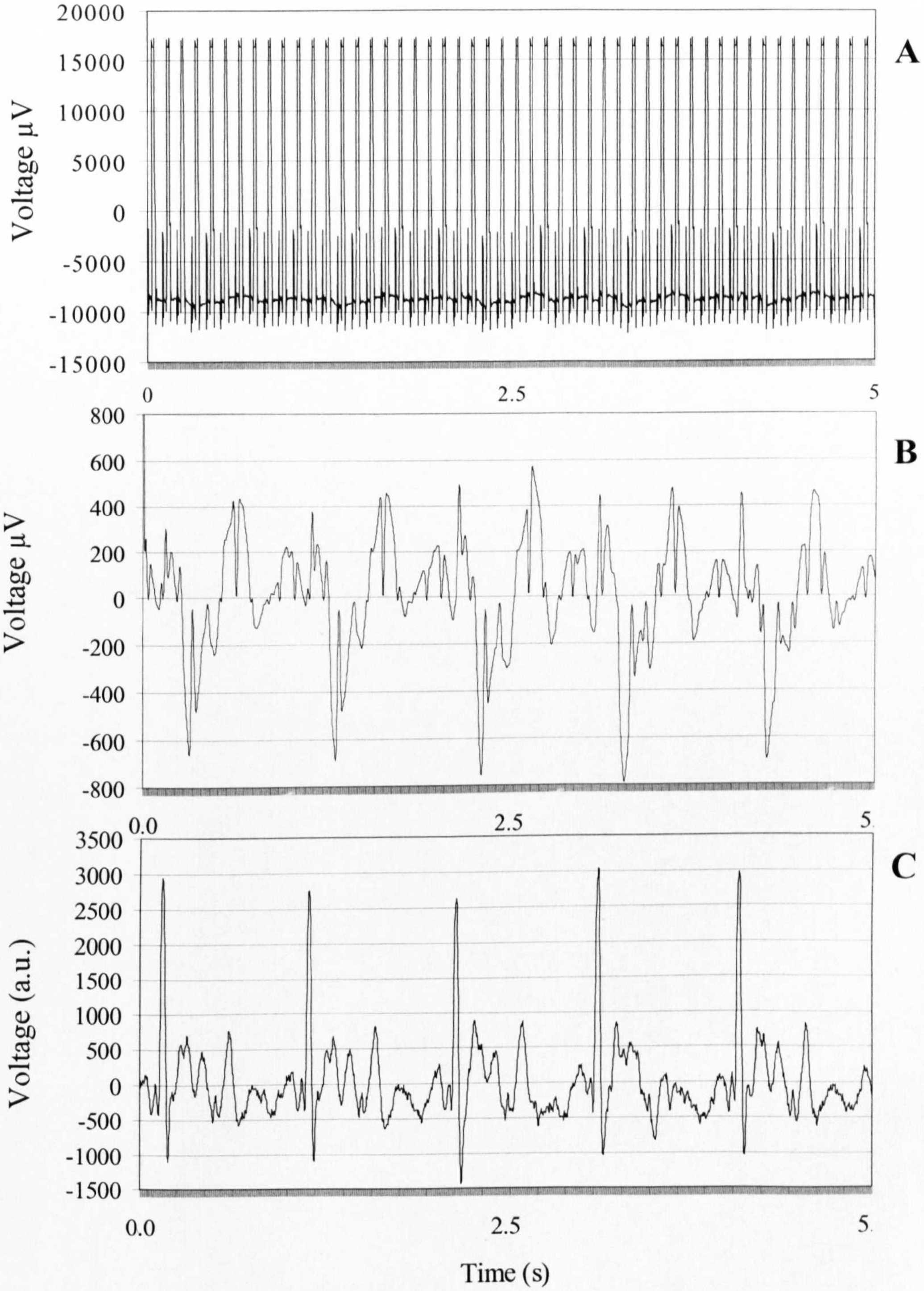

Figure 6.5: Typical ECG trace before (A) and after (B) gradient artefact correction, along with a VCG trace (C) recorded over the same period of time and plotted without any correction.

The ECG traces produced before and after gradient artefact correction are shown in Figure 6.5A and B. These data are taken from Subject 1 who provided the highest quality ECG trace, in which no saturation of the ECG signal occurred. Figure 6.5C shows a corresponding VCG trace. Figure 6.6 shows the average and standard deviation of the pulse artefact on the trace recorded from electrode TP10 in the same subject before and after pulse artefact correction using markers derived from either ECG or VCG traces. Data from different cardiac cycles (both uncorrected and corrected) were aligned by using the R-peaks identified from the VCG trace in all cases before the averaging was employed. This was all done using the 'segmentation' and 'averaging' functions within Brain Vision Analyzer.

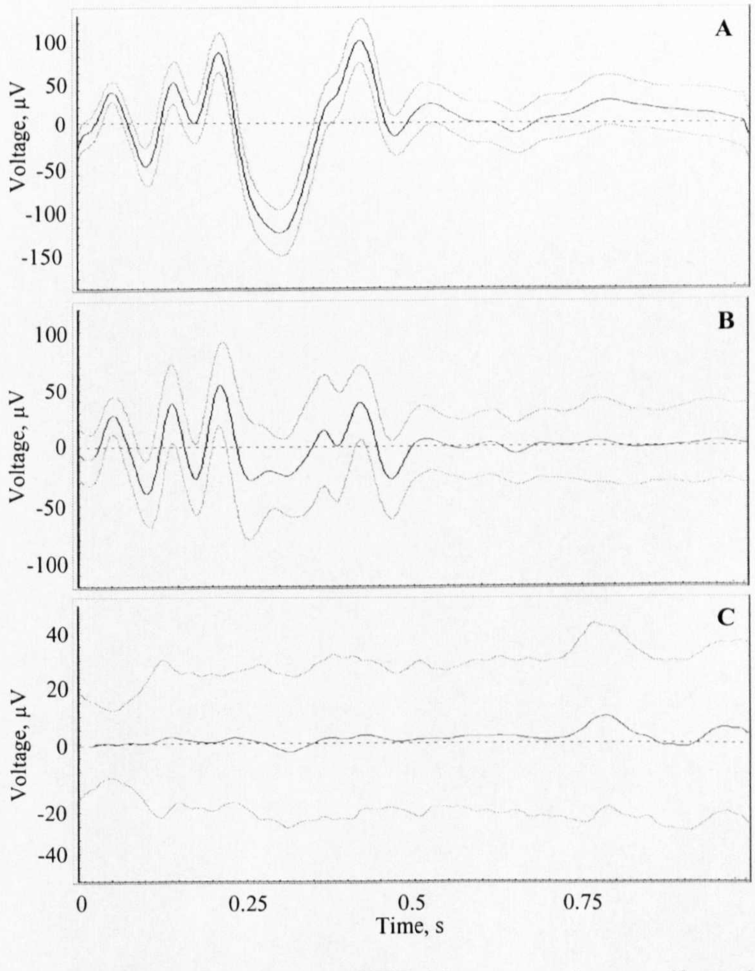

Figure 6.6: EEG trace from channel TP 10 averaged over all cardiac cycles occurring in a 2 minute period before (A) and after correction using R-markers derived from the ECG (B) and VCG (C) recordings, with the dashed lines indicating the standard deviation of each average waveform. In these traces, time zero corresponds to the occurrence of the R-peak in the VCG recording.

6.5.2 Experiment 2: Increasing the range of frequencies of detected neurological signals.

One subject was excluded from further analysis due to the very weak driven activity displayed in data recorded outside the scanner. However, clear peaks of electrical activity occurring at multiples of the frequency of visual stimulation were evident in the data acquired from the other four subjects. Data recorded from one subject in conditions (2.ii) and (2.iii) showed evidence of large movement within the scanner (this was confirmed by evaluation of the registration parameters generated during motion correction of the MR images which showed displacement of more than 5 mm) and so was not used in the subsequent analysis. The remaining three subjects all showed neuronal activity at 20 Hz and higher harmonics of the stimulus frequency in data recorded both with and without synchronisation. A comparison of data acquired in the scanner with and without synchronisation is shown in Figure 6.7(A&B). Modulus spectra of the data recorded in the stimulus off (red) and stimulus on (blue) periods are shown with the peaks resulting from neuronal activity highlighted by arrows. Although the differences in data recorded with and without synchronisation are not significant below 50 Hz they rapidly become apparent at the higher frequencies. Figure 6.7(C&D) shows the result of subtracting the spectra recorded in the on and off conditions.

The comparison of the average signal measured across all subjects at 60 Hz (which corresponded to the highest frequency neuronal signal that was obviously evident in the data) with that present at frequencies corresponding to the adjacent gradient artefact peaks is detailed in Table 6.2. The results show that the data recorded with synchronisation have a significantly higher contrast to noise ratio.

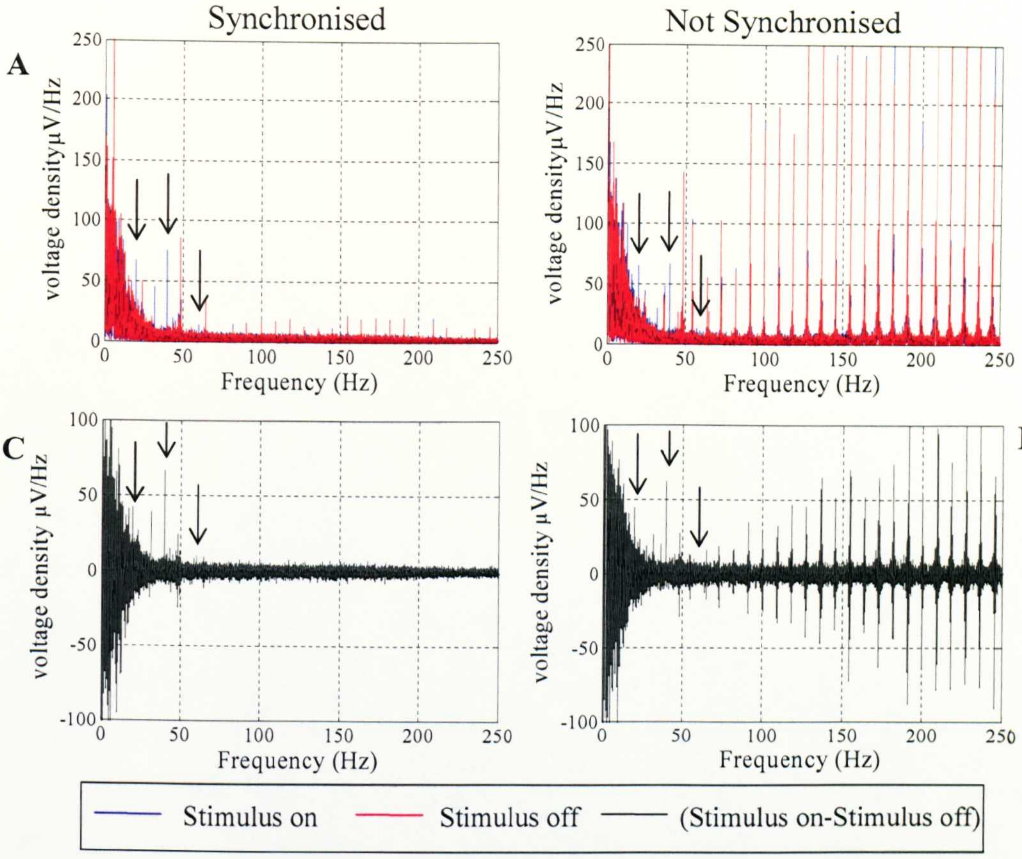

Figure 6.7: A and B show the modulus of the FFT of the signal from channel Oz, after gradient and pulse artefact correction periods for synchronised and unsynchronised data acquisition. C and D show the difference in the "stimulus on" and "stimulus off". Arrows indicate spikes of neuronal activity occurring at harmonics of the 10 Hz visual stimulus frequency.

	Power at 60Hz/Power at 54.54Hz	**Power at 60Hz/Power at 63.63Hz**
Synchronised, TR=2s	1.8±0.7	0.6±0.1
Not synchronised, TR=2s	0.8±0.2	0.3±0.1

Table 6.2: The ratio of signal amplitude at 60 Hz (corresponding to neuronal activity at the 6th harmonic of the frequency of visual stimulation) to that occurring at frequencies corresponding to adjacent harmonics of the slice acquisition frequency (54.45 and 63.63 Hz). The ratio was calculated after correction of gradient and pulse artefacts, from the channel showing maximum neuronal activity for each subject (Oz or Pz) and then averaged over all subjects. The quoted errors correspond to the standard deviation over all subjects.

6.6 Discussion

Comparison of the average gradient artefact (Figure. 6.2B) and the gradient waveforms (Figure. 6.2A & 6.3) indicates that the largest artefacts are generated in the recording from lead F7 by the gradient pulses used for slice selection at the start of each slice acquisition and those used for crushing transverse magnetisation after signal acquisition (at $t \sim 50$ ms). A slightly smaller artefact is generated by the gradient pulses used for the k-space pre-excursion in the phase-encode direction just prior to signal acquisition. Counter-intuitively, the large switched magnetic field gradients used to form the EPI echo train and the associated gradient blips used for phase do not generate significant artefacts despite in the former case reaching rates of change of gradient of 100 $\mathrm{Tm^{-1}s^{-1}}$. This is a consequence of the fact that the dominant spectral contribution to these gradient waveforms occurs at the ~ 900 Hz gradient switching frequency and harmonics of this frequency, which are well above the 250 Hz filter cut-off frequency used in the EEG recording. The effect of the low-pass filtering is also evident from the form of the average artefact trace. This shows that the gradient artefacts generated by each gradient ramping period of a few hundred microseconds persist over times of a few milliseconds in the EEG trace. The exact form of the artefact varies according to the positions of the electrodes and associated leads relative to the applied field gradients and indeed may change between scan sessions if the electrodes are not positioned identically within the scanner on each occasion. However the general features of the artefact waveforms described above are common to all channels.

In the cases where the gradient waveform is not synchronised with respect to the EEG sampling, the standard deviation of the voltage (Figure. 6.2D and 6.2E) can be seen to be largest at time points where the average gradient artefact waveform varies most rapidly with time - an effect that would be expected to result from small temporal shifts of the artefact waveform across repeated slice acquisitions. As a consequence, the standard deviation follows the modulus of the temporal derivative of the artefact waveform. Figure 6.2C shows that with synchronisation and appropriate choice of *TR* the standard deviation can be reduced to a few microvolts. The residual artefact presumably results from head movement leading to small changes in head position that affect the magnitude of the induced gradient artefact, and from digitisation noise (a value of 0.5 μV per bit was used in digitising the EEG signal).

The improvement in gradient artefact correction that can be achieved via synchronisation is also evident in the data shown in Figure 6.4. Although synchronisation clearly increases the level of artefact attenuation at all frequencies, the improved performance is more pronounced at higher frequencies (> 50Hz), which is in accordance with the findings of Mandelkow *et al [8]*. This is a consequence of the relatively rapid temporal variation of the residual artefact caused by timing errors (Figures 6.2D&E), so that the dominant residual artefact contribution occurs at high frequency. Table 6.1 illustrates the same overall findings as Figure 6.4 but averaged over all subjects. However, the results do not give such dramatic differences in values for the three situations as depicted in the figure for each individual subject. This is probably due to the fact this is a different measure of the effectiveness of synchronisation for improvement of artefact correction. Here, the standard deviation is that of the EEG signal, after gradient correction, calculated over time. Therefore the fluctuations measured will be partly due to brain activity as well as residual gradient artefacts.

Large gradient artefacts are evident in the raw ECG trace shown in Figure 6.5A. These tend to be larger than the gradient artefacts in recordings from the scalp electrodes for a number of reasons relating to the process of electromagnetic induction, and the fact that the ECG voltage is measured as the difference in potential between the reference lead positioned on the scalp and the ECG lead positioned at the base of the back. In particular, the long ECG lead length, the larger cross section of the torso compared with the head and the fact that the peak rate of change of magnetic field produced in the torso is larger than that occurring in the head, when the head is positioned at the gradient coils' isocentre, as is the case when imaging the brain, all act to increase the magnitude of the artefact in the ECG trace. The largest positive and negative amplitudes of the artefact are close to the ± 16.38 mV maximum voltages that can be sampled by the EEG system, and in the two other subjects studied here, this range was exceeded resulting in voltage clipping so that the ECG trace could not easily be gradient artefact corrected. In the case of the data shown in Figure. 6.5A, good correction of the gradient artefact was possible (Figure. 6.5B). In contrast to the raw ECG data, the VCG trace shown in Figure. 6.5C shows little evidence of gradient artefact. This results from the tighter low-pass filtering used in the recording, as well as the closer proximity of the electrodes and leads used to measure the VCG. The close proximity of the electrodes will reduce the emf induced within the system as the conducting loops will be smaller than in the case of the ECG system (refer to Chapter 5). It was consequently not necessary to apply gradient artefact correction to this trace. Comparison of Figures 6.5B and C also shows that by virtue of its relative insensitivity to the flow artefact, the VCG trace provides a clearer depiction of R-peaks. From experience this allows straightforward automatic calculation of R-peak marker timings for use in pulse artefact correction, whereas using the direct detection method on the ECG trace generally requires user intervention to reposition a large fraction of incorrectly positioned markers (often > 80 %).

The average pulse artefact waveform formed from two minutes of uncorrected data recorded from electrode TP10, which is plotted in Figure 6.6A, has a well defined form with a standard deviation that is relatively small compared with the magnitude of the average artefact voltage. Analysis of the average waveform generated from the corrected data shows that pulse artefact correction based on markers generated from a good ECG trace significantly attenuates the pulse artefact, with the peak to peak magnitude reduced from approximately 200 μV to around 70 μV (Figure 6.6B). The standard deviation of the waveform is relatively large however, indicating a significant amount of variation across cardiac cycles and thus suggesting that not all R peak markers were placed correctly. Using the markers from the VCG trace to correct the pulse artefact provides significantly improved artefact removal, with very little sign of residual artefact in the average waveform (Figure. 6.6C). This is evident from the small peak to peak voltage range of about 5 μV. The standard deviation of the corrected waveform is also reduced in magnitude and more constant over time, compared with Figure. 6.6B This demonstrates that the temporal positioning of the markers using the VCG trace was more precise, making the correction of the pulse artefact using this method more accurate.

Although this comparison is somewhat limited in scope, it is evident from the data presented that use of the scanner's VCG recording offers an alternative approach to identification of the time of onset of the pulse artefact where difficulties in obtaining an adequate quality ECG trace occur. This situation most commonly occurs due to saturation of the ECG amplifier by the large gradient artefacts. The main disadvantage of the VCG-based approach described here is that it relies on the use of a separate recording system which is currently linked to a particular scanner manufacturer's physiological recording system. It is likely however to be available from other manufacturer's scanners soon, making the VCG-based method accessible to a wider group of combined EEG/fMRI users. This approach has now been successfully used in other combined EEG/fMRI studies [16], including work at 7 T where the increased magnitude of the pulse artefact causes particular difficulties [17, 18]. Clearly by devoting more channels of the EEG system to recording the ECG signal, a VCG-like measurement could be made using a modified version of the EEG apparatus, and availability of a larger dynamic range would also limit the possibility of saturation of the amplifier by large artefacts induced on ECG leads. Implementation of a two lead measurement would allow reduced sensitivity to the gradient artefact, while four leads are likely to be required to reduce the amplitude of the flow artefact in the recording used for R-peak identification.

The advantages of the implementation of synchronisation in recording neuronal activity are evident from the data shown in Figure 6.7 and Table 6.2. From Figure 6.7A it is clear that driven activity can be detected at frequencies up to 60 Hz when synchronisation is employed, whereas the high frequency responses are difficult to detect in Figure. 6.7B, in which the neuronal response is obscured by the presence of many peaks resulting from residual gradient artefacts. Comparison of Figures 6.7C and D shows that these residual artefacts are not eliminated by subtraction of data acquired in the stimulus on and stimulus off periods. This is a consequence of the variability of the residual artefact resulting from the timing errors that occur when synchronisation is not employed. Interestingly, the small amount of residual artefact that is evident in both active and passive plots shown in Figure. 6.7A is significantly reduced in magnitude compared with the induced neuronal activity in the difference spectrum shown in Figure. 6.7C. This finding indicates that the residual artefact under these circumstances remains the same across a number of stimulus on and stimulus off periods. The most likely explanation for this finding is that the residual gradient artefact evident in Figure 6.7A results from changes in head position during the recording causing changes in the spatial form of the gradient artefact across electrodes, but that the head movement is slow enough for artefact fluctuations to persist on average over the 10 s stimulus cycle time leading to significant cancellation in the difference spectra.

These data illustrate that synchronisation is more important for measuring neuronal activity at the higher frequencies, as would be expected from the data shown in Figure 6.4. The contrast to noise measurements detailed in Table 6.2 illustrate that the implementation of synchronisation provides a significant and valuable increase of the contrast to noise by about a factor of two around the 60 Hz peak. The increase in magnitude of the residual artefacts with frequency that is displayed in Figure. 6.7D implies that a further gain in contrast to noise ratio might be expected at higher frequency. However, this expectation could not be tested here, as the visual stimulus employed did not elicit measurable activity at frequencies above 60 Hz, even when measurements were made outside the scanner. The ability to record EEG signals in this higher frequency range during simultaneous fMRI opens up the possibility of studying the haemodynamic correlates of evoked and spontaneous gamma activity. Further artefact suppression via post-processing methods, such as beam-former based analysis [16] may however be required and warrants further investigation. What is certain is that synchronisation will be an imperative step for the detection of this high frequency neuronal activity where a high SNR is necessary to detect it.

6.7 Conclusion

In conclusion, it has been shown that synchronisation of the EEG and MR scanner clocks [8] significantly improves the quality of the EEG data acquired in studies of neuronal function via combined EEG/fMRI, provided that the chosen *TR* is a multiple of the EEG clock period. The results indicate that the largest improvements occur *in vivo* at frequencies above about 50 Hz. This frequency range is not accessible in current combined EEG/fMRI experiments due to the use of strong, low-pass filtering which is needed to eliminate the residual gradient artefacts that are present when synchronisation is not employed [8]. It has also been shown that the VCG trace provides a viable alternative to a conventional ECG measurement for accurately detecting the timing of occurrence and subsequent correction of the pulse artefact in the EEG recording. The four lead VCG recording is less affected by gradient artefact and allows a trace that is relatively unaffected by the flow artefact to be formed and used for R-peak detection. Using synchronisation and pulse artefact correction based on VCG-derived markers, it has proved possible consistently to record visually-driven neuronal responses occurring at 60 Hz during combined EEG/fMRI experiments carried out at 3 T.

6.8 References

1. Goldman, R.I., J.M. Stern, J. Engel, and M.S. Cohen, *Simultaneous EEG and fMRI of the alpha rhythm.* Neuroreport, 2002. **13**(18): p. 2487-2492.
2. Laufs, H., K. Krakow, P. Sterzer, E. Eger, A. Beyerle, A. Salek-Haddadi, and A. Kleinschmidt, *Electroencephalographic signatures of attentional and cognitive default modes in spontaneous brain activity fluctuations at rest.* Proceedings Of The National Academy Of Sciences Of The United States Of America, 2003. **100**(19): p. 11053-11058.
3. Lemieux, L., A. Salek-Haddadi, O. Josephs, P.J. Allen, N. Toms, C. Scott, K. Krakow, R. Turner, and D.R. Fish, *Event-Related fMRI with Simultaneous and Continuous EEG: Description of the Method and Initial Case Report.* Neuroimage, 2001. **14**: p. 780-787.
4. Salek-Haddadi, A., K.J. Friston, L. Lemieux, and D.R. Fish, *Simultaneous EEG-Correlated Ictal fMRI.* Neuroimage, 2002. **16**: p. 32-40.
5. Allen, P.J., O. Josephs, and R. Turner, *A Method for removing Imaging Artifact from Continuous EEG Recorded during Functional MRI.* Neuroimage, 2000. **12**(2): p. 230-239.
6. Allen, P.J., G. Poizzi, K. Krakow, D.R. Fish, and L. Lemieux, *Identification of EEG Events in the MR Scanner: The Problem of Pulse Artifact and a Method for Its Subtraction.* Neuroimage, 1998. **8**(3): p. 229-239.
7. Naizy, R.K., C.F. Bechmann, G.D. Iannetti, J.M. Brady, and S.M. Smith, *Removal of fMRI environment artifacts from EEG data using optimal basis sets.* Neuroimage, 2005. **28**(3): p. 720-737.
8. Mandelkow, H., P. Halder, P. Boesiger, and D. Brandeis, *Synchronisation facilitates removal of MRI artefacts from concurrent EEG recordings and increases usable bandwidth.* Neuroimage, 2006. **32**(3): p. 1120-1126.
9. Pruessmann, K.P., M. Weiger, M.B. Scheidegger, and P. Boesiger, *SENSE: Sensitivity encoding for fast MRI.* Magnetic Resonance In Medicine, 1999. **42**(5): p. 952-962.
10. Chia, J.M., S.E. Fischer, S.A. Wickline, and C.H. Lorenz, *Performance of QRS detection for cardiac magnetic resonance imaging with a novel vectorcardiographic triggering method.* Journal of Magnetic Resonance Imaging, 2000. **12**(5): p. 678-688.
11. Fischer, S.E., S.A. Wickline, and C.H. Lorenz, *Novel Real-Time R-Wave Detection Algorithm Based on the Vectorcardiogram for Accurate Gated Magnetic Resonance Acquisitions.* Magnetic Resonance In Medicine, 1999. **42**: p. 361-370.
12. Philips, M.S., *Magnetic Resonance: Achieva Release 2.5 series. Application Guide: Volume 3: Cardiac Imaging.* 2007, Philips Medical Systems: Best, Netherlands.
13. Debener, S., M. Ullsperger, M. Siegel, K. Fiehler, D. Yves von Cramon, and A.K. Engel, *Trial-by-Trial Coupling of Concurrent Electroencephalogram*

and Functional Magnetic Resonance Imaging Identifies the Dynamics of Performance Monitoring. Journal of Neuroscience, 2005. **25**(50): p. 11730-11737.

14. Gonçalves, S.I., J.C. de Munck, P.J.W. Pouwels, R. Schoonhoven, J.P.A. Kuijer, N.M. Maurits, J.M. Hoogduin, E.J.W. Van Someren, R.M. Heethaar, and F.H. Lopes Da Silva, *Correlating the alpha rhythm to BOLD using simultaneous EEG/fMRI: Inter-subject variability.* Neuroimage, 2006. **30**(1): p. 203-213.

15. Laufs, H., A. Kleinschmidt, A. Beyerle, E. Eger, A. Salek-Haddadi, C. Preibisch, and K. Krakow, *EEG-correlated fMRI of human alpha activity.* NeuroImage, 2003. **19**(4): p. 1463-1476.

16. Brookes, M.J., K.J. Mullinger, C.M. Stevenson, P.G. Morris, and R.W. Bowtell, *Simultaneous EEG source localisation and artifact rejection during concurrent fMRI by means of spatial filtering.* NeuroImage, 2008. **40**(3): p. 1090-1104.

17. Debener, S., K.J. Mullinger, R.K. Niazy, and R.W. Bowtell, *Properties of the ballistocardiogram artefact as revealed by EEG recordings at 1.5, 3 and 7 Tesla static magnetic field strength.* International Journal of Psychophysiology, 2008. **67**(3): p. 189-199.

18. Mullinger, K.J., M.J. Brookes, C.M. Stevenson, P.S. Morgan, and R.W. Bowtell, *Exploring the feasibility of simultaneous EEG/fMRI at 7 T.* Magnetic Resonance Imaging, 2008. **In Press**.

Chapter 7

Effect of Simultaneous EEG recording on MRI Data Quality

7.1 Introduction

Chapters 5 and 6 have demonstrated the large amount of work that has been, and continues to be, carried out, with the aim of reducing the artefacts in EEG recordings made in combined EEG and fMRI studies. This work has of course, been imperative in making it possible to combine these imaging techniques. In contrast, as discussed in Chapter 5, the study of the degradation of MR images due to the presence of the EEG equipment has been somewhat neglected since it has proved possible to acquire fMRI data in the presence of EEG equipment without making significant modifications to the MRI techniques or hardware. However, as simultaneous EEG and fMRI is applied across more areas of research, it is important to understand fully the effect that the combined approach has on the quality of the data acquired using both modalities.

Here, the aim was to characterise the artefacts generated in MR images by the presence of commercially available EEG recording hardware as a function of field strength and number of electrodes. To enable a full investigation of the sources of image degradation it is important to understand the physical mechanisms which are likely to cause the effects observed.

7.2 Background and Theory

The review of work which relates to this area of research in Chapter 5 showed that the majority of studies have concentrated on the characterisation of artefacts in fMRI data due to the EEG system, rather than exploration of the mechanisms underlying the degradation of image quality, with investigations being somewhat qualitative in nature. There are a number of possible sources of degradation of MR images, the most important being: (i) magnetic susceptibility effects; (ii) the perturbation of the RF fields involved in excitation and detection of the MR signal.

7.2.1 Magnetic susceptibility effects (B_0-inhomogeneity) and detection

The EEG cap causes susceptibility effects if the wires, electrodes or conductive gel have a significantly different magnetic susceptibility, χ, from the tissues of the head. Although the differences in magnetic susceptibility are likely to be small ($\chi \approx 0$ for air, $\chi = -9\times10^{-6}$ for water and $\chi = -9.2\times10^{-6}$ for copper), the resulting field deviation can cause a significant variation in the NMR resonance frequency, ω. This is because

$$B = (1+\chi)\mu_0 H \tag{7.1}$$

(where H is the magnetic field intensity and B is the magnetic flux density) and:

$$\omega = \gamma B \tag{7.2}$$

where γ is the magnetogyric ratio which is equal to 42.58MHz/T for ^{1}H nuclei. Therefore a small change in the local magnetic field due to a change in magnetic susceptibility can lead to a significant variation in ω, causing spins to dephase. Consequently the presence of the EEG electrodes and leads can introduce artefacts in MR images due to the magnetic field inhomogeneity. These artefacts take two main forms. First, field inhomogeneities may cause image distortion. If we take the average field offset due to the changes in χ to be ΔB_0 and the range of fields across a slice to be δB_0 then

$$\Delta\omega_0 = \gamma\Delta B_0$$

and

$$\delta\omega_0 = \gamma\delta B_0 \tag{7.3}$$

where $\Delta\omega_0$ is the average frequency offset and $\delta\omega_0$ is the frequency range across the slice. If $\Delta\omega_0/2\pi$ is similar in magnitude or greater than the frequency separation of pixels (typically 10-50 Hz in echo planar images) distortion of the image will occur. The other effect that may occur is signal drop-out. If the variation in frequency across the imaging slice is large, the signal in gradient echo images will be reduced as the spins will dephase causing signal reduction. Significant dephasing and consequent signal loss will occur in gradient echo images if the product of $\delta\omega_0$ and TE approaches 2π in magnitude. Clearly the extent of signal drop-out and image distortion resulting from magnetic susceptibility effects depends upon how greatly the magnetic susceptibilities of the materials used differ and the spatial arrangements of electrodes and leads with respect to the subject's head and applied field.

To characterise the extent of the magnetic susceptibility effects on the images, it is helpful to acquire B_0 maps. A 3D Gradient Echo (GE) sequence can be used to provide this information. As discussed in earlier chapters, GE sequences are sensitive to magnetic susceptibility effects as unlike spin echo sequences they do not employ a 180° RF refocusing pulse, making them ideal for creating the B_0 maps required. Instead of using a 180° RF pulse to refocus the spins and create the echoes; the echoes, and therefore image, are created by gradient reversals. Figure 7.1 illustrates, in 2D, how changes in the local field cause changes in the local phase of the image.

Gradient echo sequence contrast is therefore weighted by a factor of e^{-t/T_2^*} where

$$\frac{1}{T_2^*} = \frac{1}{T_2} + \frac{1}{T_2'} \qquad [7.4]$$

and T_2' is inversely proportional to the magnetic field inhomogeneity in each imaging voxel. A typical pulse sequence diagram for 3D-GE imaging is shown in Figure 7.2. By taking the phase and modulus images from this sequence one can obtain information about B_0 variation and therefore estimate the magnitude of susceptibility effects on the MR images.

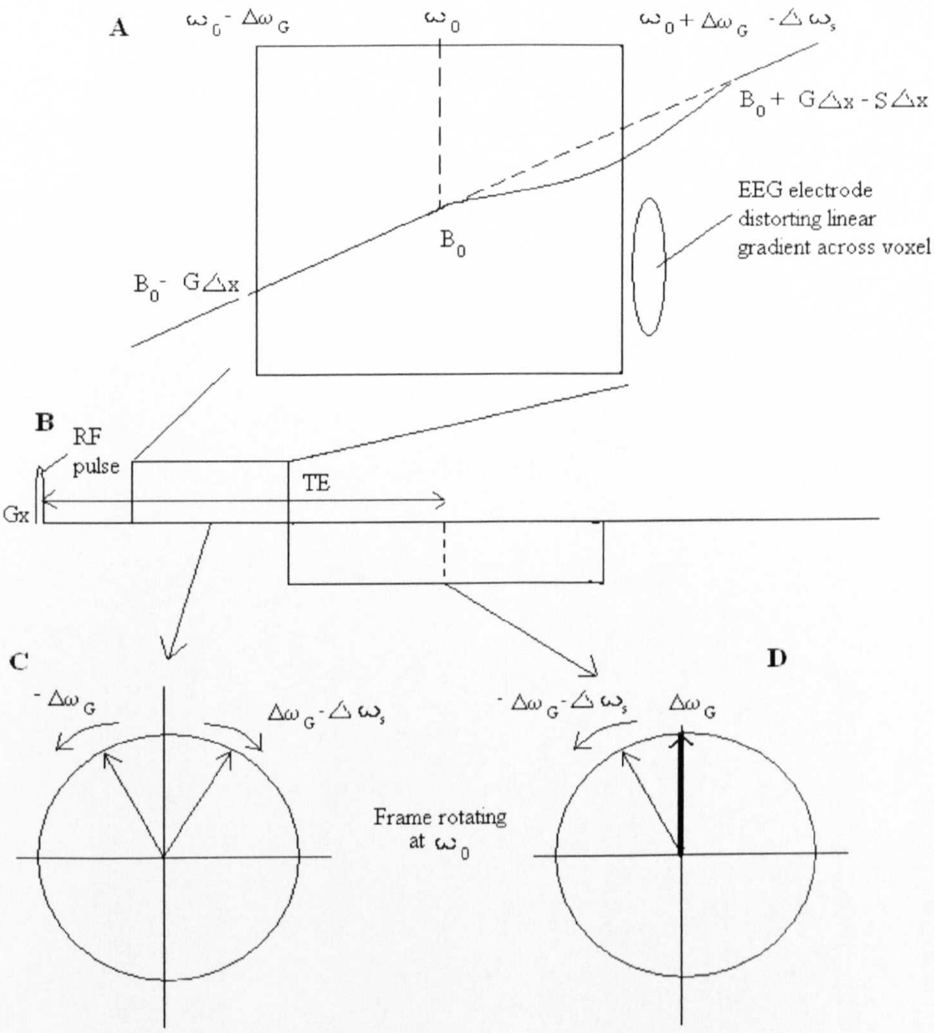
A
$\omega_0 - \Delta\omega_G$
ω_0
$\omega_0 + \Delta\omega_G - \Delta\omega_s$
$B_0 + G\Delta x - S\Delta x$
EEG electrode distorting linear gradient across voxel
B_0
$B_0 - G\Delta x$
B
RF pulse
TE
Gx
C
D
$-\Delta\omega_G$
$\Delta\omega_G - \Delta\omega_s$
$-\Delta\omega_G - \Delta\omega_s$
$\Delta\omega_G$
Frame rotating at ω_0

Figure 7.1: A schematic diagram to demonstrate what happens to the spins in a single voxel in a GE sequence with the read gradient applied in the x-direction. A: The variation of the B_0 field across the voxel due to the applied gradient, G, leads to a change of $\Delta\omega_G$ in the resonant frequency of the spins and added variation due to the magnetic susceptibility effect field, S, leads to a further change, $\Delta\omega_s$ in the resonant frequency of the spins. B: The gradient applied to produce the gradient echo C: The spins begin to dephase according to the local magnetic field therefore some will precess faster that others depending on the susceptibility effects local to those spins. D: After the gradient reversal dephasing due to the applied gradient, G is reversed. However the effect of the magnetic susceptibility will not change and therefore some spins will go beyond the starting point, the resultant signal in the image will therefore be reduced.

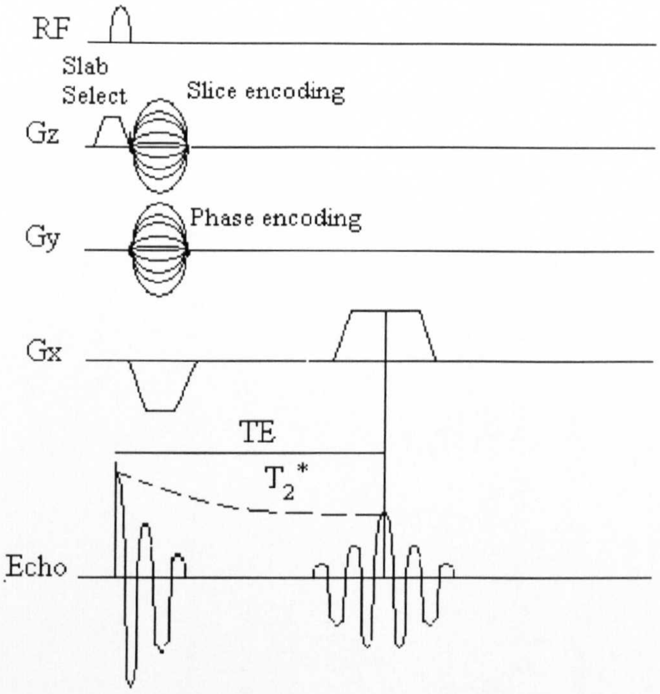

Figure 7.2: A pulse sequence diagram for 3D-GE imaging.

Phase and modulus images can be obtained by virtue of the fact that MR images are acquired using phase-sensitive detection. Detection of the NMR signal after the application of a RF pulse often involves phase-sensitive detection (PSD), which means using two receivers operating in quadrature. The reason for this method of detection is the way the NMR signal evolves. During the application of an RF pulse, of duration τ and strength B_1, along the x-axis in the rotating frame, the magnetisation rotates in the zy' plane through an angle $\theta=\gamma B_1\tau$ resulting in the magnetisation, M, of the system at the start of acquisition being transformed into the following state:

$$\begin{aligned} M_x &= 0 \\ M_y &= M_0 \sin\theta \, . \\ M_z &= M_0 \cos\theta \end{aligned} \qquad [7.5]$$

The evolution of the signal can then be described by the Bloch equations:

$$
\begin{aligned}
M_x &= M_0 \sin\theta \sin(\omega_L t) \exp\left(\frac{-t}{T_2}\right) \\
M_y &= M_0 \sin\theta \cos(\omega_L t) \exp\left(\frac{-t}{T_2}\right) \\
M_z &= M_0\left[1-(1-\cos\theta)\exp\left(\frac{-t}{T_1}\right)\right]
\end{aligned}
$$

[7.6]

where ω_L is the Larmor frequency, as described in Chapter 2. A receiver that is sensitive to the y-component of the magnetization will detect an induced emf, V_{NMR} that is proportion to M_y therefore:

$$
V_{NMR} \propto M_y = M_0 \sin\theta \cos(\omega_L t) \exp\left(\frac{-t}{T_2}\right).
$$

[7.7]

The signal is clearly oscillating and will decay with the time constant T_2, and is known as a free induction decay (FID).

The PSD works by the multiplication of V_{NMR} with a reference signal V_{ref} followed by integration of the product over a period δt ($\omega_L \delta t >> 1$). Assuming the reference signal is also oscillating, then V_{ref} can be written as $V_{ref} = 2\cos\omega t$. Therefore integrating over the product gives a detected signal of:

$$
\begin{aligned}
V_1 &= \int_{t-\delta t}^{t} V_{NMR} V_{ref}\, dt \\
&= \int_{t-\delta t}^{t} M_0 \sin\theta \exp\left(\frac{-t}{T_2}\right) 2\cos(\omega_L t)\cos(\omega t) dt \\
&= M_0 \sin\theta \exp\left(\frac{-t}{T_2}\right)\left\{ \int_{t-\delta t}^{t} \cos((\omega_L+\omega)t) dt + \int_{t-\delta t}^{t} \cos((\omega_L-\omega)t) dt \right\}.
\end{aligned}
$$

[7.8]

Since the integral is evaluated over many cycles of the waveform and $(\omega_L+\omega)\delta t$ is large then the first term will be close to zero. Conversely, if the frequency $(\omega_L-\omega)$ is sufficiently small compared with the reciprocal of the integration time $(\delta t)^{-1}$ the term $\cos((\omega_L-\omega)t)$ will be approximately constant over the period of integration. Therefore Equation 7.8 can be approximated to:

$$V_1 = M_0 \sin\theta \exp\left(\frac{-t}{T_2}\right)\cos((\omega_L - \omega)t)\delta t\,.$$

[7.9]

Most spectrometers also employ a second PSD which is in quadrature (*i.e.* *π/2* out of phase) with the first detector. This gives a second output, V_2 which is given by:

$$V_2 = M_0 \sin\theta \exp\left(\frac{-t}{T_2}\right)\sin((\omega_L - \omega)t)\delta t\,.$$

[7.10]

V_1 and V_2 therefore reflect the x and y components of the transverse magnetisation in the rotating frame. Since these are two quadrature components, the full FID can be described as a complex quantity

$$\begin{aligned} F(t) &= V_1(t) + iV_2(t) \\ &= M_0 \sin\theta \exp\left(\frac{-t}{T_2}\right)(\cos(\omega_L - \omega)t + i\sin(\omega_L - \omega)t) \\ &= M_0 \sin\theta \exp\left(\frac{-t}{T_2}\right)\exp(i(\omega_L - \omega)t) \end{aligned}$$

[7.11]

As the signal contains a real and imaginary part in the form $c=a+ib$, the phase image can be obtained from the fact that $\tan\theta=a/b$ and the modulus image can be obtained from $\sqrt{(a^2+b^2)}$.

7.2.2 B$_1$-Inhomogeneity

The other main cause of signal changes and global variation in SNR is perturbation of the RF magnetic field. As the RF pulse is a time-varying magnetic field, $B_1(t)$, then distortion of the B_1 field will effect the angle by which the spins are flipped. This is because, as discussed in Chapter 2, the flip angle, α, and the B_1 field are related by

$$\alpha = \gamma B_1 \tau$$

[7.12]

where τ is the length of time the RF pulse is applied for. Therefore by varying the time that the RF pulse is applied for, or the magnitude of B_1, the angle through which the magnetization will be tipped will vary, thus changing the strength of the signal that is subsequently produced. As the NMR signal used to create the MR image is dependent on the amount of transverse magnetisation generated by the RF pulse, when the B_1 field varies spatially unwanted spatial variation of the signal intensity will be produced. The strength of the signal received from a given region is also dependent on the value of B_1 in that region and can give rise to further intensity variation in the presence of any spatial inhomogeneity of B_1.

When materials of high electrical conductivity are exposed to RF, large surface current densities which act to screen the RF field from the interior of the material are generated. These currents also disturb the B_1-field in regions that are in close proximity to the conductor. Consequently it can be expected that electrically conducting material in EEG caps will cause some perturbation of the B_1-field, leading to artefactual intensity variation in MR images. In addition, the interaction between the RF field and conducting material increases the effective resistance of the RF coil. Since a resistance acts as a source of noise, this effect can lead to a reduction in the SNR of images obtained in combined EEG/fMRI studies [1].

The final cause of disturbance to the RF field will occur if the wires of the EEG cap have a length which is close to a multiple of half wavelengths of the RF since a standing wave may then be set up in the wire. In this situation, the RF pulse will be strongly perturbed by the wire and therefore again distort the B_1 field. To excite the spins the frequency of the applied RF pulse must be chosen to match ω, this frequency is known as the Larmor frequency, ω_L. From Equation 7.2 it is clear that the frequency and therefore the wavelength of the RF pulse will depend upon the B_0 field applied and therefore it is possible that the resonant effect will occur in the wire at one field strength only.

There is also the possibility that the gradient switching during MRI will cause eddy currents to be set up in the conductive materials of the EEG cap thus producing magnetic fields, which might distort the image. However, these effects are minimised by using small electrodes and preventing large, highly conducting loops being formed in the cap design by weaving the wires intot he cap and twisting them together.

Here, the aim was to characterise the artefacts generated in MR images by the presence of commercially available EEG recording hardware as a function of field strength and number of electrodes. Experiments were conducted using 32 and 64 electrode caps on Philips Achieva MR systems operating at 1.5, 3 and 7 T. They were carried out on both human volunteers and a phantom to investigate the effects of the EEG cap on MR images. Use of MR-based, B_0 and B_1 mapping techniques allowed assignment of the source of artefacts whilst analysis of image SNR from EPI data sets allowed the identification of the severity of the effect on data typically used in fMRI experiments.

7.3 Methods and Analysis

Data were acquired from human subjects (5 in total) and a spherical phantom on Philips Achieva MR systems operating at 1.5, 3 and 7 T. Each subject was scanned at all three field strengths to allow direct comparisons between data acquired on each of the scanners to be made. The body RF coils were used for signal excitation at 1.5 and 3 T, while eight channel, head RF coils were used for signal reception at these fields. A quadrature birdcage coil was used for signal excitation and reception at 7 T. The plastic-walled, spherical phantom used for these experiments had an 18 cm outer diameter and 17 cm inner diameter. It was filled with saline, doped with Gd-DTPA so as to yield a T_1 of approximately 700 ms at 3 T, similar to that of white matter [2]. Images were acquired in the presence of 32 and 64 electrode MR-compatible EEG lycra caps (EasyCap: Herrsching, Germany) and with no cap in place. Both EEG caps employed sintered Ag/AgCl ring-electrodes arranged in an equidistant montage. Electrodes, with a 1.2 cm outer diameter and 0.6 cm inner diameter, including plastic adapters and 5 kΩ resistors, and light-duty braided copper wires, with an approximate diameter of 0.3 mm, were used for connection to BrainAmp MR EEG amplifier(s) (Brainproducts, Munich, Germany) during MR scanning. Abralyte 2000 conductive and abrasive gel was used to apply the electrodes to the scalp or phantom surface. The quantity of gel placed between the electrodes and the surface of the phantom was equivalent to the amount typically used when EEG recordings are acquired from human subjects (<1 ml per electrode). A thin layer of the conducting gel was spread over the surface of the phantom to mimic the effect of the scalp in human subjects. The ECG and EOG leads were also connected to the "face" of the phantom (as shown in Figure 7.3).

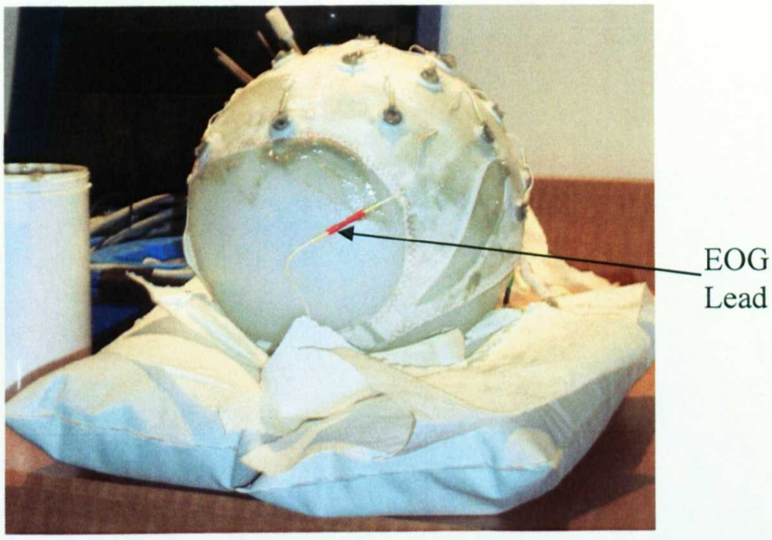

Figure 7.3: The positioning of the EEG cap on the phantom with the path of the EOG lead shown.

Four different imaging procedures were carried out.

(i) B_0 maps were generated using 3-D spoiled GE data acquired with 2 mm isotropic resolution using an echo time of 20 ms and TR=23 ms at all field strengths. The resulting phase maps were unwrapped (to allow for magnetisation rotating through angles greater than 2π during the TE period) and then scaled by $2\pi TE$ to yield maps of the field offset in Hz ($1\text{Hz}=2.35\times10^{-8}\text{T}$). The phase unwrapping technique used here is described by Saad *et al [3]*. This a simple technique whereby phase images are divided into sections according to discontinuities in the image and then 2π is added or subtracted to the sections to form a continuous image. Subsequently field variations occurring on a large length scale (*e.g.* due to poor shimming) were eliminated by subtracting a smoothed version of the field map (formed from a 2nd order polynomial fit) on a plane by plane basis. This emphasized the effects of the EEG electrodes and wires which produce more localised field inhomogeneity that was not eliminated by the fitting procedure.

(ii) RF inhomogeneity was assessed by generating 3-D flip-angle maps using a pulsed, steady-state sequence to measure the effects of RF inhomogeneity. This sequence uses two RF pulses of the same flip angle, α, followed by delays TR_1 and TR_2 where $TR_1 < TR_2 << T_1$ with gradient echoes then used to create signals S_1 and S_2 (Figure 7.4) [4]. The way in which this sequence allows measurement of the flip angle is described below.

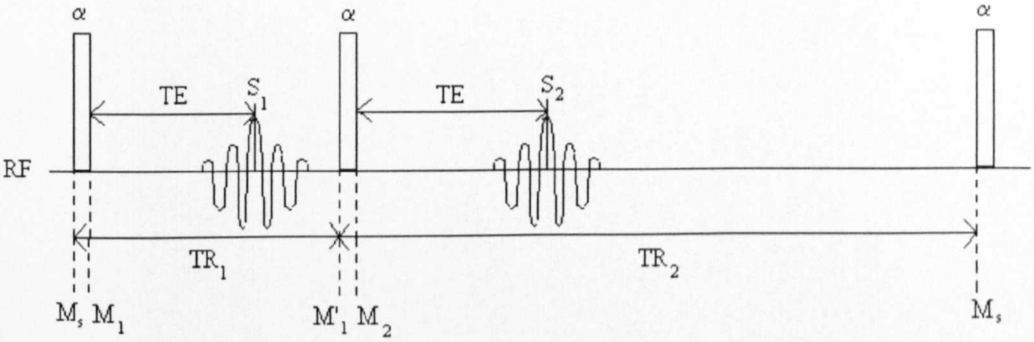

Figure 7.4: A diagram of the RF pulses involved in a double-delayed spoiled gradient echo (DD-SPGR) pulse sequence.

Following the nomenclature in Figure 7.4 [5] it is known that before the first RF pulse in each repetition of the sequence the longitudinal magnetisation has a steady state value, M_s. After application of the first RF pulse in the sequence, the longitudinal magnetisation, M_1 is given by:

$$M_1 = M_s \cos\alpha \, . \tag{7.13}$$

The transverse component is refocused with a gradient echo to produce a signal at time TE given by:

$$S_1 = M_s K \sin\alpha \tag{7.14}$$

where $K = exp(-TE/T_2^*)$.

Since the longitudinal magnetisation just preceding the second RF pulse must be equal to M_1 if $TR_1=0$ and following the form of the Bloch equation for M_z given in Equation 7.6 then the longitudinal magnetisation immediately preceding the second RF pulse is:

$$M_1' = M_0(1-E_1)+M_sE_1\cos\alpha$$

[7.15]

where $E_1=exp(-TR_1/T_1)$.

Spoiler gradients remove any transverse coherences at the end of TR_1. Consequently the longitudinal magnetisation immediately after the second RF pulse is given by:

$$M_2 = M_1'\cos\alpha\ .$$

[7.16]

The transverse signal from the second RF pulse is again sampled as a gradient echo at a time *TE* after this second RF pulse and has the value:

$$S_2 = M_1'K\sin\alpha\ .$$

[7.17]

The longitudinal magnetisation at the end of the TR_2 interval must equal the steady state longitudinal magnetisation at the beginning of the sequence, M_s. Also if $TR_2=0$ then $M_s=M_2$. Therefore following the pattern of Equation 7.15 the magnetisation at the end of the relaxation time TR_2 must have the value

$$M_s = M_0(1-E_2)+M_1'E_2\cos\alpha$$

[7.18]

where $E_2=exp(-TR_2/T_1)$.

Substituting Equation 7.15 into the above and expanding yields:

$$M_s = M_0(1-E_2)+M_0E_2(1-E_1)\cos\alpha+M_sE_1E_2\cos^2\alpha\ .$$

[7.19]

Rearranging to get M_s gives:

$$M_s = M_0\left[\frac{(1-E_2)+E_2(1-E_1)\cos\alpha}{1-E_1E_2\cos^2\alpha}\right].$$

[7.20]

To obtain the normalised signal level, S_1/M_0 Equation 7.20 is substituted into 7.14 and after rearrangement gives:

$$\frac{S_1}{M_0} = K\sin(\alpha)\left[\frac{(1-E_2)+E_2(1-E_1)\cos\alpha}{1-E_1E_2\cos^2\alpha}\right].$$

[7.21]

Similarly, to obtain the normalised signal level S_2/M_0 Equation 7.15 is substituted into 7.17 to give:

$$S_2 = K\sin(\alpha)[M_0(1-E_1)+M_sE_1\cos\alpha]$$

[7.22]

which after substitution of Equation 7.20 into the above and rearrangement yields

$$\frac{S_2}{M_0} = K\sin(\alpha)\left[\frac{(1-E_1)+E_1(1-E_2)\cos\alpha}{1-E_1E_2\cos^2\alpha}\right].$$

[7.23]

The ratio of the signals, R, is then:

$$R = \frac{S_2}{S_1} = \frac{(1-E_1)+E_1(1-E_2)\cos\alpha}{(1-E_2)+E_2(1-E_1)\cos\alpha}.$$

Assuming that the first order approximation can be applied to the exponential terms then expanding the above ratio produces:

$$R = \frac{(TR_1/T_1)+(TR_2/T_1)\cos\alpha-(TR_1/T_1)(TR_2/T_1)\cos\alpha}{(TR_2/T_1)+(TR_1/T_1)\cos\alpha-(TR_1/T_1)(TR_2/T_1)\cos\alpha}$$

[7.24]

since second order terms and higher are being ignored as $TR_1<TR_2<<T_1$ Equation 7.24 can be simplified to give:

$$R = \frac{1+n\cos\alpha}{n+\cos\alpha}$$

[7.25]

where $n=TR_2/TR_1$, such that the ratio of signal intensities is independent of the relaxation times T_1 and T_2. Therefore rearranging Equation 7.25 to find the flip angle, α one obtains:

$$\alpha = \cos^{-1}\left[\frac{Rn-1}{n-R}\right]$$

[7.26]

which can be now used to calculate the flip angles throughout the image.

This sequence was implemented on each of the scanners using a pulse sequence written by David Foxhall of Philips Medical Systems [5]. Data were acquired on a single volunteer and on the phantom. Flip angle maps with 2 mm isotropic resolution were generated with TR_1=12ms and TR_2=60ms, and with a nominal flip angle setting of 60°. Each scan took approximately 20 minutes.

MATLAB (Mathworks Inc.) scripts, also written by David Foxhall [5], were used to calculate the flip angle from the data obtained, using Equation 7.26. The problem of division by zero when creating these maps was overcome by only calculating values for regions where the signal in both the images created was greater than four times the standard deviation in a region of the images lying outside the head or phantom. Images were normalised using the average flip angle over the object of interest thus allowing more straightforward identification of any regions significantly affected by RF inhomogeneities. The standard deviation of the normalised flip angle was calculated to characterise the magnitude of variation across the phantom at each field strength.

(iii) A standard multi-slice EPI sequence was implemented with a 64×64 matrix, TR=4.2s, flip angle of 85° and isotropic voxel size (phantom: 3mm; head: 3.3 mm) with no slice gap using echo times conventionally employed at each field strength (1.5 T: 60ms; 3 T: 40ms; 7 T: 25ms [6]). The number of slices was chosen to allow for full head or phantom coverage (45 and 52 slices respectively) and the pixel bandwidth in the phase-encode direction was set to approximately 28 Hz at all field strengths. Data were acquired on 5 human subjects (2 female, 3 male with a mean age of 29) as well as on the phantom with fifty volumes acquired for each arrangement (32, 64 electrode and no cap). After motion correction, using MCFLIRT within FSL, registering to the central volume and high-pass filtering, using a square filter with a cut off at 0.033Hz, to remove any scanner drift, the SNR of the data was assessed by pixel-wise calculation of the ratio of the temporal standard deviation to mean. This ratio was then averaged over appropriately defined ROI's giving a measure of the temporal SNR within that region. ROI's of approximately 800 voxels in size (reduced to 400 voxels at 7 T to avoid regions of significant drop-out) were positioned in white matter (WM) and in locations showing minimal signal dropout due to either B_1 or B_0 inhomogeneity thus providing a measure of reduction in the global image SNR due to loading of the RF coil by the conducting material in the EEG leads and electrodes.

The extent of signal loss due to field inhomogeneity from the caps was also measured in the EPI data acquired from the phantom. This was done by counting the number of pixels within masked regions of the images, whose intensity fell below 5 or 10 % of the mean value within the phantom. Two different masked regions were employed: the first covered the entire spherical phantom, while the second covered the whole phantom except for a 1.1 cm thick layer at its surface. The second region was chosen to provide an indication of signal drop-out effects in the brain due to EEG electrodes and wires positioned on the scalp, and consequently separated from brain tissue by about 1 cm on average [2].

(iv) The effect of the EEG recording apparatus on anatomical images, acquired using a standard MPRAGE sequence [7] with SENSE factor 2, was also assessed. These images had 1.1 mm isotropic resolution and 282 mm FOV in all directions. The slices covered the whole head or phantom. The resulting images were then surface rendered to show the effects of the wires and electrodes on the surface of a 3D image.

All imaging procedures were carried out on the phantom for both caps at the three field strengths. EPI and MPRAGE data were acquired from the head at all field strengths for both caps, but B_0 and flip-angle mapping was not carried out at any field strength using the 64 channel cap on the human head due to concerns over potential RF heating. For the same reason B_0 and B_1 mapping was not carried out at 7 T on the human head with the 32 electrode cap in place.

7.4 Results

The vast quantity of images acquired makes it difficult to show all the data that were collected. Representative slices from the phantom and head have therefore been identified and are displayed. However, the values which are displayed in the tables of this chapter are calculated using all of the data collected which was relevant to each calculation.

7.4.1 B_0-Inhomogeneity:

Figure 7.5 shows field maps which were acquired from similar axial slices at the three field strengths with the 64 and 32 electrode caps and no cap in place. Localised field inhomogeneity resulting from individual electrodes, which increases in severity with field strength, is evident in these maps. This behaviour is also apparent from Table 7.1 which details the standard deviation of the field offset, in Hz, and the range of fields within which 95 % of pixel values within the phantom lie for the different arrangements. An increase in field offsets due to the presence of the cap is not as clear in data acquired from the human subject at 3 T (Figure 7.6(A&B)), due to the fact that the inhomogeneities from the electrodes are highly localised and therefore are likely to only penetrate the scalp and skull rather than the brain. The dominant source of field perturbation instead appears to be susceptibility variations across the tissues of the head. Even in the phantom, other sources of field inhomogeneity such as air bubbles and the plastic screw used for sealing the sphere cause significant residual field inhomogeneity in the absence of the EEG caps (Figures 7.5 C, F &I).

Field Strength (Tesla)	64 Electrode Cap		32 Electrode Cap		No Cap	
	95 percentile range	Standard deviation	95 percentile range	Standard deviation	95 percentile range	Standard deviation
1.5	27	7.9	33	9.6	16	5.5
3.0	30	9.4	35	9.7	16	5.6
7.0	57	14	50	13	47	12

***Table 7.1:** The 95 percentile range and standard deviation of B_0 field offset values (in Hz, to 2 significant figures) measured in the entire phantom after the removal of low spatial frequency field variations.*

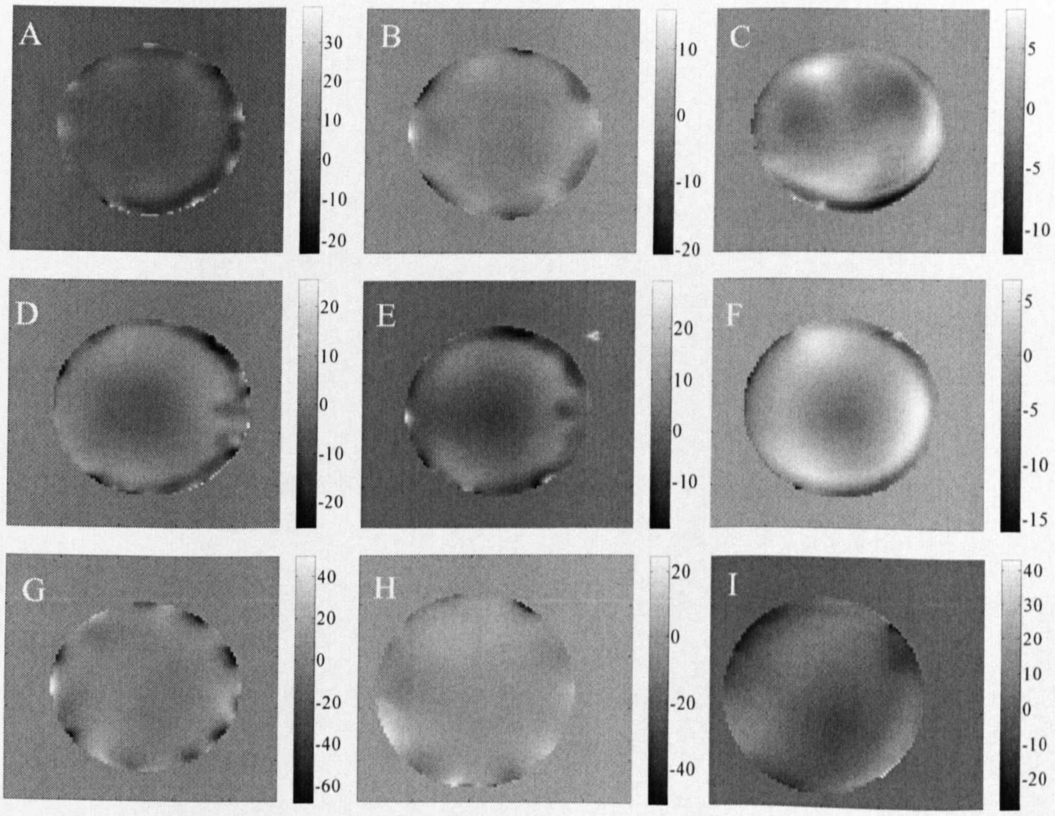
A
30
20
10
0
-10
-20
B
10
0
-10
-20
C
5
0
-5
-10
D
20
10
0
-10
-20
E
20
10
0
-10
F
5
0
-5
-10
-15
G
40
20
0
-20
-40
-60
H
20
0
-20
-40
I
40
30
20
10
0
-10
-20

***Figure 7.5:** B_0 field maps (in Hz) acquired from the phantom, shown after removal of large scale field variations at 1.5 T (A-C), 3 T (D-F) and 7 T (G-I) with the 64 electrode cap (left) 32 electrode cap (centre) and no cap (right) on.*

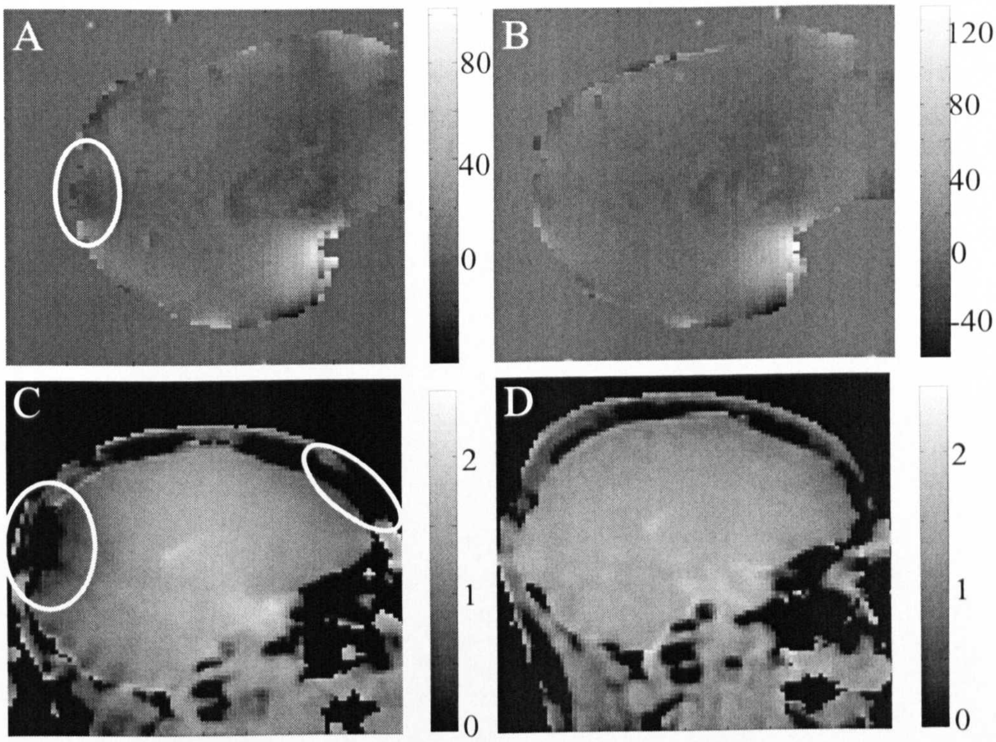

Figure 7.6: Effects of 32 electrode cap at 3 T on B_0 maps (in Hz) (A&B) and flip angle maps (normalised to average flip angle) (C&D). A&C were acquired with the cap on (regions affected are highlighted) and B&D are with no cap. Data were acquired from the same subject with B_1 and B_0 maps acquired in the same scan session for each situation.

7.4.2 B_1-Inhomogeneity:

Figure 7.7 shows normalised flip angle maps acquired from the phantom at 1.5, 3 and 7 T in the presence of the 32 and 64 electrode caps along with no cap in place. Figures 7.7A-C show maps acquired from similar axial slices to those displayed in Figure 7.5D-F. Comparison of Figures 7.7A (64 electrode cap), B (32 electrode cap) and C (no cap) indicates that the presence of individual electrodes does not cause significant B_1 inhomogeneity. However, the cap's presence causes a significant increase in the spatial variation of the flip-angle produced in the phantom, as shown by the increased standard deviations of relative flip angle in Table 7.2. This effect can be related to Figures 7.7D-L which show the flip angle variation in a more inferior axial slice close to the paths of the ECG and EOG leads. These images reveal a greater cap-induced flip angle inhomogeneity which increases with field, becoming much worse at 7T.

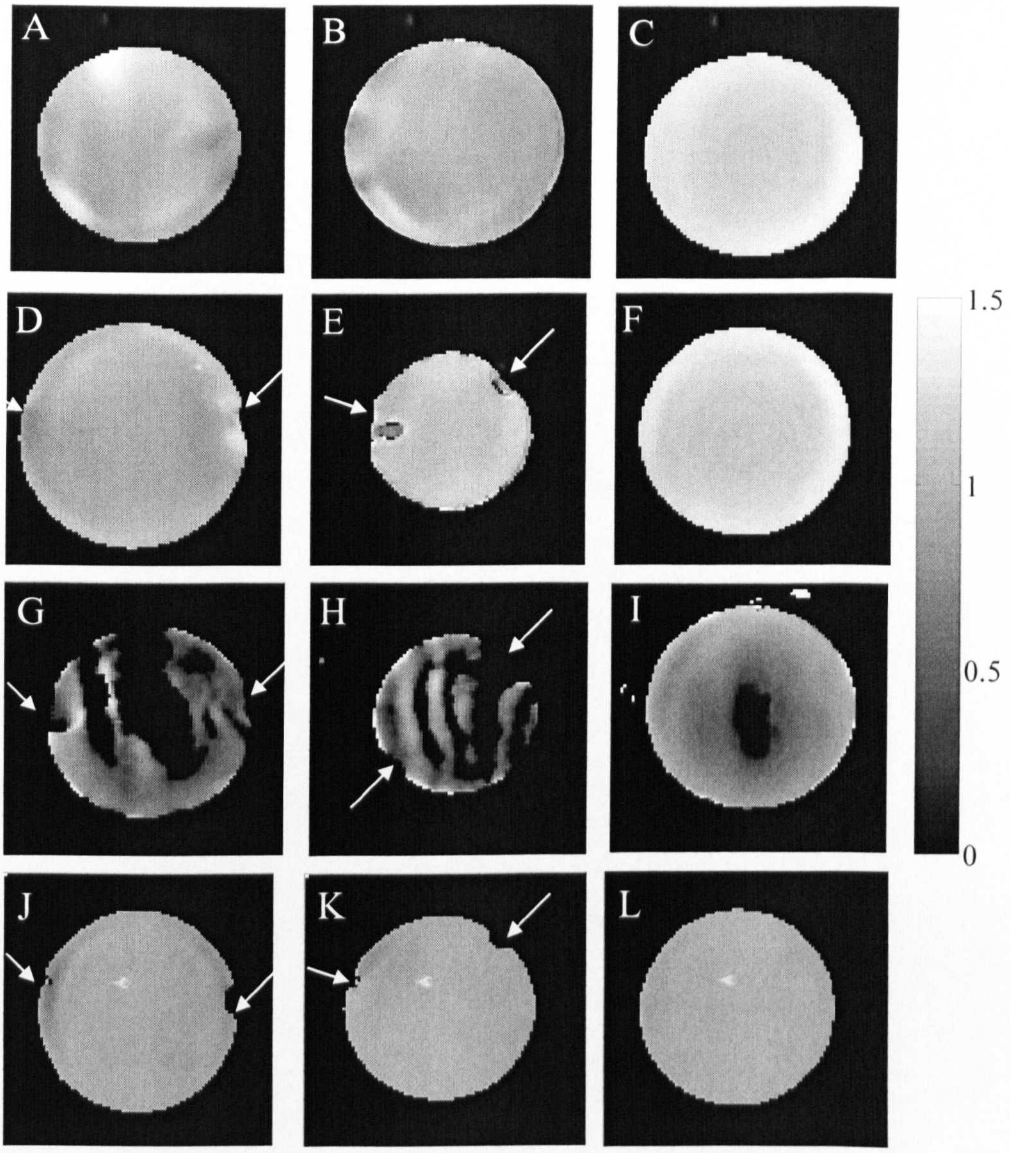

Figure 7.7: Flip angle maps of the phantom (scaled by the nominal flip angle) with the 64 electrode cap (left), the 32 electrode cap (centre) and no cap (right). A-C show maps acquired at 3 T from similar slices to that shown in Fig. 7.5. The maps shown in the rest of figure are taken from more inferior slices and show the effect of B_1 perturbations occurring in proximity to the ECG and EOG wires (highlighted) at 3 T (D-F), 7 T (G-I) and 1.5 T (J-L). A more inferior slice is shown for the 64-electrode cap compared with the 32-electrode cap as the path of the EOG and ECG wires was different on these caps. The thresholding process described in Section 7.3 leads to the generation of significantly sized areas in the 7 T maps where the flip angle can not be characterised.

Field Strength (Tesla)	64 Channel	32 Channel	No Cap
1.5	0.05	0.08	0.02
3.0	0.12	0.16	0.08
7.0	0.44	0.43	0.34

Table 7.2: Standard deviation of relative flip angle within the phantom.

This effect also occurs in the head where a significant reduction in flip angle is seen in occipital and frontal areas (Figures 7.6 C&D). These areas are in proximity to the ECG and EOG leads which are significantly longer than the leads linked to the other cap electrodes (58 and 20 cm longer respectively than the Tp9 lead). The corresponding B_0 maps (Figure 7.6 A&B) do not show large field gradients in these areas, indicating that signal reduction found close to these leads is unlikely to be due to B_0 field inhomogeneity .

7.4.3 MPRAGE data

The path of the ECG and EOG leads, as well as individual electrode positions, could be identified in the 3 T MPRAGE images of the head, shown in Figure 7.8. Signal reduction underlying these longer leads causes artefactual indentations in the surface of the volume-rendered images, as highlighted in Figures 7.8A and B.

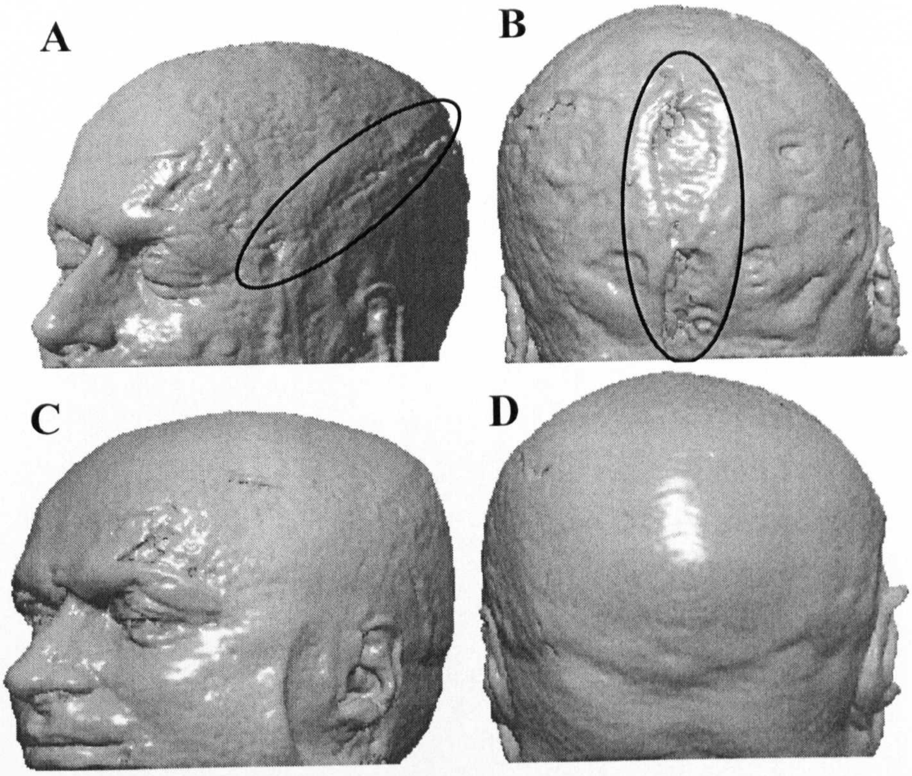

Figure 7.8: Effect of 32 electrode cap at 3 T on 3D surface rendered MPRAGE images. A&B: Images with 32 electrode cap, highlighted regions are the paths of the EOG (A) and ECG (B) wires. C&D: The same images with no cap in place.

7.5.3 Effects of Caps on EPI data:

Figure 7.9 shows images of a similarly positioned single slice extracted from multi-slice EPI data sets acquired from the phantom at 1.5, 3 and 7 T with the 32 and 64 electrode caps in place and with no cap present. It is evident that the ring electrodes cause small regions of signal drop-out at the periphery of the phantom, as a result of local B_0-field inhomogeneities that can be seen in the field maps of Figure 7.5. Similar effects occur for electrodes in the two caps, but a greater proportion of the periphery is affected by the 64 channel cap because of the larger number of electrodes.

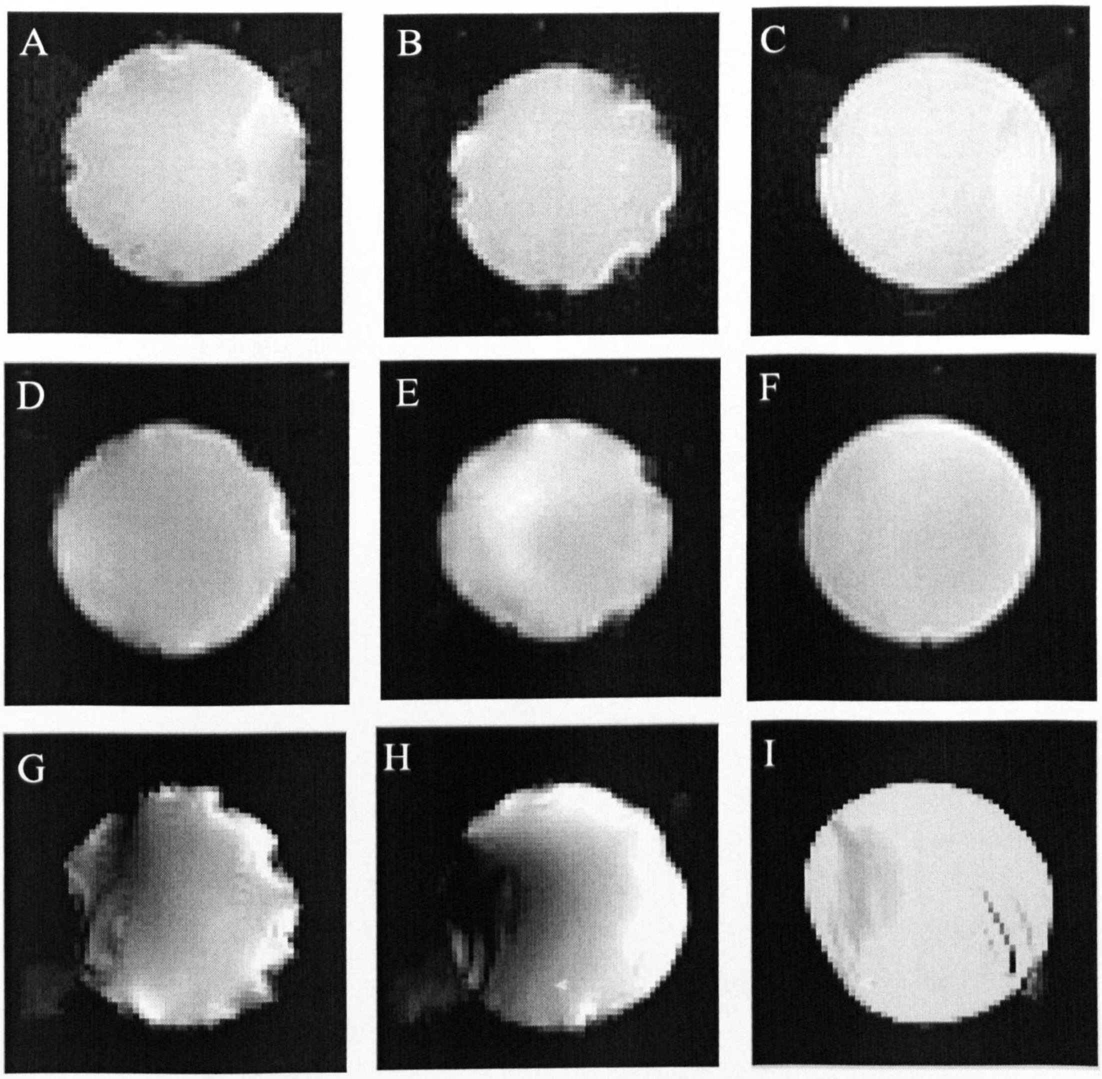

Figure 7.9: EPI data of a similar slice of the phantom at 1.5 T (A-C), 3 T (D-F) and 7 T (G-I) with 64 electrode cap (left), 32 electrode cap (centre) and no cap on (right).

These effects are localised and mainly manifest themselves in the scalp and skull rather than the brain itself and hence cannot clearly be seen in the EPI data from the human subject, as illustrated in Figure 7.10.

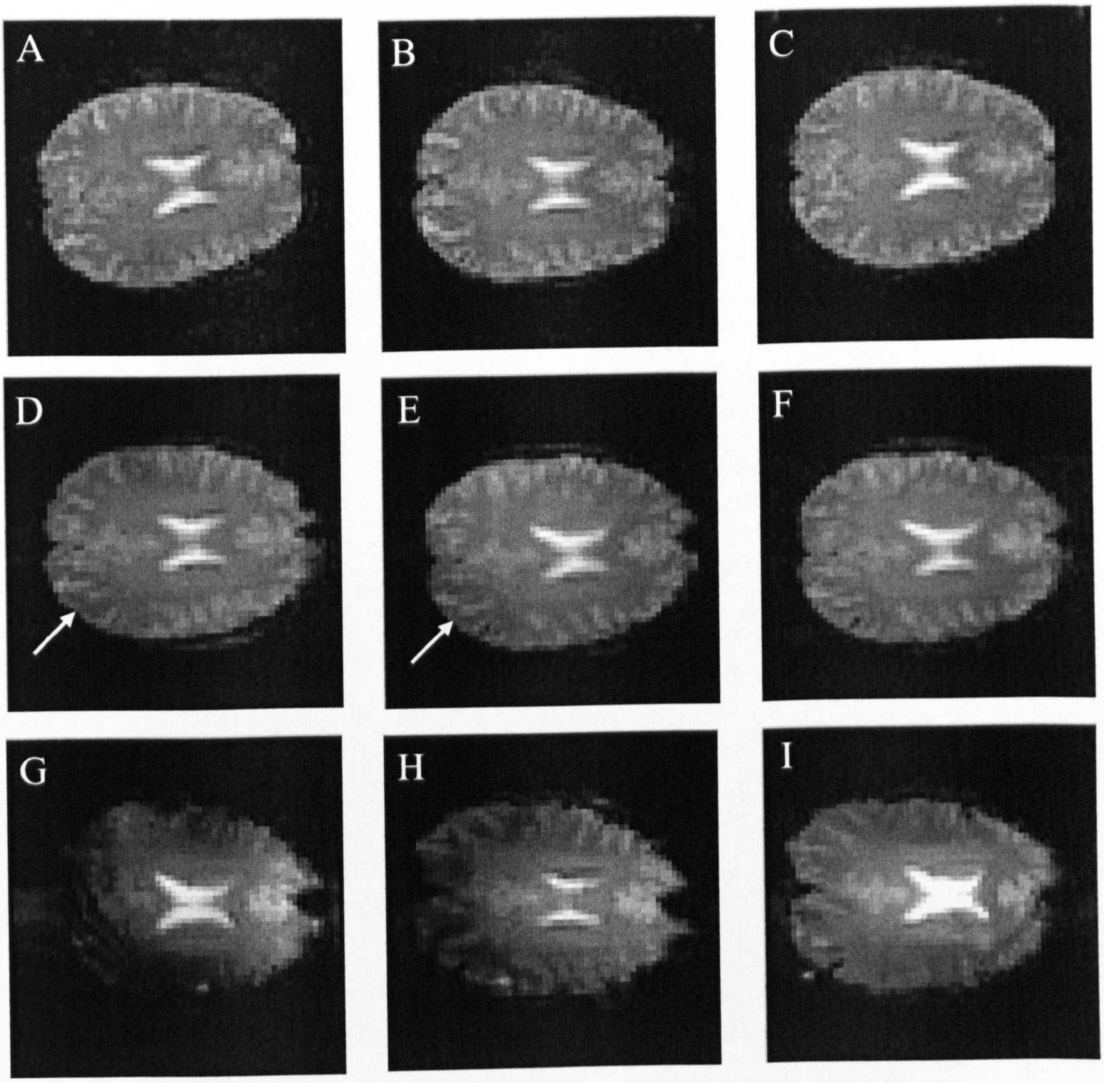

Figure 7.10: Representative slice of EPI data for a single subject at 1.5 T (A-C), 3 T (D-F) and 7 T (G-I) with 64 electrode cap (left), 32 electrode cap (centre) and no cap (right) on.

The dominant effect at 7 T due to the presence of the caps is an exacerbation of the large scale intensity variation, resulting from increased B_1 inhomogeneity. Although this effect is less obvious in the data acquired at lower field, there was a slightly reduced signal intensity in the left occipital lobe at 3 T, as highlighted in Figure 7.10 D&E due to the ECG lead perturbing the B_1 field.

7.5.3.1 SNR:

Table 7.3 details the ratio of the temporal standard deviation to average signal averaged over the white matter ROI for each arrangement, along with the percentage change in this ratio due to the presence of either the 32 or 64 electrode caps. The values quoted are the averages over the five subjects studied.

Field Strength (Tesla)	No Cap	32 Channel	% Change	64 Channel	% Change
1.5	0.0166±0.0007	0.0214±0.0005	27±8	0.0225±0.0004	26±10
3.0	0.0097±0.0001	0.0102±0.0004	4±4	0.0106±0.0002	14±5
7.0	0.0076±0.0003	0.0089±0.0002	18±4	0.0097±0.0007	28±13

Table 7.3: Average ratio of temporal standard deviation:mean in a WM ROI in EPI data. The percentage change indicates the reduction in SNR due to each of the caps. Values were calculated by averaging over all subjects with the relative error of these values then found.

7.5.3.2 Signal Dropout

Field (T)	Masked region	64 Channel		32 Channel		No Cap	
	Threshold	5%	10%	5%	10%	5%	10%
1.5	**Whole Phantom**	0.010	0.027	0.010	0.023	0.012	0.028
	Inner Region	0	0.00010	0.00031	0.0014	0.000080	0.00036
3.0	**Whole Phantom**	0.051	0.078	0.015	0.029	0.012	0.021
	Inner Region	0.0024	0.0059	0.00016	0.00085	0.0010	0.0025
7.0	**Whole Phantom**	0.10	0.16	0.11	0.17	0.027	0.044
	Inner Region	0.086	0.14	0.11	0.18	0.014	0.023

Table 7.4: EPI data were used to measure the signal dropout due to each cap on the phantom. The table shows the ratio of the number of pixels lost relative to the total number within the phantom when the images are thresholded to exclude voxels with less than 5% or 10% of the mean pixel intensity. The masked region spanned either the whole phantom or an inner region excluding a 1 cm thick spherical shell at the periphery of the phantom.

The reduction in flip angle caused by the B_1 and B_0 inhomogeneities due to the presence of the caps has been shown to result in a loss of signal in EPI data. Table 7.4 characterises this signal dropout in the EPI data collected from the phantom.

7.5 Discussion

The B_0 field maps acquired from the phantom (Figure 7.5) show that each electrode generates significant local perturbation of the magnetic field, the exact form of which depends on the orientation of the electrode with respect to the field. Similar affects were produced by individual electrodes in the two caps, but a greater proportion of the periphery was affected by the 64 electrode cap because of the larger number of electrodes. The data reported in Table 7.1 shows that the presence of the EEG cap increases the width of the distribution of field values within the phantom and that the width is increased at higher field strength. Although, it might be expected from Equation. 7.3 that the values in Table 7.1 would scale linearly with field strength, the fact that they increase less rapidly with field probably reflects the higher performance of the shimming systems used in the 3 and 7 T scanners, which limits to some extent the increase in field inhomogeneity at the higher fields. The distribution widths are not strongly affected by the number of electrodes. This is probably because the greater overlap of the fields from the different electrodes in the case of the 64 electrode cap slightly reduces the depth into the phantom that the field inhomogeneities extend, counterbalancing the increased surface area of the phantom over which inhomogeneities are produced. Such behaviour results from the dipolar nature of the field perturbation from each individual electrode, producing regions of both increased and reduced field, whose overlap in the case of multiple electrodes leads to a reduction of the depth to which the field perturbation extends. The local field gradients that are evident in Figure 7.5 generate localised areas of signal drop-out and distortion at the surface of the phantom in the echo planar images shown in Figure 7.9, which are most severe in the images acquired at high field. The electrodes do not however cause significant drop-out in the echo planar images of the brain shown in Figure 7.10. This is a result of the localised nature of the field inhomogeneities which consequently do not extend from the site of electrodes at the scalp into the brain. The field maps obtained from the human subject at 3 T (Figures

7.6 A&B) bear out this observation, as they display little noticeable effects of the electrodes relative to the larger field inhomogeneities generated by the head itself (particularly the sinuses).

The effects of B_1 inhomogeneity pose more significant problems for image data quality in the case of the EEG caps studied here. Table 7.2 shows that the introduction of either EEG cap causes a noteworthy increase in the standard deviation of the relative flip angle within the phantom. The flip-angle maps shown in Figure 7.7 indicate the dominant source of B_1 inhomogeneity is not the electrodes, but rather the EOG and ECG leads. This is also evident from the MPRAGE data acquired from the human subject (Figure 7.8) where the presence of these leads causes an artefactual indentation of the scalp in the volume-rendered data. The exact reason that these leads cause a much stronger local perturbation of the B_1 field than the other leads needs further investigation. However any explanation is likely to relate to the main distinguishing feature of these leads compared with those attached to other electrodes, which is their greater length: the ECG and EOG leads used here are 58 and 20cm longer respectively than the Tp9 lead. The fact that there are significant effects at all three field strengths means that the interaction is unlikely to be a resonant effect where the lead length matches an integral number of half wavelengths of the RF, since this wavelength changes by a factor of 4.67 between 7 and 1.5 T.

At 7 T where RF must be applied at 300 MHz it is evident from Figure 7.7I that the spherical phantom itself causes significant flip-angle inhomogeneity. This is a well known phenomenon at high-field, which results from the increased effects of electrical conductivity and relative permittivity on the applied electromagnetic fields when the RF wavelength approaches the size of the object being imaged [8]. Addition of the conducting material of the cap, and particularly the EOG and ECG leads then causes a further significant degradation of the B_1 homogeneity which is clearly seen in Figures 7.7G&H.

The flip angle maps obtained from the human subject at 3 T (Figures 7.6C&D) show that the effects of the EOG and ECG leads on B_1 homogeneity are also manifested in the human head, leading to areas of flip angle reduction in occipital and frontal areas.

The effect of the ECG lead is seen as an area of reduced signal intensity in the EPI data obtained at 3 T (Figures 7.10D&E), an effect which we have noted in a number of other previous studies. The effects of much greater B_1 inhomogeneity are evident in the EPI data acquired from the phantom (Figures 7.9G-I) and the human head (Figures 7.10G-I) at 7 T. In the latter case, introduction of the EEG caps leads to a further increase of the signal intensity at the centre of the head relative to that at the periphery. These effects lead to spatial variation in the sensitivity of detection of activation in fMRI data analysis, as observed in the experiments described in Chapters 8 and 9. In particular a larger fractional BOLD signal change is needed in areas of signal drop-out for identification of statistically significant signal changes.

Table 7.4, which characterises the signal drop-out that occurred in the echo planar images of the spherical phantom (Figure 7.9), shows that at 1.5 and 3 T the majority of the signal loss occurs at the periphery of the phantom so that the fraction of pixels affected is much smaller when only the inner region rather than the whole phantom is considered. Signal drop-out at these fields mainly reflects the effect of B_0 inhomogeneity, which as discussed above is confined to regions close to the electrodes, and increases with field strength. Table 7.4 also shows that at 7 T, the signal drop out caused by the introduction of the caps is more severe and is not limited to regions at the surface of the phantom, since the fraction of voxels lost in the whole phantom is similar to that found when considering just the inner region. This is a consequence of the dominance of the effect of EEG-cap-induced B_1 inhomogeneity at the higher field.

Table 7.3, which details the ratio of temporal standard deviation to average signal intensity in a white matter ROI, shows that the SNR increases with field strength with or without the EEG cap in place, as would be expected [9]. The decrease in SNR due to the presence of the EEG cap at 1.5 T found here is in agreement with the findings of Lazeyras [10] where a change of approximately 26% was found due to the presence of 16, silver plated, gold electrodes. The increase in SNR is greater between 1.5 T and 3 T compared with 3 T to 7 T, this is most likely because the relatively large voxel sizes used here mean that at 7 T the increased importance of physiological noise [11] moderates the gain in intrinsic SNR. Table 7.3 also shows that the conducting material in the caps reduces the SNR, with the 64 electrode cap having a significantly larger effect than the 32 electrode cap at 3 and 7 T. The change in SNR due to the presence of the conducting materials of the cap appears to be lowest at 3 T. Assuming that the NMR signal strength is unaffected by the presence of the cap the change in the SNR depends largely on the ratio of the magnitude of the extra noise due to the cap's loading of the RF coil to the magnitude of other noise sources. Both would be expected to increase with field strength, but it appears that between 1.5 and 3 T the latter increases more rapidly, whilst between 3 and 7 T the increase in cap-induced noise is greater; this can be visualised in the schematic diagram of Figure 7.11. In the case of the data acquired at 7 T, it is possible that introduction of the cap has also somewhat reduced the signal strength due to the direct effects of B_1 inhomogeneity or indirect effects in mis-setting of the flip angle.

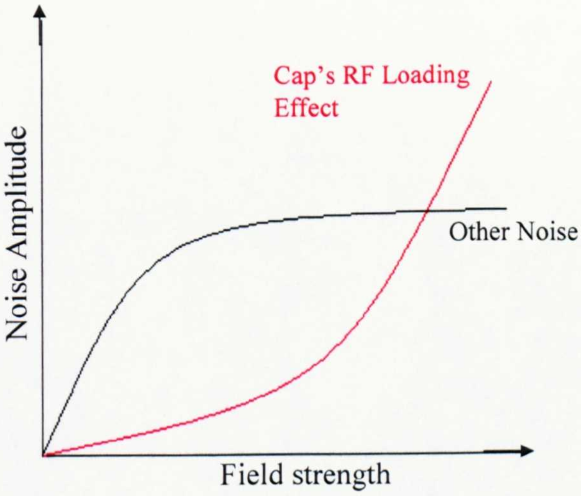

Figure 7.11: A schematic diagram to show how noise sources effect the SNR of EPI data with field strength.

It is worth noting that the reduction in SNR due to the EEG caps was relatively small even in the worst case (64 electrode cap at 7 T) and that the use of a WM region, in which the physiological noise is lower than in grey matter, along with the relatively long *TR* used for this experiment to allow for whole head coverage and the large voxel size, gives these data a high base SNR, leading to a high sensitivity to cap-induced changes. The results described here are similar to those previously reported by Vasios *et al* [12] who described a 12% reduction in WM SNR due to their 32-channel ink-cap system, and Scarff *et al [1]* who showed a reduction of about 30 %

in SNR in WM at 3 T when comparing MR data acquired with 64 and 256 electrodes in place, using a different EEG cap system.

Given the findings here, it can be concluded that image quality is affected by the number of electrodes in the EEG cap and the field that is used. The SNR is reduced by the presence of the cap with the reduction increasing as the number of electrodes increases. However, the SNR with the cap on at 7 T is comparable to that with no cap at 3 T, and similarly for 3 T and 1.5 T, so reduction in SNR could be overcome by using higher field strengths when combining these imaging techniques. The signal dropout increases with field strength, but the work described here indicates that this is likely to be mainly due to the longer ECG and EOG wires causing B_1 inhomogeneity. This dropout problem therefore could possibly be overcome by increasing the flip angle used in the EPI sequence and therefore increasing the signal from the affected regions. This has the disadvantage of increasing the SAR levels, however, as well as reducing the SNR in the rest of the image. Another possible solution to this problem is to modify the cap design so that the ECG and EOG leads do not run in close proximity to the head. With the methods described in Chapter 6 where the VCG can be used to record the cardiac cycle, the ECG lead is superfluous and therefore could be removed altogether, thus improving image quality in the occipital lobes.

7.6 Conclusion

Using B_0- and B_1-mapping techniques we have measured the static and RF magnetic field inhomogeneities generated by commercially available 32 and 64 electrode EEG caps at three different field strengths. The resulting field maps have been used to explain the artefacts produced by the caps in echo planar images of the kind which would normally be used in combined fMRI/EEG experiments.

The results indicate that the electrodes are the dominant source of B_0 field inhomogeneity, but the localised nature of the field perturbation that they produce means that the effect on the signal intensity from the brain is not significant relative to the field inhomogeneity produced by the head itself. In the particular EEG caps investigated here, RF inhomogeneity linked to the longer EEG and EOG leads does have a weak effect on the signal intensity in echo planar images of the brain acquired at 3 T and this effect merits further investigation. Use of higher resistance material (*e.g.* carbon or ink rather than copper) in lead fabrication might be expected to reduce the interaction with the RF field. At 7 T the introduction of either a 32 or 64 electrode caps causes a significant deterioration of the B_1 homogeneity, which is already relatively poor even in the absence of the EEG system. This effect also appears to be linked to the longer EEG leads, as the B_1 homogeneity is less affected in superior regions. It is worth noting that techniques for the amelioration of the effects of B_1 inhomogeneity at high field are actively being developed [8, 13] and could also be employed to overcome the effects of EEG caps on the B_1 field.

Measurements of the standard deviation of white matter signal in EPI time series indicate that the introduction of the EEG cap causes a small reduction in the image SNR, which increases with the number of electrodes in agreement with previous findings [1]. Despite the increased effect of B_0 and B_1 inhomogeneities, the SNR in the EPI data obtained at 7 T from the human brain is still greater than that obtained with no cap in place at 3 T, indicating that attempts to implement simultaneous EEG and fMRI recording at 7 T are very worthwhile [12, 14] as discussed further in Chapter 8. However, difficulties in recording good quality EEG data at this higher field strength must also be considered and therefore presently 7 T may not be the optimal environment for conducting combined EEG-fMRI experiments.

7.7 References

1. Scarff, C.J., A. Reynolds, B.G. Goodyear, C.W. Ponton, J.C. Dort, and J.J. Eggermont, *Simultaneous 3-T fMRI and high-density recording of human auditory evoked potentials.* Neuroimage, 2004. **23**: p. 1129-1142.
2. Lu, H., L.M. Nagae_Poetscher, X. Golay, D. Lin, M. Pomper, and P.C.M. van Zijl, *Routine Clinical Brain MRI Sequences for use at 3.0 Tesla.* Journal of Magnetic Resonance Imaging, 2005. **22**: p. 13-22.
3. Saad, N. and S. Peled. *Easy 3D Phase Unwrapping.* in *ISMRM: 13th Annual meeting.* 2005. Miami.
4. Yarnykh, V.L. and C. Yuan. *Actual Flip Angle Imaging in the Pulsed Steady State.* in *Proceedings of ISMRM.* 2004. Kyoto, Japan.
5. Foxhall, D., *IR:B1 Mapping.* 2005, Philips Medical Systems: Cleveland. p. A manual of how the B1 mapping patch and associated MATLAB scripts were created.
6. Van der Zwaag, W., *Techniques for High-performance fMRI,* in *Sir Peter Mansfield Magnetic Resonance Centre, School of Physics and Astronomy.* 2006, University of Nottingham: Nottingham. p. 190.
7. Mugler, J.P. and J.R. Brookeman, *3-Dimensional Magnetization-Prepared Rapid Gradient-Echo Imaging (3dmp-Rage).* Magnetic Resonance In Medicine, 1990. **15**(1): p. 152-157.
8. Adriany, G., P.F. Van de Moortele, F. Wiesinger, S. Moeller, J.P. Strupp, P. Andersen, C. Snyder, X.L. Zhang, W. Chen, K.P. Pruessmann, P. Boesiger, T. Vaughan, and K. Ugurbil, *Transmit and receive transmission line arrays for 7 Tesla parallel imaging.* Magnetic Resonance In Medicine, 2005. **53**(2): p. 434-445.
9. Edelstein, W.A., G.H. Glover, C.J. Hardy, and R.W. Redington, *The Intrinsic Signal-to-Noise Ratio in NMR Imaging.* Magnetic Resonance In Medicine, 1986. **3**(3): p. 604-618.
10. Lazeyras, F., I. Zimine, O. Blanke, S.H. Perrig, and M. Seeck, *Functional MRI with simultaneous EEG recording: Feasibility and application to motor and visual activation.* Journal of Magnetic Resonance Imaging, 2001. **13**(6): p. 943-948.
11. Krueger, G. and G. Glover, *Physiological noise in oxygenation-sensitive magnetic resonance imaging.* MAGNETIC RESONANCE IN MEDICINE, 2001. **46**(4): p. 631-637.
12. Vasios, C.E., L.M. Angelone, P.L. Purdon, J. Ahveninen, J. Belliveau, and G. Bonmassar, *EEG/(f)MRI measurements at 7 Tesla using a new EEG cap ("InkCap").* Neuroimage, 2006. **33**(4): p. 1082-1092.
13. Katscher, U. and P. Bornert, *Parallel RF transmission in MRI.* NMR In Biomedicine, 2006. **19**(3): p. 393-400.

14. Mullinger, K.J., M.J. Brookes, C.M. Stevenson, M. Clemence, P.S. Morgan, C.P. Nockowski, S. Profusz, and R.W. Bowtell, *Exploring the feasibility of simultaneous EEG/fMRI at 7T.* Proc. ISMRM 2007, 2007.

Chapter 8

Combining EEG with fMRI at 7T: What is Possible?

8.1 Introduction and Background

Chapter 6 has shown that the combination of EEG with fMRI is feasible in the environment of a high field scanner. As already discussed, the combination of these techniques has been put to a wide range of uses [1-6] with the scope of applications for these combined techniques ever growing. This chapter aims to explore the advantages of conducting simultaneous EEG-fMRI at 7T. This has involved the careful consideration of subject safety and data quality. A number of experiments are described which investigate the feasibility of simultaneous EEG-fMRI at 7 T. Following the presentation of results obtained from phantoms, further experiments performed on human subjects are detailed. These allow the presentation, for the first time, of data showing simultaneous detection of neuronal activity by both modalities at ultra-high field strength using commercially available equipment.

The vast majority of combined EEG/fMRI studies described in the literature have been carried out on MR scanners operating at fields of 1.5 and 3 T. It has however been demonstrated that it is highly advantageous to use ultra-high field (7 T), for fMRI studies. In particular, it has been shown that there is an increase in the overall BOLD contrast to noise ratio with field strength making it easier to detect small activations at higher fields [7] due to elevated sensitivity to susceptibility effects. It has also been established that there is a higher sensitivity to activity in tissue and a reduced sensitivity to the effect of large draining veins with increasing field strength, which leads to a higher spatial resolution of BOLD effects at higher field strength. This phenomenon results from the fact that the T_2 of blood at 7 T is much shorter than that of grey matter whereas at 1.5 T the blood has a T_2 that is comparable or longer than that of grey matter. Therefore, intravascular BOLD effects cannot be selectively reduced by choosing longer *TE*s at low field, but can at higher field strengths [8]. The reduction of large signals from the draining veins allows subtler changes in grey matter to be detected using higher fields as well as providing increased spatial resolution [9]. Finally Gati *et al.* have shown that the signal to noise ratio increases linearly with field strength, as previously predicted by Edelstein *et al [10]*. These factors all result in a significantly increased BOLD contrast to noise ratio (CNR) [9, 11], thus indicating that the implementation of fMRI at ultra-high field is desirable. However, when considering BOLD imaging at higher field strengths it is also important to consider the effect of physiological noise on the SNR of the time course. Natural fluctuations due to respiration, cardiac and other physiological noise sources that aren't fully understood yet also increase with field strength. Therefore although the image SNR will increase linearly with field strength the physiological noise results in a reduction from a linear relationship between temporal SNR and field strength as shown by Krueger *et al [12, 13]*. Triantafyllou *et al [14]* showed that at a given spatial resolution the ratio of the physiological noise to thermal noise always increased with field strength. However, this effect was reduced by moving to smaller voxel sizes showing that at high field strength smaller voxels are advantageous for the collection of high temporal SNR fMRI data.

Implementation of combined EEG/fMRI studies at 7 T would therefore offer valuable enhancement of the fMRI data quality and is therefore well worth pursuing [15]. There are however, a number of technical and safety issues which have to be addressed, with regards to placing the EEG system in an increased static magnetic field, before EEG studies can be conducted simultaneously with fMRI data acquisition at 7 T. By increasing the field strength one will clearly encounter larger artefacts in the EEG recording due to motion and blood flow effects. The motion artefacts will increase in magnitude since

$$e.m.f. = -\frac{d\phi}{dt} \qquad [8.1]$$

where ϕ is the rate of change of flux and as the B_0 field increases there will be a greater density of flux lines resulting in an increase in the magnitude of the voltage produced by electromagnetic induction due to movement of conducting material in a larger magnetic field. Therefore any movement of the subject's head during scanning causes larger artefacts in EEG recordings and also any vibrations of the conducting elements of the EEG system will generate larger interference than at lower field strengths. Induced voltage increases may also result from the use of larger gradient strengths and higher gradient slew rates in scanning procedures: an increase which may be required to ameliorate the greater effects of magnetic susceptibility that arise at high field. The pulse artefact also increases with increasing field strength [16]. This is because it is believed that some, if not all, of the pulse artefact is due to movement of the head as well as movement of the electrodes due to the pulsation of the scalp. The blood flow effect, which is due to the movement of charged particles (the blood) within a magnetic field, also increases with static magnetic field strength. This phenomenon is characterised by the Hall Effect which can be characterised by:

$$V = dBv \tag{8.2}$$

where V is the induced voltage, B is the magnetic field (in Tesla), d is the diameter of the vessel and v is the average blood velocity perpendicular to the field [17]. It is clear from this equation that the voltage produced from the flow of blood will increase as the field increases thus producing larger artefacts in EEG recordings. Adoption of measures that limit the amplitude of these unwanted voltages at source or which subsequently attenuate their magnitude in recorded EEG data via post-processing methods is therefore of even greater importance when working at 7 T compared with lower field.

One must also consider safety issues when using EEG caps at higher magnetic field. We know from previous chapters that the RF magnetic field is tuned to the Larmor frequency, ω_L, which increases with B_0 (Equation 2.15). The higher frequency at higher field strength means that a greater RF power must be used to generate a given B_1-field strength, while the reduction in RF wavelength may lead to elevated interactions of the applied RF with the electrodes and wires of the EEG system. The result of these interactions is a greater potential for heating as described by Lemieux *et al. [18]*. The main effects are induced heating in current-limiting resistors and heating due to the eddy currents in the electrodes and gel, both these phenomena occurring due to the RF field. The first problem can be overcome by correctly choosing the resistor values to be compatible with the RF field that will be applied as:

$$\Delta T_s = R_{th} \frac{V_{rms}^2}{R}$$

[8.3] from [18]

where ΔT_s is the surface temperature rise in the steady state (which should not exceed 20 °C [18]), R_{th} is the thermal resistance, V_{rms} is the rms voltage (which can be derived from the SAR, and is therefore related to the RF power) and R is the chosen resistance. The second potential cause of heating, eddy currents, causes the rate of change of temperature in and around the electrodes to vary according to:

$$\frac{dT}{dt} = \frac{\sigma}{c\rho}\left({dB_1}/{dt} \right)^2 G$$

[8.4] from [18]

where c is the heat capacity, σ is the conductivity and ρ is the density of the electrode, *G* is a geometric factor which takes into account the volume and area of the conductor (for example, for a disk electrode of radius r then $G=r^2/8$ [19]) and *dB/dt* is the rate of change of the magnetic component of the RF field. Therefore as the frequency of the RF field increases to match the Larmor frequency, the temperature change would rapidly increase if the magnitude of B_1 were kept constant across B_0 field strengths. However, this is not the case, since as shown in Table 8.1, the available B_1 field decreases with increasing B_0 on the scanners used in this work. Consequently the potential for heating due to eddy currents does not significantly increase with field strength. Table 8.1 also illustrates the maximum gradient switching values given the worse case scenario, with the electrodes positioned 10 cm from the magnet's isocentre. This shows the relative heating due to gradient switching compared with that of the RF pulses is insignificant. The heating tests carried out by Lemieux *et al.* were only conducted at 1.5 T and it was concluded that with correct precautions combined EEG and fMRI could be carried out safely. Although the values of maximum peak *dB/dt* of our systems and that used by Lemieux are of the same order of magnitude, with all the other interactions to take into consideration the previous work does not give much indication of what may happen at 7 T. The potential for generating a locally high specific absorption rate

(SAR) in tissue, as well as the possibility of significant heating of the EEG leads and/or electrodes must therefore be carefully considered [18].

The work by Lemieux *et al.* has been followed up with experimental work by Lazeyras *et al.* [20] who found heating effects occurred when high SAR values were used. Although these heating effects were significant, with a maximum increase of 6.1 ^{o}C over a three minute period using a sequence with a SAR value of 2.6 Wkg^{-1}, they were still found to be well within safety guidelines. Interestingly, a number of sequences with varying SAR levels were run and it was found that the heating of the EEG electrodes increased almost linearly with SAR. This indicates that when a sequence with a high SAR value is tested and no heating is observed it is unlikely that heating will occur during any MR sequence of lower SAR at the given field strength. This research was conducted in similar conditions to the work by Lemieux *et al*, although the EEG system had no built-in resistors to reduce heating in the electrodes. The conclusions reached by the two groups were similar, that at 1.5 T combined EEG-fMRI can be conducted safely, although Lazeyras *et al* suggested that resistors were not needed to reduce heating effects in the EEG.

B_0 Field strength	**3 T**	**7 T**
Maximum Slew rate ($T\ m^{-1}\ s^{-1}$)	200	200
Maximum *dB/dt* due to gradients ($T\ s^{-1}$)†	20	20
Maximum B_1 field strength (μT)	20	10
Maximum *dB/dt* due to RF field ($T\ s^{-1}$)	16.1×10^3	18.7×10^3

Table 8.1: The maximum possible values of dB/dt on the 3 T and 7 T Philips Achieva systems for both gradient switching and RF pulses. †Values calculated assuming electrodes are 10 cm from the bore isocentre (Obtained from Philips personnel).

Angelone *et al.* [21] carried out simulations with the aim of evaluating the change in SAR with field strength and number of electrodes applied to the scalp. Their simulations used a model of the EEG system with electrodes and leads represented as perfect electric conductors. Although this is not the case for our system, as there are

5 kΩ resistors in each electrode, this approach should provide a good indication of tissue heating. It was found that the introduction of the conducting components of the EEG system at 7 T caused a significant increase in the calculated value of the peak local SAR. This effect became stronger as the number of electrodes/leads was increased (a maximum of 124 leads/electrodes were considered) and was larger at 7 T than at 3 T. In further work, the same group have made experimental measurements of RF heating at 7 T on a conducting, head–shaped phantom, for a variety of EEG electrode and lead arrangements using an end-cap TEM RF coil [15, 21]. Despite the long, 33 minute, experimental duration and the very high maximum local SAR of 15.5 Wkg^{-1} that was employed, the largest temperature rise which was found in these experiments was about 10 ^{0}C and occurred in the conducting paste of electrode Cz (Table 3 in Ref [21]). These authors suggested that the RF power input to the system should be scaled relative to their findings, so that SAR limits for tissue are not exceeded when EEG systems are present. In related work carried out at 7 T by Vasios *et al. [15]*, temperature changes in the presence of their "InkCap", a standard EEG cap and a QuickCap (which is a commercially available EEG cap that is MRI-compatible up to 4 T) were recorded. The results of this study were that the standard EEG cap and QuickCap caused heating at the monitored electrode sites when a high-powered TSE sequence was applied. The maximum temperature increase, of up to 6.6 ±0.09 °C, was significant when the MRI compatible cap was used. However, temperature increases measured using the InkCap were not significantly different to those measured on the phantom alone. The InkCap was subsequently used successfully in the first combined EEG/fMRI experiment carried out at 7 T [15].

Widespread implementation of simultaneous EEG/fMRI at 7 T is likely to occur most rapidly if the use of commercially available MR-compatible EEG systems can be extended from lower fields to 7 T. Here, I therefore describe research I have conducted into the feasibility of recording EEG signals from human subjects at 7 T using one commercially available, MR-compatible EEG system (BrainAmp MR amplifier, Brain Products, Munich, Germany), focusing on safety testing and the steps that have been taken to maximise the quality of the EEG recordings made in the electromagnetically hostile environment of a 7 T scanner. This involved systematic measurement of the sources of noise in EEG recordings made in the 7 T scanner whilst no scanning was taking place and measurement of RF heating effects on a gel phantom in the presence of a 32 electrode EEG cap (EasyCap, Herrsching, Germany) when a relatively high-SAR imaging sequence was used. Having found no significant safety concerns and identified an arrangement that limited scanner-induced noise, simultaneous EEG/fMRI experiments employing visual stimulation were then successfully carried out on a total of five human subjects. After the implementation of the standard average artefact subtraction technique [22, 23] beamformer-based analysis (described in Chapter 4 and in [24]) of the EEG data was conducted. This allowed the identification of driven responses and alpha-band, event-related desynchronisation in each subject.

8.2 General Equipment

The experiments described here were carried out using Philips Achieva 7 T MR scanners (Philips Medical Systems, Best, Netherlands). Some of the data shown in this chapter were collected at the Philips site in Cleveland, Ohio, USA with the rest recorded in Nottingham. The reason for this is that for some of the experiments it was necessary to use the expertise of the Philips staff on site. Also going to the Philips site enabled us to access equipment which was not yet available in Nottingham. Throughout this chapter clear distinctions will be made to identify where data were collected. A BrainAmp MR EEG amplifier, Brain Vision Recorder software (Brain Products, Munich, Germany) and the BrainCap MR electrode cap (EasyCap, Herrsching, Germany) with 32 electrodes, as described in Chapter 4, were used. The EEG cap employed sintered Ag/AgCl ring-electrodes with a 1.2 cm outer diameter and 0.6 cm inner diameter, each incorporating a plastic adapter and a 5 kΩ safety resistor. Light-duty, braided copper wires, of approximately 0.3 mm thickness, were used to connect the electrodes to the amplifier.

8.3 Noise Sources in EEG from Magnet Hall

Chapter 6 described the work that has been carried out to combat noise sources due to the scanning process at 3 T. However, no experiments were performed to eliminate noise sources within the room prior to scanning because these sources were not found to be problematic. However, in the introduction to this chapter, factors, such as vibration, which produce larger amplitude inference at higher field strength, have been highlighted and it is therefore important to investigate these ambient noise sources in the 7 T environment.

8.3.1 Methods

To investigate these other sources of noise, initial EEG recordings on a phantom positioned in the 7 T magnet were made with the scanner inactive. For these experiments, the 32 electrode cap was placed on a 20-cm-diameter, plastic spherical phantom containing saline-loaded, agar gel. A thin layer of Abralyte 2000 gel was placed between the outer surface of the phantom and the electrodes to mimic the skin. The same gel was used to provide connections between each of the electrodes and the gel layer (with impedance <10 kΩ at each electrode), thus producing conducting paths that would mimic those found on the scalp. The phantom was placed inside the RF coil and positioned at the scanner's isocenter with the EEG amplifier positioned at the rear of the magnet approximately 130 cm axially from isocenter. The distance of the amplifier from the isocenter is limited by the length of the EEG leads. It is desirable to place the amplifiers in the lowest possible field, but increasing the lead length can cause an increase in induced artefacts thus longer leads than those provided by Brain Products were not used.

The first series of EEG recordings (to identify noise sources) were conducted at the Philips site in Cleveland, USA. This was because Philips staff had greater knowledge of how to sequentially turn off elements of the scanner hardware. The elements which were turned off included the magnet's cryo-cooler pumps, the cooling air-flow to the magnet bore and gradient coil, the gradient amplifiers and the screened room lighting. In addition, the effectiveness of a variety of measures for limiting vibration of the EEG amplifier and leads were assessed. Initially the amplifier was mounted on the beam that runs through the scanner bore and which is suspended from the ends of the magnet. Padding was placed between the amplifier and the beam and the amplifier was weighted down in an attempt to limit vibration.

Subsequent experiments were conducted in Nottingham using the knowledge gained from the earlier recordings in Cleveland. Here the amplifier was mounted on a cantilever arrangement (180 cm length) projecting into the rear of the magnet (Figure 8.2). This was supported from the floor of the screened room and so was mechanically isolated from scanner vibrations. Two minutes of data were recorded for each arrangement at both sites. For ease of analysis, the data were Fourier transformed and a single power spectrum formed by averaging the power spectra from the individual channels.

8.3.2 Results and Discussion of Noise Sources

8.3.2.1 Cleveland Site

Although many parts of equipment were turned off and a variety of measures were undertaken to see how best to reduce the environmental noise, only those elements that made a significant difference to the quality of the EEG data are reported here. Figure 8.1 shows the effect of switching off different elements of the MR scanner equipment on the average EEG power spectrum. Each data set resulted from two minutes of recording made with no scanning taking place and the traces were formed by averaging power spectra across all leads usually used for recording of neuronal activity (*i.e.* excluding the ECG and EOG leads). It is evident from Figure 8.1 that the dominant source of noise is the cryocooler pumps, since when these are switched off the series of peaks occurring at harmonics of the approximately 2.4 Hz pumping frequency disappear. It seems most likely that the interference from the pumps results from transmission of mechanical vibration to the EEG amplifier and leads via the patient support beam, although airborne electromagnetic interference cannot be entirely ruled out as the cause. Noise due to the cryocooler pumps has been noted previously in EEG recordings made at lower field [25]. However for Philips MR scanners operating at 3 or 1.5 T field strengths this is not a problem because the cryocooler pumps are automatically switched off during scanning. In contrast the pumps have to be manually turned off on our Philips 7 T system. It is clearly important that this is done during all combined EEG/fMRI experiments carried out at 7 T, although doing so leads to increased helium boil-off (as mentioned in Chapter 3).

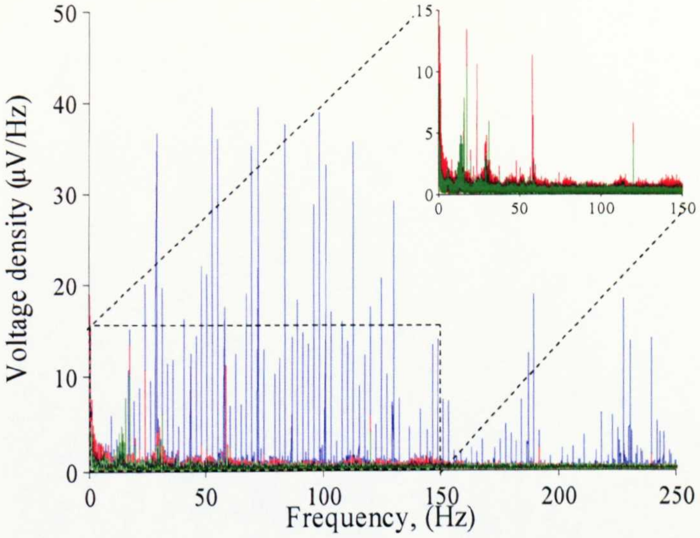

Figure 8.1: Effects of turning off different elements of the MR scanner apparatus on the FT of the EEG signal averaged over all channels. All equipment on (blue), cryocooler compression pumps turned off (red) and room lights, gradient and patient airflow also turned off (green).

Figure 8.1 also indicates that the noise spikes occurring at frequencies of 60 and 120 Hz, corresponding to harmonics of the US mains frequency, are reduced by turning off the lights in the screened room. Switching off the cooling air-flow to the magnet bore and gradient coil was also found to result in a significant reduction in noise in the EEG recording especially at lower frequencies (Figure 8.1). This noise also seemed to result from vibration of the beam supporting the patient bed, upon which the EEG amplifier sat. Since it is not possible to scan with the air-flow off, alternative methods of reducing the effect of these vibrations were explored.

8.3.2.2 Nottingham Site

Insertion of padding under the EEG amplifier and application of weights on its upper surface was found to result in some reduction of the noise pick-up, but greater noise attenuation was obtained by mounting the EEG amplifier on a cantilevered beam (made in-house), which was inserted into the magnet bore without making mechanical contact with the magnet, as shown in Figure 8.2.

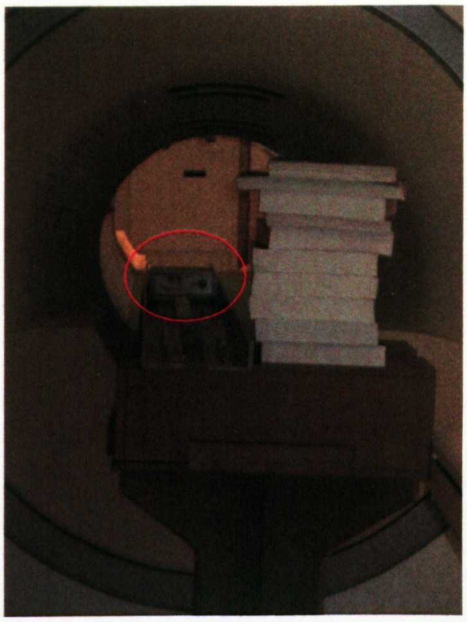

Figure 8.2: The set up of the amplifier (highlighted) on the cantilever beam to isolate it from any bed vibrations.

Figure 8.3, which shows data recorded during a different session with the air-flow on, indicates that the vibrational isolation provided by this beam significantly reduces the low frequency noise. This final arrangement with the compression pumps off, room lights off, and the amplifier and associated equipment mounted on the cantilever beam was used for human studies.

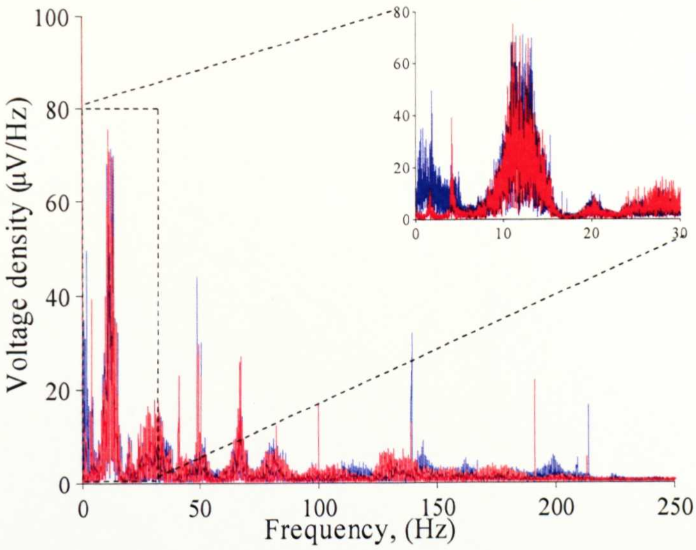

Figure 8.3: Effect of balancing an EEG amplifier on a cantilever beam (red) compared with not (blue) on the FT of the EEG signal averaged over all channels.

8.4 Preliminary Experiments

8.4.1 Methods

8.4.1.1 Heating tests using birdcage coil

Although the EEG system used has been safety tested by Brain Products at magnetic fields up to 3 T, the company has not tested it at 7 T. Heating tests were therefore carried out before any human EEG recordings could take place. This initial testing was conducted in Cleveland using the phantom set up described in Section 8.3.1, with a quadrature birdcage coil employed for signal excitation and reception within the MRI system.

A Luxtron Fibre Optic Thermometer Labkit with TrueTemp software was used to measure temperature changes. Probes were placed between four electrodes (Ref.– [sited between Fz and Cz], Pz, T7 and T8) and the phantom. These electrodes were chosen to give an equal spread of positions and orientations over the head to get an idea of possible heating due to any localised gradient or RF effects. Temperature fluctuations were monitored over 21 minutes during execution of a high-powered TSE sequence employing an average RF power of 9.87 W. With no significant heating found (Figure 8.4) experiments on human subjects were deemed safe for this RF coil.

8.4.1.2 Human Experiments using the birdcage coil:

All the experiments conducted on human subjects that are described in this chapter were carried out in Nottingham, with approval of the local ethics committee. Experiments were carried out on 3 healthy volunteers (aged 23, 24 and 26). A standard multi-slice single-shot EPI sequence was implemented with TR=2.2 s, 20 coronal slices and 420 dynamics. These parameters were chosen to satisfy the requirements for synchronisation which are outlined in Chapter 6. The coronal slices were positioned over the visual cortex and shimming was only carried out over this area. This resulted in the minimum distortion and signal loss possible which was significantly less than that experienced in the EPI images shown in Chapter 7. The TE was set to 25 ms, so as to give the optimal BOLD contrast [7]. A 64×64 matrix and a $3\times3\times3.5$ mm^3 voxel size were used. Respiratory and cardiac traces were recorded using the Philips physiological monitoring equipment as discussed in Chapter 6. The EEG sampling and imaging gradient waveforms were synchronised by driving the BrainAmp clock cycle using a 5 kHz signal derived from the 10 MHz imaging spectrometer clock, again as described in Chapter 6 [26] and by Mandelkow *et al. [27]*. The head was held in place using a vacuum cushion to reduce the ballistocardigram (BCG) and movement effects.

The scanning was carried out under the optimal conditions identified from the noise testing experiments. A simple visual stimulus consisting of a flashing (10 Hz) checkerboard was presented for 30 cycles of 10 s with the stimulus on and 20 s with no stimulation. This was to allow collection of both the EEG and BOLD data. The BOLD signal takes longer to recover to baseline than the electrical signals, so a longer off period was implemented than in the studies described in Chapter 6.

A standard T_1 weighted MPRAGE sequence with SENSE factor 2, 256mm FOV and 1 mm^3 isotropic resolution was applied at 3 T to each subject so as to provide a clear map of the scalp surface from which the electrode positions could be identified.

8.4.2 Analysis of Human data

Analysis of fMRI data was carried out using standard techniques in SPM99 with the results corregistered to an anatomical of that subject.

Off-line EEG signal correction was based on averaging and then subtracting gradient and pulse artefacts. Artefact removal was carried out using the optimised techniques outlined in Chapter 6. Data were filtered from 1-250 Hz to remove any DC offset and high frequency noise. Fourier transforms of the data in the "stimulus-on" and "stimulus-off" periods were taken with a total duration of 300 s of data used in each FFT. This FFT analysis was carried out using the techniques described in the second study of Chapter 6. The additional process of downsampling the data to 600 Hz was carried out to allow implementation of the beamformer algorithm.

MPRAGE image data acquired at 3 T were used to determine the electrode positions. This was done by looking at the distortions produced in the image by the presence of the electrodes as shown in Figure 7.7. This procedure was needed to allow the application of a beamformer to the data. The beamformer (as described in Chapter 4 and by Brookes *et al.* *[24]*) can localise induced changes of cortical activity and in this instance, more importantly, can be used as a noise cancellation technique. The latter is clearly a significant advantage when there is residual noise in the data due to the environment in which the data were collected. The beamformer relies on the assumption that no two sources of neuronal activity are correlated, which limits the applications of this technique. However, for the purpose of this study this assumption does not pose a problem as the visual cortex is based in the occipital lobe and although bilateral the two areas are close enough together that the activation normally appears as one source. For the purpose of this study the outer sphere for the forward solution was fitted with a bias to the posterior of the head as that is where the activity of interest was expected and therefore where the best fit was required. Since consideration of the recordings from the electrodes at the front of the head was also important for the beamformer to perform optimally, the biasing used was only weak.

Using the beamformer, a pseudo-T statistic, Ŧ, was calculated for each voxel in the source space using the data in the frequency band of interest (19.5-20.5 Hz). The location within the head that produced the maximum power in the frequency band of interest, identified from the Ŧ-map, was subsequently chosen as the site of a virtual electrode, VE. The time course from the VE including all frequencies was found for the *x*-, *y*- and *z*-components whose axes are based on the fiducial points (bridge of the nose, right and left auricular points) identified on the subject using the anatomical image. The FTs of these time courses were then taken and compared with those obtained from the actual EEG electrodes.

8.4.3 Results and Discussion of the Preliminary Experiments

8.4.3.1 Heating using the birdcage coil.

The temperature rise found at each of the four electrodes that were monitored was less than 0.5 °C over the 21 minute scanning period as can be seen in Figure 8.4.

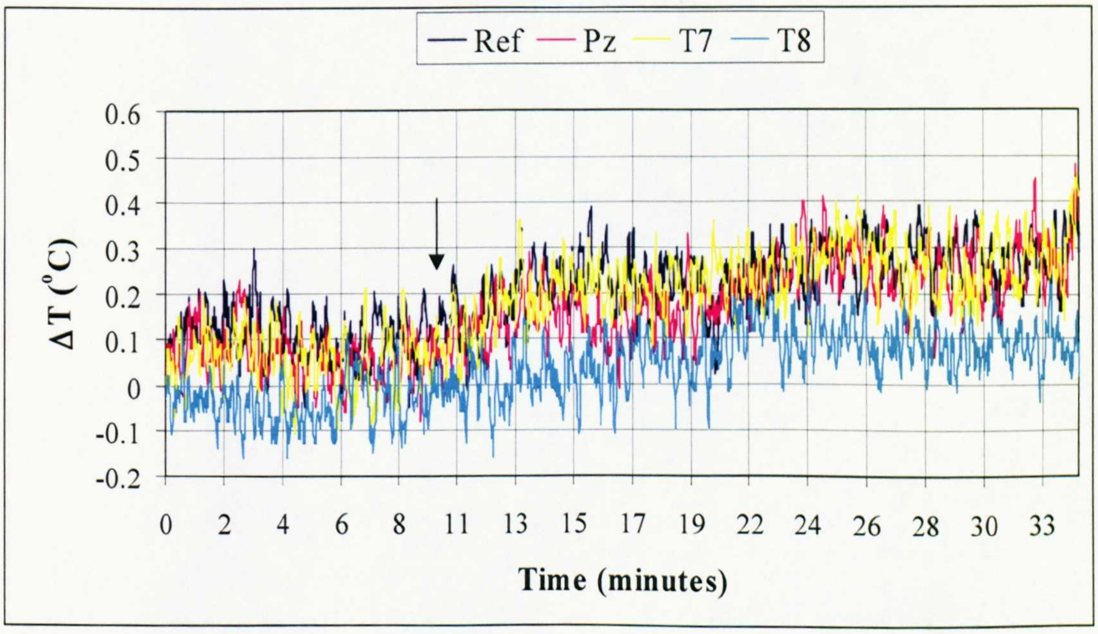

Figure 8.4: A plot to show the change in temperature (relative to starting temperature) at each electrode monitored before and during a high-powered TSE sequence. The arrow indicates the onset of the TSE sequence.

These results appear surprising given the results of Chapter 7, where interactions between the B_1 field and EEG cap are shown, and in light of the fact that more significant heating has been found by other groups with thermometers placed in similar positions relative to the electrodes and phantom [15, 21]. Explanations for these discrepancies can be found in section 8.5.3.1. Given the results shown here (along with repeatability measurements) it has been deemed safe to put the Brain Products cap on humans at 7 T when using our birdcage T/R coil.

8.4.3.2 Human Experiments using the birdcage coil.

This preliminary work was carried out on three subjects with results from one, representative subject shown here. None of the subjects reported any sensation of heating whilst scanning took place, confirming the heating results from the phantom. A comparison of the FT of the EEG signals obtained from electrode Oz, which exhibited the largest neuronal activation of all the channels, during the on (active) and off (passive) periods (Figure 8.5A) shows strong electrical signals occurring at 20 Hz and higher harmonics of the visual stimulus frequency.

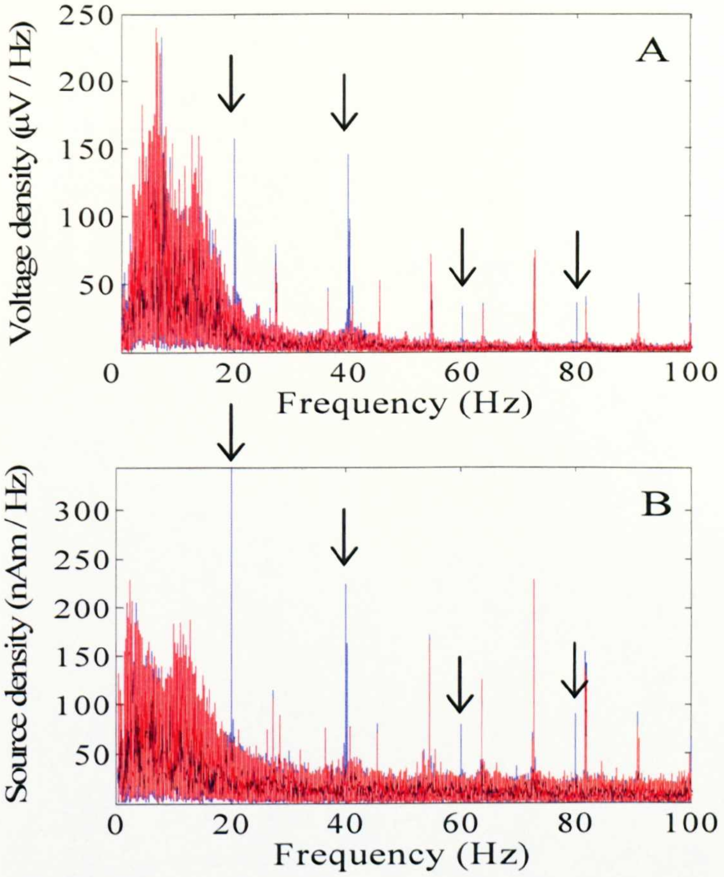

Figure 8.5: FT of the signal for active (blue) and passive (red) contrast windows for electrode Oz (A) and the y-component of the VE (B). Arrows indicate peaks of interest.

Although neuronal activation could be detected, there was still noise in the signal especially at lower frequencies, which could make studying alpha band activity particularly problematic.

A beamformer was employed as a method of noise reduction as well as a technique to test whether the activity identified in the BOLD and EEG data had the same spatial origin. Figure 8.6A shows the ~~T~~-statistic image reflecting electrical activity in the 19.5-20.5 Hz frequency band, which corresponds with the BOLD activation map shown in Figure 8.6B.

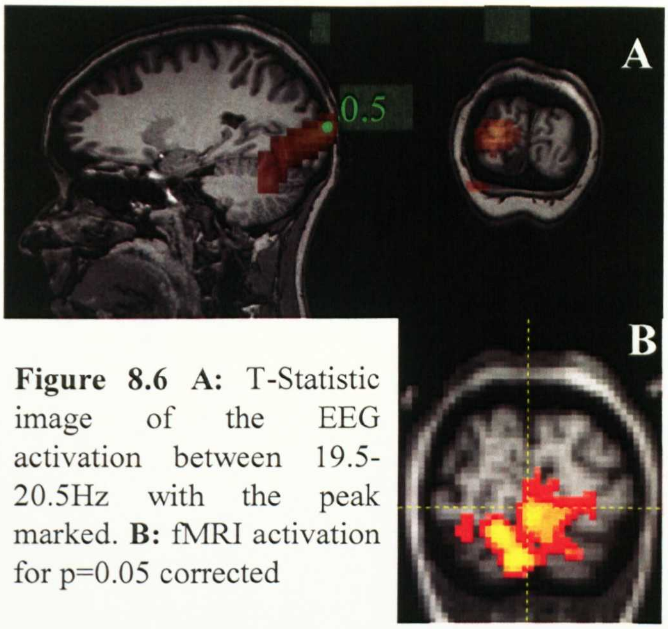

Figure 8.6 A: T-Statistic image of the EEG activation between 19.5-20.5Hz with the peak marked. **B:** fMRI activation for p=0.05 corrected

Spatial resolution is relatively poor, but it is clear from the results shown in Figure 8.6 that the source of activity for both modalities has the same location. In this preliminary work limitations existed in the co-localisation of the BOLD data to the anatomical MR images because the coronal slices were distorted to an extent and the fractional volume of the head spanned by these data were relatively small.

Figure 8.5B shows the FT of the largest component of the temporally varying dipole strength from a VE placed at the site of peak activity (Figure 8.6A). Comparison with Figure 8.5A indicates an improvement in the ratio of signal peak strength to noise has been achieved via use of the beamformer. This finding agrees with the beamformer theory and the results presented by Brookes *et al.* [24].

8.4.4 Conclusion to the Preliminary Experiments

This preliminary work indicated that for a T/R quadrature birdcage coil it was safe to conduct EEG experiments with fMRI at 7 T. It also revealed that it was possible to get both EEG and BOLD data from simultaneous scans with both modalities producing results which convincingly showed neuronal activity. From this work it was clear that developing the methods to further improve the data quality from both modalities would be advantageous as this would increase the chances of being able to implement single trial EEG/fMRI or detect neuronal activity in the higher frequency gamma band where amplitudes are diminished.

8.5 Optimised Experiment

Although the approach used in the preliminary experiments allowed successful recording of EEG data at 7 T and the comparison of the results with BOLD data, there are a number of further improvements which have been made to the final experimental technique. The majority of these improvements were made possible by the introduction of new equipment to the department in the middle of 2007. The new equipment was thus available for use in the final six months of the work undertaken for this thesis.

The main pieces of equipment that have been introduced are the Polhemus system (Polhemus Isotrack) and a new RF coil arrangement (Nova Medical, Wilmington, MA) consisting of a 29 cm inner diameter, quadrature, birdcage RF coil designed to have a spherical region of uniformity of approximately 16 cm diameter, which was used for transmission, and a 16 channel, dome-shaped receiver coil with an inner diameter of 19 cm, allowing parallel imaging techniques to be used. The Polhemus system allows an easier, less time consuming, method of locating electrode positions on the head than using the MPRAGE image data. The Polhemus system uses electromagnetic fields to determine the position of a receiver relative to the transmitter. The transmitter and receiver each contain three orthogonal antennas. The transmitter is stationary and generates low frequency magnetic fields in three orthogonal directions. This is detected by the receiver (a stylus pen) which is traced over the head (to get the head shape) and is also used to mark each electrode position. A mathematical algorithm computes the receiver's position and orientation relative to the transmitter [28] based on the detected magnetic field. Using the Polhemus rather than MPRAGE data provides increased accuracy when locating electrode positions and therefore improves the results obtained with the beamformer technique.

During the visit to Cleveland a prototype SENSE coil was made available. This enabled initial experiments to be conducted, which highlighted the advantages of using the SENSE coil for simultaneous EEG-fMRI. These experiments showed that using the same parameters for *TE*, *TR* and number of slices, but adding in a SENSE factor of 2 reduced the magnitude of the gradient artefact. This is because lower rates of change of the gradients can be employed with the application of SENSE as explained in Section 3.5.3. Alternatively for different experiments greater head coverage could be obtained with the same *TR*. Therefore it is desirable to use the SENSE coil for simultaneous EEG-fMRI experiments.

8.5.1 Methods

8.5.1.1 Heating using the SENSE coil

The prototype SENSE coil was not tested for heating effects in the presence of the EEG cap during my time in Cleveland. Therefore when the 16 channel SENSE coil became available for use in Nottingham it was necessary to carry out further heating tests. The 18-cm-diameter gel phantom which was used for these measurements was made by heating an aqueous solution containing 4 % agar and 0.5 % NaCl by weight. The EEG cap was placed directly on to the phantom and the impedance of all electrodes was measured to be less than 10 kΩ (including the contribution of the 5 kΩ safety resistors).

A Luxtron Fibre Optic Thermometer Labkit (LumaSense Technologies, Ballerup, Denmark) was used to monitor temperature changes at eight different locations on the surface of the phantom. Seven of the probes were placed at the site of electrodes. These were the reference electrode, which was positioned between Fz and Cz, and the ECG electrode, which was fixed to the bottom of the phantom, along with electrodes Fp1, Fp2, Cz, Fc5 and Fc6. An eighth temperature recording was made at a position where the ECG lead came into contact with the surface of the phantom. The ECG lead was significantly longer than the other leads (> 65 cm longer) and therefore might be expected to exhibit different interactions with the RF field (especially in light of the results descried in Chapter 7). Temperature changes were monitored over 20 minutes during the execution of a Turbo Spin Echo sequence employing an average RF power of 8.77 W, corresponding to an SAR value of 2 Wkg^{-1} according to the scanner software.

8.5.1.2 Human Experiment using the SENSE coil

Experiments were carried out on two healthy volunteers (aged 23 and 24). A standard multi-slice, gradient echo EPI sequence was implemented with *TE* = 25 ms, a SENSE factor of 2 [29], 2 mm slice thickness and 2 mm in-plane resolution and a 12.8 x 12.8 cm^2 field of view. Eighteen, trans-axial slices were acquired with a *TR* of 2.2 s, chosen to be an exact multiple of the 200 μs EEG clock period thus allowing the EEG equipment to sample the gradient artefact precisely [26, 27]. A saturation band was placed over the front of the head and a flip angle of 95° was used to minimise signal loss and the effects of distortion. This approach resulted in the production of images of far better quality than the data presented in Chapter 7. All other parameters for the EPI sequence remained the same as in the preliminary experiments. The set up of the physiological monitoring and EEG equipment was also identical to that used in the preliminary experiments. However, due to the reduced internal diameter of the new head coil it was not possible to use vacuum cushion to try to reduce the BCG artefact.

The scanning was carried out under the optimal, accessible conditions that had been identified from the noise testing experiments: this involved switching of the cryo-cooler pumps and the lights in the shielded room, and mounting the EEG amplifier on the cantilever arrangement. A simple visual stimulus consisting of a flashing (15 Hz) checkerboard was presented for 30 cycles each consisting of 10 s with the stimulus on and 20 s with no stimulation. The stimulus was back-projected onto a semi-opaque screen positioned at the end of the patient-bed and viewed by the subject using prism goggles. The checkerboard stimulus spanned approximately 9° of the subject's central visual field. At the end of the fMRI session, a 50-slice, whole-head EPI data set was acquired with the position of the central 18 slices identical to that used in the fMRI experiment and the *TR* set to 10 s. These data were collected to assist with subsequent co-registration of the fMRI data to anatomical images with 1 mm isotropic resolution, which were subsequently acquired from the same subjects using a standard MPRAGE sequence [30]. The locations of the EEG electrodes on the scalp surface were recorded using a Polhemus isotrack 3D digitiser (Polhemus, Vermont, USA) and the shape of the subject's head was also digitised using this system. The 3D digitised head shape was then fitted to the head shape extracted from the subject's anatomical MRI scan in order to compute the location of each electrode with respect to the brain anatomy.

8.5.2 Analysis of Human data

Analysis of the fMRI data was carried out using standard techniques in SPM5 (FIL, London). The whole-head EPI data were co-registered to the 1 mm resolution anatomical images of that subject and the same transform was applied to the fMRI data.

Off-line EEG signal correction was based on averaging and then subtracting gradient and pulse artefacts. Gradient artefact correction employed an average artefact waveform of 2.2s duration, formed by averaging over the 420 *TR*-periods, using the markers generated by the MR scanner at the beginning of each *TR*-period for alignment. No frequency filtering or down-sampling was applied in the gradient artefact removal process. Subsequently, the data were down-sampled to 600 Hz using the "change sampling rate" function in the Brain Vision Analyser software. This employs cardinal splines, with an anti-aliasing filter. Pulse artefact correction was carried out based on R-peak markers derived from the VCG trace which were temporally aligned with the EEG data using in-house software as described in Chapter 6 and [26].

Once the initial correction for artefacts had been carried out, the data were exported to MATLAB (Mathworks). As the reversing checkerboard stimulus was phase-locked to the stimulus onset, the data from all of the "stimulus-on" periods could be concatenated together for spectral analysis. The same process was applied to the data acquired during the "stimulus-off" periods. This resulted in a total of 300 s of data for each state. These data were band-pass filtered to the 1 to 250 Hz frequency range to remove any low frequency drift and high frequency noise. Fourier transforms of the data in the stimulus-on and stimulus-off periods were then calculated and subsequently compared so as to allow identification of neuronal activity.

The beamformer [24] was then used in an identical manner to that described previously to produce a Ŧ-map of the driven response at 29.5-30.5 Hz. Subsequently a VE time-course was created. The oscillatory alpha power response was also studied by creating a Ŧ-map related to power in the 8 to 12 Hz frequency band, again comparing the active and passive states. The envelope of oscillatory activity in the alpha frequency band was then calculated for the VE time-course. This is given by the absolute value of the analytical signal [31]. This approach allowed an average across trials to be calculated, which is not possible with raw oscillatory data, since the signal is not phase locked across trials.

8.5.3 Results and Discussion

8.5.3.1 Heating using the SENSE coil

The results shown in this section are from the heating tests conducted in Nottingham on the 16 channel SENSE coil. Figure 8.7 shows that the maximum temperature rise measured at each of the eight positions that were monitored during execution of a relatively high-SAR, TSE sequence of 20 minutes' duration was less than 0.4 °C. The results are consequently similar to those shown in Figure 8.4.

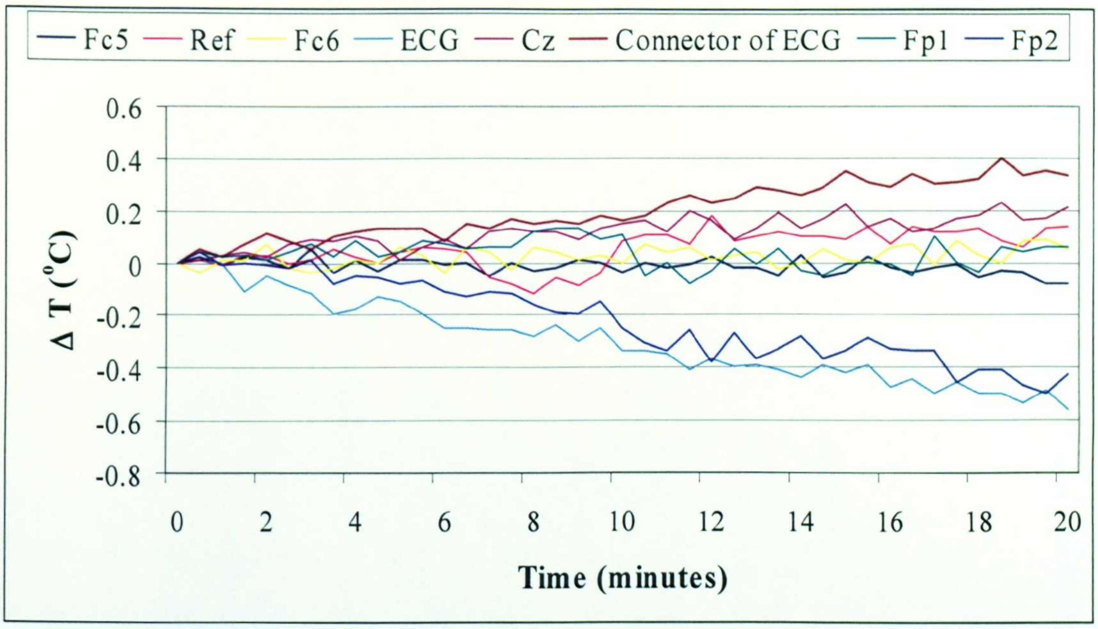

Figure 8.7: A plot to show the change in temperature (relative to initial temperature) at each electrode monitored during a high-powered TSE sequence. The scanning sequence started at time 0.

Like the results obtained from the quadrature birdcage coil, which are shown in Section 8.4.3.1, the changes in temperature are significantly less than those measured in previously described RF heating tests on EEG electrodes and leads at 7 T [15, 21]. However, this discrepancy is not too surprising since as well as using different types of electrode and lead to those studied here, the prior work also employed much higher SAR values (>10 Wkg^{-1} versus 2 Wkg^{-1}) that are not easily accessible on our system. Scaling the temperature rise measured here with the SAR level [20] and experimental duration produces a peak temperature increase that is not too dissimilar from that found in prior work. It should however be noted that the scanner-reported SAR levels are based on scanner-manufacturer-specific models, so that a comparison of values reported by different systems should be made with some caution. The fact that the temperature measurement at some electrodes showed no change or a small temperature decrease in our experiments, may indicate that the temperature variation in our experiment was dominated by changes in ambient temperature. The other possible, although unlikely, cause for the discrepancy between studies may be due to the monitoring of different electrodes, which happened to have a reduced heating effect, in this study compared to previous studies. It is improbable however that higher heating would have been found elsewhere as the ECG wire showed the greatest interaction with the B_1 field (Chapter 7) and exhibited minimal heating effects at both sites monitored along this wire. Given the findings of Stevens *et al.* [32] one would expect the heating of this wire to be at a maximum at the electrode end and therefore it is unlikely that significant heating occurred anywhere along the wire. The low temperature changes that were recorded gave us confidence that RF heating effects would not be significant in the planned fMRI experiments on human subjects, particularly in light of the fact that the scanner-reported SAR level for the multi-slice gradient echo EPI sequence used in the fMRI experiments was more than 30 % lower than that of the TSE sequence employed in the heating measurements.

8.5.3.2 Human Experiments using the SENSE coil.

With the use of the SENSE coil, the subjects again did not report any sensation of heating, confirming the results of the phantom testing on this coil. In the EEG spectra that are displayed in this section, data from the "stimulus-on" periods are shown in blue whilst those from the "stimulus-off" periods are shown in red. Figure 8.8A-C show spectra obtained from electrodes O1, O2 and Oz overlying visual cortex in Subject 1. A peak at 30 Hz, corresponding to neuronal activation at twice the checkerboard presentation frequency, is evident in all three spectra and the spectrum from electrode O2 also exhibits a smaller peak at 60 Hz. As in the preliminary data, the spectra recorded during both periods are dominated by residual gradient artefacts which cause the spectral peaks that occur at multiples of the 8.18 Hz slice acquisition rate. These are most likely to result from imperfect correction of the gradient artefact via the average artefact subtraction approach, which is usually a consequence of changes in the artefact waveform during the recording. Such changes may result from subject movements that lead to changes in the position of electrodes and leads relative to the applied gradients [26]. In Figure 8.9A, which shows data from electrode O1 recorded from Subject 2, neuronal activity at 30 and 60 Hz is also evident, as is the presence of residual gradient artefacts.

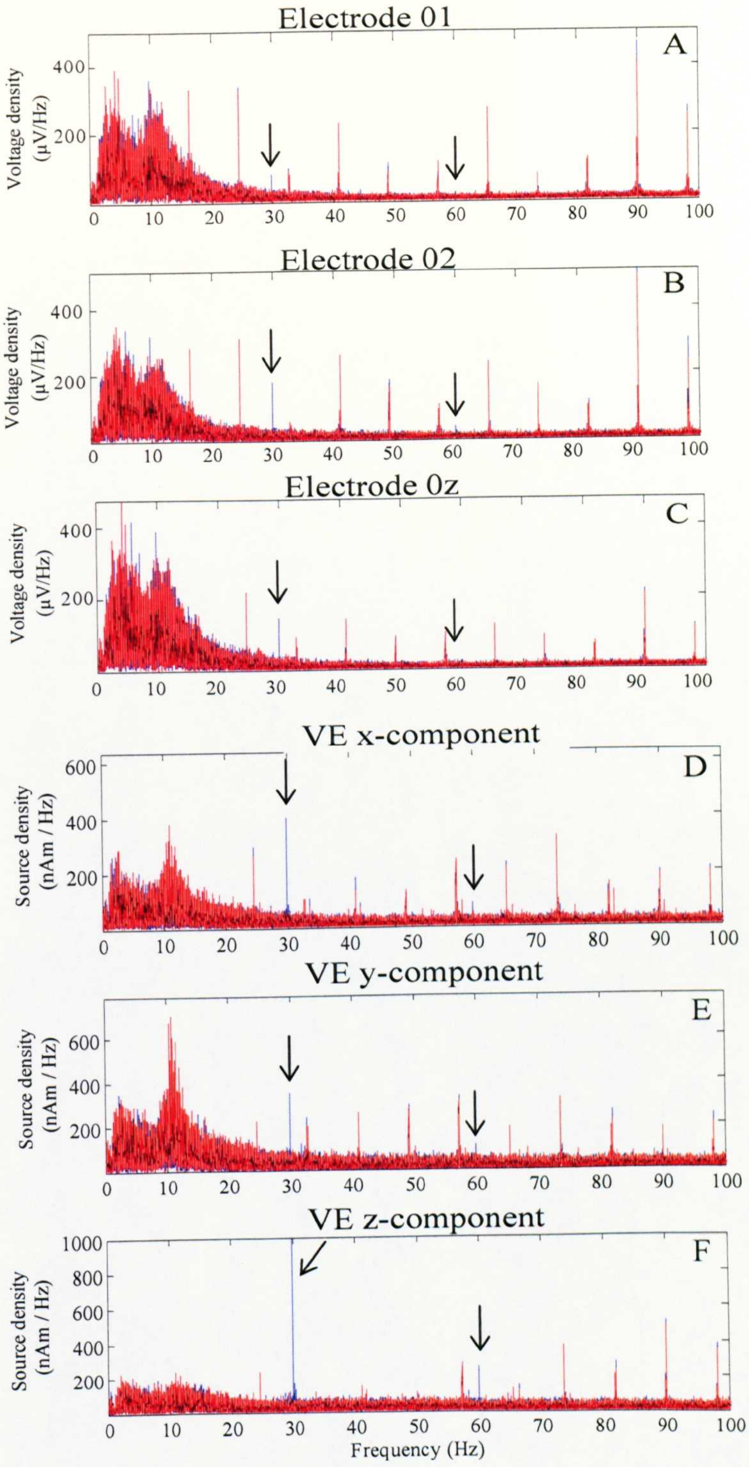

Figure 8.8: FT of the signal for active (blue) and passive (red) contrast windows for subject 1. The top three power spectra show results for electrodes covering the visual cortex (O1 (A), O2 (B), and Oz(C)). The bottom plots show power spectra corresponding to the x-(D) y-(E) and z-(F) orientated dipolar components at the virtual electrode location. Arrows indicate peaks of interest corresponding to harmonics of the stimulus presentation frequency.

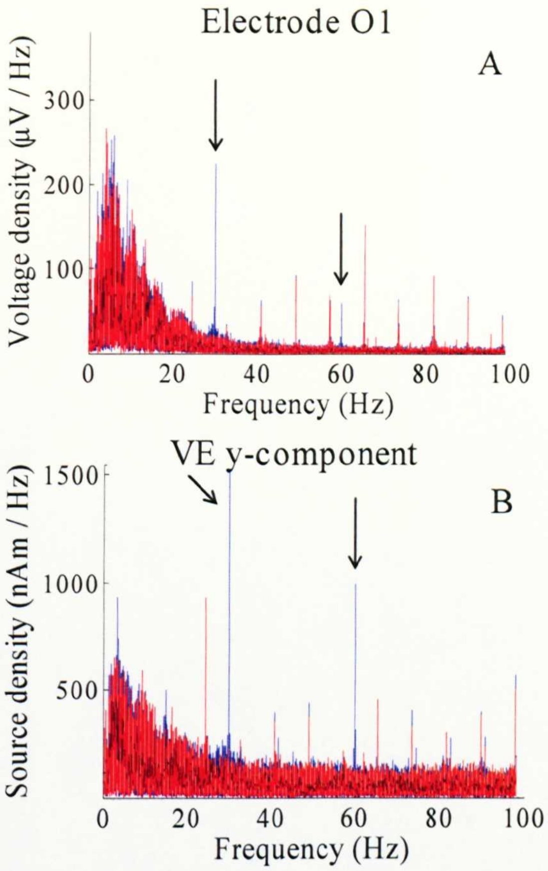

Figure 8.9: FT of the signal for active (blue) and passive (red) contrast windows for electrode O1 (A) and the y-component of the VE (B) for subject 2. Arrows indicate peaks of interest corresponding to harmonics of the stimulus presentation frequency.

Spatial filtering via beamformer analysis [24] was again employed to reduce the effect of residual gradient artefacts and also to provide information about the site of stimulus-driven electrical activity for comparison with the fMRI data. Two different ~~T~~-statistic maps were created for each subject. The first, which depicts the driven response occurring in the 29.5-30.5 Hz frequency range, is shown overlaid on each subject's anatomical image in Figure 8.10(A and D). The areas highlighted in these images co-localise well with those appearing as active in the corresponding fMRI data also shown in Figure 8.10(C and F). This agreement extends to the strongly unilateral form of the response shown in the maps based on both the BOLD effect and the driven electrical response in Subject 1. This biasing of the response is not evident in the data from Subject 2 and may reflect the fact that perhaps only one half of the visual field was strongly stimulated in Subject 1, although this was not part of the experimental design.

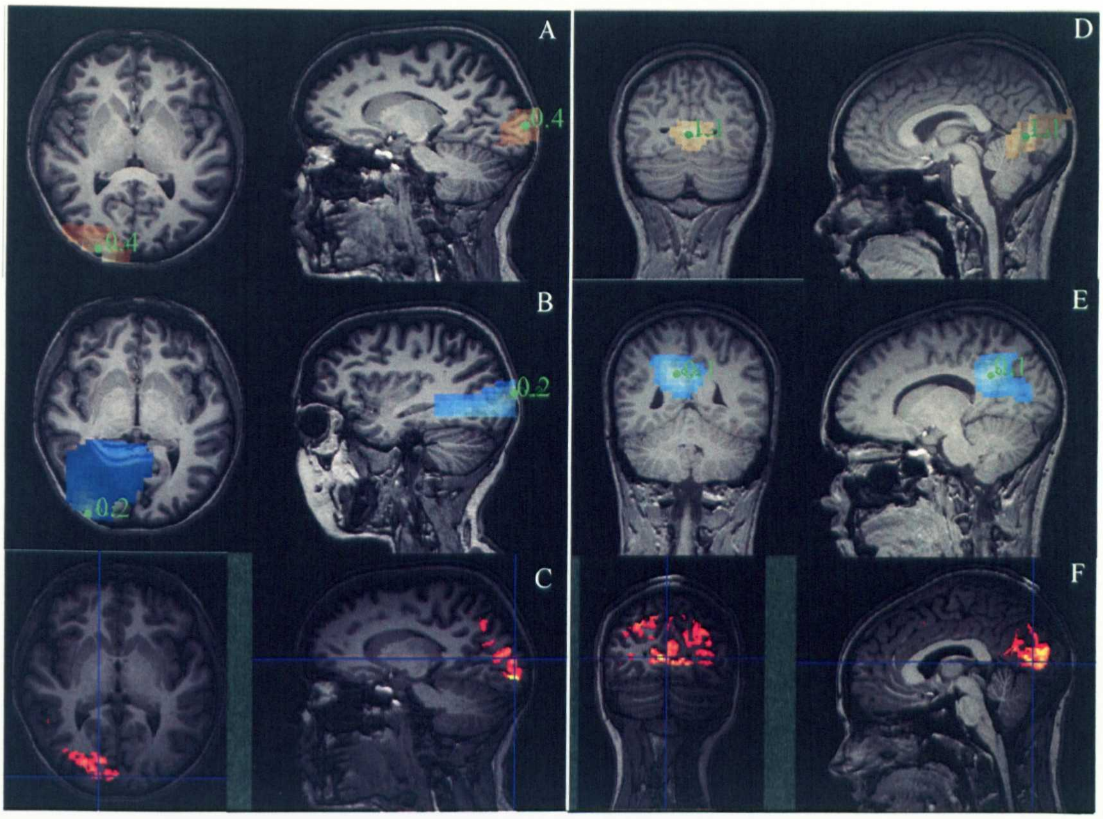

Figure 8.10: Experimental results from the two subjects studied are shown: the left panel shows results for subject 1 whilst the right shows results for subject 2. ~~T~~–statistic images of the EEG activation due to the driven response in the 29.5-30.5 Hz frequency band (A&D). Areas showing significant event-related reduction in alpha power are shown in B&E. BOLD activation thresholded at p=0.05 corrected is shown in C&F. The green dots and numbers indicate the position of the virtual electrode and the ~~T~~-value at that point.

Virtual electrodes were placed at the locations marked in Figures 8.10A&D where the highest ~~T~~-values occurred and the temporal variations of the *x*-, *y*- and *z*-dipole components were measured at these sites. The spectra produced from the resulting data from Subject 1 are shown in Figure 8.8 (D-F). The component directed along the *z*-direction (which is normal to the plane formed by the left and right auricular points and the tip of the nose) is largest in this subject. Comparison of Fig. 8.8F and Fig. 8.8B shows that the spatial filtering action of the beamformer reduces the effect of the residual gradient artefacts relative to the driven electrical responses. In particular the 30 Hz driven response forms the largest peak in Figure 8.8F, which is not the case in any of the spectra from individual electrodes. This is also the case in the virtual electrode data (*y*-component) from Subject 2, which is shown in Figure 8.9B.

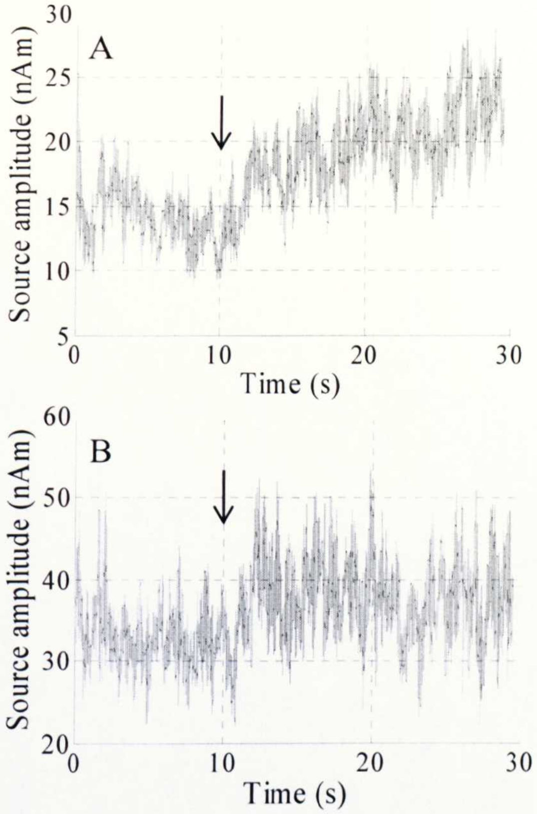

Figure 8.11: Power envelopes of alpha band event related desynchronisation for the VE axis with the maximum change for subject 1 (A) and subject 2 (B). Envelopes have been averaged across trials. The stimulus was applied over the time range 0-10 s, with the stimulus offset marked by an arrow.

It is evident from these plots that as well as suppressing the residual gradient artefacts, use of the beamformer also reduces the low frequency noise relative to brain signals with a dipolar signature. This increases the possibility of detecting stimulus-induced changes in alpha power. A second Ŧ-statistic image for each subject was generated showing areas where the power in the 8-12 Hz frequency band was significantly decreased when the visual stimulus was applied. Figure 8.10(B&E) shows the areas where significant event-related desynchronisation (ERD) in the alpha band occurred when the checkerboard was present. The areas showing significant alpha ERD are somewhat larger than, but reasonably overlapping with, areas showing a significant driven response. This is in agreement with the results of previous combined EEG/fMRI experiments carried out at 3 T[24]. Virtual electrodes were again sited at the locations showing the largest Ŧ-value and Figure 8.11 shows the time-course of the power envelope of the oscillatory power in the 8-12 Hz frequency range averaged across all trials for the two subjects. These show a significant and rapid decrease in alpha power when the stimulus is applied with a concomitant increase after the stimulus offset.

8.6 Conclusion

The experiments described here show that simultaneous EEG/fMRI experiments can be successfully carried out at 7 T using a commercial MR-compatible EEG amplifier system and 32-electrode cap. In tests of RF heating which were carried out with the EEG cap mounted on a head-sized conducting gel phantom, using a birdcage transmit coil with 16 channel receive RF coil, a maximum temperature rise of less than 0.4 °C was measured after the execution of TSE sequence with a scanner-reported SAR of 2 Wkg^{-1} and a duration of 20 minutes. Further experiments carried out on phantoms indicated that noise/interference in the EEG recordings made at 7 T can be significantly reduced by switching off the cryo-cooler pumps during scanning and mounting the EEG amplifier on a cantilever, which helps to reduce low frequency vibration.

Using this set-up, along with other modifications, combined EEG/fMRI experiments based on visual stimulation and a simple block paradigm were successfully carried out on two subjects. Synchronization of the EEG and scanner clocks facilitated the process of gradient artefact correction and a VCG recording was used to identify R-peaks for pulse artefact correction. Further artefact attenuation was achieved by using a beamformer spatial filter in analyzing the EEG data. The results obtained from both subjects showed clear electrical activation at 30 and 60 Hz, corresponding to twice and four times the frequency of reversal of the checkerboard used for visual stimulation. Significant event-related desynchronisation (ERD) in the alpha band was also identified. Comparison of T-statistic maps produced for both these effects using the beamformer showed reasonable spatial agreement with areas of activation identified from analysis of the fMRI data.

The methodology described here provides a sound basis for implementation of further simultaneous EEG/fMRI experiments at 7 T allowing the exploitation of the improved BOLD CNR that is available at high field.

8.7 References

1. Debener, S., M. Ullsperger, M. Siegel, K. Fiehler, D. Yves von Cramon, and A.K. Engel, *Trial-by-Trial Coupling of Concurrent Electroencephalogram and Functional Magnetic Resonance Imaging Identifies the Dynamics of Performance Monitoring.* Journal of Neuroscience, 2005. **25**(50): p. 11730-11737.

2. Goldman, R.I., J.M. Stern, J. Engel, and M.S. Cohen, *Simultaneous EEG and fMRI of the alpha rhythm.* Neuroreport, 2002. **13**(18): p. 2487-2492.

3. Laufs, H., A. Kleinschmidt, A. Beyerle, E. Eger, A. Salek-Haddadi, C. Preibisch, and K. Krakow, *EEG-correlated fMRI of human alpha activity.* NeuroImage, 2003. **19**(4): p. 1463-1476.

4. Lemieux, L., *Electroencephalography-correlated functional MR imaging studies of epileptic activity.* Neuroimaging Clinics of North America, 2004. **14**(3): p. 487-+.

5. Lemieux, L., A. Salek-Haddadi, O. Josephs, P.J. Allen, N. Toms, C. Scott, K. Krakow, R. Turner, and D.R. Fish, *Event-Related fMRI with Simultaneous and Continuous EEG: Description of the Method and Initial Case Report.* Neuroimage, 2001. **14**: p. 780-787.

6. Scarff, C.J., A. Reynolds, B.G. Goodyear, C.W. Ponton, J.C. Dort, and J.J. Eggermont, *Simultaneous 3-T fMRI and high-density recording of human auditory evoked potentials.* Neuroimage, 2004. **23**: p. 1129-1142.

7. Van der Zwaag, W., *Techniques for High-performance fMRI*, in *Sir Peter Mansfield Magnetic Resonance Centre, School of Physics and Astronomy.* 2006, University of Nottingham: Nottingham. p. 190.

8. Duong, T.Q., E. Yacoub, G. Adriany, X. Hu, K. Ugurbil, and S.-G. Kim, *Microvascular BOLD contribution at 4 and 7T in the human brain: Gradient-echo and spin-echo fMRI with suppression of blood effects.* Magnetic Resonance In Medicine, 2003. **49**(3): p. 1019-1027.

9. Gati, J.S., R.S. Menon, K. Ugurbil, and B.K. Rutt, *Experimental Determination of the BOLD Field Strength Dependence in Vessels and Tissue.* Magnetic Resonance In Medicine, 1997. **38**: p. 296-302.

10. Edelstein, W.A., G.H. Glover, C.J. Hardy, and R.W. Redington, *The Intrinsic Signal-to-Noise Ratio in NMR Imaging.* Magnetic Resonance In Medicine, 1986. **3**(3): p. 604-618.

11. Yacoub, E., A. Shmuel, J. Pfeuffer, P. Van De Moortele, G. Adriany, K. Ugurbil, and X. Hu, *Investigation of the initial dip in fMRI at 7 Tesla.* NMR in Biomedicine, 2001. **14**: p. 408-412.

12. Krueger, G. and G. Glover, *Physiological noise in oxygenation-sensitive magnetic resonance imaging.* MAGNETIC RESONANCE IN MEDICINE, 2001. **46**(4): p. 631-637.

13. Krueger, G. and G.H. Glover, *Neuroimaging at 1.5 T and 3 T: comparison of oxygenation-sensetive magnetic resonance imaging.* Magnetic Resonance In Medicine, 2001. **45**: p. 595-604.

14. Triantafyllou, C., R.D. Hoge, G. Krueger, C.J. Wiggins, A. Potthast, G.C. Wiggins, and L.L. Wald, *Comparison of physiological noise at 1.5T, 3T and 7T and optimization of fMRI acquistion parameters.* Neuroimage, 2005. **26**: p. 243-250.

15. Vasios, C.E., L.M. Angelone, P.L. Purdon, J. Ahveninen, J. Belliveau, and G. Bonmassar, *EEG/(f)MRI measurements at 7 Tesla using a new EEG cap ("InkCap").* Neuroimage, 2006. **33**(4): p. 1082-1092.

16. Debener, S., K.J. Mullinger, R.K. Niazy, and R.W. Bowtell, *Properties of the ballistocardiogram artefact as revealed by EEG recordings at 1.5, 3 and 7 Tesla static magnetic field strength.* International Journal of Psychophysiology, 2008. **67**(3): p. 189-199.

17. Brown, B.H. and R.H. Smallwood, *Medical Physics and Physiological Measurement.* First ed. 1981: Blackwell Scientific Publications. 558.

18. Lemieux, L., P.J. Allen, F. Franconi, M.R. Symms, and D.R. Fish, *Recording of EEG during fMRI Experiments: Patient Safety.* Magnetic Resonance In Medicine, 1997. **38**: p. 943-952.

19. Roth, B.J., A. Pascual-Leone, L.G. Cohen, and M. Hallett, *The heating of metal electrodes during rapid-rate magnetic stimulation:a possible safety hazard.* Electroencephalography and Clinical Neurophysiology, 1992. **85**: p. 116-123.

20. Lazeyras, F., I. Zimine, O. Blanke, S.H. Perrig, and M. Seeck, *Functional MRI with simultaneous EEG recording: Feasibility and application to motor and visual activation.* Journal of Magnetic Resonance Imaging, 2001. **13**(6): p. 943-948.

21. Angelone, L.M., A. Potthast, F. Segonne, S. Iwaki, J.W. Belliveau, and G. Bonmassar, *Metallic Electrodes and Leads in Simultaneous EEG-MRI: Specific Absorption Rate (SAR) Simulation Studies.* Bioelectromagnetics, 2004. **25**: p. 285-295.

22. Allen, P.J., O. Josephs, and R. Turner, *A Method for removing Imaging Artifact from Continuous EEG Recorded during Functional MRI.* Neuroimage, 2000. **12**(2): p. 230-239.

23. Allen, P.J., G. Poizzi, K. Krakow, D.R. Fish, and L. Lemieux, *Identification of EEG Events in the MR Scanner: The Problem of Pulse Artifact and a Method for Its Subtraction.* Neuroimage, 1998. **8**(3): p. 229-239.

24. Brookes, M.J., K.J. Mullinger, C.M. Stevenson, P.G. Morris, and R.W. Bowtell, *Simultaneous EEG source localisation and artifact rejection during concurrent fMRI by means of spatial filtering.* NeuroImage, 2008. **40**(3): p. 1090-1104.

25. Mulert, C., P. Hepp, L. Jager, S. Karch, G. Leicht, H.-J. Moller, U. Hegerl, and O. Pogarell. *Simultaneous measurement of 40Hz electrical activity and the corresponding BOLD-signal: Methodological issues.* in *Human Brain Mapping*. 2006. Florence: Elsevier.

26. Mullinger, K.J., P.S. Morgan, and R.W. Bowtell, *Improved Artefact Correction for Combined Electroencephalography/Functional MRI by means of Synchronization and use of VCG Recordings.* Journal of Magnetic Resonance Imaging, 2008. **27**(3): p. 607-616.

27. Mandelkow, H., P. Halder, P. Boesiger, and D. Brandeis, *Synchronisation facilitates removal of MRI artefacts from concurrent EEG recordings and increases usable bandwidth.* Neuroimage, 2006. **32**(3): p. 1120-1126.

28. Polhemus, *Fastrak Manual.* 5th ed. 2005, Colchester, Vermount, USA.

29. Pruessmann, K.P., M. Weiger, M.B. Scheidegger, and P. Boesiger, *SENSE: Sensitivity encoding for fast MRI.* Magnetic Resonance In Medicine, 1999. **42**(5): p. 952-962.

30. Mugler, J.P. and J.R. Brookeman, *3-Dimensional Magnetization-Prepared Rapid Gradient-Echo Imaging (3dmp-Rage).* Magnetic Resonance In Medicine, 1990. **15**(1): p. 152-157.

31. Blackledge, J.M., *Digital signal processing.* 2003, Chichester: Horwood Publishing.

32. Stevens, T.K., J.R. Ives, and R. Bartha. *Energy Coupling between Electric Fields and Conductive Wires: Image Artifacts and Heating.* in *Joint Annual meeting ISMRM-ESMRMB*. 2007. Berlin.

Chapter 9

Combined EEG/fMRI study of the response to periodic visual stimulation.

9.1 Introduction

The work presented thus far in this thesis has focussed upon technical improvements whose implementation enhances the quality of EEG and MRI data collected in a simultaneous manner. It has also been shown that it is possible to record EEG-fMRI data simultaneously at 7 T provided that a number of special measures are taken. The work described in this chapter exploits the improvements in data quality provided by the novel methodology introduced in previous chapters in experiments carried out at 3 T. The overall goal of this work is to obtain a greater understanding of the correlation between the neuronal and haemodynamic responses of the brain.

There are two main aims of the experiments described here. The first is to investigate how the amplitude of the alpha power preceding a visual stimulus modulates the magnitude of the BOLD response to that stimulus. Correlations between the driven evoked response (measured from the EEG) and the BOLD response will be considered. The second experiment aims to investigate the variation of the evoked electrical response and the BOLD response to visual stimuli of varying frequency, where the frequencies are set according to the Individual's Alpha Frequency (IAF). The IAF is defined throughout this work as the frequency at which the maximum magnitude in the Fourier transform of the voltage recorded from occipital electrodes with the subject's eyes closed, between the frequencies of 8 and 12 Hz, occurred.

It is clear from these aims that this study involves the investigation of a number of complex neuronal processes. Many of these have been studied using a single neuroimaging technique (*i.e.* either using EEG or fMRI) but, to our knowledge, the simultaneous recording and investigation of these processes has not been carried out before. By exploiting the recently developed ability to carry out simultaneous EEG and fMRI recordings it is hoped that further understanding may be gained about the meaning of the alpha rhythm and how the neuronal and haemodynamic responses are linked.

9.2 Background

As discussed in Chapters 1 and 4, alpha rhythm was first recorded in 1929 by Hans Berger [1, 2] and since then the study of this frequency band has been prolific. There is a general consensus within the neuroscience community that a full understanding of activity in this frequency band will help vastly in the understanding of brain function. This is highlighted in Niedermeyer's [3] statement that oscillatory EEG activity is a "phenomenon with important psychophysiological implications." Although studies of alpha power are numerous and observations, such as the presence of the alpha rhythm being strongest in a subject when the eyes are shut and the subject is awake, are well documented, the understanding of the precise functional role of the alpha rhythm is still poorly understood.

It is generally thought that the alpha rhythm has an inhibitory influence on cortical activity. This hypothesis is well documented, for a review refer to [4]. The basis of this hypothesis is clear: when one engages in a task, a reduction in alpha power is generally observed. This is known as event related desynchronisation (ERD). Further evidence for this hypothesis is provided by a multitude of studies such as the one by Rahn *et al [5]* who showed that if alpha power is low when a stimulus is presented, a larger visual evoked potential (VEP) of the N1-P2 component is measured than if the stimulus is presented when the alpha power is high. Findings such as these are reiterated in a review by Basar [6]. Responses to the perception of visual stimuli are also reported to be heightened when the preceding alpha power is low compared to when it is high [7-9]. Hanslmayr *et al* [8] extended previous work with the observation that those subjects who have inherently lower alpha power perceive stimuli to a greater extent than those with naturally high alpha power. This experimental evidence leads one to the conclusion that alpha power has an inhibitory role within the brain. With this inhibitory theory in mind, it is logical to expect that large alpha rhythm results in less neurons firing upon presentation of a stimulus leading to a smaller increase in the energy demand of the neuronal network than when the alpha power is low. Since we know that the BOLD response is linked to neuronal energy demands (Chapter 4), the intuitive initial hypothesis is that high alpha power preceding a stimulus will cause a reduction in the amplitude of the BOLD response compared to when alpha power is low at the time of stimulation.

This hypothesis seems logical until one considers other, equally well conducted, experiments from different groups who report that the preceding alpha power has the opposite effect on the neuronal response to a stimulus. The main body of this work comes from Brandt's group [10-12]. They have reported an increase in the peak-to-peak amplitude of the N1-P2 visual evoked response with increasing relative alpha power preceding the stimulus [11]. They also report a similar finding when considering the N1 peak, showing that high alpha power preceding a stimulus results in an elevated amplitude of the N1 peak in the evoked response [10]. Intriligator *et al [13]* investigated differences across a number of subjects demonstrating that a subject with high alpha power generally has a larger P300 response to a visual stimulus than one with low alpha power. Although Intriligator's study did not investigate within-subject correlations the between subject correlations appear to agree with the findings of Brandt. It has also been shown by a number of groups that when conducting memory tasks, good performers have high preceding alpha power [9]. With regards to tasks related to perceptual performance, it appears again that there are inconsistencies in experimental results, with some groups finding that high alpha power leads to better perceptual performance [14]. Hanslmayr [8] discusses these discrepancies in perceptual performance tasks, suggesting that differences in the experimental paradigm may be the cause of the inconsistency: for example a memory component was involved in Babiloni's study which was not present in Hanslmayr's. However, this body of results suggest that perhaps there is more than one explanation for the role of alpha power within the brain and that it is not purely inhibitory in function.

This concept of more than one type of alpha power was discussed in detail by Basar *et al [6]*. Even in 1950 the idea that the alpha band did not purely consist of a single component with one function was put forward by Grey Walter who said:

> "*We have managed to check the alpha band rhythm with intra cerebral electrodes in the occipital-parietal cortex; in regions which are practically adjacent and almost congruent one finds a variety of alpha rhythms, some of which are blocked by opening and closing eyes, some are not, some are driven by flicker, some are not, some respond in some way to mental activity, some do not. What one can see in the scalp is a spatial average of a large number of components, and whether you see an alpha rhythm of a particular type or not depends on which component happens to be the most highly synchronised process over the largest superficial area; there are complex rhythms in everybody.*" [15]

This idea, which is echoed in [6], along with the experimental evidence explored above suggests that a second interpretation of what alpha power represents can be proposed. The premise behind this explanation is that alpha power represents activation of extensive networks engaged in internal (introspective) mental activity and is therefore negatively related to processing directed towards external stimuli (personal communication with Peter Liddle). This interpretation therefore describes alpha power as an excitatory rather than inhibitory process, with the 'stimulus' for activation being internal rather than external.

Although definitive evidence for this hypothesis is somewhat scarce, there are a number of results suggesting that this is a plausible explanation which helps elucidate some of the observations already obtained using combined EEG-fMRI that were discussed in Section 5.3.1.1. Although group analysis showed a general negative correlation between alpha power measured in the resting state and the corresponding BOLD activity [16-18], on an individual basis results from other studies have shown a far more varied correlation between BOLD and alpha power. Some subjects have been shown to exhibit positive correlations of the alpha and BOLD responses, whilst in other subjects negative correlations were found [19]. Another study conducted more recently has confirmed these findings producing similar results [20] where some correlations were negative and others positive; but all correlations were highly significant. These results suggest that the internal networks producing the recorded alpha power increase the activation of the brain in some areas (responsible for internal processing) while at the same time reducing the neuronal activity in other areas (responsible for dealing with external stimuli). The temporal variation of the strength of correlated activity found in some subjects [19] could also be explained by this hypothesis, as the degree of internal, excitatory activity occurring over time is likely to vary, thus changing the correlations seen.

Observation of negative correlations between perceptual performance and alpha power can be explained by this hypothesis: if a large number of internal processes (high alpha power) are occurring, attention would be deflected from the external stimuli reducing perceptual performance. Equally with memory tasks, where an internal mechanism is clearly necessary, a high degree of activity in internal networks may assist with the memory task thus producing an increased performance [9]. Further evidence for an internal excitatory network has been provided by Cooper *et al* [21] who found that alpha power was increased when an internally directed mental task was undertaken compared to an externally directed attention task. If the alpha power mechanism is indeed excitatory it is easier to see how high alpha power could lead to an increase in VEP in some instances whilst a decrease in others. Depending on the internal networks being used, the effect of the alpha activity means that the presentation of a stimulus may produce a stronger response (positive correlation of alpha power and VEP) or weaker response (negative correlation). It is hard to tease out from the EEG recordings on the skull which alpha network is dominant. This difficulty arises from the fact that the focal neuronal signals are blurred over extensive areas of the skull thus only an additive measurement of all the rhythms present can be obtained and knowing the source of the dominant network can be hard [15] resulting in discrepancies between studies.

Although the amplitude of the alpha power on presentation of a stimulus clearly has an effect on the amplitude of the evoked potential (EP) the phase of the alpha power has also been shown to affect to the amplitude of the EP. It appears that the phase of the alpha power is reset due to stimulus presentation an increase in amplitude of the EP has been recorded when a stimulus is presented at certain points within the phase cycle [10]. The phases which result in the largest EPs have been found to lie around the zero crossing point of the alpha cycle [12]. It has also been shown that phase-locking of alpha power preceding stimulus presentation occurs when the timing of the presentation of a stimulus can be predicted [6] suggesting that the alpha power is a "functionally relevant signal". Evidence of phase resetting is also shown in

Hanslmayr's work on performance of memory and perceptual tasks [9]. They conclude that phase resetting may be responsible for good performance of each of these tasks. However, Becker *et al* [22] argue that a "complete phase reset is not possible since such a behaviour would prevent the consistently reported inverse relationship between pre-stimulus and post-stimulus alpha enhancement." This statement is intuitive to some degree, since if the phase of the alpha power preceding a stimulus was solely responsible for the amplitude of the evoked response, the amplitude of the preceding alpha power would not have any effect which, from other findings reported in this chapter about the relationship of the amplitude of the alpha power and the EPs, we know does not hold. The work by Becker [22] suggests a minimal role for phase resetting in dictating the amplitude of the EP.

Given the previous findings summarised above, a definitive, single hypothesis characterising the effect that the alpha power preceding a stimulus has on the BOLD response is difficult to derive. There are a number of different hypotheses which one can draw from the results above. These include the initial hypothesis presented, in which it was stated that the strength of the BOLD response is reduced by high preceding alpha power, as the alpha rhythm is a signature of inhibition. In this case the inhibiting effect of high alpha power preceding a stimulus would be expected to cause fewer neurons to fire and thus the energy demands of the neurons to be less causing a reduced BOLD response. However, the alternative hypothesis that the alpha power reflects an excitatory response to internal processes would lead one to predict different consequences following the presentation of a stimulus. In this case a number of different components of the alpha rhythm may affect the response to a visual stimulus. The strength of the BOLD response will depend on which component of the alpha rhythm is dominant at the time of stimulus presentation. If the internal excitatory processes require the visual cortex to be inactive, then the BOLD response may be low when high preceding alpha power is present. Whereas, if the internal processes are unaffected by visual stimulation, one may expect a larger neuronal and BOLD response if high alpha power is present leading up to stimulus presentation. Therefore, this hypothesis would predict different effects on the BOLD response depending upon the component of the alpha power measured in an individual. This hypothesis would therefore suggest that the experimentally measured correlation of preceding alpha power and BOLD response may differ across subjects. The data recorded within this study will thus direct the conclusions as to the role of alpha power in the processing of visual stimuli.

When considering the effect of the frequency of visual stimulation on the BOLD response more experimental evidence is already available [23-27]. However, to date, all the studies investigating this phenomenon have chosen pre-determined frequencies for stimulation irrespective of the frequency of individual subject's natural rhythms. Analysis of the data in earlier investigations was also carried out on a group basis, so that differences which may have been observed on an individual basis have not been documented. Studies by Ozus *et al [25]*, Singh *et al* [27] and Thomas *et al* [26] concluded that the maximal BOLD response could be obtained using a stimulus flashing at 8 Hz. Earlier results obtained using PET [23] are in agreement with this conclusion, where the percentage change in regional CBF was found to be maximal when the stimulus was presented at approximately 8 Hz. This frequency has been commonly used in recent fMRI studies where a simple flashing visual stimulus has been employed. A more recent study by Hagenbeek *et al* [24] explored the variation of the BOLD response amplitude (within a predefined ROI) with frequency of visual stimulation across different subjects. They found that the peak BOLD response occurred at frequencies varying between 9.3 and 15 Hz in different individuals. Averaged over all subjects, the peak activation occurred at 11.6 Hz in the first experiment and 12 Hz in the second (the second experiment was identical to the first, using the same subjects, but was carried out at a different time). These values are clearly higher than described in previous reports. Hagenbeek *et al* suggested that this anomaly may be due to a number of differences in their experimental methodology compared to that used in previous investigations. They stated that although the peak in the BOLD response was found at a frequency which was higher than most subjects' IAF there may be a correlation between the frequency of the peak in a BOLD response and the IAF of the subject.

Koch *et al* [28] investigated the haemodynamic and EEG responses to visual stimuli of varying frequency. In their experiments, Near-Infrared Spectroscopy (NIRS) was used to measure the haemodynamic responses with the change in the deoxyhaemoglobin during stimulus presentation monitored (as little change was observed in the oxyhaemoglobin). Koch *et al* found that there was no correlation between the frequency at which the maximum reduction in deoxyhaemoglobin concentration occurred and the IAF of the subject. The minimum in deoxyhaemoglobin concentration for all subjects was found to occur for frequencies of stimulation lying between 7 and 8 Hz. This finding agrees with those of other groups who have measured BOLD or CBF changes during visual stimulation [23, 25-27].

Singh *et al* [27] also investigated the amplitude of the driven evoked response using EEG. The frequencies the visual stimuli were presented at were independent of IAF (as in the BOLD-based studies described above) and the maximum driven response was found to occur at 8 Hz averaged over all subjects. This finding is in agreement with the majority of the BOLD studies, but contradicts the EEG findings of Koch *et al* and other groups where the IAF was considered in the stimulus frequency and subsequent analysis. The simultaneously acquired EEG data from Koch's study [28] showed that the strength of the driven response from the EEG data is dependent on the IAF and was maximal when the stimulation frequency matched the IAF. This finding agrees with previously reported work [29, 30] which showed that the peak in the VEP occurred when the stimulus was presented at the alpha frequency of the individual. These results suggest some sort of increase in the strength or size of the neuronal network used when the stimulus frequency is close to the IAF. This could be explained by the excitatory theory of alpha power. Networks required for internal processes are often functionally active, therefore it is likely there are many synaptic links resulting in a strong, well defined network. When a stimulus is presented at the natural frequency of this network, the network will be driven easily leading to a larger driven evoked response than would be generated if a different driving frequency were employed. If this hypothesis is correct then those subjects who have a large driven evoked response at their IAF may be expected to have a lower IAF as it is probable that the network responsible for production of the alpha power is larger and therefore resonates at a lower frequency. Evidence from Koch *et al* [31] supports this theory as they showed exactly this effect, of a lower IAF resulting a in larger driven evoked response.

Linking this theory about the resonance of networks with the BOLD response is difficult as the way in which energy demands change with frequency is hard to predict. However, it is possible that driving a system at its resonant frequency is less energy demanding than driving at other frequencies [32] and therefore one might predict that the BOLD response will be reduced when the stimulus is presented at the IAF. This however, contradicts the finding of Koch *et al* [28] which suggest that the BOLD response is independent of IAF and peaks at approximately 8 Hz in all subjects.

It is clear from the above summary of the previously published research that there are still vast gaps in our understanding of the alpha rhythm, evoked responses and the relationship to energy demands which are measured indirectly via the BOLD response. The set of experiments described in this chapter aims to use the advances in simultaneous EEG-fMRI to collect high quality EEG and fMRI data which can be used to address some of these questions. Here, I describe two experiments conducted on the Philips Achieva 3 T MR scanner, using the Brain Products MR compatible EEG system. Experiment 1 focuses on the correlation between the alpha power preceding a visual stimulus and the corresponding BOLD response. This experiment also allows analysis of the correlation of the strength of the BOLD response with the magnitude of the driven evoked potentials produced by the stimulus. Experiment 2 is concerned with determining whether the frequency of visual stimulation has a bearing on an individual's BOLD response, and in particular explores the relationship between the BOLD and electrical responses for visual stimuli presented at frequencies that are fixed relative to IAF.

9.3 Methods

9.3.1 Subject Screening

Due to the nature of this study it was important to use subjects who exhibited an easily detectable alpha rhythm with a well defined frequency. Twenty subjects were screened, with this process usually taking place a couple of weeks before carrying out the fMRI study. The screening involved of recording EEG responses only. This was done by using the Brain Products MR-compatible EEG system (Brain Products, Munich, Germany) with 30 electrodes on the scalp, following the international 10-20 system, along with ECG and EOG electrodes, as described in previous chapters. The subject was asked to lie in a darkened, quiet room. Data were recorded for five minutes with subjects opening and closing their eyes every 30 seconds and markers recorded by the EEG system at the start of each event. Data were analysed using Brain Vision Analyzer (Version 1.05.0005) software with data segmented according to the eyes-open or –closed states. Fourier transforms were taken of each segment and then segments corresponding to the same state (*i.e.* eyes open/closed) were averaged. If the Fourier transforms exhibited a clear peak in the alpha frequency range and this peak had an amplitude greater than 95 μV/Hz on recordings from occipital electrodes, when the subject's eyes were closed, they were asked to return for the full study. Figure 9.1 shows Fourier transforms of example data sets acquired for two subjects. The first subject was not asked to return for the full study (Figure 9.1A) whilst the second subject was asked to return (Figure 9.1B). It is clear the importance of screening the subjects from this figure as although a peak in the alpha frequency band can be easily detected for one subject the other shows no obvious IAF.

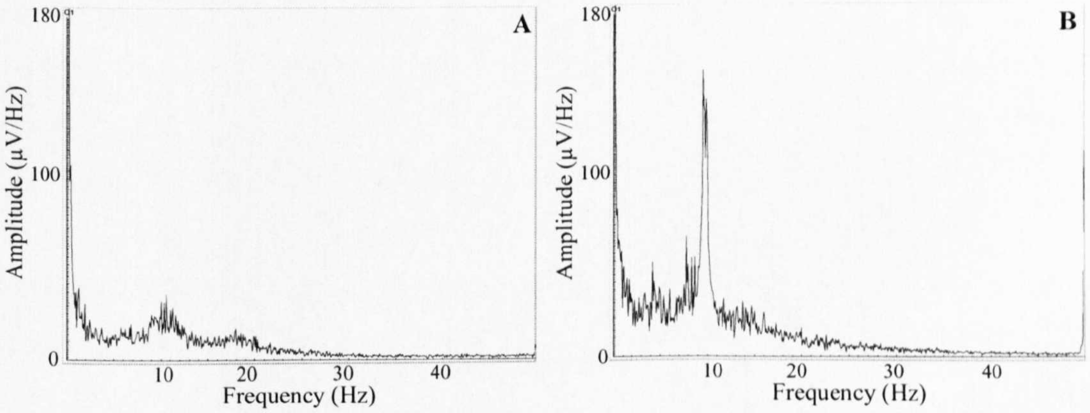

Figure 9.1: The average Fourier transform of 5 30second epochs of EEG data acquired from electrode O1 for 2 subjects with their eyes closed. A: a subject with no clear IAF who was not asked to return for the full study. B: a subject with a clear IAF who met the screening criteria and was asked to return.

9.3.2 Experimental method

9.3.2.1 General

All the experiments carried out in this chapter were performed with the approval of the local ethics committee. The majority of equipment used for both experiments was the same as that used in the work described in Chapter 6.

MRI data were collected using a Philips Achieva 3 T MR scanner (Philips Medical Systems, Best, Netherlands) employing a whole body RF coil for signal excitation and an eight-channel, head coil for signal reception. A standard, multi-slice EPI sequence was implemented with $TR = 2.2$ s, $TE = 40$ ms, a 64 × 64 matrix, 3.25 × 3.25 mm^2 in-plane resolution and a slice thickness of 3 mm. 20 transverse slices were acquired, using a SENSE factor of 2 [33]. A flip angle of 95° was set on the scanner to reduce the effect of the B_1 inhomogeneities on signal strength in the visual cortex, as described in Chapter 7. Cardiac and respiratory cycles were simultaneously recorded using the scanner's physiological monitoring system (vector cardiogram (VCG) [34] and respiratory belt) whose outputs are sampled at 500 Hz. Further details on the how the VCG works can be found in Section 6.3.

EEG data were recorded using a BrainAmp MR EEG amplifier, Brain Vision Recorder (Version 1.05.0005) software (Brain Products, Munich, Germany) and a BrainCap electrode cap (EasyCap, Herrsching, Germany) with 30 electrodes positioned on the scalp according to the international 10-20 system, and additional ECG and EOG electrodes. The BrainAmp system uses a sampling rate of 5 kHz and incorporates hardware filters which limit the frequency range of the recorded signals to 0.016-250 Hz, with a roll-off 30 dB/octave at high frequency. The cap provides a reference electrode positioned between Fz and Cz (Figure 4.9A). Synchronisation of the scanner clocks as described in Chapter 6 and in references [35, 36] was again employed. Triggers marking the beginning of each volume acquisition were recorded.

A whole head anatomical image and digitised electrode positions relative to the head were acquired to help with subsequent beamformer analysis. The anatomical image was acquired using a standard MPRAGE sequence [37] with 1 mm^3 isotropic resolution (increased to 1.1 mm^3 for some subjects with large heads so as to allow for whole head coverage). The locations of the EEG electrodes on the scalp surface were recorded using a Polhemus isotrack 3D digitiser (Polhemus, Vermont, USA) and the shape of the subject's head was also digitised using this system (for an explanation of how this works refer to Section 8.5). Using an in-house written MATLAB program, the 3D digitised head shape was then fitted to the subject's anatomical MRI scan in order to allow computation of the location of each electrode with respect to the brain anatomy, as described in Chapter 8.

Both of the experiments were performed in the darkened scanner room with the subject as relaxed as possible and with their eyes open. Eyes remained open to allow maximum VEP and BOLD responses to be elicited by the visual stimulus, even though alpha power is reduced in this state. The eyes-open state has been previously described to be adequate for studying differences in alpha power by Intriligator *et al* [13] and therefore was deemed the most practical state for subjects to be in for these experiments. Visual stimuli were presented using Presentation software (Version 11.0; Neurobehavioural Systems, Albany, NY) and flashing LED goggles. Each eye was stimulated with red light from 4 LEDs. The LEDs were mounted onto the end of optical light guides (2.5 cm in diameter and 2 m in length) as shown in Figure 9.2. Use of these guides allowed the electrical sources driving the LEDs to be placed at a distance of approximately 2 m from the EEG cap and associated equipment, thus reducing the effect of interference in the EEG recording. To verify that interference from the electrical sources was not directly picked up by the EEG system, initial experiments were performed in which an EEG cap was placed on a phantom (similar to that used for the noise recordings in Chapter 8) and the LED equipment was set up. 2 minutes of EEG data were recorded whilst the LEDs were driven at 8 Hz. An FFT of the recorded data showed no significant peaks at 8 Hz or higher harmonics. Markers were placed within the EEG data files at the beginning and end of each stimulus presentation so exact timings could be used in both the fMRI and EEG data analysis. In each of the experiments, the presentation of stimuli relative to fMRI acquisition was jittered, this enabled better sampling of the haemodynamic response as outlined in Section 4.2.2.5. Twelve subjects (5 male, 7 female with a mean age of 26) were selected to take part in the full study, which involved carrying out both experiments and the other scans described above. The experiments were carried out in two separate scan sessions on the same day. These sessions were separated by time spent collecting the digital head shape data using the Polhemus system. This break between experiments helped to ensure the subject's comfort and to reduce the effects of fatigue.

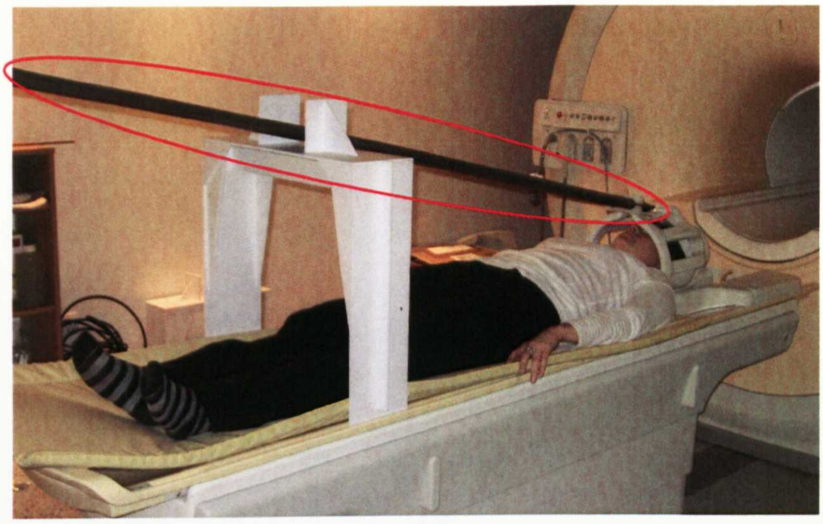

Figure 9.2: Experimental setup of the optical light guides (highlighted).

9.3.2.2 Experiment 1: Oscillatory rhythms and the BOLD response

To allow there to be a significant natural variation in the amplitude of the alpha power preceding a stimulus it was necessary to acquire data over a large number of cycles of the stimulus. 40 cycles of an 8 Hz stimulus were presented with each trial consisting of 5 s on and 30 s off. The 8 Hz stimulus frequency was chosen to give the maximal BOLD response according to previous findings [23, 25-27]. The on-period was chosen to be short so that the BOLD response was unlikely to reach a steady state and was therefore most likely to be affected by the preceding alpha power. The off-period was chosen to be long to ensure the BOLD response had returned to baseline, and to allow alpha power to build-up following stimulus offset. 660 volumes of fMRI data were acquired taking approximately 24.5 minutes.

9.3.2.3 Experiment 2: Stimulus Frequency Variation

To re-determine the IAF of the subject, the same experiment carried out for the screening was performed immediately before the full experiment. This is necessary as the individual's alpha frequency can vary over time as shown in Table 9.1. The variation in the IAF over time was not found to be significant when conducting a Student's paired T-test however, given the purpose of this experiment it is clear that the IAF on the day of recording must be used. This variation in IAF over time also highlights the need for the simultaneous acquisition of the EEG and fMRI data to ensure exactly the same brain activity is measured as variations cannot be predicted.

Subject	IAF on Day of Screening	IAF on Day of Full study
1	10.7±0.2	9.6±0.3
2	10.6±0.05	10.3±0.1
3	8.8±0.1	8.6±0.05
4	9.9±0.2	9.4±0.1
5	9.5±0.1	9.8±0.2
6	11±0.1	11.1±0.05
7	10.6±0.05	10.5±0.1
8	10.6±0.3	10.3±0.2
9	9.6±0.2	9.8±0.3

Table 9.1: The variation of IAF between screening and the day of the full experiment. Errors show the full width three quarters maximum.

The IAF of the subject was then defined as the frequency of the peak in the Fourier transform in the frequency range 8-12 Hz with the subjects eyes closed. For the majority of subjects this peak was sharp with an uncertainty of approximately 0.2 Hz in the definition of the IAF. The IAF measured in this session agreed with the IAF recorded in the screening session to within 0.5 Hz in all subjects. With the IAF defined, stimuli were presented at (0.6, 0.8, 0.9, 1, 1.1, 1.2, 1.4)×IAF (these factors were termed 'IAF scaling factors'). Stimuli of different frequencies were presented pseudo-randomly across trials, with a total of 5 trials per frequency. For each frequency the light was on for 15 ms of the period of the flashing stimulus, where:

$$period = \frac{1}{scaling\ factor \times IAF}$$

This followed the methods used by Koch *et al* [28] as closely as possible. In each cycle the stimulus was on for 8 s and off for 20 s. These parameters were chosen to ensure the maximum in the BOLD response due to the driving frequency was reached without compromising patient comfort by making the experiment long. It was not necessary to enable the alpha power to build up, as in Experiment 1, thus allowing a reduction in the off period relative to that used in Experiment 1. 470 volumes of fMRI data were acquired resulting in a scan duration of approximately 17.5 minutes.

9.4 Analysis

9.4.1 General

9.4.1.1 fMRI

Image processing (realignment, and spatial smoothing with a 3 mm FWHM Gaussian kernel) was carried out using SPM5 (FIL, London). After realignment, two subjects' data were removed from further analysis for either experiment as the motion parameters were greater than a voxel size and therefore the EEG and fMRI data quality were assumed to be poor. fMRI models were set up for all trials within an experiment with correction for global effects and use of standard filtering (high pass cut-off at twice the trial length and the canonical hrf as a temporal smoothing kernel). The results of this analysis, thresholded at $p<0.001$ (corrected), were used to identify regions of interest (ROI) in the visual cortex for each subject.

9.4.1.2 EEG

Off-line EEG signal correction for both studies was based on averaging and then subtracting gradient and pulse artefacts, as implemented in Brain Vision Analyzer [38, 39], and described in previous chapters. Gradient artefact correction employed an artefact template formed from the average over all *TR*-periods, using the scanner-generated markers. Pulse artefact correction was based on methods developed in Chapter 6 where R-peak markers derived from the VCG trace are used [36]. After artefact correction, data were down-sampled to 600 Hz sampling rate using the 'change sampling rate' function within Analyzer and then exported into MATLAB

(Mathworks). A regularised vector beamformer was used for further analysis. The precise details of the beamformer analysis are described in the context of the different experiments below.

9.4.2 Experiment 1: Oscillatory rhythms and the BOLD response

Data from one further subject had to be removed from analysis for this experiment as it was clear that they had fallen asleep during the experiment. Evidence that this subject had fallen asleep came from analysis of the BOLD and driven responses which showed little neuronal activity after the first 10 trials. Also motion parameters from the EPI data showed a sudden movement suggesting a sudden relaxing of the head, indicative of the subject falling asleep. Also when asked, the subject said they thought they might have fallen asleep giving further justification for the exclusion of this subject.

9.4.2.1 EEG

Following the initial artefact correction described above, the vector beamformer described in Chapters 4 and 8 was applied to the EEG data [40, 41] so as to further improve artefact rejection and allow the spatial localization of electrical activity [40]. The presence of artefacts within these data could severely affect the results since unaveraged fluctuations due to spontaneous changes in brain activation were being measured. In order to localise stimulus related changes in alpha power, a pseudo-T statistic, Ŧ, was calculated for each voxel within the source space using data in the frequency band of interest, 8-12 Hz. The active window was taken to be $0<t<4.5$ s, and the passive window $5<t<9.5$ s where the stimulus onset was at $t=0$ s and calculations followed Equation 4.9. From the Ŧ-map, the location in the head that produced the maximum change in power between the active and passive states in the frequency band of interest (in this case a negative value denoting the desynchronisation of alpha power on stimulus presentation) was identified and chosen as the site of a virtual electrode (VE). This process was repeated for the frequency band 15.5-16.5 Hz in which the driven neuronal activity was largest. For each virtual electrode position a time course was subsequently obtained for the x-, y-

and z-dipolar components. The alpha power preceding each stimulus presentation was calculated using Equation 9.1

$$Q^2 = Tr\left|\mathbf{W}^T\mathbf{C}\mathbf{W}\right| \qquad [9.1]$$

where Q^2 is the power, **W** are the beamformer derived weights and **C** is the covariance matrix of the data (refer to Chapter 4 and [41] for more details). This expression was used to calculate the alpha power for both the 2 s immediately preceding stimulus presentation and the 0.42 s immediately preceding stimulus presentation. The shorter time window was chosen because the majority of similar EEG studies conducted previously have looked at the effected of the alpha power in a 0.15 s - 1 s time window preceding the stimulus [8, 10-12, 42]. Power projected using Equation 9.1 can be underestimated severely if the total duration of data used in construction of the covariance matrix (and weights) is too small [43]. A window width of 0.42 s was therefore chosen as the shortest possible time frame that would yield an accurate power estimate (due to the nature of the algorithm implemented), and be comparable to previous EEG studies. The longer time window was also chosen to probe the longer term effects of the alpha power on the BOLD response. Once the powers had been calculated, trials were sorted and binned into quartiles according to the preceding alpha power. The average power of trials in each bin was recorded, and the error was taken to be the standard deviation over the trials within the bin. This process was repeated for the driven frequency band where the power within the 4.5 s period of stimulus presentation was calculated and quartile bins were formed accordingly.

9.4.2.2 fMRI

A time course of the BOLD response was obtained from the ROI defined using the methods described in Section 9.4.1.1 and then segmented according to the onset of the stimuli. The average haemodynamic response of the trials falling into each of the bins obtained from EEG analysis was calculated (10 trials per bin). Due to the jittering of the stimulus relative to the fMRI acquisition, dividing up the trials involved interpolating the data before trial segmentation. The BOLD response was taken to be the percentage change between average signal over the range ±1.5 s around the time of the maximum response and the baseline (last 5 s of data from the averaged response for that bin). The errors were taken to be the standard deviation over individual trials. This procedure was carried out for the three different situations, binning according to the 0.42 s or 2 s of preceding alpha power or the power of the driven response. Correlations between the EEG and the BOLD responses were then studied.

9.4.3 Experiment 2: Stimulus Frequency Variation

Data from one subject (a different person from that excluded in Experiment 1) had to be removed from analysis for this experiment as they fell asleep during this part of the study. This subject was identified to be asleep from observations similar to those made in Section 9.4.2.

9.4.3.1 EEG

Pseudo-T statistical (Ŧ) maps showing the spatial location of the driven activity were constructed. In order to make the beamformer sensitive to the driven activity, rather than alpha desynchronisation, it was necessary to choose data in which the naturally occurring oscillatory neuronal responses were attenuated as much as possible. This was achieved by averaging over all the trials at either (0.6 or 1.4)×IAF. These frequencies are the furthest removed from the IAF of the subject and therefore the least likely to be affected by residual oscillatory rhythms when creating the Ŧ-map. The data were filtered at (0.6 or 1.4)×IAF±2Hz and a Ŧ-map of the driven response was obtained. A timecourse of the electrical response from a VE placed at the site of the peak activity in the Ŧ-map was obtained for each driving frequency. The Fourier transform of the timecourse for each IAF scaling factor was calculated and the maximum power at the driving frequency ±0.1 Hz was found. It is interesting to note that because the stimulus was only on for 15 ms within each cycle of the stimulus (rather than half of the cycle) the maximum driven response was found at the driving frequency rather than twice this frequency (the maximum response occurs at twice the stimulus frequency when square wave stimuli are used as was the case in Chapters 6, 8 and the first experiment of this study).

9.4.3.2 fMRI

Using the ROI described in Section 9.4.1.1, the haemodynamic responses corresponding to each scaling factor were averaged together to form an average haemodynamic response for each frequency of stimulation The magnitude of the BOLD response was then calculated for each frequency as described in Section 9.4.2.2.

9.5 Results and Discussion

9.5.1 Experiment 1: Oscillatory rhythms and the BOLD response

A key to the confidence level one can place in the results presented in any work is the quality of the experimental measurements. This is paramount for this study, as natural fluctuations in responses to the same stimulus are being considered (on a single trial basis in the EEG recordings, and after averaging over only a few trials in the case of the fMRI data). Figure 9.3 shows example EEG and BOLD responses averaged over all trials falling in the upper and lower quartiles, after ordering according to the strength of the preceding 0.42 s of alpha power or according to the driven response. The EEG responses shown correspond to the envelope of oscillatory activity, given by the absolute value of the analytical signal derived from [44] the VE component showing the greatest response in the frequency band of interest. The position of the VE was determined using T-maps, as shown for a representative subject in Figure 9.9. The displayed responses were generated by averaging over the 10 trials forming the upper or lower quartiles. This figure shows that the EEG and BOLD responses are well characterised by averaging over 10 trials and thus demonstrate the high quality of data obtained in this study. A clear difference in the amplitude of the EEG responses in the top and bottom quartiles according to each binning criteria can be seen. However, the differences in the associated BOLD responses are less prominent and will be discussed in depth in the following sections.

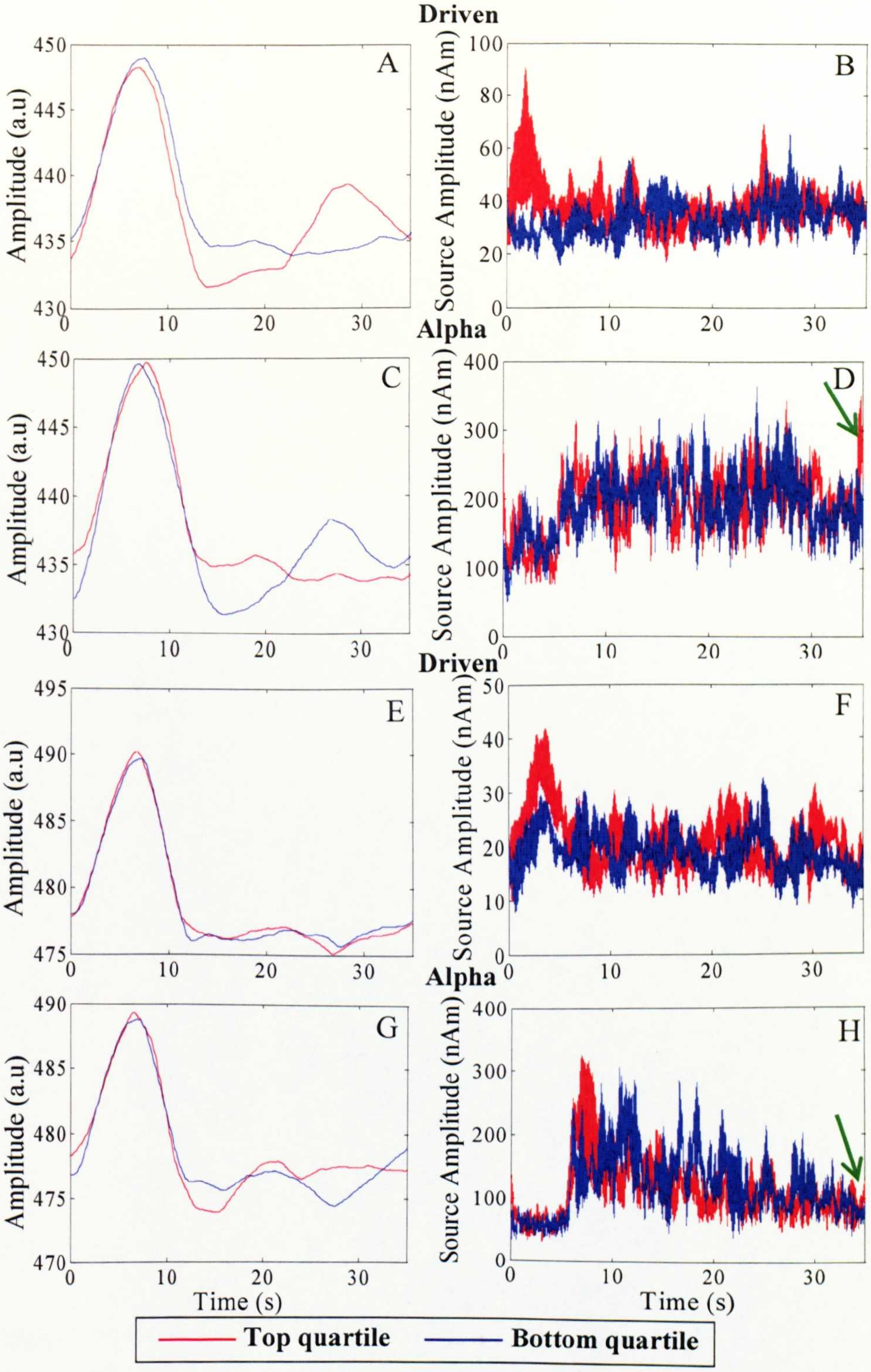

Figure 9.3: The driven (B&F) & alpha power (D&H) VE responses in the top and bottom quartiles when binned according to the driven power and preceding 0.42 s alpha power (marked with arrows) respectively, for two subjects (Subject 1:A-D, Subject 2:E-H). The associated haemodynamic responses are shown in A, C, E & G. The associated ~~T~~-maps for subject 2 are shown in Figure 9.9. For each figure, 0 s corresponds to the stimulus onset.

Figure 9.4 illustrates the quality of the EEG data on a single trial basis. It shows a section of the VE trace (from the component with maximum response) of the driven and alpha power response for one individual. Figure 9.4A shows the response in the driven frequency band revealing the clear onset and duration of each response as well as showing the variability in amplitude across trials. Figure 9.4B shows how the alpha power fluctuates significantly across trials and this figure also exhibits the reduction of power in this frequency band immediately after stimulus presentation. From this figure it is therefore clear that calculation of the power in the EEG response on a trial by trial basis was justified.

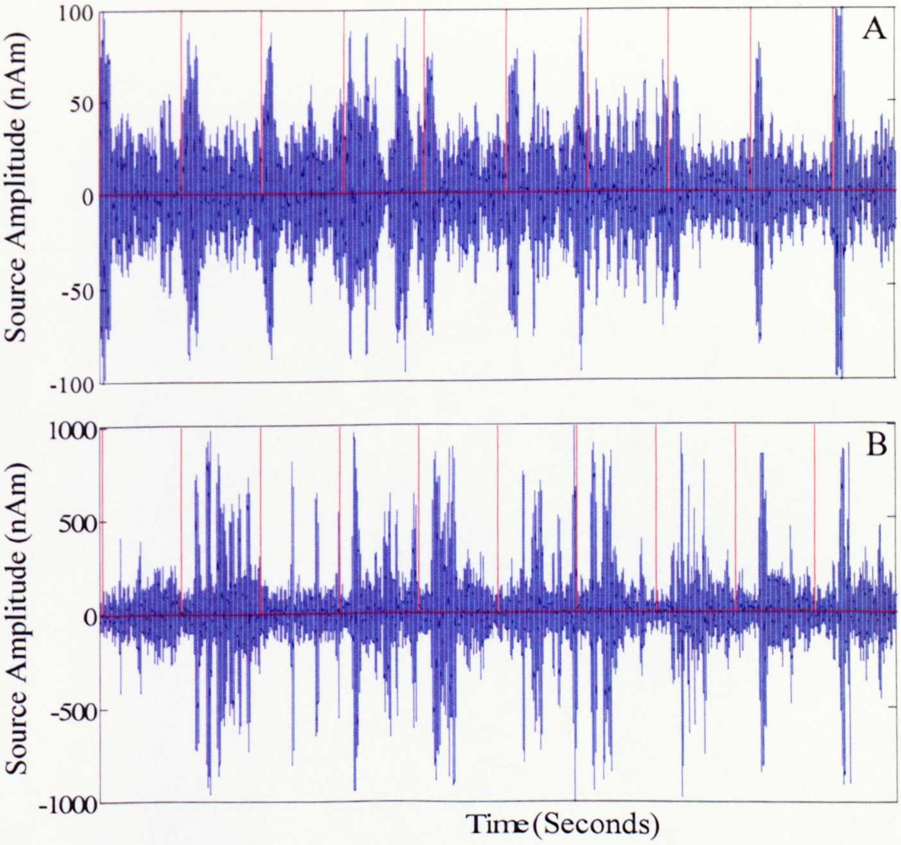

Figure 9.4: The 15.5-16.5 Hz driven (A) and 8-12 Hz alpha power (B) responses recorded from one component of the VE. Stimulus presentation is denoted by the red vertical lines (35 s between presentation of stimuli).

The percentage change in the haemodynamic response when binned into quartiles according to the driven response for each individual is shown in Figure 9.5. This figure shows that there is no obvious correlation between the power of the driven response measured with the EEG, and the BOLD response. Although the error bars are not shown on this figure (to make the figure easier to interpret) the standard deviation of the BOLD responses within a quartile was, on average, around 0.5-1 %. Therefore in the vast majority of subjects there was no significant change in the BOLD response within the error range, despite the EEG driven response varying by approximately a factor of two between the upper and lower quartiles over all the subjects.

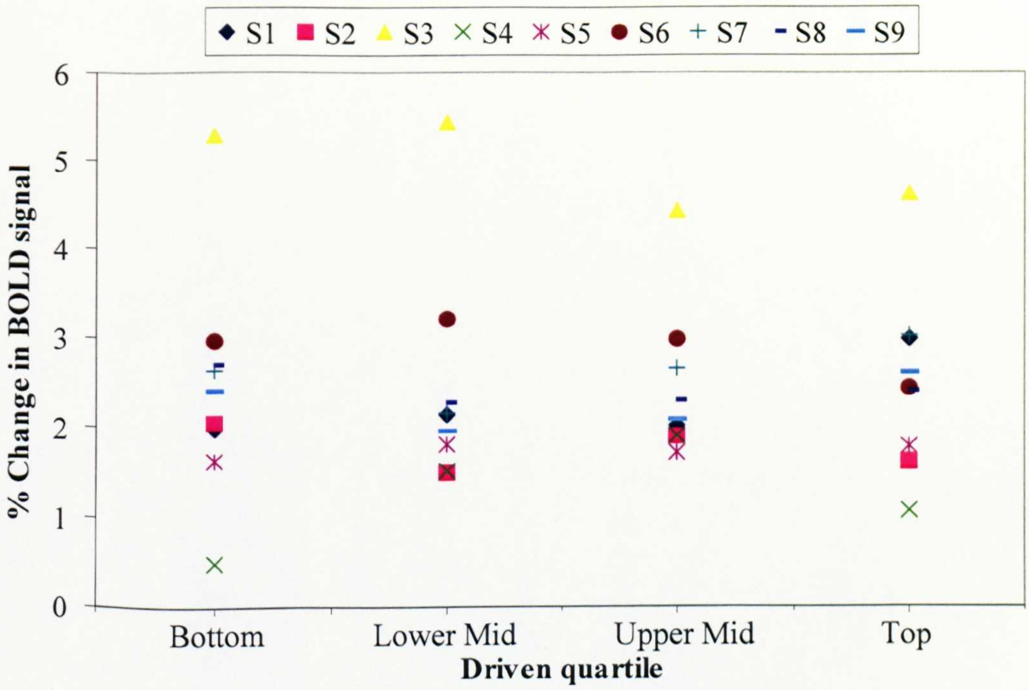

Figure 9.5: The percentage change in BOLD signal ((max-min)/max in hrf) for each subject when the BOLD responses are binned according to the driven power (15.5-16.5 Hz) during stimulation.

Similar plots are shown in Figure 9.6 for the case where the data has been binned according to the alpha power in the 0.42 s preceding the stimulus (Figure 9.6 A) or according to the alpha power in the 2 s preceding the stimulus (Figure 9.6 B). These graphs again show little correlation between the alpha power and the strength of the BOLD response. The errors in the BOLD signal have again not been shown for purposes of clarity, but were similar in size to the driven response errors on average lying between 0.6-1.1 %. These plots also show that, for the majority of subjects, binning the BOLD responses according to the preceding alpha power in a short or long time window did not produce a significant difference in the strength of the average response across bins. This is despite the fact that in the case of the shorter time window, there is a variation of approximately a factor of four in the preceding alpha power in the bottom and top quartile. It does appear that in some subjects there is a slight increase in the BOLD response between the top and bottom quartiles while in others there is a slight decrease. These differences between subjects mean that no within subject correlations between the variations in strength of the BOLD response and electrical activity corresponding to either the driven response or the alpha power preceding stimulation were found, despite the high quality of the acquired data.

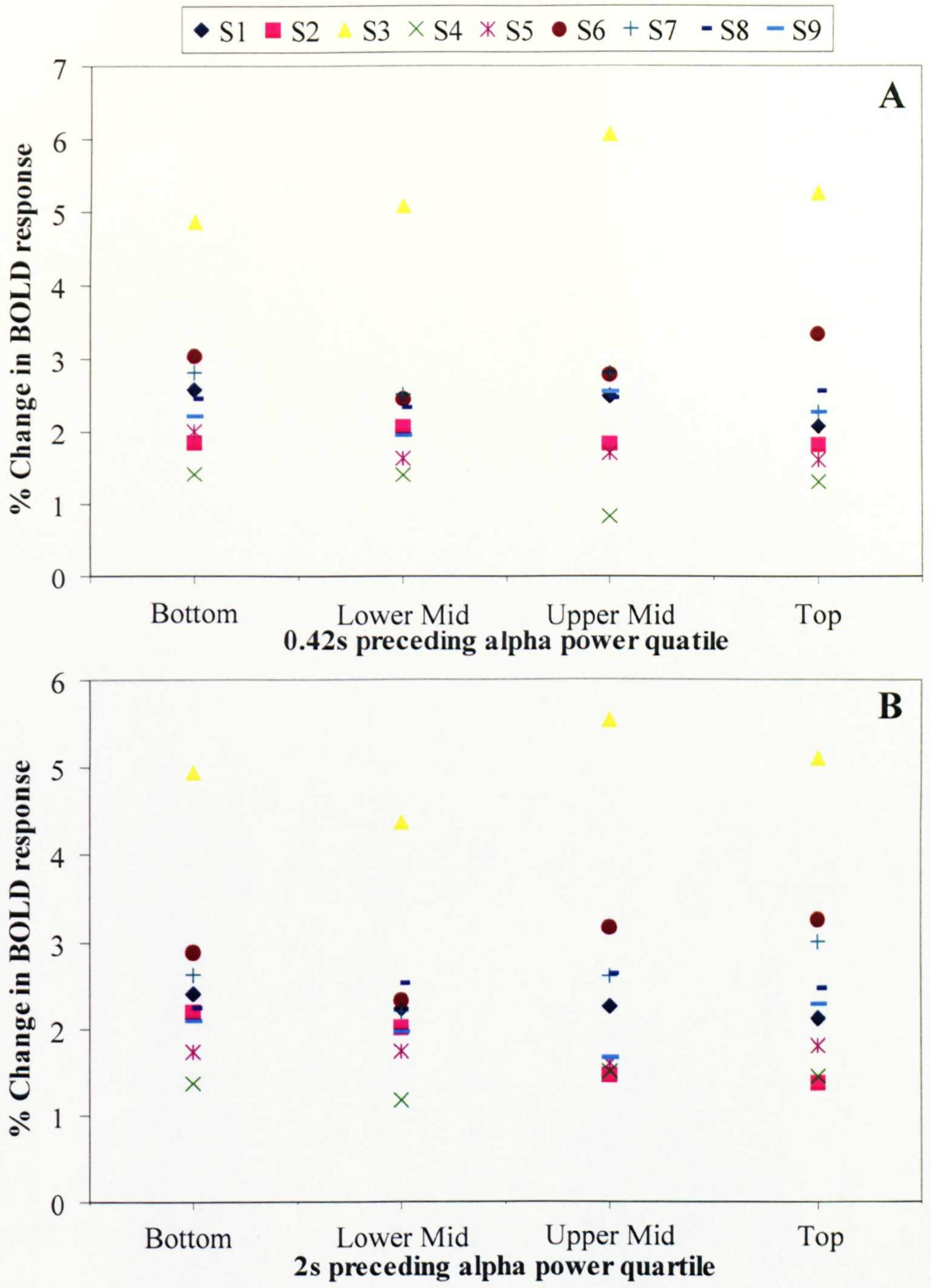

Figure 9.6: The percentage change in the BOLD signal ((max-min)/max in hrf) for each subject when the BOLD responses are binned according to the alpha power (8-12 Hz) in either the 0.42 s (A) or 2 s (B) preceding stimulus onset.

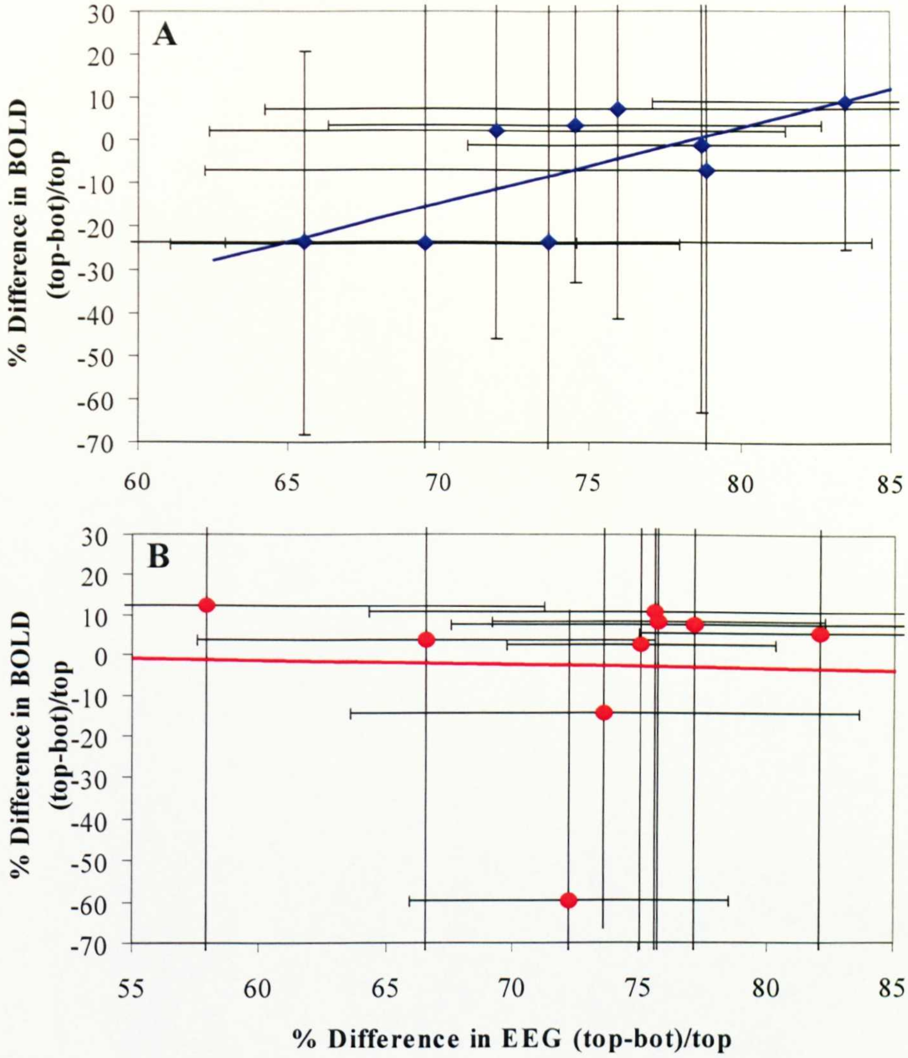

Figure 9.7: Average fractional difference of the BOLD response between the upper and lower quartiles binned according to the preceding 0.42 s (A) or 2 s (B) of alpha power, plotted against the similar fractional difference in preceding alpha power for each subject. Errors bars show the standard deviation of the signals within the bins, with lines of best fit shown in colour.

A correlation between the range of measured alpha power levels in the 0.42 s preceding stimulation and the range of strengths of the BOLD response was found however, when considering variation across subjects. Figure 9.7A shows the fractional difference in the BOLD response measured in the top and bottom quartiles (binned according to the alpha power in the preceding 0.42 s) as a function of the similarly calculated fractional difference in alpha power in the preceding 0.42 s. The quantities on the axes of these graphs were calculated according to the following equations:

$$\%\ Difference\ in\ EEG = 100 \times \frac{P_{top} - P_{bottom}}{P_{top}}$$

where P_{top} is the average power in the top quartile for a single subject and P_{bottom} is the similar power for the bottom quartile.

$$\%\ Difference\ in\ BOLD = 100 \times \frac{\Delta BOLD_{top} - \Delta BOLD_{bottom}}{\Delta BOLD_{top}}$$

where $\Delta BOLD_{top}$ is the BOLD response (see Section 9.4.2.2) for the top quartile of responses when binned according to the EEG data for a single subject and $\Delta BOLD_{bottom}$ is the similar measure for the bottom quartile responses.

In Figure 9.7A the line of best fit has an R^2 value of 0.4801 corresponding to p=0.05 showing that this correlation is significant. This correlation is not observed however, when the BOLD responses were sorted according to the preceding 2 s of alpha power (R^2=0.007 for the line of best fit) as can be seen in Figure 9.7B. Although neither of the correlations would be significant at the criterion of $p<0.05$ if a rigorous Bonferroni correction were applied to allow for the fact several hypothesis have been tested and therefore should be regarded with some caution until replication. The difference in the significance of the correlations suggests that the correlation found when binning according to the alpha power in the 0.42 s preceding a stimulus is unlikely simply to be an artefact of the analysis techniques.

The correlations observed here show that there is no significant correlation between the alpha power in the 2 s period preceding a simple flashing visual stimulus and the BOLD response in the visual cortex either within or between subjects. However, although there is no apparent intra-subject correlation between the BOLD response and alpha power in a short time window (0.42 s) preceding the simple visual stimulus, when a range of response levels across subjects are considered a pattern emerges. These findings do not support the initial hypothesis that an increase in preceding alpha power leads to a decrease in the BOLD response for visual stimulation, thus suggesting that the alpha rhythm does not play a purely inhibitory role. The results show that the higher preceding alpha power causes an increase in the BOLD response in some subjects and a decrease in others, compared to the response occurring when the alpha power is low (Figure 9.7A). This difference in responses across subjects is accompanied by a difference in the magnitude of the EEG response across the subjects resulting in the observed inter-subject correlation. One may postulate that the magnitude of the change in EEG response between the top and bottom quartile may reflect differences in the neuronal activity occurring at the time of stimulus presentation (*i.e.* the generators of the neuronal activity that is measured are different). If this is the case one can propose an explanation of the correlation observed in Figure 9.7A along the following lines. Those subjects where the variation in alpha power immediately preceding stimulation across trials is small could be showing the signature of a neuronal network whose processing of internal stimuli (thinking, daydreaming or using memory for instance) inhibits the processing of external stimuli and thus a larger BOLD response is observed when the alpha power is low preceding stimulation. On the other hand, those subjects who show a large difference in the amplitude of the alpha power between quartiles could employ a network of neuronal activity which does not inhibit the processing of external stimuli and in fact enhances that processing. This finding is complemented by the work of Diukova *et al* [20] and Gonçalves *et al* [19] who both reported differences between subjects when considering the correlations of the BOLD response and alpha power at rest, suggesting differences in the neuronal networks that are operating. The differences in the correlation between the VEP and the alpha power that have been reported by various groups [5, 10] are also consistent with this finding. However, correlation of the VEP to the preceding alpha power has not been considered in this study.

Possible explanations for different neuronal networks operating for different subjects to produce recorded alpha power are numerous [4, 22]. It may simply be because of the varying thought processes of the different subjects. However, it is also worth noting that it may be to do with a biorhythmic cycle of the body (the ultradian rhythm [45]) which varies over a period of approximately 90 minutes. The correlation of the P300 to alpha power has been shown to vary on this time scale within subjects [45]. In our study the time of scanning was not taken into account and therefore it is possible that the cause of the differences in the alpha power measured across subjects was partly due to the natural biorhythmic cycles of the subjects.

Interestingly, when considering the same correlation between BOLD responses in the upper and lower quartiles when sorting according to the strength of the driven response, no obvious correlation between the EEG and BOLD was found (Figure 9.8). The line of best fit has an R^2 value of 0.2519 corresponding to p=0.2 and thus the correlation is insignificant although clearly a greater correlation is present than that identified when binning according to the 2 s of alpha power preceding the stimulus (Figure 9.7B).

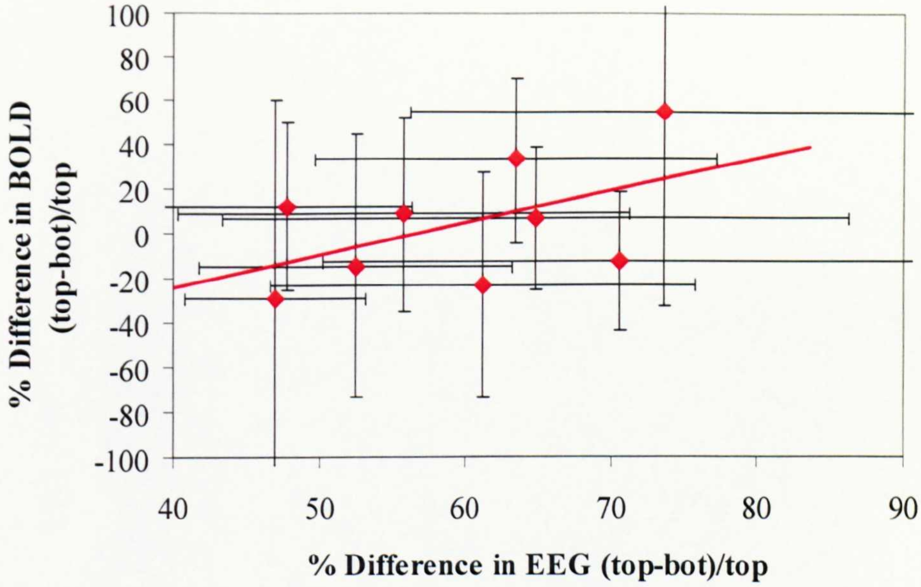

Figure 9.8: Average fractional difference of the BOLD response between the upper and lower quartiles binned according to the driven power, plotted against the similar fractional difference in driven power for each subject. Error bars show the standard deviation of the signals within the bins, with the line of best fit shown in colour.

On initial inspection, this lack of correlation appears a very surprising and somewhat alarming result since generally within the neuroscience community it is understood that the strength of the BOLD response depends upon the level of the neuronal activity produced by a stimulus. This belief is well-founded, with a large literature showing that the BOLD response is a reflection of the strength of neuronal activity.

A particularly pertinent result, which reflects this relationship is the positive correlation between the BOLD and driven response for high and low contrast visual stimuli reported in recent work using simultaneous EEG and fMRI [40]. However, as mentioned numerous times throughout this work the exact mechanisms underlying the BOLD response are not fully understood. In work by Stevenson *et al [46]*, where MEG and fMRI have been used to study correlations between BOLD and neuronal activity produced by visual stimuli in the form of drifting gratings of varying contrasts, it has been shown that the VEP varies linearly with stimulus contrast, whereas the BOLD response is tuned and reaches a maximum before the maximum contrast is reached. Therefore in Stevenson's work [46] there is a discrepancy between the behaviour of the BOLD response and VEP. Her work has shown that the gamma response also behaves similarly to the BOLD response, but does not match it entirely and, in fact, the beta response appears to best match the BOLD response in terms of the spatial localisation. Therefore it may be that the driven response measured with EEG does contribute to the amplitude of the BOLD response to some extent but the contributions from the other frequency bands of this rich neuronal signal result in the correlations measured in the study described in this chapter to become insignificant. Figure 9.7 also supports this explanation since it shows that the alpha power preceding the presentation of the stimulus has an effect on the amplitude of the BOLD response and therefore the driven component of the EEG signal is unlikely to be solely responsible for the strength of the BOLD response.

Another plausible reason for the lack of correlation between the strength of the driven response and the BOLD response could be the effect of phase resetting. If indeed, the driven response is due to the phase resetting of neuronal activity already present within the brain [12] then this process will not necessarily cause an increase or decrease in energy demands in the brain and therefore the BOLD response would not change in amplitude as the strength of the driven response varied. It is also possible that the measured correlation of the driven response with the BOLD response is small due to the way in which we selected the ROI, from which the BOLD response was measured. Since the selected ROI covered the whole of the primary visual cortex (Figure 9.9) it is possible that any tuning of a specific focal area of the visual cortex due to the driven response has been obliterated by the dominance of the signals from the rest of the ROI. Investigating whether this hypothesis is correct could be done in a number of ways, such as using the time course from the driven response as the regressor in the model of the haemodynamic response and seeing if the resulting parametric map differed significantly from that obtained using the simple box-car model. Alternatively, one could divide up the visual cortex according to either retinotopic maps or anatomical landmarks and take smaller ROI's which may reveal a correlation between the VEP and the BOLD response in a specific area of the visual cortex. However, there was not sufficient time available but may be investigated in future work by the author.

Another possible explanation of the lack of correlation between the BOLD and driven responses is that the fluctuations in the responses measured in the EEG data are due to noise rather than differences in brain activity. These noise sources may be relate to the hostile environment in which the scanning took place, although the good quality of the EEG data shown in Figures 9.3 and 9.4 mean that this is unlikely to be the case. Performing the same study on subjects outside of the MR scanner using EEG alone would enable us to see if the fluctuations within the driven responses were of similar amplitudes to those measured during simultaneous EEG-fMRI recordings which could eliminate residual scanner artefacts as an explanation of the low correlation.

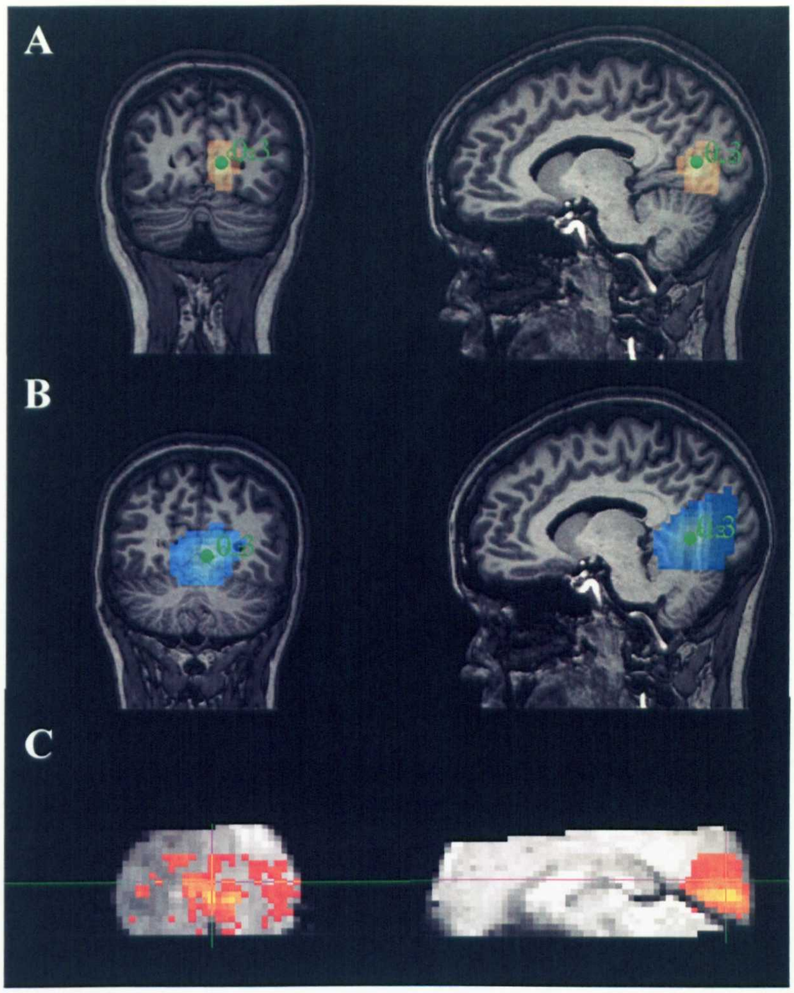

Figure 9.9:~~T~~-statistic images for one, representative subject. A: the EEG activation due to the driven response in the 15.5-16.5 Hz frequency band and B: the areas showing significant event-related desynchronisation in alpha power (8-12 Hz). C shows the BOLD activation thresholded at p=0.001 corrected with active areas outside the visual cortex removed. This region was taken to be the ROI for the subject and used as a mask to obtain the haemodynamic response. The green dots and numbers indicate the position of the virtual electrodes for this subject and the ~~T~~--values at those points.

9.5.2 Experiment 2: Stimulus Frequency Variation

Figure 9.10 shows how the magnitude of both the BOLD and driven response vary with the frequency of stimulation. In this figure, the amplitude of each response has been normalised to the mean response amplitude over all frequencies, on a subject by subject basis. In Figures 9.10A&B the strengths of the BOLD and driven responses are plotted against the frequency expressed in terms of each subject's IAF (IAF scaling factor). The lines of best fit are quadratic curves fitted to the central five frequencies. These central frequencies around the IAF were chosen for fitting so that any effects specific to frequencies close to the IAF could be explored. Given the findings of previous studies [23, 25-27], a peak in the BOLD response was expected around 8 Hz, but if there were any localised differences in this curve in close proximity to the IAF they may be identified by choosing this narrow set of frequencies. Also by selecting these frequencies the band of interest was approximately the same as the alpha frequency band which was of most interest in this study. It is clear from the curves, fitted to the central frequencies, that while the BOLD response appears to reduce slightly when the stimulus frequency is close to the IAF (Figure 9.10A), the associated power of the EEG response increases around the IAF (Figure 9.10B).

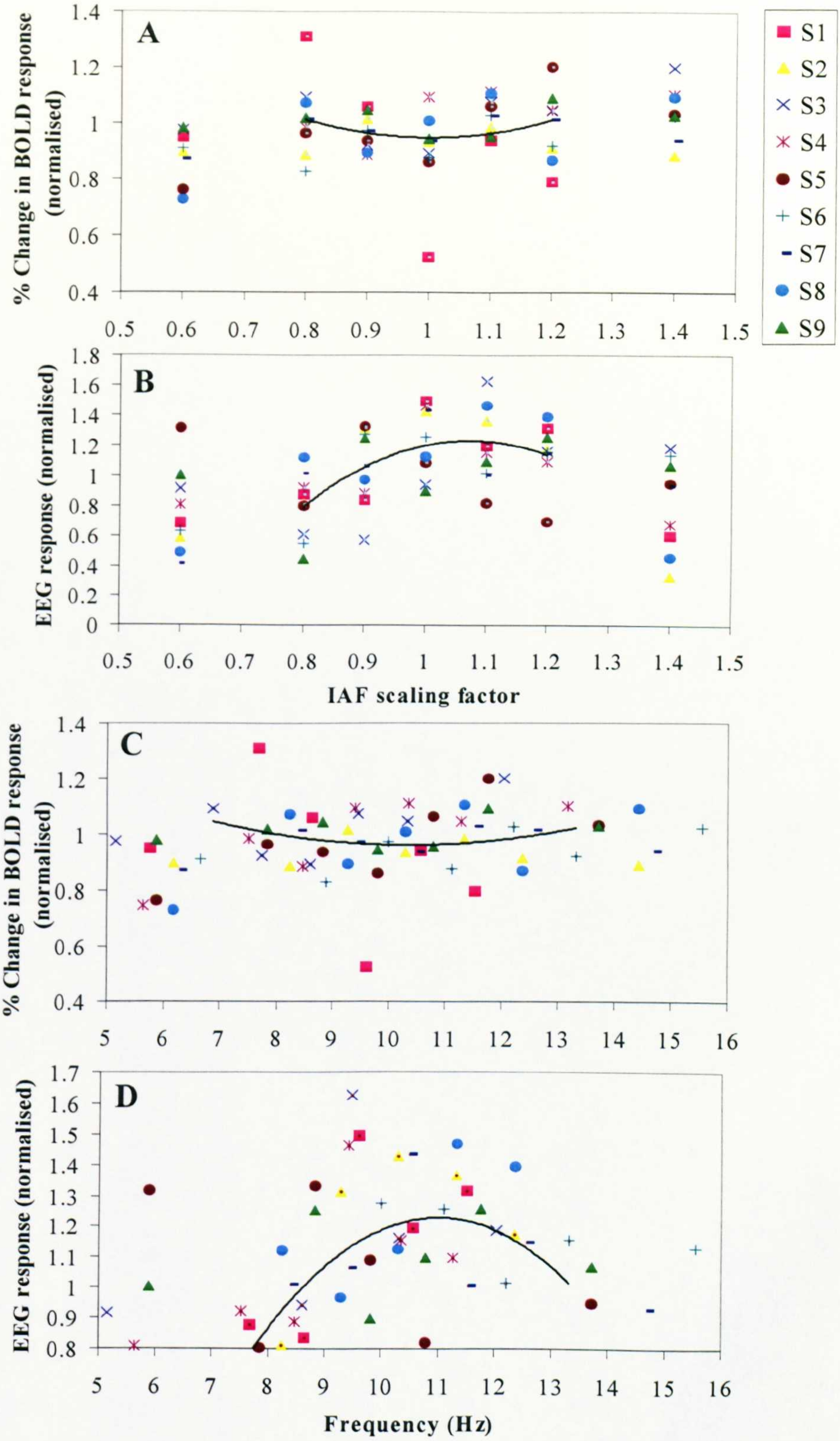

Figure 9.10: The normalised BOLD (A&C) and EEG (B&D) responses to stimuli presented at a variety of frequencies relative to subject's IAF plotted against IAF scaling factor (A&B) or frequency (C&D). Quadratic lines of best fit show general trends.

To test for the significance of these fits, an analysis of variance (ANOVA) statistical test was performed on each curve shown in Figure 9.10. This is based on an F-test which represents the ratio of the improvement in prediction that results from fitting the model, relative to the inaccuracy that still exists in the model. Therefore a high F-ratio suggests the model fits the observed data [47]. Here the quadratic fits are tested against the null hypothesis of a basic model which is a constant value equal to the mean of the data. Performing an ANOVA statistical test on the central five frequencies showed the curves had a significance of $p=0.007$ and $p=0.134$ for EEG and BOLD responses respectively. Although considering this frequency range the BOLD response curve appears to only show a trend which is not statistically significant, when the three central frequencies are considered then $p=0.024$ showing that the dip in the BOLD response at the IAF is significant and the peak in the EEG response around the IAF is also significant. Plots C&D in Figure 9.10 show the same data but plotted against absolute frequency rather than frequency scaled to the IAF. Again the lines of best fit are fitted to the central frequencies which are defined to be in the alpha frequency band (*i.e.* 8-12 Hz). The frequency of the minimum in the strength of the BOLD response is at approximately 10.5 Hz whilst the peak in the EEG response is at approximately 11 Hz. Using these lines of best fit, the ANOVA statistical test was performed, the curves were found to have a significance of $p=0.055$ and $p=0.125$ for EEG and BOLD respectively. Neither of these values show significance and when a narrower frequency band (9-11 Hz) was considered, the significance reduced further.

Although from Figure 9.10B it is unclear if the peak in the driven response occurs exactly at the IAF or 1.1×IAF, other groups [28-30] have found a peak at the IAF of the subject. The dip that is evident in the BOLD data shown in Figure 9.10A has not been documented in previous studies [23-27]. This may be purely because of the frequencies of stimulation employed in previous studies as the smallest steps between stimulation frequencies in the alpha frequency band was 2 Hz [25, 27] meaning the dip may have been missed. Even with smaller increments in the frequency of stimulation this dip may not have been observed since it cannot easily be seen when averaged across subjects, since, as shown in Figure 9.10C the frequency of this dip clearly varies across subjects. It is harder however, to understand why this dip was not observed by Koch *et al [28]* since the stimulation that they used was very similar to that employed in our study, with similar small increments in the frequency of stimulation being used. Koch *et al* did however, make their subjects close their eyes which may have caused them to respond in a different way to the stimuli. Also the techniques used to measure the responses in the two studies (NIRS and BOLD) are of course different. This may explain why they did not observe an increase in deoxyhaemoglobin corresponding to the decrease observed in the BOLD data. The findings related to the driven response agree between the two studies however, suggesting that the responses to the stimuli were similar in both cases and the difference in measurement techniques is most likely to be the explanation for the apparent discrepancy in the haemodynamic measurements.

The reason for the dip in the BOLD response and the peak in the EEG response may be due to a resonant effect of the neuronal networks. As discussed in Section 9.2, the networks responsible for the alpha power are in use regularly and are likely to be extensive with strong synaptic links. If a stimulus is presented at the frequency of natural oscillation of these networks a resonance may be set up within them thus causing a large driven response to be recorded. In general, driving a system at its resonant frequency is less energy demanding than if one drives it off resonance [32] thus potentially explaining the dip in the BOLD response corresponding to the peak in the driven response. This explanation for the observed results corresponds to the excitatory theory for the alpha network; if the alpha network was purely inhibitory then this premise would not hold.

9.6 Conclusions

By implementing the methodological developments described in the previous chapters of this thesis we have recorded simultaneous EEG and fMRI data of high quality in functional experiments involving visual stimulation. The high quality of these data has enabled comparisons of the EEG and BOLD measurements using averages over a small number of trials. This demonstrates that investigations of the effect of natural fluctuations in brain activity during stimulus presentation can be conducted in a simultaneous manner allowing a greater understanding of brain function to be achieved. Using the methodology described in this thesis, the high data quality which has been demonstrated in this chapter, has been exploited in other studies that have recently been carried out at the Sir Peter Mansfield Magnetic Resonance Centre. This includes recording fluctuations in the gamma frequency band whilst performing fMRI at 7 T [48]. This is the first demonstration, to our knowledge, of the recording of high frequency neuronal activity in combined EEG-fMRI at ultra-high field. Also investigations into the correlation between the driven response and the BOLD response due to visual stimuli of varying contrasts have been carried out [40]. These studies point towards future work which will be discussed in more detail in the final chapter.

The results from Experiment 1 suggest that significant correlations between the preceding alpha power or driven response and the BOLD response are not apparent on a trial by trial basis in single subjects. However, when the range of response levels across subjects are considered a pattern emerges linking the alpha power immediately preceding a visual stimulus and the BOLD response. With the data available from this study a precise explanation for these findings is not possible, although they may reflect the operation of more than one type of network in the generation of the alpha rhythm across different subjects. However, further investigations where the phase of the preceding alpha fluctuations as well as responses in other frequency bands such as beta and gamma are considered, are needed before such an explanation can be deemed conclusive.

The data from Experiment 2 suggests that resonance within neuronal networks is set up when a stimulus is presented at the IAF of the subject. This resonant effect results in an increased EEG response, but reduced BOLD response at the IAF of the subject. However, since these results contradict previous findings from Koch *et al* [28] further investigations should be carried out to corroborate these results. These investigations could include conducting similar investigations on more subjects and using a range of stimulus frequencies spanning the maximum in the individual's beta band response to see if similar phenomena are observed.

9.7 References

1. Berger, H., *Uber das Elektrenkephalogramm des Menschen.* Arch. Psychiatrie Nerv, 1929. **87**: p. 527-570.
2. Berger, H., *On the Electroencephalogram of Man.* Electroencephalography and Clinical Neurophysiology, 1969. **Supplement 28**: p. 37-73.
3. Niedermeyer, E. and F. Lopes Da Silva, *Electroencephalography: Basic Principles, Clinical Applications and Related Fields. Chapter: The normal EEG of the waking adult.* 3rd ed. 1993, Baltimore: Williams and Wilkins. 1164.
4. Klimesch, W., P. Sauseng, and S. Hanslmayr, *EEG alpha oscillations: The inhibition-timing hypothesis.* Brain Research Reviews, 2007. **53**: p. 63-88.
5. Rahn, E. and E. Basar, *Enhancement of visual evoked potentials by stimulation during low prestimulus EEG stages.* International Journal of Neuroscience, 1993. **72**: p. 123-136.
6. Basar, E., M. Schurmann, C. Basar-Eroglu, and S. Karakas, *Alpha oscillations in brain functioning: an integrative theory.* International Journal of Psychophysiology, 1997. **26**: p. 5-29.
7. Ergenoglu, T., T. Demiralp, Z. Bayaraktaroglu, M. Ergen, H. Beydagi, and Y. Uresin, *Alpha rhythm of the EEG modulates visual detection performance in humans.* Cognitive Brain Research, 2004. **20**: p. 376-383.
8. Hanslmayr, S., A. Aslan, T. Staudigl, W. Klimesch, C. Herrmann, and K.-H. Bauml, *Prestimulus oscillations predict visual perception performance between and within subjects.* Neuroimage, 2007. **37**: p. 1465-1473.
9. Hanslmayr, S., W. Klimesch, P. Sauseng, W. Gruber, M. Doppelmayr, R. Freunberger, and T. Pecherstofer, *Visual discrimination performance is related to decreased alpha amplitude but increased phase locking.* Neuroscience Letters, 2005. **375**: p. 64-68.
10. Brandt, M.E., *Visual and auditory evoked phase resetting of the alpha EEG.* International Journal of Psychophysiology, 1997. **26**: p. 285-298.
11. Brandt, M.E., B.H. Jasnsen, and J.P. Carbonari, *Pre-stimulus spectral EEG patterns and the visual evoked response.* Electroencephalography and Clinical Neurophysiology, 1991. **80**: p. 16-20.
12. Jansen, B.H. and M.E. Brandt, *The effect of the phase of prestimulus alpha activity on the averaged visual evoked response.* Electroencephalography and Clinical Neurophysiology, 1991. **80**: p. 241-250.
13. Intriligtor, J. and J. Polich, *On the relationship between EEG and ERP variability.* International Journal of Psychophysiology, 1995. **20**: p. 59-74.
14. Babiloni, C., F. Vecchio, S. Cappa, P. Pasqualetii, S. Rossi, C. Minussu, and P.M. Rossini, *Pre and poststimulus alpha rhythms are related to conscious visual perception: a high resolution EEG study.* 2006. **16**: p. 1690-1700.

15. Walter, W.G., *Normal rhythms: their devlopment, distribution and significance. In Electroencephalography (D.Hill and G,Parr (Eds)).* 1950, London: McDonald.

16. Goldman, R.I., J.M. Stern, J. Engel, and M.S. Cohen, *Simultaneous EEG and fMRI of the alpha rhythm.* Neuroreport, 2002. **13**(18): p. 2487-2492.

17. Laufs, H., A. Kleinschmidt, A. Beyerle, E. Eger, A. Salek-Haddadi, C. Preibisch, and K. Krakow, *EEG-correlated fMRI of human alpha activity.* NeuroImage, 2003. **19**(4): p. 1463-1476.

18. Laufs, H., K. Krakow, P. Sterzer, E. Eger, A. Beyerle, A. Salek-Haddadi, and A. Kleinschmidt, *Electroencephalographic signatures of attentional and cognitive default modes in spontaneous brain activity fluctuations at rest.* Proceedings Of The National Academy Of Sciences Of The United States Of America, 2003. **100**(19): p. 11053-11058.

19. Gonçalves, S.I., J.C. de Munck, P.J.W. Pouwels, R. Schoonhoven, J.P.A. Kuijer, N.M. Maurits, J.M. Hoogduin, E.J.W. Van Someren, R.M. Heethaar, and F.H. Lopes Da Silva, *Correlating the alpha rhythm to BOLD using simultaneous EEG/fMRI: Inter-subject variability.* Neuroimage, 2006. **30**(1): p. 203-213.

20. Diukova, A., P.F. Liddle, A. Plodowski, P.S. Morgan, and D.P. Auer. *Simultaneous recording of the alpha rhythm and fMRI-BOLD.* in *Human Brain Mapping.* 2006. Florence: Elsevier.

21. Cooper, N.R., R.J. Croft, S.J.J. Dominey, A.P. Burgess, and J.H. Gruzelier, *Paradox lost? Exploring the role of alpha oscillations during externally vs. internally directed attention and the implications for idling and inhibition hypotheses.* International Journal of Psychophysiology, 2003. **47**: p. 65-74.

22. Becker, R., P. Ritter, and A. Villringer, *Influence of ongoing alpha rhythm on the visual evoked potential.* Neuroimage, 2008. **39**(2): p. 707-716.

23. Fox, P.T. and M.E. Raichle, *Stimulus rate dependence of regional cerebral blood-flow in human striate cortex, demonstrated by positron emission tomography.* Journal of Neurophysiology, 1984. **51**(5): p. 1109-1120.

24. Hagenbeek, R.E., S.A.R.B. Rombouts, B.W. van Dijk, and F. Barkhof, *Determination of Individual Stimulus-Response Curves in the Visual Cortex.* Human Brain Mapping, 2002. **17**: p. 244-250.

25. Ozus, B., H.-L. Liu, L. Chen, M.B. Iyer, P.T. Fox, and J.-H. Gao, *Rate Dependence of human visual cortical response due to brief stimulation: An event-related fMRI study.* Magnetic Resonance Imaging, 2001. **19**: p. 21-25.

26. Thomas, C.G. and R.S. Menon, *Amplitude Response and Stimulus Presentation Frequency Response of Human Primary Visual Cortex Using BOLD EPI at 4T.* Magnetic Resonance In Medicine, 1998. **40**: p. 203-209.

27. Singh, M., S. Kim, and T.-S. Kim, *Correlation Between BOLD-fMRI and EEG Signal Changes in Responses to Visual Stimulus Frequency in Humans.* Magnetic Resonance In Medicine, 2003. **49**: p. 108-114.

28. Koch, S.P., J. Steinbrink, A. Villringer, and H. Obrig, *Synchronisation between Background Activity and Visually Evoked Potential Is Not Mirrored*

by Focal Hyperoxygenation:Implications for the Interpretation of Vascular Brain Imaging. The Journal of Neuroscience, 2006. **26**(18): p. 4940-4948.

29. Pigeau, R.A. and A.M. Frame, *Steady-state visual evoked responses in high and low alpha subjects.* Electroencephalography and Clinical Neurophysiology, 1992. **84**: p. 101-109.

30. Townsend, R.E., A. Lubin, and P. Naitoh, *Stabilization of alpha frequency by sinusoidally modulated light.* Electroencephalography and Clinical Neurophysiology, 1975. **39**: p. 515-518.

31. Koch, S.P., S. Koendodgen, J. Steinbrink, A. Villringer, and H. Obrig. *Resting state alpha-frequency predicts amplitude of evoked electrophysiological and vascular response during visual stimulation.* in *Human Brain Mapping.* 2006. Florence, Italy: Elsevier.

32. Tipler, P.A., *Physics for scientists and engineers.* 4th ed. 1999, New York: W.H. Freeman and Company. 1335.

33. Pruessmann, K.P., M. Weiger, M.B. Scheidegger, and P. Boesiger, *SENSE: Sensitivity encoding for fast MRI.* Magnetic Resonance In Medicine, 1999. **42**(5): p. 952-962.

34. Chia, J.M., S.E. Fischer, S.A. Wickline, and C.H. Lorenz, *Performance of QRS detection for cardiac magnetic resonance imaging with a novel vectorcardiographic triggering method.* Journal of Magnetic Resonance Imaging, 2000. **12**(5): p. 678-688.

35. Mandelkow, H., P. Halder, P. Boesiger, and D. Brandeis, *Synchronisation facilitates removal of MRI artefacts from concurrent EEG recordings and increases usable bandwidth.* Neuroimage, 2006. **32**(3): p. 1120-1126.

36. Mullinger, K.J., P.S. Morgan, and R.W. Bowtell, *Improved Artefact Correction for Combined Electroencephalography/Functional MRI by means of Synchronization and use of VCG Recordings.* Journal of Magnetic Resonance Imaging, 2008. **27**(3): p. 607-616.

37. Mugler, J.P. and J.R. Brookeman, *3-Dimensional Magnetization-Prepared Rapid Gradient-Echo Imaging (3dmp-Rage).* Magnetic Resonance In Medicine, 1990. **15**(1): p. 152-157.

38. Allen, P.J., O. Josephs, and R. Turner, *A Method for removing Imaging Artifact from Continuous EEG Recorded during Functional MRI.* Neuroimage, 2000. **12**(2): p. 230-239.

39. Allen, P.J., G. Poizzi, K. Krakow, D.R. Fish, and L. Lemieux, *Identification of EEG Events in the MR Scanner: The Problem of Pulse Artifact and a Method for Its Subtraction.* Neuroimage, 1998. **8**(3): p. 229-239.

40. Brookes, M.J., K.J. Mullinger, C.M. Stevenson, P.G. Morris, and R.W. Bowtell, *Simultaneous EEG source localisation and artifact rejection during concurrent fMRI by means of spatial filtering.* NeuroImage, 2008. **40**(3): p. 1090-1104.

41. Van Veen, B.D., W. van Drongelen, M. Yuchtman, and A. Suzuki, *Localization of Brain Electrical Activity via Linearly Constrained Minimum*

Variance Spatial Filtering. IEEE Transactions on Biomedical Engineering, 1997. **44**(9): p. 867-880.

42. Basar, E. and M. Schurmann, *Functional aspects of alpha oscillations in the EEG.* International Journal of Psychophysiology, 2001. **39**: p. 151-158.
43. Brookes, M.J., J. Vrba, S.E. Robinson, C.M. Stevenson, A.M. Peters, G.R. Barnes, A. Hillebrand, and P.G. Morris, *Optimising experimental design for MEG beamformer imaging.* Neuroimage, 2008. **39**: p. 1788-1802.
44. Blackledge, J.M., *Digital signal processing.* 2003, Chichester: Horwood Publishing.
45. Polich, J., *On the relationship between EEG and P300:individual differences, again and ultradian rhythms.* International Journal of Psychophysiology, 1997. **26**: p. 299-317.
46. Stevenson, C.M., M.J. Brookes, and P.G. Morris. *The relationship between fMRI and MEG: Visual contrast response.* in *ISMRM.* 2008. Toronto.
47. Field, A., *Discovering Statistics Using SPSS.* 2nd ed. 2005, London: Sage Publications Limited. 779.
48. Brookes, M.J., K.J. Mullinger, G.B. Geirsdottir, C.M. Stevenson, P.G. Morris, and R.W. Bowtell. *Improved artifact rejection for simultaneous EEG/fMRI at 7T using a high EEG channel density and a vector beamformer.* in *ISMRM 2008.* 2008. Toronto.

Chapter 10

Conclusion

10.1 Summary

The work described in this thesis is directed at improving the methodology for simultaneous EEG-fMRI acquisition and applying this knowledge to studies requiring simultaneous data acquisition. This involves understanding the sources of the artefacts in both modalities and the extent to which each of these artefacts limits the acquisition of high quality data.

The sources of artefact in the EEG data due to the MR scanner are discussed in Chapter 5. This chapter highlights the main artefacts in the EEG data as being the gradient and pulse artefacts. Chapter 6 introduces methods which have been developed to improve correction of both of these artefacts. This involves synchronising the EEG and MR scanner clocks to improve the gradient artefact correction; with the results showing that less post-processing filtering is necessary when synchronisation is implemented, as residual artefacts are reduced. This synchronisation allows neuronal signals at higher frequencies to be detected, an attribute which is also demonstrated within this chapter. The work described in Chapter 6 also shows that it is possible to acquire a cleaner cardiac trace than is achievable using the conventional ECG recording (from the EEG system) via the use of the vector cardiogram (VCG), available on the Philips MR scanners. This leads to an easier and more effective VCG-based method for detecting the R-peaks which are a necessary input for the average artefact subtraction (AAS) algorithm used to remove the pulse artefact.

The sources of artefacts in the MR images due to the presence of the EEG hardware are less well characterised than those in the EEG data. Chapter 7 therefore presents the results from a series of experiments aimed at understanding the exact effect the MR compatible EEG system has on the MRI data quality. The results show that the B_0-inhomogeneities are mainly due to the electrodes rather than the leads. The extent of these inhomogeneities is small and localised; therefore they only penetrate the scalp and skull and have no significant effect on brain regions in echo planar images. The B_1-inhomogeneities pose a larger problem for the acquisition of echo planar images. The effects of the longer leads running to the EOG and ECG electrodes are significant, and penetrate into the brain. This RF inhomogeneity has a weak effect on the signal intensity in the echo planar images at 3 T with the effect increasing at 7 T. Investigations into the effect on the SNR due to the introduction of either a 32 or 64 channel cap show that there is a slight reduction in image SNR, which increases with number of electrodes. However, the SNR in image data acquired at 7 T with the 64 channel cap on is still greater than that found in data acquired at 3T with no cap on.

The findings of Chapter 7, along with other advantages of ultra-high field MRI, led us to investigate of the feasibility of performing simultaneous EEG-fMRI at 7 T. Chapter 8 highlights the safety issues to be considered when introducing an EEG system into a high-field MR environment and documents the results of a number of heating tests. From the results of these tests it was deemed safe to perform simultaneous EEG-fMRI at 7 T using the MR compatible Brain Products EEG system with a Philips MR scanner. After a series of tests to identify the main sources of EEG noise in the RF screened room it was found that with the cryocooler pumps off, room lights off and EEG equipment isolated from the vibrations of the MR scanner, it was possible to record EEG and fMRI simultaneously at 7 T on humans. This chapter therefore presents the first results concurrently recorded EEG-fMRI data generated at 7 T using commercially available equipment. We showed that it is possible to detect both driven and oscillatory responses as well as the BOLD response to a visual stimulus. This work has enabled potential benefits of combined EEG/fMRI at 7 T, including the higher BOLD contrast to noise ratio, to be realised in further experiments.

By exploiting the methodology described in the earlier chapters of the thesis, a study was undertaken with the aim of obtaining a greater understanding of the correlation between the neuronal and haemodynamic responses of the brain. The results of this study are presented in Chapter 9. Due to the nature of this investigation, where correlation of the EEG and BOLD responses were being investigated over a small number of trials, it was imperative to have both: simultaneous recordings of EEG and BOLD data and high data quality. This study showed that with the implementation of the techniques which have been described in previous chapters high data quality was achievable. The results showed no significant correlations between the preceding alpha power or driven response and the BOLD response on a trial by trial basis in single subjects. However, when the range of response levels across subjects were considered, a pattern emerged, corresponding to a correlation between the alpha power immediately preceding a visual stimulus and the BOLD response. A second experiment conducted in this study investigated the correlation of the amplitude of the driven neuronal and BOLD responses to visual stimuli of varying frequencies. The results of this experiment show that, whilst an increase in the EEG response at the individual alpha frequency (IAF) is observed, a corresponding decrease in the BOLD response is found at the IAF. The results suggest that a resonance within neuronal networks maybe set up when a stimulus is presented at the subject's IAF.

10.2 The Future

Although the measurements reported in Chapter 9 are, in themselves, very interesting and it is possible to propose a number of hypotheses which would explain the findings, it is important to state that there are a number of other investigations which should be conducted before definitive conclusions are drawn from the data presented in this chapter. When investigating the correlation between the oscillatory neuronal rhythms and the BOLD response there are a number of natural avenues to pursue in order that more information may be drawn from the data already presented. It would be useful to compare the EEG responses in the MR scanner with data similarly acquired outside the magnetic field. By carrying out this investigation the potential explanation that the differences in the EEG responses measured on a trial by trial basis were merely due to noise could be eliminated. Also investigating the phase of the oscillatory rhythms at the time of stimulus presentation may help to explain the differences that were observed in the BOLD and EEG responses. To enable this study, modifications to the experimental paradigm used in Chapter 9 would be necessary so that data from more trials could be acquired. A full analysis of all the EEG frequency bands and how each one correlated to the BOLD response would be a lengthy, but interesting and important progression of this work. This might demonstrate which frequency band is most relevant to the BOLD response. It may be possible to then use the response from a specific frequency band, or combination of bands, to form a regressor in the general linear model to enable a more accurate method for identifying the source of the BOLD activity. It might well prove useful to take these investigations to higher field strengths (7 T) where higher CNR will provide a greater ability to detect small changes in the BOLD response. The move to higher field strength may also allow the areas of BOLD activation due to a stimulus to be identified with greater accuracy. However, care would have to be taken not to compromise the EEG data quality significantly when making the transition to higher field. By conducting some, or all, of the further experiments discussed here the author hopes to gain further understanding of the mechanisms behind brain function.

A natural progression of the work aimed at improving gradient artefact correction, using average artefact subtraction (AAS), is to investigate the effects of movement on the template formed and subsequent artefact removal. Although comparisons of different artefact removal techniques and the quality of the remaining data have been made [1] little consideration has been given to the optimal number of volume acquisitions to average over when performing AAS so as to obtain the 'best' signal quality. The act of movement during scanning changes the gradient artefact waveform at each electrode. Therefore if a single template is formed over the whole scan period, residual artefacts will remain throughout the data set. It is optimal to average over all volumes in the absence of movement; however, the best number of volumes to include in the average becomes less intuitive once movement has occurred within a scan session. I believe it should be possible to incorporate the motion parameters from the fMRI data into the process of correction for the gradient artefact using AAS, thus improving the performance of this correction technique.

10.3 Concluding Remarks

The implementation of simultaneous EEG-fMRI allows an investigator to take advantage of the power behind this multi-modal imaging technique with the high spatial resolution of the fMRI and the superior temporal resolution of the EEG.

Here, improvements to the pre-existing methodology have led to a greater understanding of the sources of the artefacts and the ability to acquire high quality data from both modalities. This has enabled recording of simultaneous EEG-fMRI data at 7 T. The techniques have also been implemented in a study which highlights the potential of this multi-modal technique in increasing our understanding of how neuronal and BOLD signals correlate.

10.4 References

1. Ritter, P., R. Becker, G. Christine, and A. Villringer, *Evaluating gradient artifact correction of EEG data acquired simultaneously with fMRI.* Magnetic Resonance Imaging, 2007. **25**: p. 923-932.

Publications

Articles in Journals:

1. Mullinger KJ, Debener S, Coxon R, Bowtell RW. Effects of simultaneous EEG recording on MRI data quality at 1.5, 3 and 7 tesla. International Journal of Psychophysiology 2008;67(3):178-188.

2. Mullinger KJ, Morgan PS, Bowtell RW. Improved Artefact Correction for Combined EEG/fMRI via Sycnhronization and use of VCG Recordings. Journal of Magnetic Resonance Imaging 2008;27(3):607-616.

3. Mullinger, K.J., Brookes, MJ, Stevenson, CM, Morgan, PS, Bowtell, RW., Exploring the feasibility of simultaneous EEG/fMRI at 7 T. Magnetic Resonance Imaging, 2008. In Press.

4. Debener S, Mullinger KJ, Niazy RK, Bowtell RW. Spatial and temporal properties of the ballistocardiogram artefact as revealed by EEG recordings at 1.5, 3 and 7 Tesla static magnetic field strength. International Journal of Psychophysiology 2007;67(3):189-199.

5. Brookes MJ, Mullinger KJ, Stevenson CM, Morris PG, Bowtell RW. Simultaneous EEG source localisation and artifact rejection during concurrent fMRI by means of spatial filtering. Neuroimage 2008; 40(3):1090-1104.

Conference Contributions:

2006

ISMRM: **1)** Mullinger KJ, Morgan PS, Auer D.P. and Bowtell RW. Functional connectivity of auditory and visual areas during rest and stimulus presentation. Abstract #3261

HBM: **1)** Mullinger KJ, Morgan PS, Bowtell RW. Improved Artifact Correction for Combined EEG/fMRI Abstract # 164 W-PM

2) Mullinger KJ, Morgan PS, Auer D.P. and Bowtell RW. Functional connectivity of auditory and visual areas during rest and stimulus presentation. Abstract #194 TH-PM

BcISMRM **1)** Mullinger KJ, Morgan PS, Bowtell RW. Improved Artifact Correction for Combined EEG/fMRI Abstract # O6

2007

ISMRM: **1)** Mullinger KJ, Brookes MJ, Stevenson CM, Clemence M, Morgan PS, Nockowski CP, Profusz S, and Bowtell RW. Exploring the feasibility of simultaneous EEG/fMRI at 7T,. Abstract # 3322

2) Mullinger KJ, Bungert AS, Coxon R, Foxhall D, Debener S, Morgan PS and Bowtell RW. Effects of Simultaneous EEG Recording on MRI Data Quality. Abstract # 3439

3) Mullinger KJ, Morgan PS, Bowtell RW. Improved Artifact Correction for Combined EEG/fMRI Abstract #3441

4) Brookes MJ, Mullinger KJ, Stevenson CM, Morris PG, Bowtell, RW. Noise Reduction in combined EEG/fMRI Using a Vector Beamformer Abstract # 699.

HBM: 1) Mullinger KJ, Brookes MJ, Stevenson CM, Clemence M, Morgan PS, Nockowski CP, Profusz S, and Bowtell RW. Exploring the feasibility of simultaneous EEG/fMRI at 7T,. Abstract # 243 M-AM

2) Mullinger KJ, Bungert AS, Coxon R, Foxhall D, Debener S, Morgan PS and Bowtell RW. Effects of Simultaneous EEG Recording on MRI Data Quality. Abstract # 244 M-PM

3) Debener S, Mullinger KJ, Niazy R, Bowtell RW. The ballistocardiogram EEG-fMRI artefact at 1.5, 3 and 7T static magnetic field strength. Abstract # 235 M-AM

2008

ISMRM: **1)** Mullinger KJ, Geirsdottir GB, Brookes MJ, Liddle PF, Bowtell RW. Exploring the relationship between natural fluctuations in electrical measures of brain activity and the BOLD response during visual stimulation. Abstract #3102

2) Brookes MJ, Mullinger KJ, Geirsdottir GB, Stevenson CM, Morris PG, Bowtell RW. Improved artefact rejection for simultaneous EEG/fMRI at 7T using high EEG channel density and a vector beamformer. Abstract # 2429

3) Brookes MJ, Mullinger KJ, Stevenson CM, Geirsdottir GB, Bowtell RW. Electrical and haemodynamic effects measured using MEG and combined EEG/fMRI. Abstract # 2430.

4) Geirsdottir GB, Brookes MJ, Mullinger KJ, Yan WX, Morris P, Bowtell RW. A model phantom for investigating concurrent EEG/fMRI. Abstract #3626